UNIVERSITY OF SOUTHAMPTON

FACULTY OF ENGINEERING AND THE ENVIRONMENT

Institute of Sound and Vibration Research

Analytical modelling of the vibration of railway track

by

Dimitrios Kostovasilis

Thesis for the degree of Doctor of Philosophy

June 2017

UNIVERSITY OF SOUTHAMPTON

ABSTRACT

FACULTY OF ENGINEERING AND THE ENVIRONMENT
Institute of Sound and Vibration Research

Doctor of Philosophy

ANALYTICAL MODELLING OF THE VIBRATION OF RAILWAY TRACK

by Dimitrios Kostovasilis

The high frequency dynamic behaviour of railway track, in both vertical and lateral directions, strongly affects the generation of rolling noise as well as other phenomena such as rail corrugation. One aspect that has received little attention is the coupling between the vertical and lateral directions. This thesis sets out to build an analytical model of a railway track with three principal targets: to improve the modelling for lateral vibration compared with existing models, to identify the most important sources of coupling between the vertical and lateral directions and to quantify the implications for rolling noise phenomena.

Simple models for the axial, torsional, vertical and lateral vibrations of beams are first introduced. The results from these models are analysed based on their dispersion curves and their characteristic behaviour is identified. Furthermore, effects of cross-section asymmetry, shear deformation, rotational inertia, restrained warping and curvature are considered, as well as the fact that the loads at the rail head do not always act through the centroid of the rail section. These beam models are then brought together to formulate a fully coupled beam model.

An elastic foundation is then introduced to the beam model to represent the railpads and the dispersion characteristics of the whole track are discussed. Subsequently, the effect of the foundation location is investigated, as well as the inclusion of additional layers of masses and springs, representing the sleepers and ballast. Two different sleeper models are introduced. The first is that of a simple mass allowed to translate and rotate, representing a single block of a bibloc sleeper. The second is that of a flexible finite length beam accounting for vertical, lateral, axial and torsional vibration, representing a monobloc sleeper, which is more widely used in railway tracks. The response of the beam model is compared against measurements performed on sleepers in the laboratory. An average error of less that 1% is observed for the natural frequency of all modes, excluding the first mode. This mode is most influenced by the sleeper cross-section variation which is not directly accounted for in the model.

Using the new track model, the forced response is analysed in terms of mobility and track decay rates. These are used to investigate the effect of vertical/lateral coupling, support eccentricity, cross-section asymmetry and track curvature. The point and cross mobilities are also compared with a more detailed model obtained using the Waveguide Finite Element approach, for both singly-symmetric and asymmetric rail sections. Finally the model is compared with three sets of measurements of mobilities and track decay rates. The first is for a test track at the University of Southampton while the other two are from an operational site at Fishbourne. The model shows improved predictions for the lateral response of the track and a means to more accurately calculate the cross mobility.

Finally, the developed track model is implemented in an existing model of rolling noise (TWINS, 'Track Wheel Interaction Noise Software'), in order to demonstrate the implications of vertical/lateral coupling, particularly through the support eccentricity and inclusion of torsion, on the noise radiated from the track. Noise measurements from the site at Fishbourne are utilised, and a comparison between the new track model and the current empirical procedure for vertical/lateral coupling in TWINS is made. Although no firm conclusions are drawn as to whether the present beam model gives improved predictions over the existing Timoshenko beam model used in TWINS, it is preferred due to the improved modelling capacity. Finally, recommendations are given for the influence of the wheel/rail contact locations on the noise radiated from a railway track, and how the empirical factor should be used.

Contents

List of Figures

List of Tables

Declaration of Authorship

I, Dimitrios Kostovasilis, declare that the thesis entitled *Analytical modelling of the vibration of railway track* and the work presented in the thesis are both my own, and have been generated by me as the result of my own original research. I confirm that:

- this work was done wholly or mainly while in candidature for a research degree at this University;
- no part of this thesis has previously been submitted for a degree or any other qualification at this University or any other institution;
- where I have consulted the published work of others, this is always clearly attributed;
- where I have quoted from the work of others, the source is always given. With the exception of such quotations, this thesis is entirely my own work;
- I have acknowledged all main sources of help;
- where the thesis is based on work done by myself jointly with others, I have made clear exactly what was done by others and what I have contributed myself;
- parts of this work have been published as: Kostovasilis et al. [1, 2]

Signed:.....

Date:.....

Acknowledgements

I would like to thank my supervisors, Prof. David J. Thompson and Dr Mohammed F.M. Hussein, for their continuous support and guidance. Both in their own ways, have helped me at various stages of my research degree, and in my personal life. My gratitude also extends to my examiners, Prof. Jens C.O. Nielsen and Dr Giacomo Squicciarini, as well as my internal reviewer Dr Neil S. Ferguson, for asking challenging questions and conducting fruitful discussions regarding my research during the viva examination and internal reviews.

For providing technical advice and assistance with the measurements presented in this thesis, I am grateful to Dr Martin G.R. Toward and Dr Michał K.K. Kalkowski, as well as the technical staff from the Institute of Sound and Vibration Research.

This thesis is the result of research funded by the Engineering and Physical Sciences Research Council, grant reference 1342762, and Network Rail under an Industrial CASE studentship. Their support is greatly acknowledged. All key data supporting the work in this thesis are openly available from the University of Southampton repository at http://dx.doi.org/10.5258/SOTON/D0097

On a more personal note, I would like to express my appreciation towards all friends and colleagues from the University of Southampton, who made every day special and unique. Special mention should be made of Dr Samuel G. Koroma, Dr Michał K.K. Kalkowski, Mr Andrea Ricci, Dr Evangelos Ntotsios and their partners, as well as Dr Giannoula Mitrou, all of whom took great care of me and offered me their friendship and companionship. For their endless encouragement, understanding, mentally challenging and restless discussions, I would like to thank Dr Sana Rashid and Mr Nikolaos Sfakianos.

Lastly and most importantly, my deepest gratitude goes to my parents, Kanella and Lampros, and my brother Konstantinos. They have not only supported me in achieving what I pursued, but also acted as a constant source of inspiration and motivation.

Nomenclature

A	Cross-section area (m^2)
A_n	Wave amplitude for wave n (m)
$\mathbf{A}$	Dynamic stiffness matrix
$\mathbf{A}_{1,2}$	Matrices for linearised eigenvalue problem
A^S	Effective area for shearing (m^2)
b	Breadth of beam cross-section (m)
c	Centre of mass
c_L	Phase velocity of compressional waves in a beam (m/s)
c_S	Phase velocity of shear waves in a beam (m/s)
c_T	Phase velocity of torsional waves in a beam (m/s)
dF	Infinitesimal force (N/m)
dM	Infinitesimal moment (Nm/m)
dx	Length of infinitesimal element (m)
$d\theta$	Subtended angle of infinitesimal element (degrees)
$\mathbf{D}^*$	Differential matrix operator
E	Young's modulus (Pa - N/m^2)
e_l	Eccentricity for lateral external load (m)
e_s	Distance between rail foot and shear centre (m)
e_v	Eccentricity for vertical external load (m)
e_y	Vertical shear centre to centroid distance (m)
e_z	Lateral shear centre to centroid distance (m)
f	Natural frequency (Hz)
f_a	Factor for effective dynamic stiffness of equivalent sleeper
$f_{co,1}$	Cut-on frequency for breathing mode (Hz)
$f_{co,2}$	Cut-on frequency for lateral shear wave of curved beam (Hz)
$f_{co,3}$	Cut-on frequency for torsional mode of a ring (Hz)
$f_{co,4}$	Cut-on frequency for vertical shear wave of curved beam (Hz)
$f_{co,a}$	Cut-on frequency for axial waves in supported rail (Hz)
$f_{co,n}$	Cut-on frequency for wave n, where n = i, iii, I or II (Hz)
$f_{co,l}$	Cut-on frequency for lateral wave of supported rail (Hz)
$f_{co,t}$	Cut-on frequency for torsional wave of supported rail (Hz)
$f_{co,v}$	Cut-on frequency for vertical wave of supported rail (Hz)

$f_{s,v/l}$	Cut-on frequency of shear waves in vertical or lateral direction (Hz)
f_w	Warping displacement measure (rad/m)
F	Point force (N)
$\mathbf{F}$	Vector of reaction forces
F_w	Warping complex amplitude
F_i	Force in the i-axis (N)
$\tilde{F}_i$	Excitation force in the i-axis (N/m)
$\tilde{F}^e_{i,c}$	Excitation force in the i-axis acting at the centroid (N/m)
$\tilde{F}^R_{i,c}$	Reaction force in the i-axis acting at the centroid (N/m)
$\tilde{F}$	External force vector
$\mathbf{F}^{ps}_{r,c}$	Effective railpad reaction force vector for rail centroid
$\mathbf{F}^{ps}_{r,f}$	Effective railpad reaction force vector for rail foot
$\mathbf{F}^{sb}_{s,b}$	Effective ballast reaction force vector for sleeper bottom
$\mathbf{F}^{ps}_{s,c}$	Effective railpad reaction force vector for sleeper centroid
$\mathbf{F}^{sb}_{s,c}$	Effective ballast reaction force vector for sleeper centroid
G	Shear modulus ($= E/2(1+\nu)$) (Pa - N/m^2)
h	Height of beam cross-section (m)
I_p	Polar moment of area (m^4)
$\hat{I}$	Moment of area accounting for effect of curvature (m^4)
I_w	Warping constant (m^6)
I_{wwy}	Warping product moment of area around the wwz axis (m^7)
I_{wwz}	Warping product moment of area around the wwy axis (m^7)
I_{wy}	Warping product moment of area (m^5)
I_{wyy}	Warping product moment of area around the wzz axis (m^6)
I_{wyz}	Warping product moment of area around the wzy axis (m^6)
I_{wz}	Warping product moment of area (m^5)
I_{wzz}	Warping product moment of area around the wyy axis (m^6)
I_y	Second moment of area about y-axis (m^4)
I_{yz}	Product moment of area (m^4)
I_z	Second moment of area about z-axis (m^4)
J	Torsional constant (m^4)
J^s	Secondary torsional constant (m^4)
$k_{b,i}$	Ballast stiffness per unit length in the i direction (N/m^2)
$k_{b,ri}$	Ballast rotational spring stiffness per unit length in the i direction (N)
k_i	Railpad stiffness per unit length in the i direction (N/m^2)
$\hat{k}_i$	Curvature due to bending along the i-axis (1/m)
$\bar{k}_i$	Curvature due to bending along the i-axis for a curved beam (1/m)
k_{ri}	Railpad rotational spring stiffness per unit length in the i direction (N)
$\mathbf{K}^D_s$	Sleeper dynamic stiffness matrix in global co-ordinates
$\mathbf{K}^D_{s,l}$	Sleeper dynamic stiffness matrix for lateral response
$\mathbf{K}^D_{s,loc}$	Sleeper dynamic stiffness matrix for response in local co-ordinates

$\mathbf{K}_{s,v}^{D}$	Sleeper dynamic stiffness matrix for vertical response
$\mathbf{K}_0$	Matrix of coefficients of $(-i\xi)^0$ in dynamic stiffness matrix
$\mathbf{K}_1$	Matrix of coefficients of $(-i\xi)^1$ in dynamic stiffness matrix
$\mathbf{K}_2$	Matrix of coefficients of $(-i\xi)^2$ in dynamic stiffness matrix
$\mathbf{K}_b$	Matrix of stiffnesses for ballast support layer
$\mathbf{K}_p$	Matrix of stiffnesses for pad support layer
l_p	Rail foot/pad width (m)
l_{ss}	Sleeper spacing distance (m)
L	Length of finite beam (m)
L_e	Effective radiating length (m)
m	Mass (kg)
$\mathbf{M}$	Mass matrix
M_i	Moment around the i-axis (Nm)
$\tilde{M}_i$	Excitation moment around the i-axis (Nm/m)
$\tilde{M}_{i,c}^{e}$	Excitation moment around the i-axis acting at the centroid (Nm/m)
$\tilde{M}_{i,c}^{R}$	Reaction moment around the i-axis acting at the centroid (Nm/m)
$\mathbf{M}_r$	Matrix of distributed inertial properties for rail
$\mathbf{M}_s$	Matrix of distributed inertial properties for sleeper layer
M_w	Bi-moment due to warping (Nm^2)
n_t	Number of terms for truncation of series expansion
$n_{y/z}$	Gradient
N	Number of eigenvalues
$\partial/\partial n$	Derivative in direction n
$\mathbf{P}$	Volume forces vector (external forces)
Q_{ir}	Static moment of area around i-axis (m^3)
R	Radius of curvature (m)
s	Propagation constant ($s = i\xi$)
S	Shear centre
t	Time (s)
$\mathbf{T}$	Co-ordinate transformation matrix
u_i	Displacement in the i-axis (m)
U_i	Complex amplitude of displacement in the i-axis (m)
$\mathbf{u}$	Vector of complex amplitudes for eigenvalue problem
$\mathbf{U}$	Receptance vector
$\tilde{\mathbf{U}}$	Vector of complex amplitudes
$\mathbf{V}$	Mobility vector
w	Width of cross-section (m)
W	Total radiated power (dB(A))
W_e	Exponential window function
W_n'	Radiated sound power per unit length for wave n (dB re 10^{-12} Watts)
x, y and z	Coordinates in principal axis system

x_0	Location of application of load from beam end (m)
y_f, z_f	Location of foundation from rail centroid (m)
y_{sb}, z_{sb}	Location of sleeper bottom surface from sleeper centroid (m)
y_{st}, z_{st}	Location of sleeper top surface from sleeper centroid (m)
α_{jk}	Receptance due to a force F_k in direction j (m/N)
β_{kn}	Partial receptance of wave n for a force F_k in direction k (m/N)
γ_{xy}, γ_{xz}	Shear strain components in the xy and xz planes due to flexure
$\bar{\gamma}_{xy}$, $\bar{\gamma}_{xz}$	Shear strain components due to flexure for a curved beam
δ_n	Real part of propagation constant for wave n
Δ	Decay rate (dB/m)
Δ_{min}	Minimum decay rate calculated based on experimental method (dB/m)
ϵ	Generalised strain vector
ϵ_0	Axial strain component due to extension
ϵ_{xx}	Axial strain
ϵ_{xy}, ϵ_{xz}	Shear strain in the xy and xz planes
η	Loss factor
θ_i	Rotation about the i-axis (rad)
Θ_i	Complex amplitude of rotation about the i-axis (rad)
κ_w	Linearised warping factor for rail foot (Nm^2)
κ_y	Vertical shear coefficient
κ_z	Lateral shear coefficient
κ_S	Shear coefficient for torsion
λ	Eigenvalue satisfying $\mathbf{A}_1'\mathbf{v}+\lambda\mathbf{A}_2'\mathbf{v}=0$
ν	Poisson's ratio
ξ	Wavenumber (rad/m)
ρ	Density ($\mathrm{kg/m}^3$)
σ	Normal stress ($= E\epsilon$)(Pa - $\mathrm{N/m}^2$)
σ	Generalised stress vector (internal forces)
τ	Shear stress ($= G\hat{\gamma}$)(Pa - $\mathrm{N/m}^2$)
ϕ	Warping function as a function of y and z (m^2)
ϕ^p	Primary warping function as a function of y and z (m^2)
ϕ^s	Secondary warping function as a function of x, y and z (m)
ψ_{jn}	Wave displaced shape per wave n in direction j
$\mathbf{\Psi}^{L,R}$	Matrix of left and right eigenvectors
ω	Circular frequency (rad/s)

Superscripts

e	Excitation forces
M	Measured
p	Primary
P	Predicted

pp	Per pad
ps	Pad/sleeper interface
pw	Per wave
R	Reaction forces
s	Secondary
sb	Sleeper/ballast interface
T	Transpose matrix operation

Subscripts

c	Centroid
e	Effective
f	Foot
F	Point of application of force
g	Global
n	Wave identifier
r	Rail
s	Sleeper
S	Shear centre
sv	Saint-Venant theory
w	Warping

Abbreviations

BEARS	Boundary Element Acoustic Radiation Software
BEM	Boundary Element Method
CHIEF	Combined Helmholtz Integral Equation Formulation
EMU	Electric Multiple Unit
FE	Finite Element
SPL	Sound Pressure Level
TDR	Track Decay Rate
TWINS	Track/Wheel Interaction Noise Software
WFE	Waveguide Finite Element

Chapter 1

Introduction

Noise and vibration from railway tracks in close proximity to residential areas are a major concern and source of annoyance for residents near those lines. Railway noise arises from various parts of the railway system. The main sources include [3, 4]: propulsion noise associated with electric traction motors or electromagnets, control units, and associated cooling fans; rolling noise attributed to imperfections of the wheel and rail running surfaces and is dominant for most railway lines; aerodynamic noise which is typically dominant for speeds in excess of 350 km/h; and curve squeal created by the lateral creepage between the wheel and rail, which becomes dominant in tight curves (e.g. tight tram curves).

Other sources exist, such as noise due to infrastructure (e.g. bridges) or noise due to local imperfections of the wheel (e.g. wheel flats) or rails (e.g. joints, welds etc.), which, including curve squeal, are local sources of noise in the railway network. On the other hand, propulsion, rolling and aerodynamic noise are present throughout the railway network, although not always at significant levels. Figure 1.1 indicates the approximate dominance of the propulsion, mechanical (rolling noise and curve squeal) and aerodynamic noise to the total noise as a function of speed according to Hanson et al. [3].

Propulsion noise has a low dependence on speed and is dominant only at low speeds [5], while aerodynamic noise becomes dominant at speeds in excess of 350 km/h [4]. Between these speed regions, rolling noise remains dominant and is considered as the main source of environmental noise from railway operations. Rolling noise has received, and still receives, a lot of attention from the scientific community and efforts are made to understand better its mechanisms of generation, in order to predict and control the noise levels of current and newly designed tracks and to design mitigation measures to reduce them.

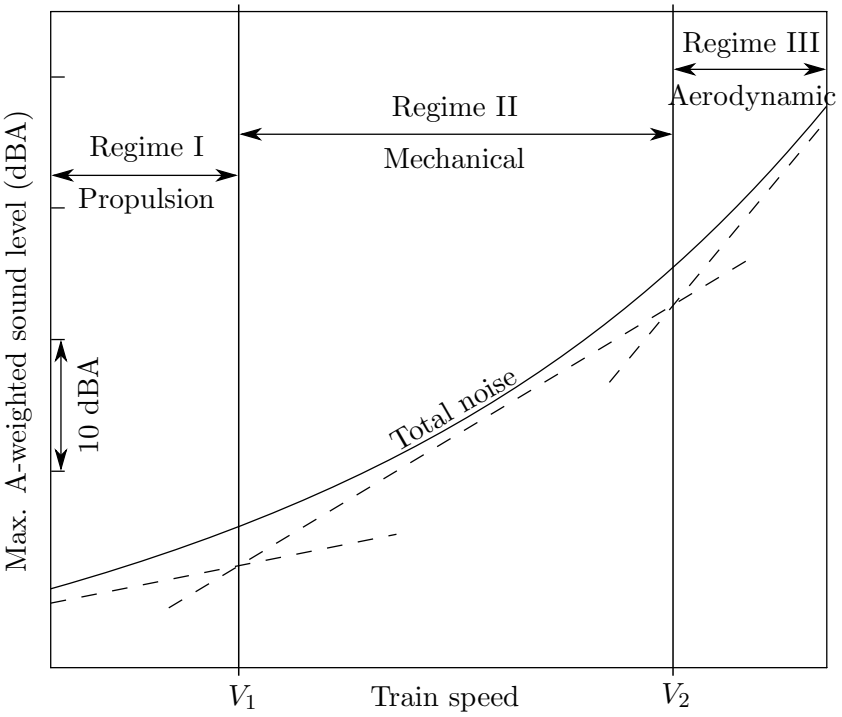

Figure 1.1: Dominant sources of railway noise at different speeds (redrawn from [3])

1.1 Literature review

Figure 1.2 shows the structure of a typical railway track, consisting of rails fastened by rail clips on concrete, wooden, plastic or metal sleepers laid in ballast above a subgrade. In order to avoid damage to the sleepers, elastic pads are placed between the rails and the sleepers in order to absorb high impact loads [4]. In addition, the stiffness of the rail pads has a significant influence on rolling noise. The vertical stiffness of the fastening mechanism is primarily controlled by the rail pad stiffness. Although the fastening clips apply a preload, their stiffness is negligible, at least for the vertical direction. The lateral stiffness of the fastening mechanism is controlled by both the rail pads and the fastening assembly. In the context of this thesis, the subgrade layer will not be considered.

In this section, an overview of previous studies on rolling noise is presented. Since the main focus of this thesis is the track (exluding the subgrade), an in-depth review of various aspects of track dynamic modelling is also presented, including modelling approaches, solution methods and existing models.

1.1.1 Rolling noise

An overview of the mechanism of rolling noise generation is shown in Fig. 1.3, where a wheel is shown running over a rail with a rough surface. It was first shown by Remington

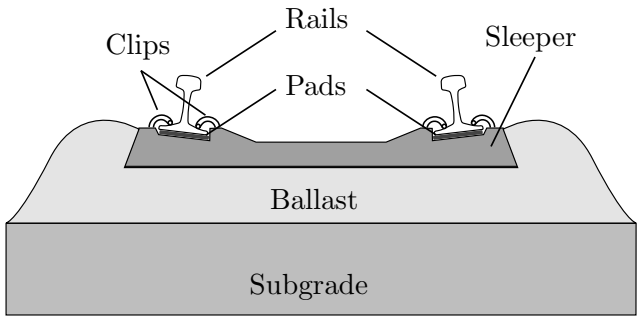

Figure 1.2: Typical railway track components

[6] that the dynamic forces generated by surface roughness during the passage of a vehicle on a tangent track are capable of exciting the wheel and rail sufficiently to cause the measured noise levels during a train pass-by. The roughness on the running surface of the wheel and rail induces a relative vibration between the two structures. This excites the wheel and track into vibration, which in turn radiates sound. For a periodic irregularity, the vibration frequency is given by the speed of the train divided by the irregularity wavelength. The dynamic characteristics of both systems also affect the relative vibration of the two bodies. At any given frequency, the radiation efficiency (relating the sound power radiated by a vibrating structure to the averaged velocity over the radiating area) and directivity of the individual system are also significant in dictating the overall contribution of each component to the total sound generated.

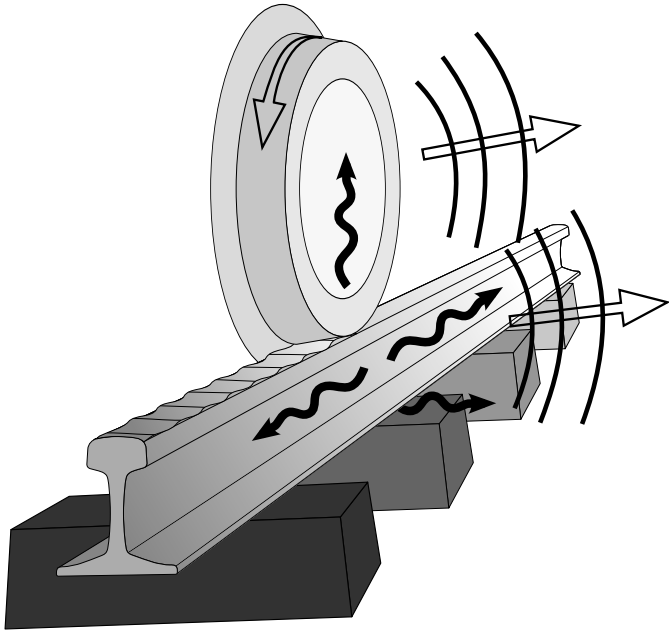

Figure 1.3: Source components of rolling noise (redrawn from Thompson [4])

Sound is perceived over a wide range of frequencies, with the audible range for a young healthy adult being between 20 Hz and 20 kHz [7]. The sensitivity of the human ear

is different at different frequencies, with the highest sensitivity observed in the range between 1 kHz and 5 kHz. In order to take into account the sensitivity of the human ear, weighting curves for the sound pressure level have been created. The most commonly used weighting is the A-weighting curve [8], shown in Fig. 1.4. A-weighted values are abbreviated with the letter A (e.g. A-weighted decibels are indicated as dB(A) or dBA). According to [4], the frequency range of interest for rolling noise currently extends from around 100 Hz to 5 kHz. Low frequencies are typically dominated by aerodynamic noise (at least at high speeds) while the A-weighting curve suppresses their overall contribution. Noise contributions at frequencies above 5 kHz are reduced due to the contact filter (see below). In the review of Knothe and Grassie [9], the upper frequency limit of interest for rolling noise is also indicated as 5 kHz.

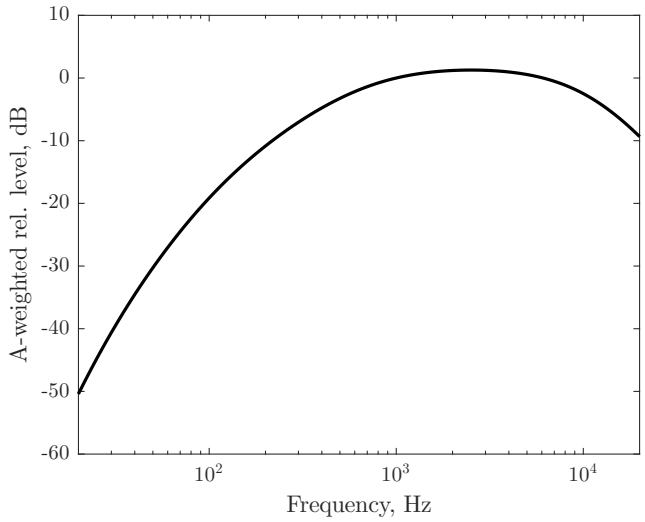

Figure 1.4: Relative decibel level based on the A-weighting curve [8]

1.1.2 Modelling of rolling noise

In early studies on rolling noise, contradictory results have been documented regarding the relative influence of wheels and rails. For example, by comparing noise measurements to predicted noise levels from a wire, Peters et al. [10] suggested that the rail is not a dominant source although it can influence the sound radiated. On the other hand, by modelling the rail as an elastic beam on a continuous support and the wheel as a rigid mass, Bender and Remington [11] concluded that the rail may dominate at mid- and high-frequencies (around 500 Hz and 5 kHz) but is less important than other sources outside those regions. In a subsequent study on rolling noise by Remington [12], improved models for both the wheel and track were used and it was found that the rail dominates in a frequency range between 400 Hz and 1.6 kHz while the wheel dominates below 300 Hz and above 2 kHz. By further extensions to the model, Remington and Stahr [13] concluded that below 2 kHz the rail dominates the sound radiated while above that frequency it is the wheel that acts as the main contributor. Both modelling

capabilities and understanding of rolling noise phenomena have since seen significant improvement. The current understanding is that the track dominates the low frequency radiated sound (below about 1-2 kHz) while the wheel dominates the higher frequency region with the rail still maintaining a significant contribution up to about 5 kHz [4, 14].

The first comprehensive analytical model of rolling noise was presented by Remington [15, 16]. It began with the wheel and rail roughness, which was filtered in order to exclude the components of roughness that have a wavelength comparable with the length of the contact area (contact filter). The wheel/rail interaction forces were derived accounting for a contact spring between the two bodies, where the rail was represented by an infinite beam in bending and the wheel as an infinite curved beam vibrating in the plane and out of the plane of curvature, accounting for the radial and axial response respectively. Cross terms for the vertical response due to lateral contact forces and vice versa were also considered. Once the contact forces were estimated, the wheel and rail sound powers were adjusted to account for ground reflection effects in the transmission path and were summed in order to produce the total wheel/rail noise level. One of the drawbacks of this work was the neglect of sound radiation from the sleepers and from the lateral motion of the rail. In addition, although the whole noise generation process was covered, the constituent parts were oversimplified. For example, an Euler-Bernoulli beam was used for the rail, which as will be seen later is insufficient for frequencies above 500 Hz.

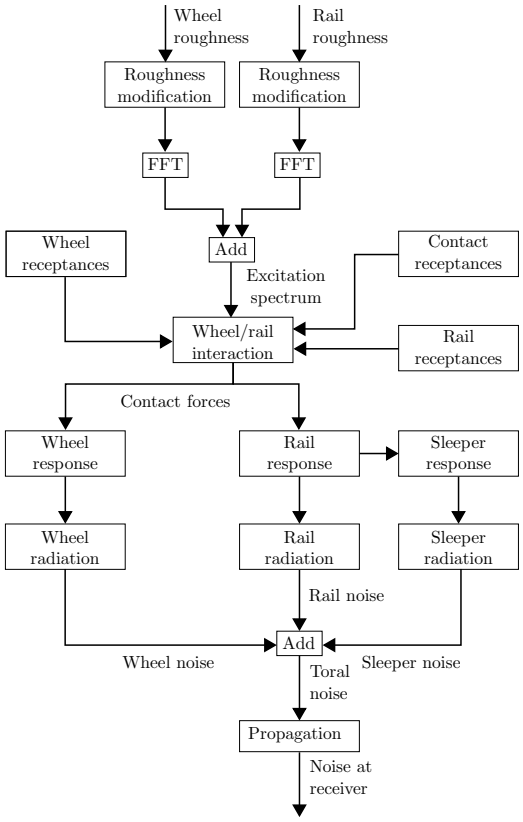

Figure 1.5: Rolling noise overall prediction model (after Thompson et al. [17])

Following a similar approach, Thompson [18, 19, 20, 21, 22] improved the description of the wheel and rail response. The Finite Element method was used for both structures (also an improved infinite beam model was considered for the rail), and the sleeper response, as well as the wheel rotation and additional contact details, were taken into account. These improvements allowed for additional aspects of rolling noise to be investigated and understood, and led to improved agreement with measurements. This work was later developed into a software package, called TWINS ('Track/Wheel Interaction Noise Software') and was validated against experiments [17, 23] for both passenger and freight vehicles. Overall the model was shown to provide good estimates of rolling noise, especially when the sound pressure was compared in 1/3 octave bands. Further comparisons with measured data have been performed since then with additional refinements of the software (e.g. [24], [25]).

The workflow of the TWINS model is shown in Fig. 1.5. Apart from the improved description of the track and wheel responses using the FE method, two more main differences are identified between TWINS and the model developed by Remington [15, 16]. Firstly, in addition to the wheel and rail receptances (displacement per unit force), in TWINS also the contact receptance is considered, and all three are combined along with the excitation spectrum to determine the wheel/rail interaction forces. Secondly, apart from the wheel and rail responses, in TWINS also the sleeper response is considered, further improving the predictions, especially at lower frequencies.

Over the past couple of decades, TWINS has been used in a variety of applications leading to better understanding of the rolling noise generation mechanism and the parameters that affect it. Some example cases where TWINS was used include a study of track components that influence rolling noise [26], the development of a tuned device for reducing track noise [27] and more recently a study of the effect of temperature on rolling noise [28]. It is also routinely used in assessing wheel designs.

In Fig. 1.6, a typical prediction using TWINS is presented, from [4], showing the contributions of wheel, rail and sleeper components to the total sound pressure level (SPL). Although this is a study for a specific wheel/track combination with a relatively soft rail pad stiffness of 200 MN/m, it reflects the typical relative contribution of each component. It is seen from this figure that the track (sleeper and rail) contributions dominate the response up to about 2 kHz (approximately 25 dB higher than the wheel at 800 Hz), while at higher frequencies the wheel dominates the response (8-10 dB higher than the rail up to 5 kHz). Thompson [29] also showed that for a particular wheel/track combination at train speeds below 120 km/h the track will have more significant contribution to the total noise level, with the wheel having a more dominant behaviour at higher speeds.

As the modes of the wheel are important at high frequencies, these are calculated in TWINS using a finite element model of the particular wheel design and input as a list

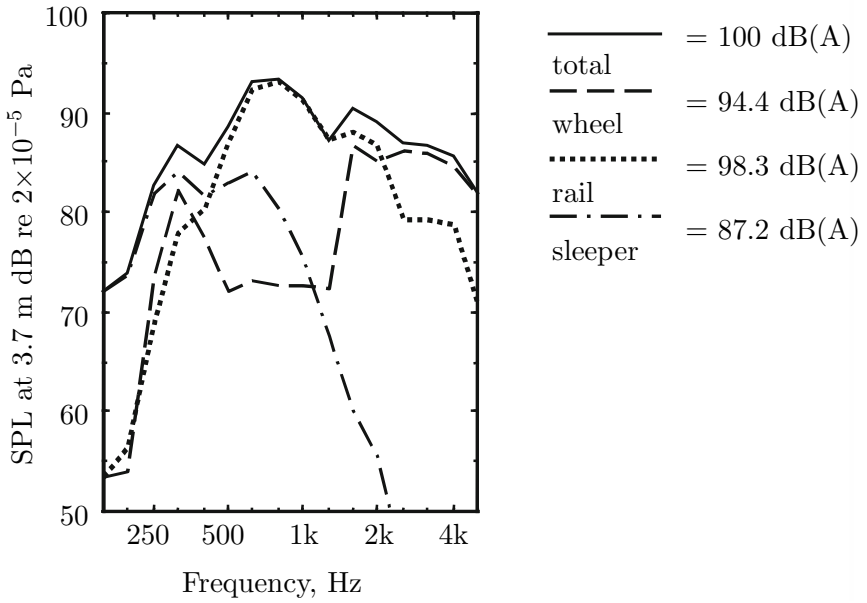

Figure 1.6: Relative contributions of wheel, rail and sleeper components to total noise based on predictions from TWINS with a rail pad stiffness of 200 MN/m (redrawn from [4, 23])

of modal parameters (natural frequencies, damping ratios and modeshapes). In order to provide rapid calculations, the track response is usually solved analytically, being represented as beam on a two-layer elastic foundation for both vertical and lateral dynamics. For the vertical response due to a lateral load and vice versa, the FE wheel model readily provides the required responses. In contrast, for the rail, empirical relationships are used based on measurements.

Vincent et al. [26] identified three main components of track radiation in the frequency range 100 Hz to 5 kHz, namely: the sleeper radiation (vertical vibration of upper side of the sleeper); the rail radiation due to vertical waves propagating along the rail; and the rail radiation due to the lateral/torsional waves propagating along the rail. It was also indicated that the relative contribution of vertical and lateral components depends mainly on the lateral position of the contact between the wheel and rail and on the attenuation of the waves along the rail (track decay rate).

The track decay rate is an important parameter in rolling noise generation. A low decay rate means that waves can propagate further along the track and thus a larger surface area of the rail vibrates, generating higher sound power. The attenuation of lateral and torsional waves is often lower than that of vertical waves, and in the case of a significant offset of the contact, the lateral component of noise may reach and even exceed the vertical component in terms of radiated power [26]. Thompson [30] indicated that the lateral rail vibration is less well described by the current beam models, as torsion tends to make the beam more flexible than the pure bending theory implies.

It is clearly seen that the dynamic behaviour of railway tracks at mid to high frequencies and their noise radiation characteristics are particularly important in the generation of rolling noise, including the response in both the vertical and lateral directions. Many analytical models can be found in the literature that focus on the vertical and to a lesser extent the lateral vibration of the track, but the coupling between the vertical and lateral directions has been considered in much less detail.

It has been shown in the literature [20] that various coupling effects will occur, especially for higher frequency excitations. These effects are mainly attributed to the form of the rail cross-section which is either singly-symmetric (mainline tracks, typical cross-section of a 60E1 rail is shown in Fig. 1.7) or fully asymmetric (tram tracks). As a result, the centroid (c) at which the inertial forces act, and the shear centre (S) at which the shear forces act, are not coincident, introducing a coupling between lateral bending and torsion [31]. In addition, for a curved track, the vertical bending will couple with the torsion and the lateral bending with the axial response [32]. Furthermore, the rails are seldom excited at the centre of the railhead by a purely vertical force. In most cases, the load will have both a vertical and a lateral component, and the contact point will be offset from the rail centreline. Finally, reaction forces from the foundation will also be a source of coupling, especially in the case of the lateral response where the foundation force is applied with some vertical eccentricity relative to the rail centroid. Although previously known, the above issues have not been studied in depth for railway applications. Therefore, the question is raised to what extent these coupling phenomena will affect the track response and noise radiation.

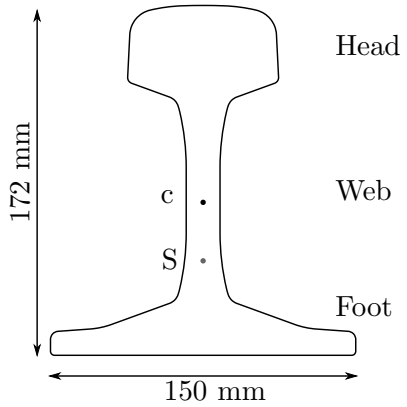

Figure 1.7: Typical rail cross-section (60E1)

1.1.3 Beam theories used for track dynamic models

The first known investigation into railway track dynamic behaviour was conducted in 1867 by Winkler. This was based on an infinite beam resting on an elastic foundation

(BOEF) [33]. Although limited, this model is still used by many researchers and engineers due to its simplicity. Since then, a lot of research has focused on many aspects of track dynamics such as, for example, the beam theories used to represent the rail, the nature of the support etc.

The dynamic properties of beams are most often studied using the Euler-Bernoulli beam theory [34]. This theory was introduced by Jacob Bernoulli in the 18th century and was later used by Leonard Euler for the investigation of elastic beams. The theory provides a simple yet reasonable model used for many engineering applications. The main assumption is that plane sections remain plane and perpendicular to the neutral axis. This means that it can be applied accurately only when the cross-section is much smaller than the wavelength of the motion. It thus tends to overestimate the natural frequencies of higher modes (of a finite beam) when this assumption no longer applies. For railway track applications, the maximum frequency of validity is shown to be approximately 500 Hz for vertical track dynamics [9], above which shear deformations and rotational inertia become significant and should be accounted for.

In an attempt to improve this model, Lord Rayleigh [35] introduced the effect of rotational inertia, and although this improved the accuracy, the natural frequencies were still overestimated. The next step was to introduce the effects of shear distortion, which would improve significantly the calculation of the natural frequencies of a beam. Timoshenko [36, 37] proposed a beam theory in which both the shear deformation and rotational inertia of the beam were taken into account, leading to a wider range of applicability. This model is applicable up to about 5 kHz for vertical vibration in typical railway track applications [29].

For most studies of railway track vibration, and depending on the frequency range of interest, the Euler-Bernoulli and Timoshenko beam theories are used for vertical track dynamics. Generally, when the interest is ground vibration, the Euler-Bernoulli beam theory is sufficient since the frequency range of interest is typically limited to about 250 Hz [4]. For investigation of rolling noise phenomena, the Timoshenko beam theory is preferred since the frequency range of interest extends up to about 5 kHz [18].

The beam on elastic foundation model can also be used to describe the lateral motion of the rail. However, in this way the lateral response is not as accurately predicted as the vertical response due to the omission of torsion [4]. Moreover, higher order lateral modes of vibration occur, such as web bending, causing greater differences between the simplified model and measurements [29].

1.1.4 Continuously and discretely-supported dynamic models

Railway track dynamic models can be separated into two main categories based on the nature of their support [9]: those with a continuous support and those with discrete supports. Although models with a continuously supported rail do not show all the features of a railway track, they demonstrate the most important characteristics of its dynamic behaviour [4]. Conventional railway tracks are supported discretely by the railpads and sleepers and thus a discretely supported model is usually more appropriate. Such models can be further divided into periodically supported models with uniform support stiffness and more general discretely supported models which may include variations in spacing and/or stiffness. Because of the complexities of the latter, either continuous or periodic supports are most often used.

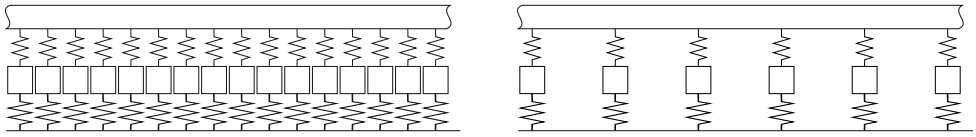

Figure 1.8: Continuous (left) and discretely (right) supported rail on double-layer elastic foundation

According to Knothe and Grassie [9], the supports are introduced in railway track dynamic models as either a single elastic layer accounting for the railpads, or as a double elastic layer support to account for the railpads and ballast, including the sleepers between them. Other more comprehensive configurations also exist, accounting for example for ballast mass, ballast shearing stiffness etc. The sleepers can be modelled as either simple masses in translation or as transverse flexible finite beams, accounting for their bending. In a continuously supported track model, the effect of the pads, sleepers and ballast are evenly distributed over the length of the rail. By introducing bending stiffness to the 'sleeper' layer in the longitudinal direction, this form of support can also be used to represent a slab track.

In the work of Grassie et al. [38], both a continuous and a discretely supported rail on a two-layer foundation were investigated and compared. It was shown that the periodicity of the supports leads to additional peaks in the frequency response functions of the rail at the so-called 'pinned-pinned' frequency around 1 kHz for vertical vibration, whereas at low frequencies, the two models gave similar results. The mode at the 'pinned-pinned' frequency is depicted in Fig. 1.9. In this mode an increase in frequency response is observed at the mid-span and a minimum at locations above a sleeper. Meanwhile, the response of the continuously supported track lies between those two results. Also the dynamic contact forces arising from excitation between the wheel and the rail were investigated by Grassie et al. [38] and found to be significantly increased at the 'pinned-pinned' frequency above a sleeper.

In an investigation by Wu and Thompson [39], it was shown that, in terms of noise radiation, the 'pinned-pinned' frequency effect (averaged over 12 force positions across a rail span) is almost negligible, giving a maximum difference of about 1.5 dB in a single one-third octave band levels for some typical track properties. For ground-borne vibration, since the range of interest typically lies below 250 Hz, the effects can also be neglected and a continuously supported model is sufficient.

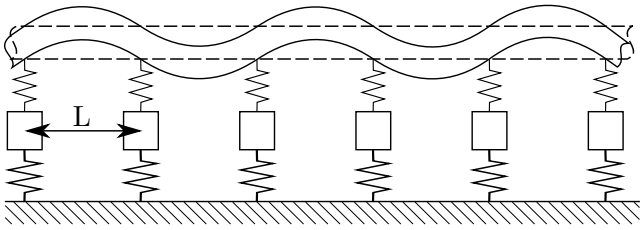

Figure 1.9: Displaced shape of rail at 'pinned-pinned' resonance frequency

When investigating the vehicle/track system, additional parametric excitation can arise due to the discrete supports. As the train is passing over the track, the wheels experience a varying stiffness along the rail. Wu and Thompson [40] found that the wheel/rail force spectra varied from the continuous model (or the moving irregularity model), especially at low frequencies. Various harmonics exist, with basic components at the sleeper-passing frequency and the 'pinned-pinned' resonance.

1.1.5 Frequency-domain and time-domain methods

For the dynamic problems considered, there are two main methods of solution [41]: in the frequency domain and in the time domain. In the former, the applied loads are assumed to vary harmonically with respect to time, and the track components are assumed to behave linearly. Then the equations of motion are solved either analytically or numerically, one frequency at a time. Some dynamic properties such as the damping can be allowed to vary with frequency. A common solution technique is to transform the problem into the wavenumber domain and obtain a solution by using an inverse Fourier transform over wavenumber. Frequency-domain models are usually based on a continuously supported track of infinite extent and only account for the steady-state response of the track. For example, Grassie et al. [38] solved the rail response to a unit load in the frequency domain, for both a periodic and continuously supported rail. For ground vibration Jones et al. [42] used the same approach for a continuously supported track on a two-layer foundation, further supported on a layered half-space. In their work, a moving harmonic load was considered.

In comparison, time-domain models are more flexible as they can account for time-varying loading, non-linear and state-dependent track properties and more detailed track configurations. Such models may be discretised using the Finite Element technique. The equations of motion are assembled in terms of the mass, stiffness and damping matrices

and are solved using a step-by-step time integration scheme. In contrast to frequency-domain models, these more readily include discrete supports but they must be truncated to have a finite length. They can take into account both the transient and steady state response of the system. For example, Nielsen and Abrahamsson [43] studied the vertical interaction between a train, represented by either a linear or non-linear discrete mass-spring-damper system, and a track, for which a linear three-dimensional model was established. The rails were discretely supported through railpads and flexible sleepers on an elastic foundation. The track structure was solved for its modal parameters and the system of coupled equations between the train and the track were presented in state-space form. Andersen et al. [44] used the finite element technique to obtain the response of a rail on an elastic foundation due to a moving load in convected co-ordinates. An Euler-Bernoulli beam was used to represent the rail and the convected co-ordinates (moving frame) method was used. Ang and Dai [45] used the moving element method to model a curved rail, in both vertical and lateral directions. In a different approach Wu and Thompson [46] studied non-linear wheel/rail interaction. In this work, the rail response was obtained using a lumped parameter model, fitted to the frequency domain receptance of an infinite Timoshenko beam on a two layer elastic foundation. Vertical/lateral coupling due to the excitation loads was included.

Although time-domain models can represent the track configuration more reliably, they are computationally more demanding and attention needs to be given to the discretisation of the system and the time integration scheme. Due to their computational demands, a limited length of track is used which should provide minimal reflections from the boundaries, otherwise special boundary conditions need to be taken into account (e.g. [44], [47]). On the other hand, frequency-domain models, can provide very good approximations to track behaviour with much less computational demand.

1.1.6 Analytical models

Many authors present models of the vertical dynamics of railway tracks, derived from the Euler-Bernoulli or Timoshenko beam on an elastic support (Winkler foundation) and variations. Grassie et al. [38] derived the response of a rail on a two-layer support, where the second layer accounts for the sleeper mass and ballast stiffness. Both continuously and discretely supported models were presented. Both Euler-Bernoulli and Timoshenko beam theories were considered as well as the moving nature of the excitation load. The solution was obtained by the method of Laplace transformation and contour integration. It was concluded that the velocity of the excitation load has negligible impact on the vertical receptance for realistic parameter values.

Duffy [48] presented a solution for both the transient and steady-state response of an Euler-Bernoulli beam on an elastic foundation excited by a moving mass. A Fourier transform was used with respect to space, while Laplace transformation was used with

respect to time. More recently Hussein and Hunt [49] used the Fourier transform technique to obtain the receptance of a floating slab track, where both the rail and the slab were represented by Euler-Bernoulli beams, interconnected by an elastic layer and further supported on an elastic foundation. A closed form response was obtained by means of contour integration. These are just a few examples of investigations of the vertical track dynamic behaviour.

By comparing experimental results of the lateral receptance of a track on concrete sleepers with a vertical track dynamic model, Grassie et al. [50] suggested that the dynamic model for the vertical behaviour can be modified to accommodate the variations in the lateral response. In their study, for a track with stiffer railpads (on wooden sleepers) good agreement was achieved between the response of a model of a beam on elastic foundation and the measurements. For softer railpads (modern track with concrete sleepers) it was found that the rail head undergoes large lateral bending vibration, independent of that of the foot, with the web acting as an elastic foundation itself. They thus used a two-layer continuous foundation model accounting for the rail head (as a Timoshenko beam) connected by a series of springs to the rail foot (continuous mass) and further connected to the second elastic layer representing the pads. Good agreement was found between this model and measurements of the track lateral receptance.

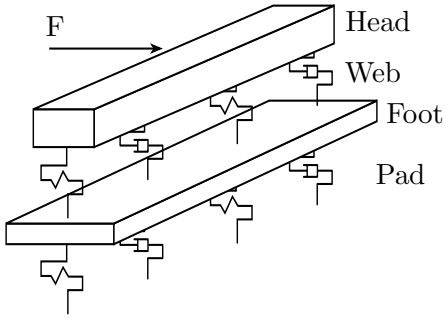

Figure 1.10: Lateral track model after Grassie et al. [50]

Hunt [51] considered the track to behave laterally as a pair of Euler-Bernoulli beams on an elastic foundation with the main aim to investigate railway crossings. The bending displacement of the rails was considered identical and thus both rails were modelled as a single beam. The rail foot was rigidly attached to the second layer representing the sleepers and the movement of the rail head relative to the rail foot was provided by the resilience of the web. The second layer (rail foot and sleepers) was also assumed to have a bending stiffness, similar to a slab track.

At higher excitation frequencies, the cross-sectional deformation of the rail has a significant impact on its response, both vertically and laterally [4]. In the vertical direction, this is mainly due to the effect of foot flapping where the foot vibrates independently of the rail head. For a UIC54 rail, a foot flapping wave cuts on at around 5 kHz, although increased vibration of the rail foot is seen from around 2 kHz and above. This is

usually neglected for rolling noise, as the highest influence occurs around the maximum frequency of interest. In contrast, the behaviour of the rail due to lateral excitation is affected by the rail cross-section deformation at much lower frequencies, with web bending and double web bending wave modes in a UIC54 rail cutting on at around 1.4 kHz and 4.6 kHz respectively.

Scholl [52, 53] presented two different approaches to investigate wave propagation along a rail. In the first, named 'three-layer' model, the rail was represented as an infinitely long strip, divided into three layers representing the rail head, web and foot as shown in Fig. 1.11(a). Different densities and Young's moduli were assigned to these parts in proportion to their widths. Although this model provided satisfactory results for the vertical and longitudinal response of the rail, it gave no information about the cross-sectional deformations of the rail. Thus a second model, named 'cross-section', was developed consisting of a combination of one-dimensional bending/axial bars accounting for the head, the web and the two sides of the foot shown in Fig. 1.11(b). For high frequencies, the constant foot thickness used was seen as a limitation.

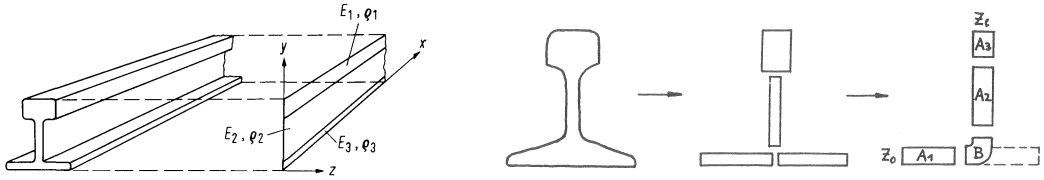

a) Three layer model b) Cross-section model

Figure 1.11: Three-layer and cross-section models from Scholl [52, 53]

In order to capture higher order modes of vertical vibration, Wu and Thompson [54] introduced a double Timoshenko beam model where the rail head (including the web) and foot are represented by separate beams along the direction of the rail, connected by continuously distributed springs, Fig. 1.12(a). Both beams are then further supported via the pads to the sleeper resting on an elastic foundation. Both a continuously and discretely supported track were considered. The results were compared against a three-dimensional FE model of a short length rail (1 m) in terms of the dispersion (wavenumber against frequency) curves and against measurement data in terms of point receptance and vibration decay rates, showing good agreement.

A similar concept of a multiple-beam configuration was used by Wu and Thompson [55] for the lateral vibration of rails, where the cross-sectional deformations become important at lower frequencies than for vertical vibration, Fig. 1.12(b). Here, the rail head and foot were treated as separate infinite beams while the web was represented as an array of beams connecting the rail head and foot, without accounting for the bending and twisting stiffness along the rail axis. This analytical model showed excellent agreement with a Finite Element model of a finite length (1 m) free rail, in terms of the dispersion relationship. The receptances due to a lateral force at the head were also compared

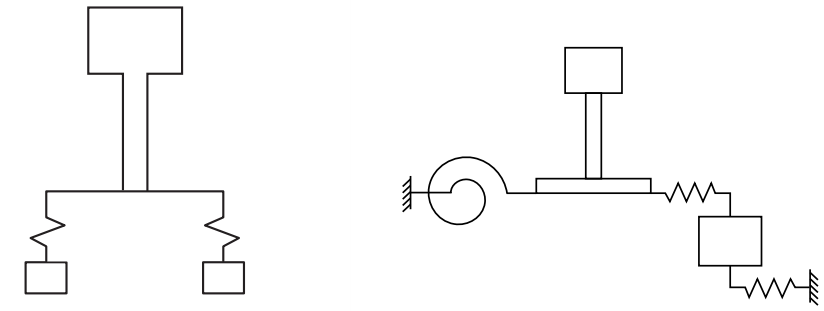

a) For vertical vibration b) For lateral vibration

Figure 1.12: Multiple-beam models from Wu and Thompson [54, 55]

with measurements, showing a good overall agreement apart from the response at the 'pinned-pinned' frequencies which can only be obtained by a discretely supported model.

Bhaskar et al. [56] developed a model including the lateral and rotational motion of the rail. The frequency range of interest in this work was up to about 2 kHz, thus it was important to account for the cross-sectional deformation occurring above 1.5 kHz. In order to validate their model, the authors used a FE model developed by Ripke and Knothe [57] choosing the same elements, in which the rail section was composed by three separate parts, representing the rail head as a beam in bending and torsion, and the rail web and foot by three plates (one for the web and one for the foot on each side of the web), as shown in Fig. 1.13. A variational method was then used for an infinite rail continuously supported on railpads, sleeper mass and ballast in order to obtain the relationship between the frequency and wavenumber (dispersion relationship) and receptance. The rail head was allowed to translate in vertical, axial and lateral directions, as well as to rotate around the axial direction. The plates were allowed uniform displacement in plane as well as in the longitudinal direction and deformation perpendicular to their plane, approximated by a cubic function. The railpad forces were applied as two springs set a distance apart equal to the width of the foot divided by $\sqrt{3}$ to account for the torsional stiffness as well. The responses of the rail were obtained by means of Fourier integrals. The axial motion was decoupled from the lateral one by assuming symmetry. Similarly, the vertical motion was decoupled from the torsional motion. A good agreement was found with the discretely supported FE model developed by Ripke and Knothe [57], with the main differences occurring due to the continuous nature of the support.

Yang [58] and Yang et al. [59], presented an improved model based on that of Bhaskar et al. [56]. The rail foot was described in more detail, by representing it as a tapered plate including bending and in-plane motions. Also the stretching of the web was accounted for. The variational principle was applied to obtain the unknown deflections for the 17 degrees of freedom and then the equations of motion were obtained based on Hamilton's

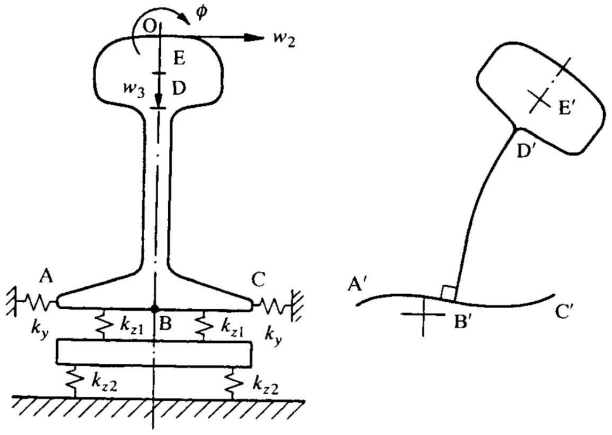

Figure 1.13: Combined beam/plate model for rail cross-section from Bhaskar et al. [56]

principle. The dispersion relationship for a free rail was presented and compared with both the simplified beam models from Wu and Thompson [54, 55] and a Finite Element model of a finite length rail (1 m). It was shown that the first vertical wave mode is more accurately represented at higher frequencies than by the model of Wu and Thompson [54, 55]. This was due to the better representation of the deformation of the rail foot, which dominates the response at higher frequencies. The first lateral bending wave was also improved compared to Wu and Thompson [54, 55] at frequencies above 2 kHz, where the tapered foot gives a better representation of the stiffness of the foot in lateral bending.

Heckl [60] studied the free propagation of coupled waves on a periodically supported Timoshenko beam. This model used the Green's function matrix approach based on Hamilton's principle (for the free beam), the superposition principle (for the inclusion of the supports) and Bloch's theorem (to account for the periodicity of the supports). The cross-section of the beam was considered uniform and the shear correction factor for bending set to unity (i.e. uniform shear stress distribution in the cross-section). Flexural, torsional and compressional waves were considered on an infinitely long rail with an infinite number of supports represented by either a mass or a spring. In this study, results were only presented in terms of dispersion curves. For the case of a single wave, passing/stopping bands were identified due to the discrete nature of the support. Although the discrete supports were shown to have a considerable influence on the dispersion relationship, their effects were enhanced due to the high stiffness used for the support, especially in the axial and lateral directions where a stiffness of 1000 MN/m was used. When several wave types were present, coupling of waves occurred leading to a different behaviour than the superposition of the individual uncoupled waves. The coupling effects were pronounced when the support location was offset from the beam centreline.

Popp and Schiehlen [61], presented a series of frequency-domain and time-domain models

for vertical and lateral track dynamics for frequencies up to 600 Hz accounting for a discretely supported track on an elastic half-space. In the frequency-domain dynamic model, the track was considered as an infinite periodic structure with period length of one sleeper bay. The rail was represented by a Timoshenko beam in the vertical and lateral directions and as a torsional rod. No axial translation was allowed for. The vertical, lateral and torsional responses were completely decoupled from one another (for both rail and sleeper behaviour). Also no cross-sectional deformation of the rail was taken into account (distortions of head and foot were omitted).

In TWINS [17], both vertical and lateral track behaviour was considered for estimating rolling noise using a Timoshenko beam on a two-layer elastic foundation. The vertical/lateral coupling was not taken into account directly within the models, although various sources of coupling were identified. Instead, an empirical parameter (X or XdB) was introduced [62]. The cross receptance was based on the geometrical average of the vertical (U_y) and lateral (U_z) receptances ($U_{yz} = 10^{XdB/20}\sqrt{U_y U_z}$), where the parameter XdB was chosen based on estimates from measurements, typically set around -10 dB.

When making predictions for the track component of rolling noise using analytical models, it is common to adjust the rail loss factor in order to obtain a good fit with measurements of track decay rate [4]. This is due to the vibration of the rail foot having a larger amplitude at higher frequencies, leading to an increased effect of the railpad damping. The material loss factor of the rail is closer to that of steel, which is of the order of 2×10^{-4} [63]. Fitting of predictions to measurements has shown that a loss factor of about 0.02 in the model gives more appropriate results [4].

1.1.7 Finite Element-based methods

The models discussed so far (solved either analytically or numerically) are based on simple beam theories and mechanical models for the vibration of beams and in some cases plates. The main limitation that applies to both the Euler-Bernoulli and Timoshenko beam theories is that they are based on the assumption that the cross-section remains plane. Thus at high frequencies, where cross-sectional deformations start to occur and more wave types exist, these beam theories will fail to provide an adequate representation of the dynamic properties of the rail [64]. In order to overcome this limitation, alternative modelling techniques can be used that allow the cross-section to be more accurately represented.

Finite Element Analysis methods have been used by many authors in order to discretise a finite length of rail. Thompson [20] used a combination of beam and plate elements to represent a finite length of rail. By taking into account the structural symmetry of the cross-section, only half of the cross-section was necessary. By considering symmetric boundary conditions in this plane, the vertical and axial modes were obtained while for

the lateral and torsional modes antisymmetric boundary conditions were considered. A similar approach was later used by Knothe et al. [64] and many other authors, employing different elements, meshes and approximations. More recently, Ryue et al. [65] used 8-noded quadrilateral solid elements, modelling only half the cross-section under the assumption of symmetry about the vertical axis, see Fig. 1.14. Due to the use of a finite length, this method is limited to identifying the frequency corresponding to a specific wavenumber and not vice versa. Also, obtaining the near field waves or receptances for an infinite rail is not straightforward. Since the cross-sectional deformations are important in the frequency range of interest, various more detailed models have been developed that are based on extensions of the FE method.

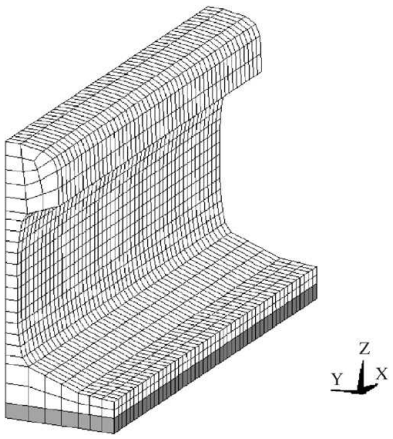

Figure 1.14: Finite-Element model of finite length of rail after Ryue et al. [65]

Thompson [20] presented a method of obtaining the dispersion relationship and receptance of an infinite beam based on the periodic structure theory (PST) of Mead [66]. This technique takes advantage of the fact that the cross-section remains constant along the rail and that its length is infinite. The structure is considered as a periodic structure, having an arbitrary period. A slice of rail 10 mm long was considered, discretised by finite elements, and the sleepers were also included in a continuously supported track. For this method, a commercial finite element software can be used to obtain the matrices of the slice of track.

The finite strip method was used by Knothe et al. [64], where only the cross-section of the rail was discretised and the elements were considered as infinite strips. The main advantages of this method over classical Finite Element Analysis are the reduced number of degrees of freedom, thus decreasing computational requirements.

Gavrić [67] introduced the waveguide finite element (WFE) method for modelling of rails, which has grown in popularity recently. In this method, as with the PST method, the infinite extent of the rail and the constant cross-section are taken into account. The cross-section is meshed using special two-dimensional finite elements, see Fig. 1.15, similar to the finite strip method. The displacement field across the cross-section is discretised by finite elements while complex exponentials are used to describe the nature

of the waves in the longitudinal direction. In the work of Gavrić [67] only the modelling of free waves propagating in a free rail was considered. Using the same method, Ryue et al. [65] determined the waves propagating in a supported rail up to 80 kHz, while the forced response due to a vertical and lateral excitation, both above a sleeper and at midspan, was obtained by Gry [68] for a rail with periodic supports. More recently, Nilsson et al. [69] used the waveguide finite element method to calculate the vibration of an infinite, continuously supported rail excited by a point force. A similar study was also performed by Li et al. [70].

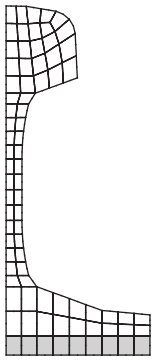

Figure 1.15: Waveguide Finite Element model after Ryue et al. [65]

The main disadvantage of the above methods is that they require extensive computational capacity and large calculation times. Thus an analytical approach could be of great benefit, depending on the required level of accuracy.

1.1.8 Modelling of sleeper response

For the majority of models discussed so far, the sleeper is either not considered, or is included as a rigid mass. The sleeper dynamic response is particularly important due to its influence on the track dynamics and the noise radiated at lower frequencies. The literature related to the modelling of the dynamic response of railway sleepers is fairly limited.

An important study of concrete monobloc sleeper vibration was performed by Grassie [71]. Measured data for the vertical vibration of a number of concrete monobloc sleepers of non-uniform cross-section were compared with a finite Timoshenko beam model. Grassie [71] obtained an effective flexural rigidity of the non-uniform sleepers, for use in the uniform model, by taking the geometric average of the flexural rigidity at the rail seat and that at the sleeper centroid. The analytical sleeper model was found to be adequate in comparison to the given data, except at the first bending mode, where the sleeper cross-section variation has the greatest effect. A way of extracting the Young's modulus from the measured data was presented, achieved by fitting the peaks of the

frequency response function at the second and third bending modes. It was also suggested that the same sleeper model can be used for lateral sleeper dynamics, although no such study has been presented. Using a supported Timoshenko beam, Janssens and Thompson [72] studied the inclusion of a ballast layer below the sleeper.

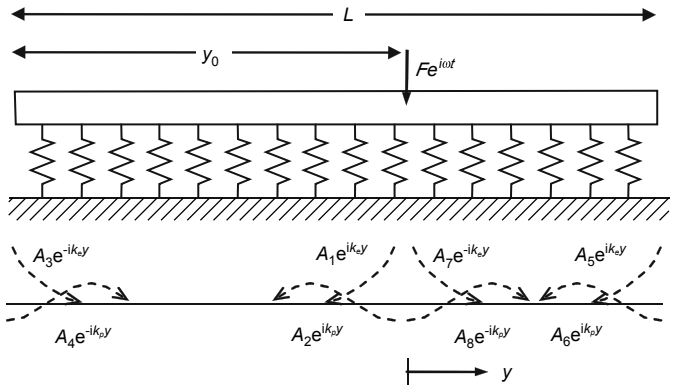

Figure 1.16: Flexible sleeper model from Thompson [4]

The above sleeper models are based on the modal behaviour of the sleeper. Another approach is based on the forced sleeper response using a wave approach. Such a method was used by Nordborg [73] when studying vertical track dynamics, where a continuously supported Euler-Bernoulli beam was used for the sleeper. Thompson [4] used this approach with a Timoshenko beam (Fig. 1.16), which as discussed by Grassie [71], is more appropriate as rotational inertia and deflections due to shear have a significant contribution. With the approach based on the forced response, it is easier to implement a frequency-dependent ballast stiffness, which is more realistic as shown by Frémion et al. [74].

Nielsen [75] investigated the acoustic optimisation of railway sleepers using a finite element model of half a sleeper. The sleeper radiation efficiency was determined using a boundary element model of the sleeper and was combined with the sleeper vibration to determine the radiated noise. It was shown that a bi-bloc sleeper with specific dimensions can lead to noise reduction of the sleeper component of up to 3 dB(A) compared with the monobloc sleeper studied.

Oregui et al. [76] used a three dimensional Finite Element model of a 14.4 m length track (24 sleeper bays) with monobloc sleepers to investigate vertical track dynamics. In this study, a comparison was made between a full track and a half track with a line of symmetry at the sleeper centreline. The lateral track vibration was constrained. The two models were compared with measurements and good agreement was found. Also, for excitation above a sleeper the half-track model needed slightly higher sleeper mass than the full track model, while for mid-span excitation agreement was satisfactory. However, the application of symmetry at the sleeper centreline resulted in the absence of some

dynamic characteristics. Finally, different configurations for the contact area between the rail and the sleeper were studied.

1.1.9 Potential sources of coupling

In the context of this thesis, coupling occurs when:

i) a vertical force produces a lateral response as well as a vertical one,

ii) a lateral force produces a torsional response as well as a lateral one,

iii) an axial force in a curved rail produces a lateral response as well as an axial one, and

iv) a torsional moment in a curved rail produces a vertical response as well as a torsional one.

Most analytical track models in the literature omit the torsion, the cross-sectional asymmetry, the effect of track curvature and the eccentric nature of the support and excitation loads. These are identified as potential sources of coupling of the rail response, mainly between the lateral and torsional motion.

In the elementary theory of torsion of beams (Saint-Venant torsion), the basic hypothesis in the formulation of the equations of motion is that no extension or shearing occurs in the plane of the cross-section and the beam is free to warp. Thus the torsion of a beam is governed only by its torsional rigidity. Vlasov [77] showed that the torsional stiffness of an I-beam depends on the bending stiffness of its flanges, resulting in flexural torsion (torsion-bending or restrained warping). This can be included in the equations of motion by accounting for the warping behaviour of the beam, and many authors have addressed this. An extensive review of the various studies on non-uniform torsion of bars has recently been conducted by Sapountzakis [78].

If the centre of mass (where inertial forces are considered to act) and the shear centre (where net shearing forces are considered to act) of a beam are not coincident, the bending and torsional vibration will be coupled. This occurs for typical rail sections (Vignole, e.g. 60E1) which are asymmetric in the vertical direction (lateral bending will couple with torsion), or in the case of tram rails (groove, e.g. 60R1), which have no plane of symmetry (both vertical and lateral bending will couple with torsion). Many authors have investigated this phenomenon in beams including, for example, Banerjee [79], Kim et al. [31], Adam [80] and Monsalve-Cano and Darío Aristizábal-Ochoa [81].

In the case of a curved beam, the torsional response will couple with vertical bending (out-of-plane with respect to the curvature), while the axial motion will couple with the lateral response (in-plane with respect to the curvature). Love [82] investigated the effect

of curvature on the vibration of free beams, neglecting the effects of rotational inertia and radial shear. In addition, it was assumed that the centroidal axis of the beam was inextensible. Morley [83] improved previous models by combining Timoshenko's beam theory for straight beams with an extensional rod and accounting for curvature. Irie et al. [84, 85] studied the in-plane and out-of-plane response of a curved Timoshenko beam, considering a harmonic excitation, for a free-clamped beam, as well as different types of curvature such as circular or elliptic.

In the above studies of curved beams, the in-plane response (i.e. radial and axial) and out-of-plane response (transverse and torsional) have been studied independently. The coupling between the two has received limited attention, mainly aimed at the development of improved beam finite elements. Gendy and Saleeb [86] studied the coupled extensional/flexural/torsional modes of beams based on the Timoshenko-Vlasov thin-walled beam theory, obtaining the differential equations of motion by employing a variational formulation. Chang et al. [87], Kim et al. [88], Kim and Kim [89] and Kim et al. [90] considered the spatial stability and free vibration of shear deformable curved beams, also accounting for restrained warping and coupling with shear deformations.

Specific studies on the effect of curvature on railway tracks is limited. Nair et al. [91] investigated the stability of a curved rail under the effect of a moving constant vertical load with the inclusion of cant and restrained warping. It was found that the critical velocity, i.e. the velocity of the load at which waves start to propagate, reduces as the curvature increases. More recently, Li et al. [92] investigated the response of a half-space due to excitation of a discretely supported curved track. Kostovasilis et al. [93, 94] used a Finite Element formulation to investigate the effect of using curved beam elements instead of piecewise straight beam elements for the representation of the track. Only a vertical moving load was considered and the authors suggested that curvature might have a higher impact when the beam is traversed by a horizontal force. Finally Dai and Ang [95], presented an analytical method to obtain the steady-state response of a curved beam on an elastic foundation, using trigonometric trial functions for approximating the displacement of the beam. None of the above works have investigated the effects of coupled vertical and lateral motion.

Apart from the coupling due to the cross-sectional properties of the beam and beam curvature, as discussed above, there are two further factors that can be considered for the vertical/lateral behaviour. Firstly, whether on a straight or curved track, the contact location of the wheel on the rail is usually off-centre in both the vertical and lateral directions. Depending on the wheel and rail profiles, possible contact locations are found across the entire rail head. When the contact location is away from the rail-head centreline, it will cause both the vertical and lateral dynamic forces to excite the torsional vibration of the rail. This behaviour is occasionally considered in time-domain vehicle/track interaction software (e.g. [96]).

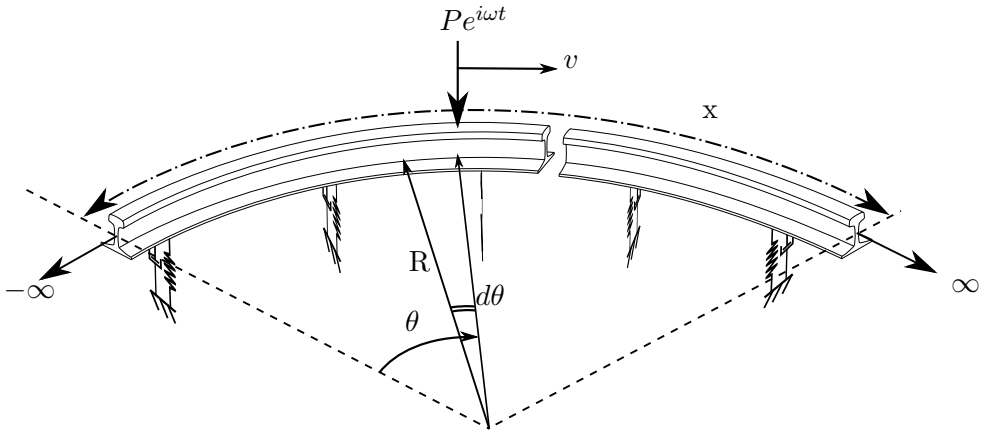

Figure 1.17: Curved beam on discrete elastic foundation (from Kostovasilis et al. [94])

In addition, the support loads (elastic foundation/railpad) act at the bottom of the rail instead of the centroid. This eccentricity will cause a further coupling between the lateral and torsional responses. Since the torsional vibration is coupled with the lateral response (and also vertical response for asymmetric rails), these effects need to be considered in order to provide a full study of the interaction.

In an attempt to understand and quantify the vertical-lateral coupling of rails, Betgen et al. [97] analysed the track mobility (velocity per unit force) and decay rates by means of measurements and a three-dimensional Finite Element model. The rail was excited at various locations across the top of the railhead for the vertical mobility and at a specified location at the side of the railhead to obtain the lateral mobility. It was shown that the simplified Timoshenko beam on elastic foundation fails to capture many important characteristics of the response and that an offset vertical excitation position significantly affects the cross mobility. The influence of the sleeper in the cross mobility in the specific study was found to be minimal while the typical value for the factor XdB used in TWINS (-10 dB) was found to give reasonable results for an offset of the excitation point by 20 mm.

1.1.10 Gaps in knowledge

As discussed above, the lateral vibration and vertical/lateral interaction of railway tracks has received limited investigation, especially in relation to rolling noise. The track vibration in both vertical and lateral directions contributes to the radiated noise and it is thus important to account for the rail radiation due to lateral/torsional waves as well as vertical ones. Various sources of coupling have been identified, affecting the lateral/torsional behaviour of the track, which can be divided into two categories:

coupling due to the beam cross-section and coupling due to the applied loads, including the foundation.

A clear gap is seen in the area of modelling the lateral vibration of the track, the coupling between the vertical and lateral directions, as well as the inclusion of torsional behaviour of the track. In addition, although flexible sleeper models have received some attention, no consideration has been given to the torsional and axial responses of the sleeper, or the effect of foundation eccentricity. Finally, for the prediction of rolling noise, the influence of the lateral contact point position, as well as the coupling of the vertical and lateral track dynamics, is considered only through empirical parameters without physical quantification.

1.2 Aims and objectives

The main aims of this thesis, formulated to address the gaps in knowledge identified in the literature review, are to:

1. understand the influence of the individual coupling sources on the rail response, for frequencies up to 5 kHz;
2. develop better understanding of the lateral vibration of railway tracks;
3. investigate the effect of lateral/torsional waves on rolling noise; and
4. assess the influence of contact point location on rolling noise.

In order to achieve these aims, the following objectives need to be satisfied:

1. develop a model for rail vibration that takes proper account of vertical/lateral coupling;
2. combine all coupling sources and incorporate them into a railway track dynamic model;
3. create a model for the dynamic behaviour of a flexible sleeper in all three principal axes and validate it with measurements;
4. validate the track response against more comprehensive models and measurements;
5. incorporate the vertical/lateral interaction model in the TWINS model for rolling noise;
6. compare rolling noise predictions against previous models and measured data.

1.3 Contributions of the thesis

The original contributions made by the investigation performed in this work are summarised as follows:

1. The effects of torsion, restrained warping and shear centre eccentricity have been considered in the modelling of the vibration of railway track. Although all three components have been previously investigated for modelling railway tracks, no complete study has been found to show their effects, especially in combination with coupling between the vertical and lateral responses. The inclusion of torsion is shown to be essential for modelling lateral track dynamics as it adds additional flexibility in the lateral direction. Restrained warping is linked to torsion, while shear centre eccentricity introduces coupling between the lateral and torsional vibration of the track. Frequency ranges above which these effects are influential are identified.

2. Curvature of railway tracks has been studied based on the developed beam model. The forced response based on various radii of curvature has been compared with a straight track, and limits are identified over which curvature can be ignored.

3. The height of the rail and sleeper above the foundation support has been properly taken into account, both for single and double layer support models. By introducing the support at its actual location, the rail foot instead of the centroid, horizontal reaction forces introduce both lateral forces and torsional moments at the centroid. A methodology is presented by which the influence of the support location in the vertical/lateral coupling can be studied. The effect of the support location on estimates of lateral pad stiffness obtained by comparing the response of the model with measurements has been considered.

4. A new model for the vibration of a flexible sleeper is developed. Previous models of sleeper vibration are extended to account not only for bending in the vertical or lateral directions, but also for torsional and extensional vibration. In addition, the location of the ballast support and rail contact are also considered. The dynamic response obtained from the model is validated with laboratory measurements for vertical and lateral bending, as well as torsion and extension.

5. Levels of cross mobility at different locations of the excitation force on the rail cross-section are obtained. These are compared with estimates using the geometrical average of vertical and lateral mobility in combination with the empirical factor XdB, where effects such as torsion, shear centre eccentricity and foundation height are omitted.

6. The developed model has been embedded in TWINS for rolling noise prediction. The influence of vertical/lateral coupling and the location of the contact force are

investigated with respect to noise emitted from a railway track, including the noise due to torsional waves.

1.4 Organisation of the thesis

This thesis is organised in seven chapters. In the current chapter, the background literature has been presented, along with the key contributions of the study.

In Chapter 2, various sources of vertical/lateral coupling through the rail are identified and are investigated independently. The effect of the coupling sources is investigated in terms of the change in the dispersion relationship for an unsupported beam. In addition, the methodology of dealing with eccentric excitation loads is introduced.

Based on the models from Chapter 2, an improved model for a beam with vertical/lateral coupled motion is presented in Chapter 3, which correctly accounts for vertical/lateral interaction compared with current beam models used for railway track applications. The presented model is validated against both a FE and a WFE model, based on the dispersion relationship for a straight rail. For a curved rail, the dispersion relationship from the FE model only is used, as the WFE model cannot account for the effect of curvature. The analytical model is further extended to account for the effect of an elastic foundation on the dispersion relationships and is again compared with the WFE model. Finally, an in-depth study is performed on the effect of varying the location of the support.

In Chapter 4, additional layers of support are introduced to represent the sleeper and ballast and their effect is investigated. Furthermore, two sleeper models are introduced: a rigid sleeper model accounting for displacements and rotations in the three principal axes, and a flexible sleeper model, accounting for extension and torsion of the sleeper as well as bending. The latter model is validated against measurements taken on a pre-stressed concrete monobloc sleeper. An equivalent model is also identified to account for the effect of rotation of a long sleeper (where the excitation force is applied at a distance from the sleeper centre) when modelling the response of a rigid sleeper in translation.

Chapter 5 presents a closed form solution for the forced response of the track based on the model from Chapter 3, also accounting for the additional support layer introduced in Chapter 4. In order to validate the model, the mobilities and track decay rates are compared with results for various other track models, including an existing Waveguide Finite Element model. Comparisons are also made with measurement data.

The developed model for vertical/lateral track dynamics is then used in Chapter 6 to obtain estimates of rolling noise in conjunction with an existing MATLAB implementation of TWINS, and results are compared with noise measurements from an operational track. A modified procedure for incorporating measured track decay rates is presented

and finally, the effects of vertical/lateral coupled vibration and contact point location on rolling noise are investigated.

Conclusions are summarised in Chapter 7 as well as recommendations for future work.

Chapter 2

Modelling the vibration of rails

As seen in Chapter 1, when modelling the vibration of rails, most authors consider the vertical vibration to be completely independent from the lateral and vice versa. Although beam models that take into account additional degrees of freedom exist in the literature, these have not been implemented for modelling the vibration of railway tracks. In total, five different sources of coupling between the vibration in different degrees of freedom are identified in this thesis, four of which are discussed in this chapter.

The first is related to the generation of longitudinal stresses as a result of shear stresses due to torsion. This behaviour is considered as a non-uniform torsion (for non-circular cross-sections) and is characterised by warping (i.e. thin-walled beams as described by Vlasov [77]).

Second, the cross-section of the rail is not symmetric (see Fig. 2.1). Most rails are symmetric in only one plane while in some cases they can be fully asymmetric (60R1 groove rail for example). In the case of a Vignole rail, the height of the shear centre and the centre of mass (centroid) are different, with the shear centre located lower than the centroid. This introduces a coupling between the lateral bending and torsional motions. For fully asymmetric cross-sections, the same will also occur between vertical bending and torsion.

Furthermore, in order to guide the railway vehicle the rails are curved in the horizontal plane. In this case, even for a doubly symmetric cross-section with no warping considered, the vertical response couples with the torsional response (these motions are out of the plane of curvature) while the axial response couples with the lateral response (motions in the plane of curvature). Curvature in the vertical plane is not considered in this work, although the same methodology can be applied.

The final source of vertical/lateral vibration coupling considered in this chapter is the location of the excitation forces. The forces are applied at the rail head and not the centroid of the rail, and may also be applied with some lateral offset from the centreline

of the web. Thus, apart from generating a purely lateral response a lateral load will also generate a torsional response. Similarly, a vertical load will also produce a torsional response if offset from the centreline.

For clarity, the equations of motion will be presented and built up from first principles in this chapter. The sources of coupling will be first investigated individually. The equations of motion are assembled in Chapter 3 to form the fully coupled rail model. Firstly, based on the generalised displacement field and strain equations, the different beam theories involving extension, torsion and vertical and lateral bending of a beam will be investigated. The inclusion of rotational inertia and foundation stiffness will also be considered in these models, although in the presentation of results in this chapter the foundation stiffness is omitted and will be discussed in Chapter 3. After the beam theories are presented, the effect of restrained warping will be taken into account in the torsion of the beam, followed by the effect of shear-centre eccentricity. In addition, inertial terms due to coupling will be considered. Finally, the effect of track curvature will be investigated.

In all the analyses shown, a Vignole rail (type 60E1) is used (unless otherwise indicated). The properties of its cross-section have been determined using COMSOL Multiphysics [98] and are listed in Table 2.1. In addition, the properties for a groove rail (type 60R1) which will be used later are also shown. The reference co-ordinate axes x, y and z are defined as the longitudinal, vertical and lateral directions respectively following the right-hand rule, as shown in Fig. 2.1.

2.1 Generalised displacement field

Figure 2.1 shows two typical rail cross-sections in the y-z plane with the centre of mass marked as c and the shear centre as S. The 60E1 section is widely used on mainline tracks whereas 60R1 is a tram rail.

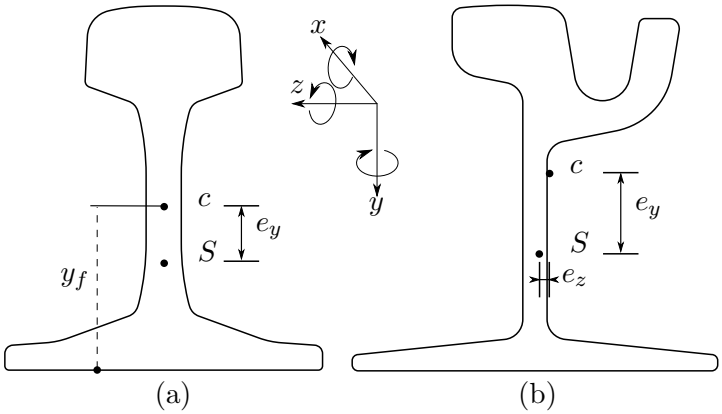

Figure 2.1: Typical rail cross-section for a) 60E1 and b) 60R1 rail profiles

Table 2.1: Rail section properties (inertial properties relative to centroid)

Property	60E1	60R1	Units
Young's modulus, E	210	210	GPa
Shear modulus, G	80.769	80.769	GPa
Density, ρ	7860	7860	kg/m^3
Poisson's ratio, ν	0.3	0.3	-
Cross-section area, A	7.67×10^{-3}	7.72×10^{-3}	m^2
Second moment of area about y-axis, I_y	512.7×10^{-8}	878.5×10^{-8}	m^4
Second moment of area about z-axis, I_z	3037×10^{-8}	3322.5×10^{-8}	m^4
Product moment of area, I_{yz}	0	-5.67×10^{-21}	m^4
Polar moment of area, I_p	3.550×10^{-5}	4301×10^{-8}	m^4
Torsional constant, J	2.212×10^{-6}	1.32×10^{-6}	m^4
Vertical shear coefficient, κ_y	0.393	0.289	-
Lateral shear coefficient, κ_z	0.538	0.495	-
Vertical shear centre eccentricity, e_y	0.033	0.032	m
Lateral shear centre eccentricity, e_z	0	0.003	m
Warping constant, I_w	2.161×10^{-8}	4.0464×10^{-8}	m^6
Warping product moment of area, I_{wy}	1.6971×10^{-7}	2.8315×10^{-7}	m^5
Warping product moment of area, I_{wz}	0	-9.004×10^{-8}	m^5
Warping product moment of area, I_{wyy}	0	2.6849×10^{-9}	m^6
Warping product moment of area, I_{wyz}	-2.41×10^{-8}	-4.313×10^{-8}	m^6
Warping product moment of area, I_{wwy}	0	4.0839×10^{-10}	m^7
Rail foot/pad width, l_p	150	180	mm
Height of centroid, y_f	81	94	mm

Based on the notation of Fig. 2.1, the displacement field of any arbitrary point (x, y, z) in the cross-section can be expressed as:

$$\begin{bmatrix} u_x \\ u_y \\ u_z \end{bmatrix} = \begin{bmatrix} u_{x,c} \\ u_{y,c} \\ u_{z,c} \end{bmatrix} + \begin{bmatrix} 0 & -\theta_{z,c} & \theta_{y,c} \\ \theta_{z,c} & 0 & -\theta_{x,c} \\ -\theta_{y,c} & \theta_{x,c} & 0 \end{bmatrix} \begin{bmatrix} 0 \\ y \\ z \end{bmatrix} + \phi_c f_{w,c} \begin{bmatrix} 1 \\ 0 \\ 0 \end{bmatrix} \tag{2.1}$$

where c denotes the centroid, u_x, u_y, u_z denote the longitudinal, vertical and lateral translations, θ_x, θ_y, θ_z are rotations about the x, y and z axes, $\phi = \phi(y, z)$ is the warping function dependent on the cross-section and $f_{w,c}$ is the warping displacement measure ($\theta_x = x f_w$). Here, u_x, u_y and u_z are assumed to be functions of the longitudinal co-ordinate x. The cross-section is assumed not to deform except for warping, thus the rotation matrix can be reduced to a 3-by-2 matrix where the terms in the first column are not used.

In Fig. 2.2 an infinitesimal element of length dx is shown along with the forces and moments acting on it, which will be used for the formulation of force equations. The external forces ($\tilde{F}$) and moments ($\tilde{M}$) per unit length are assumed to act in the positive direction of the co-ordinate system and consist of excitation forces and reaction forces due to the foundation, where k_x, k_y and k_z are the translational stiffnesses per unit length along the respective axis and k_{rx}, k_{ry} and k_{rz} are the corresponding rotational stiffnesses.

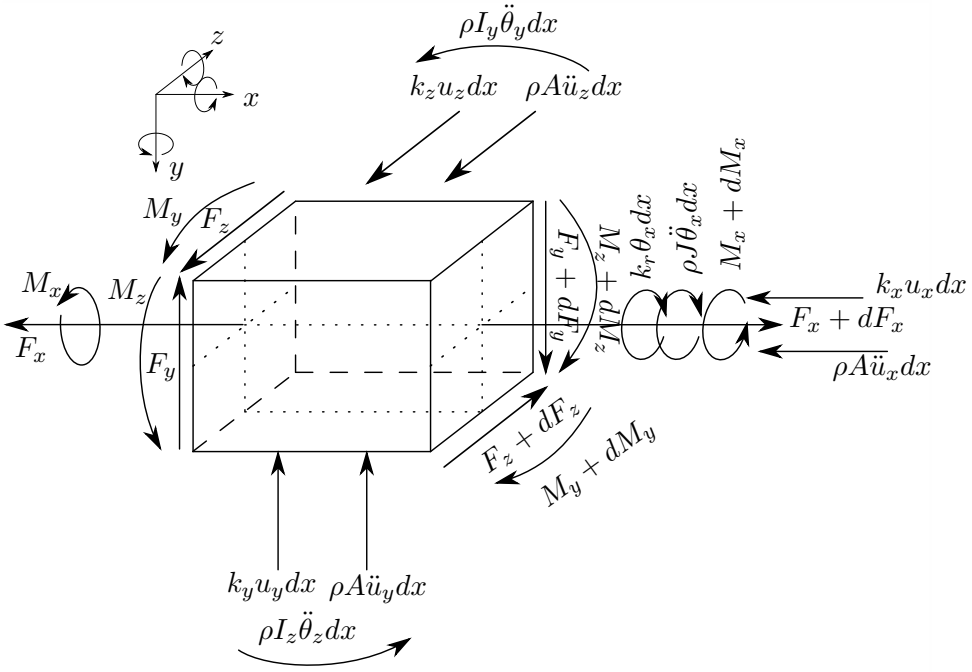

Figure 2.2: Forces acting on infinitesimal element

2.2 Strains and stresses in Cartesian co-ordinates

According to Love [82], the linear components of strain in Cartesian co-ordinates are:

$$\epsilon_{xx} = \frac{\partial u_x}{\partial x} \tag{2.2}$$

$$\gamma_{xy} = \frac{\partial u_y}{\partial x} + \frac{\partial u_x}{\partial y} \tag{2.3}$$

$$\gamma_{xz} = \frac{\partial u_z}{\partial x} + \frac{\partial u_x}{\partial z} \tag{2.4}$$

By combining Eq. (2.1) with Eqs (2.2)–(2.4) the following relationships are obtained:

$$\epsilon_{xx} = u'_{x,c} - y\theta'_{z,c} + z\theta'_{y,c} + \phi f'_w \tag{2.5}$$

$$\gamma_{xy} = u'_{y,c} - \theta_{z,c} - (\phi_{,y} + z)\theta'_{x,c} + \phi_{,y}(f_w + \theta'_{x,c}) \tag{2.6}$$

$$\gamma_{xz} = u'_{z,c} + \theta_{y,c} + (y - \phi_{,z})\theta'_{x,c} + \phi_{,z}(f_w + \theta'_{x,c}) \tag{2.7}$$

where the prime ($'$) indicates a derivative with respect to the longitudinal co-ordinate ($\partial/\partial x$), $\phi_{,y}$ indicates a derivative with respect to the vertical co-ordinate ($\partial\phi/\partial y$) and $\phi_{,z}$ indicates a derivative with respect to the lateral co-ordinate ($\partial\phi/\partial z$). Here, the 'dummy terms' $\phi_{,y}\theta'_{x,c}$ and $\phi_{,y}\theta'_{x,c}$ are introduced to allow for collection of terms at a later stage. The remaining strains, namely ϵ_{yy}, ϵ_{zz} and γ_{yz}, are assumed to be zero for the given beam model (i.e. no consideration is given to dilatation or Poisson's effects).

The normal and shear stresses can be calculated using the Young's modulus (E) and shear modulus (G), based on the generalised Hooke's law, as:

$$\sigma_{xx} = E\epsilon_{xx} \tag{2.8}$$

$$\tau_{xy} = G\gamma_{xy} \tag{2.9}$$

$$\tau_{xz} = G\gamma_{xz} \tag{2.10}$$

2.3 Force-deformation equations

Having obtained appropriate equations for the strain-displacement and stress-strain relationships, the stress resultants acting on the cross-section can be calculated by integrating the appropriate stresses over the cross-sectional area.

The force/deformation equations from normal stresses are derived as:

$$F_x = \int_A \sigma_{xx} dA = \int_A E\epsilon_{xx} dA \tag{2.11}$$

$$M_y = \int_A \sigma_{xx} z dA = \int_A E\epsilon_{xx} z dA \tag{2.12}$$

$$M_z = -\int_A \sigma_{xx} y dA = -\int_A E\epsilon_{xx} y dA \tag{2.13}$$

$$M_w = \int_A \sigma_{xx} \phi dA = \int_A E\epsilon_{xx} \phi dA \tag{2.14}$$

where M_w is the warping moment (or bi-moment). The warping moment is a pair of moments acting in opposite directions to each other at the rail foot and rail head, as shown in Fig. 2.3. This is also shown for convenience as a triple-headed arrow in the direction of the longitudinal axis.

Similarly, the force/deformation equations from shear stresses are derived as:

$$F_y = \int_A \tau_{xy} dA = \int_A G\gamma_{xy} dA \tag{2.15}$$

$$F_z = \int_A \tau_{xz} dA = \int_A G\gamma_{xz} dA \tag{2.16}$$

$$M_x = \int_A \left(\tau_{xz} y - \tau_{xy} z\right) dA = \int G\left(\gamma_{xz} y - \gamma_{xy} z\right) dA \tag{2.17}$$

$$M_x^s = \int_A \left(\tau_{xy}\phi_{,y} + \tau_{xz}\phi_{,z}\right) dA = \int_A G\left(\gamma_{xy}\phi_{,y} + \gamma_{xz}\phi_{,z}\right) dA \tag{2.18}$$

where M_x^s is the non-uniform torsion moment due to warping.

All the forces and moments are shown in Fig. 2.2 with the exception of the warping and non-uniform torsion moment. These force/deformation equations will be used in the subsequent sections along with the appropriate strain relationships.

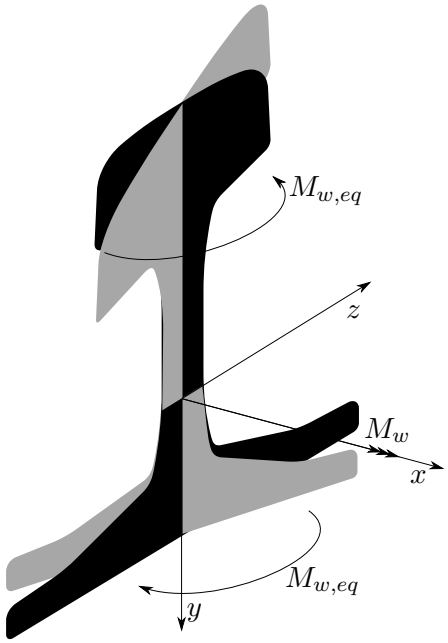

Figure 2.3: Bi-moment acting in a positive direction

2.4 Beam theories

In this section, the vibration of the beam in the axial, torsional, vertical and lateral directions is investigated individually.

2.4.1 Rod in extension

In considering the extension of a rod, only axial displacements are allowed. Under this assumption, the axial strain-displacement equation from Eq. (2.5) takes the form:

$$\epsilon_{xx} = u'_x \tag{2.19}$$

By taking the sum of the forces in the axial direction acting on the element in Fig. 2.2, the following relationship is obtained:

$$-F_x + (F_x + \frac{\partial F_x}{\partial x}dx) - k_x u_x dx - \rho A \ddot{u}_x dx = -\tilde{F}_x dx \tag{2.20}$$

which reduces to

$$-\frac{\partial F_x}{\partial x} + k_x u_x + \rho A \ddot{u}_x = \tilde{F}_x \tag{2.21}$$

where F_x is the axial force, $\tilde{F}_x$ is the external axial force per unit length, u_x is the axial displacement of the beam and k_x is the foundation stiffness in the x direction per unit

length. dx is the length of the infinitesimal element while ρ is the density of the beam and A is the cross-sectional area.

Inserting Eq. (2.19) into Eq. (2.11), the axial force is given by:

$$F_x = \int E\epsilon_{xx} dA = EA\epsilon_{xx} = EAu'_x \tag{2.22}$$

and hence from Eq. (2.21) the equation of motion is given by:

$$-EAu''_x + k_x u_x + \rho A\ddot{u}_x = \tilde{F}_x \tag{2.23}$$

By assuming that the response is harmonic both in space and time, a relationship can be derived between the frequency and the wavenumber, known as the dispersion relationship. The response is assumed to be harmonic with circular frequency ω (rad/s) and wavenumber ξ (rad/m), expressed as:

$$u_x = U_x e^{i\omega t} e^{-i\xi x} \tag{2.24}$$

where U_x denotes complex amplitude. When taking a derivative of a variable with respect to time t, the following relationship applies:

$$\frac{\partial u_x}{\partial t} = i\omega U_x e^{i\omega t} e^{-i\xi x} = i\omega u_x \tag{2.25}$$

Similarly, taking the derivative with respect to the longitudinal coordinate x, the following is obtained:

$$\frac{\partial u_x}{\partial x} = -i\xi U_x e^{i\omega t} e^{-i\xi x} = -i\xi u_x \tag{2.26}$$

Thus the equation of motion in the frequency-wavenumber domain becomes:

$$EA\xi^2 u_x + k_x u_x - \rho A\omega^2 u_x = \tilde{F}_x \tag{2.27}$$

The dispersion relationship (where $\tilde{F}_x = 0$) for a rod in extension is then given by:

$$EA\xi^2 + k_x - \rho A\omega^2 = 0 \tag{2.28}$$

which gives

$$\xi = \sqrt{\frac{\rho A\omega^2 - k_x}{EA}} \tag{2.29}$$

and is plotted in Fig. 2.4 for k_x=0 for the 60E1 section properties listed in Table 2.1. Here it is seen that the wavenumber increases in proportion to ω^1, and in the absence of support only obtains real values thus indicating propagating waves. The phase velocity defined as ω/ξ is given by $c_L = \sqrt{E/\rho}$ which is independent of the cross-section. In the

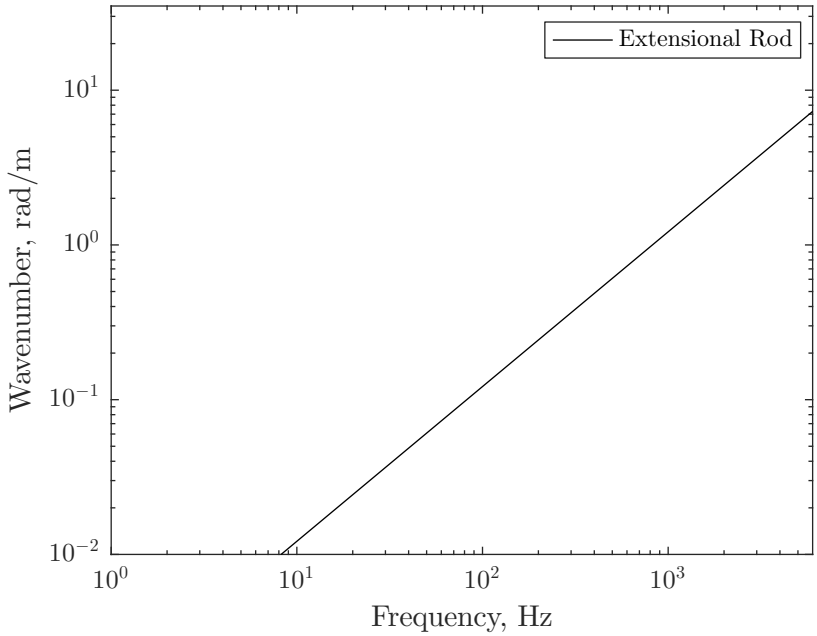

Figure 2.4: Dispersion relationship for the 60E1 rail in extension with properties listed in Table 2.1

case of a supported rail, a cut-on frequency exists, below which free waves cannot occur. This is given from Eq. (2.28) for zero wavenumber as:

$$f_{co,a} = \frac{1}{2\pi}\sqrt{\frac{k_x}{\rho A}} \tag{2.30}$$

where the frequency $f = \omega/2\pi$ has units Hz. Results including the support stiffness will be presented in Chapter 3.

2.4.2 Rod in torsion

The torsional vibration of a rod is developed here based on the internal forces occurring from a statics point of view. Then the inertial forces are considered to account for its dynamic behaviour. Based on the Saint-Venant theory for pure torsion [99], the cross-section is free to warp (unrestrained warping). The basic hypothesis for this theory is that the warping of the cross-section is the same for all cross-sections along the beam. Thus, there is no shear strain in the plane of the cross-section or longitudinal extension, with only tangential stresses due to torsion arising in the cross-section. The warping of the cross-section depends on the rate of change of angle of twist, i.e. $f_w = \theta_x'$ of the cross-section and the warping function. It also follows in the static case that the warping is constant along the x axis and thus the torsion will be uniform. The displacements of

the cross-section during torsion will be (see Eq. (2.1)):

$$u_x = \phi_S(y,z) f_w \tag{2.31}$$

$$u_y = -z\theta_x \tag{2.32}$$

$$u_z = y\theta_x \tag{2.33}$$

and the equivalent strains:

$$\epsilon_{xx} = \frac{\partial u_x}{\partial x} = 0 \text{ (since } f_w \text{ is constant)} \tag{2.34}$$

$$\gamma_{xy} = \frac{\partial u_y}{\partial x} + \frac{\partial u_x}{\partial y} = \theta'_x \left(\frac{\partial \phi_S}{\partial y} - z \right) \tag{2.35}$$

$$\gamma_{xz} = \frac{\partial u_z}{\partial x} + \frac{\partial u_x}{\partial z} = \theta'_x \left(\frac{\partial \phi_S}{\partial z} + y \right) \tag{2.36}$$

where the warping function $\phi_S(y,z) = \phi_S$ with respect to the shear centre needs to be determined. By taking the stress equilibrium equation in the axial direction it follows that [99]:

$$\frac{\partial \sigma_{xx}}{\partial x} + \frac{\partial \tau_{xy}}{\partial y} + \frac{\partial \tau_{xz}}{\partial z} = 0 \tag{2.37}$$

Substituting Eqs (2.34)–(2.36) in Eq. (2.37), the warping function must satisfy:

$$\frac{\partial^2 \phi_S}{\partial y^2} + \frac{\partial^2 \phi_S}{\partial z^2} = 0 \tag{2.38}$$

within the domain of the cross-section. Similarly, it can be shown that to satisfy equilibrium at the boundaries of the cross-section, it is required that [99]:

$$\frac{\partial \phi_S}{\partial n} = z n_y - y n_z \tag{2.39}$$

where $\partial/\partial n$ is the derivative normal to the boundary and n_y and n_z are the normals of the boundary in the y and z directions respectively. The warping function for the 60E1 rail is shown in Fig. 2.5, derived using the commercial Finite Element package COMSOL [98].

Assuming the same formulation applies for dynamic analysis (i.e. that the wavelength is assumed to be long compared with the lateral dimensions of the beam), and by taking the sum of the moments about the x-axis, including the reaction and inertial forces, it follows that:

$$-M_x + \left(M_x + \frac{\partial M_x}{\partial x} dx \right) - k_{rx}\theta_x dx - \rho I_p \ddot{\theta}_x dx = -\tilde{M}_x dx \tag{2.40}$$

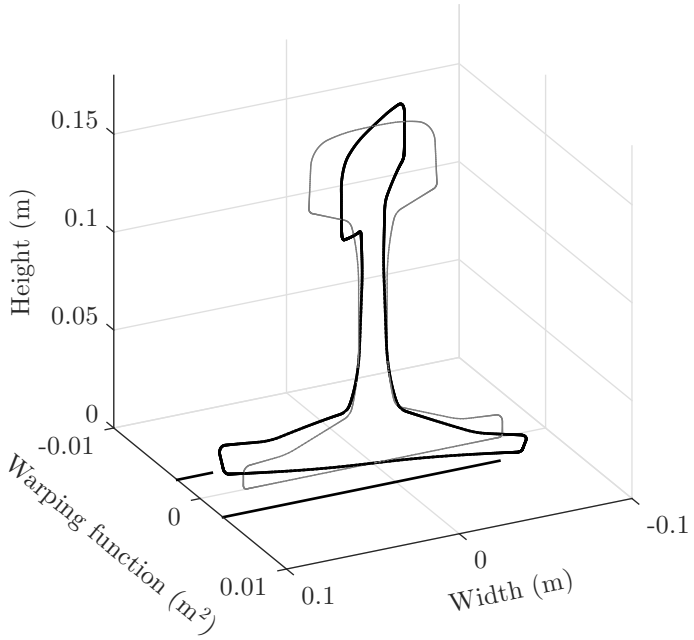

Figure 2.5: Warping function for 60E1 rail

which reduces to

$$-\frac{\partial M_x}{\partial x} + k_{rx}\theta_x + \rho I_p \ddot{\theta}_x = \tilde{M}_x \tag{2.41}$$

where $\tilde{M}_x$ is the external torque, k_{rx} is the rotational foundation stiffness about the x direction per unit length and I_p is the polar moment of area given by:

$$I_p = \int \left(y^2 + z^2\right) dA \tag{2.42}$$

Then the torsional (Saint-Venant) strain equation follows as:

$$\gamma_{sv} = \theta_x' \tag{2.43}$$

The torsional moment is then given through Eq. (2.17) by:

$$M_x = \int \left(G\gamma_{xz}y - G\gamma_{xy}z\right) dA = G \underbrace{\int \left(y^2 + z^2 + y\frac{\partial \phi_S}{\partial z} - z\frac{\partial \phi_S}{\partial y}\right) dA}_{J} \theta_x' = GJ\theta_x' \tag{2.44}$$

where J denotes the torsional constant. For circular bars, the torsional constant is equal to the polar moment of area, I_p, but this is not necessarily the case for non-circular bars.

By combining Eq. (2.41) with Eq. (2.44), the equation of motion of the system can be obtained as:

$$-GJ\theta_x'' + k_{rx}\theta_x + \rho I_p \ddot{\theta}_x = \tilde{M}_x \tag{2.45}$$

Assuming harmonic motion in both time and space, the dispersion relationship for a rod in torsion is obtained as:

$$GJ\xi^2 + k_{rx} - \rho I_p \omega^2 = 0 \tag{2.46}$$

which reduces to

$$\xi = \sqrt{\frac{\rho I_p \omega^2 - k_{rx}}{GJ}} \tag{2.47}$$

which has a similar form to the corresponding relation for extension, Eq. (2.29).

This is plotted in Fig. 2.6 for the case of k_{rx}=0 for the 60E1 section properties listed in Table 2.1. The wavenumber again increases proportional to ω^1. The phase velocity

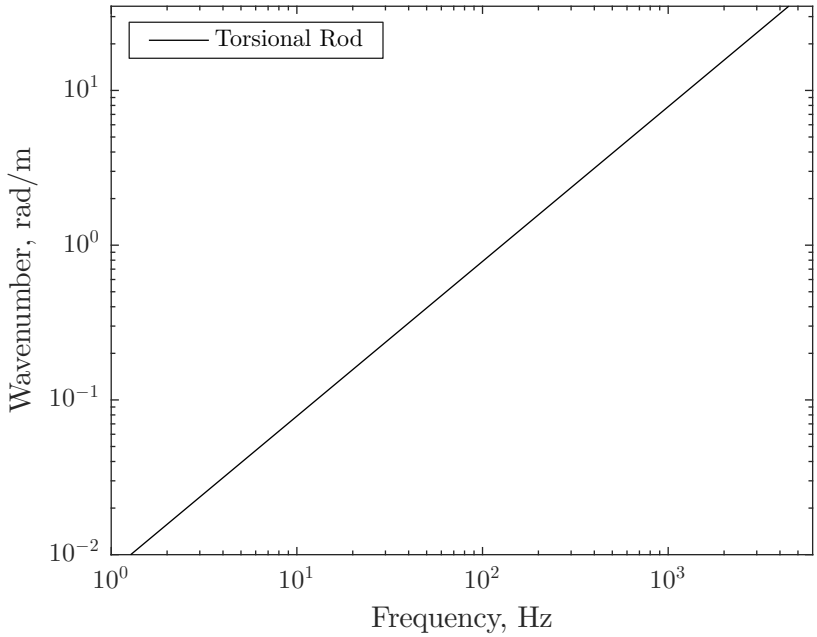

Figure 2.6: Dispersion relationship for the 60E1 rail in torsion with properties listed in Table 2.1

is $c_T = \sqrt{GJ/\rho I_p}$ which for the 60E1 rail is approximately $c_S/4$ since $J/I_p \approx 1/16$, where $c_S = \sqrt{G/\rho}$ is the phase velocity of shear waves in the material. In the case of a supported rail, a cut-on frequency exists, given from Eq. (2.46) for zero wavenumber as:

$$f_{co,t} = \frac{1}{2\pi}\sqrt{\frac{k_{rx}}{\rho I_p}} \tag{2.48}$$

2.4.3 Classical beam bending

When studying the transverse vibration of beams, the classical Euler-Bernoulli beam theory is often used. The main assumptions are that the cross-section does not deform

and it remains plane and normal to the deformed axis (centroid). If the infinitesimal element of Fig. 2.2 is considered, by summing the forces for the vertical direction the following is obtained:

$$-F_y + \left(F_y + \frac{\partial F_y}{\partial x}dx\right) - k_y u_y dx - \rho A \ddot{u}_y dx = -\tilde{F}_y dx \tag{2.49}$$

which reduces to

$$-\frac{\partial F_y}{\partial x} + k_y u_y + \rho A \ddot{u}_y = \tilde{F}_y \tag{2.50}$$

where F_y is the shear force, $\tilde{F}_y$ is the external force, u_y is the vertical displacement of the beam and k_y is the foundation stiffness in the y direction per unit length.

Since the only degrees of freedom considered are the displacement along the y axis and rotation about the z axis, Eq. (2.5) becomes:

$$\epsilon_{xx} = -y\theta_z' \tag{2.51}$$

The bending moment acting in the beam can then be found from Eq. (2.13) as:

$$M_z = -\int_A \epsilon_{xx} E y dA = E I_z \theta_z' \tag{2.52}$$

with

$$I_z = \int_A y^2 dA$$

where I_z is the second moment of area around the z-axis. The product EI_z constitutes the flexural rigidity of the beam. For small displacements, the following approximation can be assumed:

$$\frac{\partial^2 u_y}{\partial x^2} \approx \hat{k}_z = \theta_z' \tag{2.53}$$

where $\hat{k}_z$ is the curvature in bending around the z-axis. Similarly, taking the sum of the bending moments, it follows that:

$$-M_z + \left(M_z + \frac{\partial M_z}{\partial x}dx\right) + \frac{1}{2}F_y dx + \frac{1}{2}\left(F_y + \frac{\partial F_y}{\partial x}dx\right)dx - k_{rz}\theta_z dx = -\tilde{M}_z dx \tag{2.54}$$

giving

$$-\frac{\partial M_z}{\partial x} - F_y + k_{rz}\theta_z = \tilde{M}_z \tag{2.55}$$

and if no external moment is applied:

$$F_y = -\frac{\partial M}{\partial x} + k_{rz}\theta_z = -EI_z\frac{\partial^3 u_y}{\partial x^3} + k_{rz}\frac{\partial u_y}{\partial x} \tag{2.56}$$

Hence Eq. (2.50) leads to:

$$EI_z \frac{\partial^4 u_y}{\partial x^4} + k_y u_y - k_{rz} \frac{\partial^2 u_y}{\partial x^2} + \rho A \ddot{u}_y = \tilde{F}_y \tag{2.57}$$

In this equation, the first term represents the effect of the flexural rigidity of the beam, the second and third terms the resistance due to the foundation, the fourth term the inertial resistance due to the beam mass and the final term the external force. In the literature, the term due to the rotational foundation stiffness is commonly ignored.

In order to obtain the dispersion relationship, the vertical displacement of the cross-section due to bending of the beam is also written in a complex form similar to the axial displacement in Eq. (2.24). By substituting this form of response into the equation of motion the following is obtained from Eq. (2.57) (for k_{rz}=0):

$$\xi^2 = \pm \sqrt{\frac{\rho A \omega^2 - k_y}{EI_z}} \tag{2.58}$$

Figure 2.7 shows the dispersion relationship for a free Euler-Bernoulli beam, i.e. $k_y = k_{rz} = 0$ for the 60E1 section properties listed in Table 2.1. The roots (ξ) occur in pairs of $\pm\xi$ and $\pm \mathrm{i}\xi$.

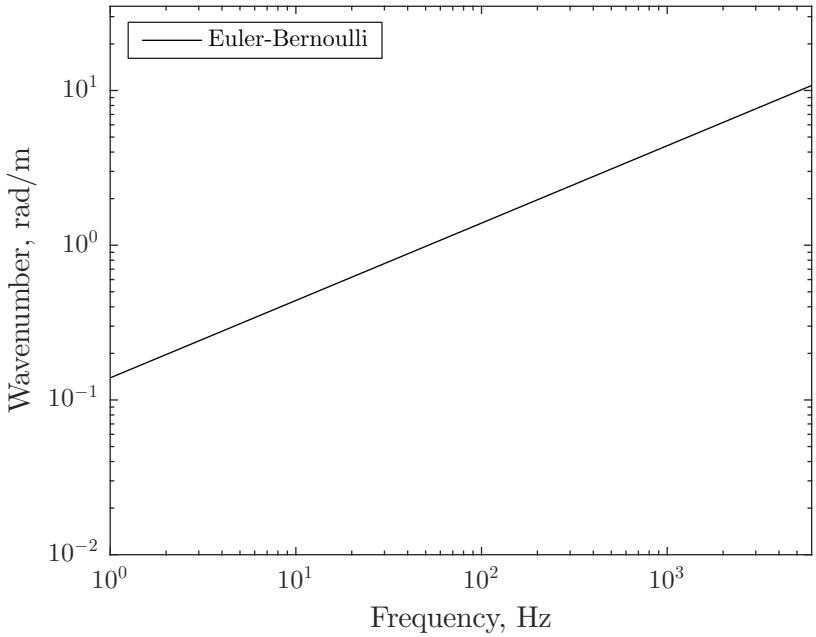

Figure 2.7: Dispersion relationship for a free Euler-Bernoulli beam with properties listed in Table 2.1 - vertical motion of rail

It is seen that the wavenumber is proportional to $\omega^{1/2}$. The corresponding wave speed is therefore frequency-dependent. Moreover, in the case of a supported rail, a cut-on

frequency exists, given from Eq. (2.58) as:

$$f_{co,v} = \frac{1}{2\pi}\sqrt{\frac{k_y}{\rho A}} \tag{2.59}$$

which corresponds to the mass of the rail bouncing on the support stiffness.

If the rotational inertia is taken into account, an additional term has to be considered in Eq. (2.57) as:

$$EI_z\frac{\partial^4 u_y}{\partial x^4} - \rho I_z\frac{\partial^4 u_y}{\partial x^2 \partial t^2} + k_y u_y + \rho A\ddot{u}_y = \tilde{F}_y \tag{2.60}$$

This is the so called Rayleigh beam [35]. The frequency-wavenumber relationship is given by the following quadratic equation for ξ^2:

$$EI_z\xi^4 - \rho I_z\xi^2\omega^2 + k_y - \rho A\omega^2 = 0 \tag{2.61}$$

which gives

$$\xi^2 = \pm\frac{\left(\sqrt{I_z(I_z\rho^2\omega^4 + 4E\rho A\omega^2 - 4Ek_y)} + I_z\rho\omega^2\right)}{2EI_z} \tag{2.62}$$

Figure 2.8 shows the dispersion relationship for a free Euler-Bernoulli beam when the rotational inertia is included (i.e. Rayleigh beam) for the 60E1 section properties listed in Table 2.1. At low frequencies, the wavenumbers from the two beam theories match

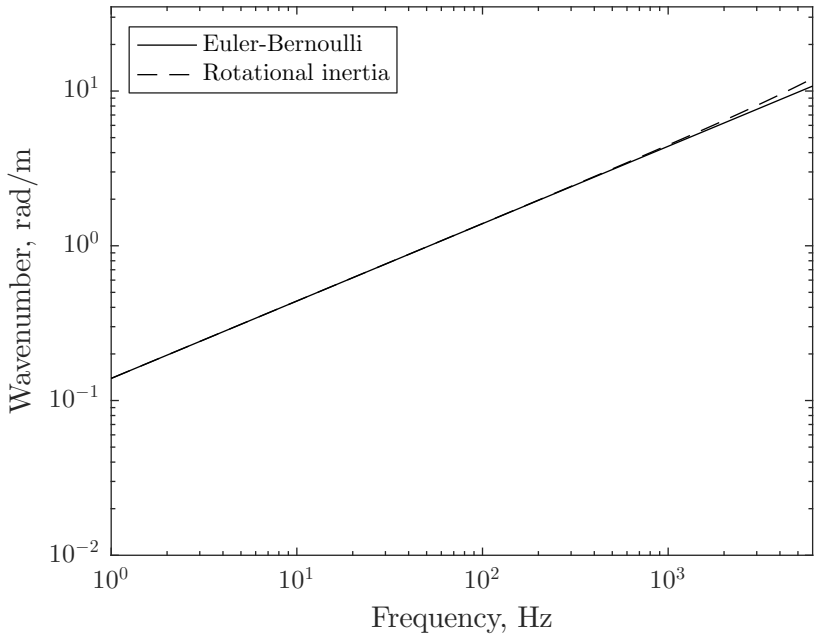

Figure 2.8: Dispersion relationship for a free Rayleigh beam including rotational inertia with properties listed in Table 2.1 - vertical motion of rail

closely. As the frequency increases, the effect of rotational inertia becomes more apparent

and the dispersion relation for the Rayleigh beam deviates from the Euler-Bernoulli beam theory.

2.4.4 Timoshenko beam theory

When considering higher frequencies, where the wavelength of the beam becomes shorter, apart from the rotational inertia shear deformations also become more significant. These where included by Timoshenko [36, 37] in the theory for the transverse vibration of beams. In Fig. 2.9 the bending of a beam including shear is shown schematically.

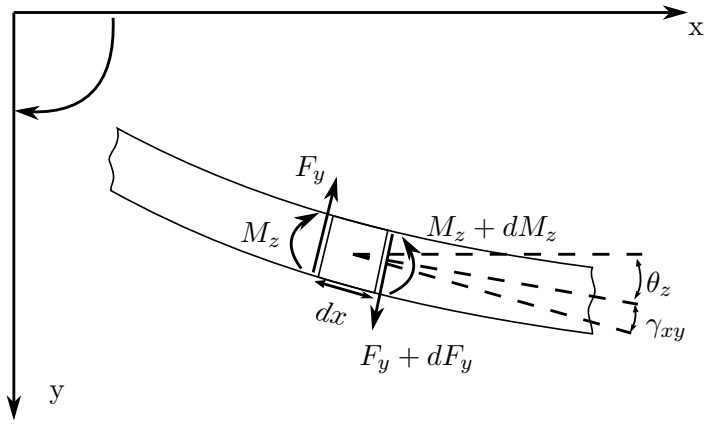

Figure 2.9: Beam bending with shear

Here θ_z denotes the angle between the x-axis and the normal to the plane of an infinitesimal element (i.e. the normal to the element face), while γ_{xy} denotes the angle between the normal to the plane of the infinitesimal element and the tangent to the beam centreline (shearing angle). Based on the above notation, and for small rotations, it follows that:

$$\frac{\partial u_y}{\partial x} = \theta_z + \gamma_{xy} \tag{2.63}$$

or

$$\gamma_{xy} = \frac{\partial u_y}{\partial x} - \theta_z \tag{2.64}$$

The above equation gives the shear strain (γ_{xy}) for a Timoshenko beam in vertical bending (denoted as $\hat{\gamma}_{xy}$), so $\hat{\gamma}_{xy} = \gamma_{xy}$. The shear force can be obtained from Eq. (2.15) as:

$$F_y = \int G\gamma_{xy} dA = GA\kappa_y \hat{\gamma}_{xy} \tag{2.65}$$

where κ_y is a correction factor depending on the cross-section known as the shear coefficient, which accounts for the effective area in shear ($A_S = \kappa A$) in the y direction.

Taking the sum of all the moments acting in the positive direction:

$$-M_z + \left(M_z + \frac{\partial M_z}{\partial x}dx\right) + \frac{1}{2}F_y dx + \frac{1}{2}\left(F_y + \frac{\partial F_y}{\partial x}dx\right)dx - \rho I_z \ddot{\theta}_z dx - k_{rz}\theta_z dx = -\tilde{M}_z \tag{2.66}$$

which reduces to

$$-\frac{\partial M_z}{\partial x} - F_y + k_{rz}\theta_z + \rho I_z \ddot{\theta}_z = \tilde{M}_z \tag{2.67}$$

The above leads to two coupled equations of motion:

$$-F_y' + k_y u_y + \rho A \ddot{u}_y = \tilde{F}_y \tag{2.68}$$

$$-M_z' - F_y + k_{rz}\theta_z + \rho I_z \ddot{\theta}_z = \tilde{M}_z \tag{2.69}$$

By substituting from Eqs (2.64), (2.65) and (2.53) this gives:

$$-GA\kappa_y(u_y'' - \theta_z') + k_y u_y + \rho A \ddot{u}_y = \tilde{F}_y \tag{2.70}$$

$$-EI_z\theta_z'' - GA\kappa_y(u_y' - \theta_z) + k_{rz}\theta_z + \rho I_z \ddot{\theta}_z = \tilde{M}_z \tag{2.71}$$

which constitute the classical dynamic equilibrium equations for a Timoshenko beam.

The differential relationships of Eqs (2.68)-(2.69), excluding foundation and inertial terms (i.e. static equations) can be written in matrix form as:

$$\begin{bmatrix} -\frac{d}{dx} & 0 \\ -1 & -\frac{d}{dx} \end{bmatrix} \begin{Bmatrix} F_y \\ M_z \end{Bmatrix} = \begin{Bmatrix} \tilde{F}_y \\ \tilde{M}_z \end{Bmatrix} \tag{2.72}$$

which can be written as

$$\mathbf{D}^* \sigma = \mathbf{P} \tag{2.73}$$

Here $\mathbf{D}^*$ denotes the differential matrix operator of the equilibrium conditions, σ denotes the generalised stress vector (internal forces) and $\mathbf{P}$ are the volume forces (external forces). According to Blaauwendraad [100], one can obtain the kinematic relations as:

$$\epsilon = \mathbf{D}^{*T}\mathbf{u} \tag{2.74}$$

where ϵ denotes the generalised strain vector, $\mathbf{u}$ the generalised field of displacements and the superscript T the transpose matrix operation. A special property of the differential matrix operator is that when it is transposed, the sign of the odd derivatives changes.

Thus, the strain-displacement relationships become:

$$\begin{Bmatrix} \hat{\gamma}_{xy} \\ \hat{k}_z \end{Bmatrix} = \begin{bmatrix} \dfrac{d}{dx} & -1 \\ 0 & \dfrac{d}{dx} \end{bmatrix} \begin{Bmatrix} u_y \\ \theta_z \end{Bmatrix} \tag{2.75}$$

Thus, the shear strain is given by:

$$\hat{\gamma}_{xy} = u_y' - \theta_z \tag{2.76}$$

and the bending strain by:

$$\hat{k}_z = \theta_z' \tag{2.77}$$

It is seen that the above relations are consistent with Eqs (2.53) and (2.64). This method will be used later to obtain the strain-displacement relationships for more complicated systems.

For the lateral bending, the same relationships can be reproduced, with only sign differences occurring due to the sign convention. Thus by analogy with Eqs (2.68) and (2.69) the equations of motion for the lateral bending read:

$$-F_z' + k_z u_z + \rho A \ddot{u}_z = \tilde{F}_z \tag{2.78}$$

$$-M_y' + F_z + k_{ry}\theta_y + \rho I_y \ddot{\theta}_y = \tilde{M}_y \tag{2.79}$$

with the strain-displacement equations for shear given by:

$$\hat{\gamma}_{xz} = u_z' + \theta_y \tag{2.80}$$

and the bending strain given by:

$$\hat{k}_y = \theta_y' \tag{2.81}$$

Again, Eq. (2.80) shows the shear strain (γ_{xz}) for a Timoshenko beam in lateral bending (i.e. $\gamma_{xz} = \hat{\gamma}_{xz}$).

In order to obtain the dispersion relationship for the Timoshenko beam, the displacement and the rotation of the cross-section due to bending of the beam are written in a complex form similar to the axial displacement in Eq. (2.24). By substituting this form of response back into the equations of motion and collecting terms for the complex amplitudes, the following is obtained:

$$\begin{bmatrix} k_y - \rho A\omega^2 + GA\kappa_y\xi^2 & -iGA\kappa_y\xi \\ iGA\kappa_y\xi & k_{rz} + GA\kappa_y - \rho I_z\omega^2 + EI_z\xi^2 \end{bmatrix} \begin{Bmatrix} U_y \\ \Theta_z \end{Bmatrix} = \begin{Bmatrix} \tilde{F}_y \\ \tilde{M}_z \end{Bmatrix} \tag{2.82}$$

which can be written as

$$\mathbf{A}(\xi,\omega)\tilde{\mathbf{U}}(\xi,\omega) = \tilde{\mathbf{F}}(\xi,\omega) \tag{2.83}$$

where $\tilde{\mathbf{U}}$ contains the complex amplitudes, $\tilde{\mathbf{F}}$ the forces and the dynamic stiffness matrix $\mathbf{A}$ is a 2-by-2 matrix of the coefficients dependent on ξ and ω. By collecting terms within $\mathbf{A}$ for ξ and ω, $\mathbf{A}$ can be written as:

$$\mathbf{A} = \mathbf{K}_0 + \mathbf{K}_p - \omega^2\mathbf{M} - i\xi\mathbf{K}_1 - \xi^2\mathbf{K}_2 \tag{2.84}$$

where

$$\mathbf{K}_0 = \begin{bmatrix} 0 & 0 \\ 0 & GA\kappa_y \end{bmatrix} \qquad \mathbf{K}_p = \begin{bmatrix} k_y & 0 \\ 0 & k_{rz} \end{bmatrix}$$
$$\mathbf{K}_1 = \begin{bmatrix} 0 & GA\kappa_y \\ -GA\kappa_y & 0 \end{bmatrix} \qquad \mathbf{K}_2 = \begin{bmatrix} -GA\kappa_y & 0 \\ 0 & -EI_z \end{bmatrix}$$
$$\mathbf{M} = \begin{bmatrix} \rho A & 0 \\ 0 & \rho I_z \end{bmatrix}$$

In order to obtain the dispersion relation, the free vibration ($\tilde{\mathbf{F}} = \mathbf{0}$) is considered. For such a case, non-trivial solutions require $|\mathbf{A}| = 0$. This is a dual (non-linear) eigenvalue problem in ξ and ω. In order to simplify the solution process, the 2×2 non-linear eigenvalue problem is rewritten as an equivalent 4×4 linear eigenvalue problem [101]. This is achieved by rewriting Eq. (2.82) in the form:

$$\mathbf{A}_1\mathbf{u} + i\xi\mathbf{A}_2\mathbf{u} = \mathbf{0} \tag{2.85}$$

where

$$\mathbf{A_1} = \begin{bmatrix} \mathbf{K}_0 - \omega^2\mathbf{M} & -\mathbf{K}_1 \\ \mathbf{0}_{7\times7} & \mathbf{I}_{7\times7} \end{bmatrix} \tag{2.86}$$

$$\mathbf{A_2} = \begin{bmatrix} \mathbf{0}_{7\times7} & \mathbf{K}_2 \\ -\mathbf{I}_{7\times7} & \mathbf{0}_{7\times7} \end{bmatrix} \tag{2.87}$$

and $\mathbf{u} = \left(\tilde{\mathbf{U}}, i\xi\tilde{\mathbf{U}}\right)^T$.

The above system of equations can be solved as an eigenvalue problem for $\lambda = -i\xi$, i.e. $\mathbf{A}_1\mathbf{u} = \lambda\mathbf{A}_2\mathbf{u}$, yielding four solutions for $\xi(\omega) = i\lambda$. Due to the forms of the various matrices, these solutions can be divided into two sets with $\mathrm{Im}(\xi_1) \leq 0$ (propagating in the positive direction) and $\mathrm{Im}(\xi_2) \geq 0$ (propagating in the negative direction), with the second set given by $\xi_2 = -\xi_1$. If damping was included there would be no solutions with $\mathrm{Im}(\xi) = 0$. Although this procedure may seem unnecessary for a simple system of two

simultaneous equations, it is introduced here as it will be used later for more complex systems.

Figure 2.10 shows the dispersion relationship for a free ($k_y = k_{rz} = 0$) Timoshenko beam in vertical bending which is compared with the Euler-Bernoulli beam model for the 60E1 section properties listed in Table 2.1.

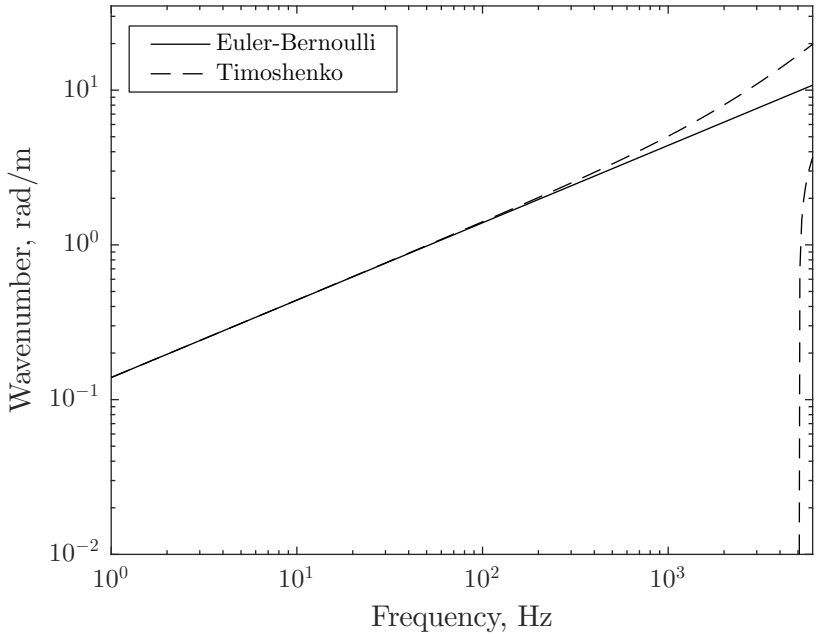

Figure 2.10: Dispersion relationship for a free Timoshenko beam with properties listed in Table 2.1 - vertical motion of rail

It is clear that for higher frequencies the results deviate significantly from the Euler-Bernoulli beam theory. The wavenumbers from the two beam theories match up to about 500 Hz with a difference of up to 7.5 %. The percentage difference between the wavenumbers for the two models increases almost linearly. At 1000 Hz the difference is approximately 15 % while at 2000 Hz it is 30 %. Similar conclusions about the validity of the Euler-Bernoulli beam have been made previously by Thompson and Vincent [62]. A second wave cuts on at about 5 kHz which corresponds to the shear wave in the Timoshenko beam theory. Its cut-on frequency can be calculated by setting ξ=0 in Eq. (2.84), i.e.:

$$|\mathbf{K}_0 + \mathbf{K}_p - \omega^2 \mathbf{M}| = 0 \tag{2.88}$$

Solving this system of equations for $\mathbf{K}_p$=0, the cut-on frequency for the shear wave is found to be:

$$f_{s,v} = \frac{1}{2\pi}\sqrt{\frac{GA\kappa_y}{\rho I_z}} \tag{2.89}$$

Below this frequency this wave is an evanescent wave with an imaginary wavenumber. At low frequencies it is similar to the evanescent wave in the Euler Bernoulli beam. Once the shear wave cuts on, it causes the bending wavenumber to tend to a slope of ω^1 at high frequencies. The corresponding phase velocity tends to the phase velocity of a shear beam, $\sqrt{G\kappa_y/\rho} = \sqrt{\kappa_y}c_S$. The second wave tends to the wavespeed of the longitudinal wave in a beam, $c_L = \sqrt{E/\rho}$.

Similarly, Fig. 2.11 shows the dispersion relationship for a free Timoshenko beam in lateral bending for the 60E1 section properties listed in Table 2.1. The wavenumbers

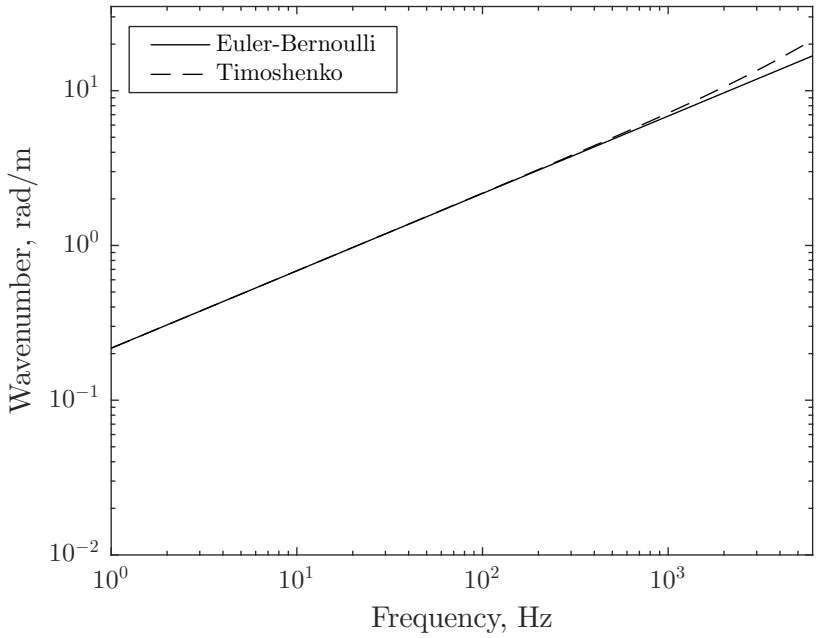

Figure 2.11: Dispersion relationship for a free Timoshenko beam with properties listed in Table 2.1 - lateral motion of rail

for Euler-Bernoulli and Timoshenko beam theories for lateral bending show a good agreement over a wider range of frequencies. The wavenumbers from the two beam theories in lateral bending of a 60E1 rail show a difference of up to 2.2% at 500 Hz, 4.4% at 1 kHz while at 2 kHz the difference is 8.5%. At the maximum frequency of interest, which is 5 kHz, the percentage difference between the wavenumbers is 18.4%. This occurs due to the fact that the shear waves cut on at a much higher frequency for the lateral direction than for the vertical direction. Here, the shear wave will cut on at

$$f_{s,l} = \frac{1}{2\pi}\sqrt{\frac{GA\kappa_z}{\rho I_y}} \tag{2.90}$$

which is approximately 14 kHz for the given parameters, almost three times as high as for vertical bending.

2.5 Effect of restrained warping

In the Saint-Venant theory for uniform torsion, the cross-section is free to warp and the warping of the cross-section is assumed constant throughout the length of the beam. This is not the case when the beam has external supports, when the torsional moment varies along the length of the beam, or as in the case of the 60E1 rail, when the beam is not prismatic [77, 102]. In this section, the equation of motion for torsion under the effect of restrained warping as well as the equation of motion for warping will be developed.

When accounting for restrained warping (thin-wall beam theory), non-uniform torsion occurs in which the warping of the cross-section is not constant. However, the warping displacement is still assumed to be $f'_w\phi_S$. Longitudinal extension can take place as a result of torsion in thin-walled beams [103]. This axial deformation due to non-uniform warping creates normal stresses ($\sigma_{xx,w}$) since Eq. (2.34) becomes:

$$\epsilon_{xx} = f'_w\phi_S = \theta''_x\phi_S \quad (\text{since } f_w = \theta'_x) \tag{2.91}$$

By taking the stress equilibrium equation in the axial direction, as in Eq. (2.37), it follows that:

$$\frac{\partial\sigma_{xx}}{\partial x} + \frac{\partial\tau_{xy}}{\partial y} + \frac{\partial\tau_{xz}}{\partial z} = 0 \tag{2.92}$$

Substituting Eqs (2.35)–(2.36) and Eq. (2.91) in Eq. (2.92), the latter becomes:

$$E\theta'''_x\phi_S + G\theta'_x\frac{\partial^2\phi_S}{\partial y^2} + G\theta'_x\frac{\partial^2\phi_S}{\partial z^2} = 0 \tag{2.93}$$

and hence

$$\frac{\partial^2\phi_S}{\partial y^2} + \frac{\partial^2\phi_S}{\partial z^2} = -\frac{E\theta'''_x}{G\theta'_x}\phi_S \tag{2.94}$$

From the last relationship, it is seen that ϕ_S is also a function of x (since $\theta_x = \theta_x(x)$), contradicting the definition of the warping function as being dependent only on y and z [78], although it is expected to vary slowly as the torsional rigidity (GJ) of the 60E1 rail profile is 40 times higher than its warping rigidity (EI_w). In order to obtain a consistent system of equations, in [78] the stresses are decomposed into primary stresses accounting for the shear stresses due to uniform torsion (Saint-Venant) and secondary stresses accounting for the shear stresses that equate to the normal stresses that arise in the non-uniform torsion theory. Additionally, the warping function is also decomposed in a similar fashion, with the primary warping function being the same as in the Saint-Venant theory and the secondary warping function being additionally a function of x.

The displacement in the axial direction is then written as:

$$u_x = \phi_S^p(y,z) f_w + \phi_S^s(x,y,z) \tag{2.95}$$

The shear stresses are then written as:

$$\tau_{xy} = \tau_{xy}^p + \tau_{xy}^s \tag{2.96}$$

$$\tau_{xz} = \tau_{xz}^p + \tau_{xz}^s \tag{2.97}$$

where the primary shear stresses are based on the strains from Eqs (2.35)–(2.36) and the secondary shear stresses are given as:

$$\tau_{xy}^s = G\frac{\partial \phi_S^s}{\partial y} \tag{2.98}$$

$$\tau_{xz}^s = G\frac{\partial \phi_S^s}{\partial z} \tag{2.99}$$

ϕ_S^s is the secondary warping function and needs to satisfy the Neumann problem within the domain of the cross-section

$$\frac{\partial^2 \phi_S^s}{\partial y^2} + \frac{\partial^2 \phi_S^s}{\partial z^2} = -\frac{E}{G}\theta_x{}'''\phi_S^p(y,z) \tag{2.100}$$

and the boundary condition

$$\frac{\partial \phi_S^s}{\partial n} = 0 \tag{2.101}$$

Then, the normal stress due to warping is:

$$\sigma_{xx,w} = E\theta_x''\phi_S^p \tag{2.102}$$

Similarly, the twisting moment can be decomposed as:

$$M_x = M_x^p + M_x^s \tag{2.103}$$

M_x^p is the Saint-Venant torsional moment, while M_x^s is the non-uniform torsion moment due to warping, evaluated due to the secondary shear stresses acting on the cross-section as:

$$M_x^s = \int \tau_{xy}^s \frac{\partial \phi_S^s}{\partial y} + \tau_{xz}^s \frac{\partial \phi_S^s}{\partial z} dA \tag{2.104}$$

If combined with Eq. (2.100) this takes the form:

$$M_x^s = -EI_w\theta_x''' \tag{2.105}$$

where the warping constant (I_w) is calculated by [78]:

$$I_w = \int (\phi_S^p)^2 dA \tag{2.106}$$

Thus the equation of motion for the twisting of the rod, Eq. (2.45), is modified to give:

$$EI_w\theta_x'''' - GJ\theta_x'' + k_{rx}\theta_x + \rho I_p\ddot{\theta}_x = \tilde{M}_x \tag{2.107}$$

Similarly, the normal stress will cause a new stress resultant, called the warping moment (or bimoment) as:

$$M_w = \int \phi_S^p \sigma_{xx,w} dA \tag{2.108}$$

$$= -EI_w\theta_x'' \tag{2.109}$$

The dispersion relationship for a rod in torsion with warping is written from Eq. (2.107) as a quadratic relationship in ξ^2 as:

$$-EI_w\xi^4 - GJ\xi^2 + k_{rx} + I_p\rho\omega^2 = 0 \tag{2.110}$$

Hence

$$\xi^2 = \pm\frac{\sqrt{G^2J^2 + 4EI_pI_w\rho\omega^2 + 4EI_wk_{rx}} - GJ}{2EI_w} \tag{2.111}$$

The above equation represents the influence of warping in the torsion for non-circular rods. At low frequencies, the response will be similar to that of simple uniform torsion, while at higher frequencies the wavenumber is increasing proportionally to $\omega^{1/2}$, as shown in Fig. 2.12. Comparing this with Fig. 2.7, it can be seen that warping has a greater effect on torsion than shear deformations has on bending. Despite this, torsion is expected to be less influential than bending in terms of rolling noise, and is thus unlikely to have a greater effect in terms of the overall noise levels.

In order to obtain the equation of motion for the warping degree of freedom, the variation of the warping moment (bimoment) in the beam needs to be considered. By comparison of Eq. (2.105) and Eq. (2.109) it follows that:

$$\frac{\partial M_w}{\partial x} = M_x^s \tag{2.112}$$

The above equation describes the equilibrium of the beam in the axial direction obtained in terms of the angle of twist [104]. If external force and inertia due to warping are considered, then the equation of motion for the warping component reads:

$$-\frac{\partial M_w}{\partial x} + M_x^s + \rho I_w\ddot{f}_w = \tilde{M}_w \tag{2.113}$$

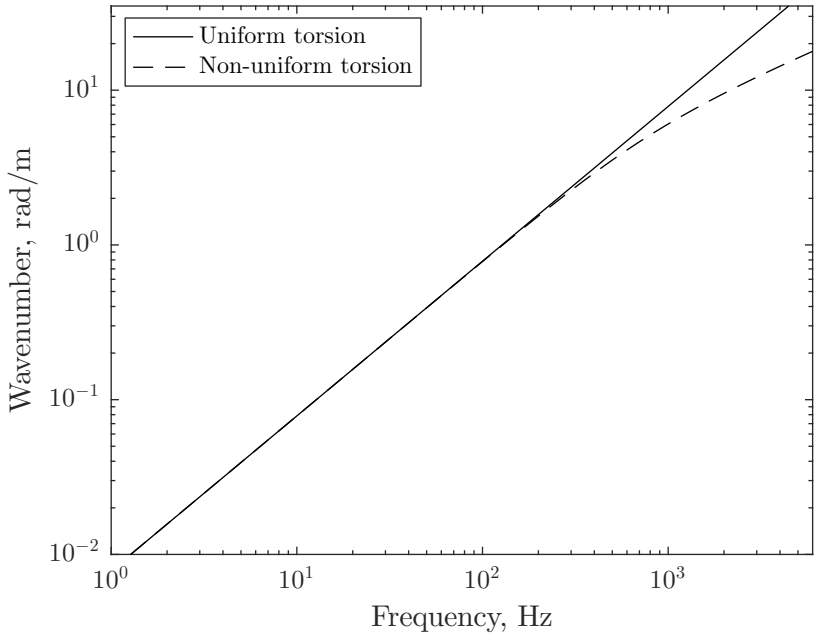

Figure 2.12: Dispersion relationship for non-uniform torsion beam with properties listed in Table 2.1

while $M_x^s = M_x - T_{sv}$ and the corresponding strain-displacement equations follow as:

$$\gamma_w = \gamma_{sv} + f_w \tag{2.114}$$

and

$$\hat{k}_w = f_w' \tag{2.115}$$

The foundation resistance to warping can also be accounted for by either a concentrated force (F) or a moment (M). In the case of a concentrated force, the resistance due to warping k_w is:

$$k_w = F\phi_F \tag{2.116}$$

where ϕ_F is the primary warping function at the point of application of the force. Similarly, in the case of a reaction moment the resistance due to warping is:

$$k_w = e_S M \tag{2.117}$$

where e_S is the distance between the location of the applied moment and the shear centre (the derivation of the foundation resistance due to warping is presented in Appendix A). Thus when accounting for foundation resistance to warping, Eq. (2.113) becomes:

$$-\frac{\partial M_w}{\partial x} + M_x^s + k_w f_w + \rho I_w \ddot{f}_w = \tilde{M}_w \tag{2.118}$$

In the following sections, and when developing the fully coupled model in Chapter 3, Eq. (2.118) will be used along with Eq. (2.107) to describe the torsional and warping responses of the rail.

2.6 Consideration of shear deformations due to restrained warping

In the above model for warping, the shear deformation due to the torsional warping is not taken into account and the secondary torsional moment is only based on the normal stresses. Similarly to the Timoshenko theory for shear deformation in bending, shear deformation can also be induced due to warping (see for example Sapountzakis [78], Pavazza [105]). Thus the rotation of the section can be separated into primary and secondary twist as:

$$\theta_x = \theta_x^p + \theta_x^s \tag{2.119}$$

with the secondary torsional curvature given as:

$$\frac{d\theta_x^s}{dx} = \frac{M_t^s}{GJ^s} \tag{2.120}$$

in which the secondary torsional constant J^s is [106]:

$$J^s = \kappa_S \left(I_p - J\right) \tag{2.121}$$

and κ_S is a correction factor for the effective shear area undergoing torsion, similar to Eq. (2.65) for vertical bending. Here, $\kappa_S = 1$ is used, similar to Gendy and Saleeb [86]. As noted by Mokos and Sapountzakis [107], for open cross-sections (e.g. I-beams) the secondary torsional moment has only a small influence on the torsional behaviour of the beam; however, its inclusion will lead to more accurate results. Thus the value of the correction factor κ^S will not influence the response of the beam significantly. The dispersion relation including shear forces due to torsional warping is depicted in Fig. 2.13, and compared with the non-uniform torsion in which shear forces are ignored (torsion-bending). The inclusion of shear forces has a small effect at high frequencies, above 3 kHz.

2.7 Influence of shear-centre eccentricity

So far, the centroidal and shear axes of the beam have been assumed to be coincident, as for symmetric cross-sections. For singly-symmetric or fully asymmetric cross-sections they are not necessarily coincident and this offset should be accounted for. Here, the

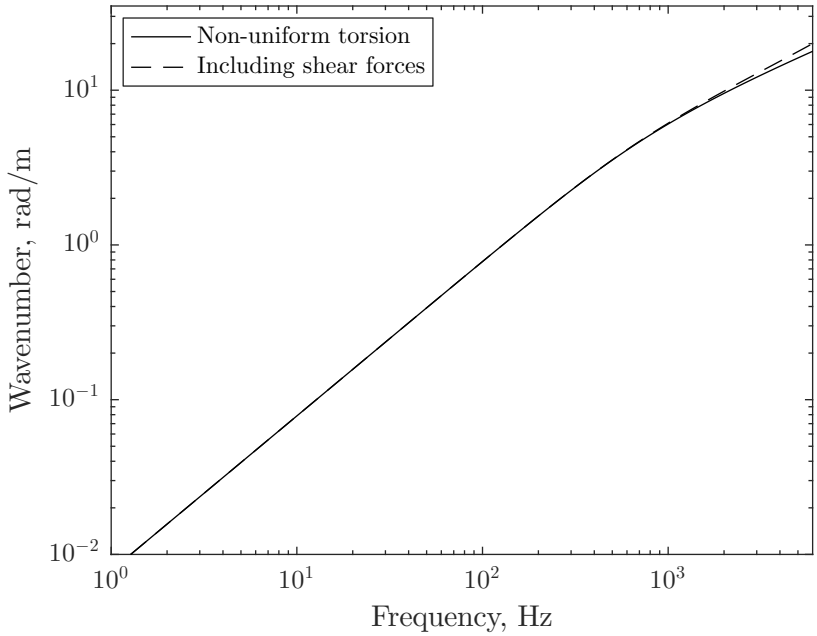

Figure 2.13: Dispersion relationship for torsion-bending beam including secondary torsional moment

centroid is used as the reference point, so the effect of all the forces and displacement fields acting at the shear centre need to be appropriately accounted for at the centroid. This process will be shown in this section based on the methodology of Kim et al. [31]. Due to the shear centre eccentricity introduced in this section, the bending in the vertical and lateral directions, as well as the torsional motion (including warping) are coupled together.

The general displacement field at the centroid is written in terms of that at the shear centre from Eq. (2.1) as:

$$u_{x,c} = u_{x,S} \tag{2.122}$$

$$u_{y,c} = u_{y,S} + e_z \theta_{x,S} \tag{2.123}$$

$$u_{z,c} = u_{z,S} - e_y \theta_{x,S} \tag{2.124}$$

$$\theta_{x,c} = \theta_{x,S} \tag{2.125}$$

$$\theta_{y,c} = \theta_{y,S} + e_y f_w \tag{2.126}$$

$$\theta_{z,c} = \theta_{z,S} + e_z f_w \tag{2.127}$$

$$f_c = f_w \tag{2.128}$$

where the distances e_y and e_z are shown in Fig. 2.1.

The transformation of the equations of motion only affects the following force components:

$$M_{x,c} = M_{x,S} + e_y F_{z,S} - e_z F_{y,S} \tag{2.129}$$

$$M^s_{x,c} = M^s_{x,S} + e_y F_{z,S} - e_z F_{y,S} \tag{2.130}$$

$$M_{w,c} = M_{w,S} + e_y M_{y,c} + e_z M_{z,c} \tag{2.131}$$

and the warping function at the centroid is expressed as:

$$\phi = \phi_S - e_z y + e_y z \tag{2.132}$$

Transforming the cross-sectional properties it follows that:

$$\begin{aligned} I_{w,c} &= \int \phi^2 dA = \int (\phi_S - e_z y + e_y z)^2 dA \\ &= I_w + e_y^2 I_y + e_z^2 I_z - 2 e_y e_z I_{yz} \end{aligned} \tag{2.133}$$

$$\begin{aligned} I_{wy} &= \int \phi z dA = \int (\phi_S - e_z y + e_y z) z dA \\ &= e_y I_y - e_z I_{yz} \end{aligned} \tag{2.134}$$

$$\begin{aligned} I_{wz} &= \int \phi y dA = \int (\phi_S - e_z y + e_y z) y dA \\ &= -e_z I_z + e_y I_{yz} \end{aligned} \tag{2.135}$$

with $I_{S,wy} = I_{S,wz} = 0$.

According to [31], the force-deformation equations for the shear forces and restrained warping are:

$$F_{y,S} = G A_{S,y} (u'_{y,S} - \theta_{z,c}) \tag{2.136}$$

$$F_{z,S} = G A_{S,z} (u'_{z,S} + \theta_{y,c}) \tag{2.137}$$

$$M^s_{x,S} = G A_{S,r} (\theta'_{x,S} + f_w) \tag{2.138}$$

$$M_{w,S} = E I_{w,S} f_w \tag{2.139}$$

and thus the forces acting at the centroid will take the form (in terms of displacements and rotations at the centroid):

$$F_{y,c} = F_{y,S} = G A_{S,y} (u'_{y,c} - \theta_{z,c}) - e_z G A_{S,y} (\theta'_{x,c} + f_w) \tag{2.140}$$

$$F_{z,c} = F_{z,S} = G A_{S,z} (u'_{z,c} + \theta_{y,c}) + e_y G A_{S,z} (\theta'_{x,c} + f_w) \tag{2.141}$$

$$M^s_{y,c} = G J_r (\theta'_{x,c} + f_w) - e_z G A_{S,y} (u'_{y,c} - \theta_{z,c}) + e_y G A_{S,z} (u'_{z,c} + \theta_{y,c}) \tag{2.142}$$

$$M_{w,c} = E I_{w,c} f_w + E I_{wy} \theta'_y + E I_{wz} \theta'_z \tag{2.143}$$

where $J_r = J^s + e_z^2 A_{S,y} + e_y^2 A_{S,z}$.

In the presence of warping, $M_{x,S} - M^s_{x,S} = M_{x,c} - M^s_{x,c}$, i.e. the effect of the shear force eccentricity is readily taken into account by the non-uniform torsion. In the absence of warping, Eq. (2.129) will have to be explicitly taken into account in the equations of motion.

Additional inertial terms are required to accommodate asymmetric cross-sections. These terms arise from the product moment of area between the y and z axis (I_{yz}), as well as terms related to warping (I_{wy} and I_{wz}), which were previously evaluated, with the inertial forces introduced as follows:

$$-M'_y + F_z + \rho(I_y - I_{wy})\ddot{\theta}_y + k_{yr}\theta_y - \rho I_{yz}\ddot{\theta}_z + \rho I_{wy}\ddot{f}_w = \tilde{M}_y \tag{2.144}$$

$$-M'_z - F_y + \rho(I_z + I_{wz})\ddot{\theta}_z + k_{zr}\theta_z - \rho I_{yz}\ddot{\theta}_y - \rho I_{wz}\ddot{f}_w = \tilde{M}_z \tag{2.145}$$

$$-M'_w + M^s_x + \rho I_w\ddot{f} + k_w f_w - \rho I_{wz}\ddot{\theta}_z + \rho I_{wy}\ddot{\theta}_y = \tilde{M}_w \tag{2.146}$$

Writing the equations of motion according to Eq. (2.84), taking into account the above equations, the matrices $\mathbf{K}_p$, $\mathbf{K}_0$, $\mathbf{K}_1$, $\mathbf{K}_2$ and $\mathbf{M}$ take the form:

$$\mathbf{K}_p = \mathrm{diag}(k_y, k_z, k_{xr}, k_{yr}, k_{zr}, k_w) \tag{2.147}$$

$$\mathbf{K}_0 = \begin{bmatrix} 0 & 0 & 0 & 0 & 0 & 0 \\ 0 & 0 & 0 & 0 & 0 & 0 \\ 0 & 0 & 0 & 0 & 0 & 0 \\ 0 & 0 & 0 & GA\kappa_z & 0 & GA\kappa_z e_y \\ 0 & 0 & 0 & 0 & GA\kappa_y & GA\kappa_y e_z \\ 0 & 0 & 0 & GA\kappa_z e_y & GA\kappa_y e_z & GJ_r \end{bmatrix} \tag{2.148}$$

$$\mathbf{K}_1 = \begin{bmatrix} 0 & 0 & 0 & 0 & GA\kappa_y & GA\kappa_y e_z \\ 0 & 0 & 0 & -GA\kappa_z & 0 & -GA\kappa_z e_y \\ 0 & 0 & 0 & -GA\kappa_z e_y & -GA\kappa_y e_z & -GJ_r \\ 0 & GA\kappa_z & GA\kappa_z e_y & 0 & 0 & 0 \\ -GA\kappa_y & 0 & GA\kappa_y e_z & 0 & 0 & 0 \\ -GA\kappa_y e_z & GA\kappa_z e_y & GJ_r & 0 & 0 & 0 \end{bmatrix} \tag{2.149}$$

$$\mathbf{K}_2 = \begin{bmatrix} -GA\kappa_y & 0 & GA\kappa_y e_z & 0 & 0 & 0 \\ 0 & -GA\kappa_z & -GA\kappa_z e_y & 0 & 0 & 0 \\ GA\kappa_y e_z & -GA\kappa_z e_y & -G(J + J_r) & 0 & 0 & 0 \\ 0 & 0 & 0 & -EI_y & EI_{yz} & -EI_{wy} \\ 0 & 0 & 0 & EI_{yz} & -EI_z & EI_{wz} \\ 0 & 0 & 0 & -EI_{wy} & EI_{wz} & -EI_w \end{bmatrix} \tag{2.150}$$

$$\mathbf{M} = \rho \begin{bmatrix} A & 0 & 0 & 0 & 0 & 0 \\ 0 & A & 0 & 0 & 0 & 0 \\ 0 & 0 & I_p & 0 & 0 & 0 \\ 0 & 0 & 0 & I_y - I_{wy} & -I_{yz} & I_{wy} \\ 0 & 0 & 0 & -I_{yz} & I_z + I_{wz} & I_{wz} \\ 0 & 0 & 0 & I_{wy} & -I_{wz} & I_w \end{bmatrix} \tag{2.151}$$

corresponding to a vector of complex amplitudes $\tilde{\mathbf{U}} = \{U_y, U_z, \Theta_x, \Theta_y, \Theta_z, F_w\}^T$.

Figure 2.14 depicts the effect of the shear-centre eccentricity on the dispersion relationship for the lateral bending and torsion of a Timoshenko beam, excluding the effect of warping. The dispersion relationship is affected between 400 Hz and 1500 Hz. Although at low frequencies the two curves correspond to predominantly bending and torsional waves, at middle frequencies the two diverge from each other leading to an exchange of wave type.

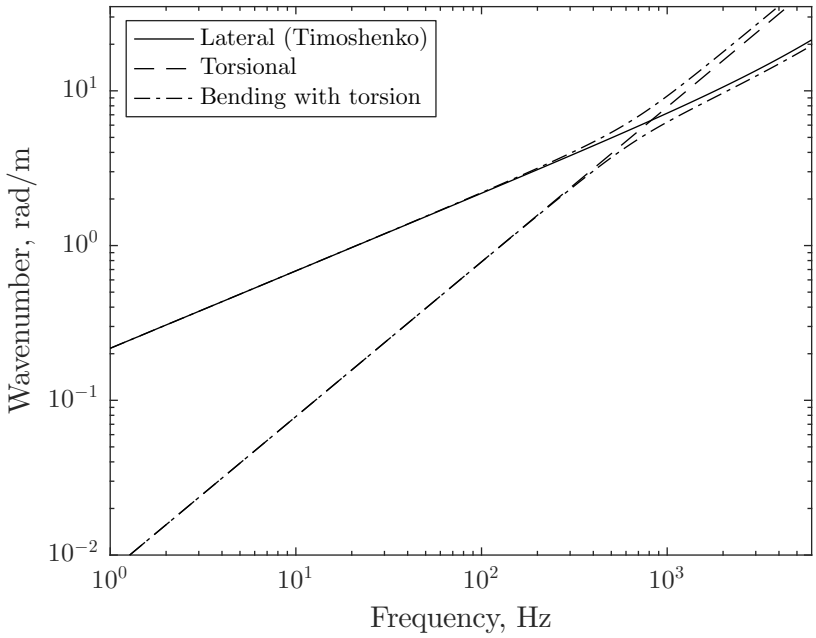

Figure 2.14: Dispersion relationship for torsion and bending coupled due to shear centre eccentricity

This phenomenon occurs in the vicinity of 800 Hz where they would otherwise cross. Due to the modal coupling between the mode shapes, the wavenumber curves do not cross each other, however, and a veering behaviour is observed close to the crossing frequency of the uncoupled wavenumbers [108, 109]. Instead of the dispersion curves crossing each other, a change in wavenumber is seen, during which the mode of the wave changes. In the case of Fig. 2.14, the wave which is initially predominantly lateral bending changes to a predominantly torsional wave and vice versa.

The cause of this behaviour is the asymmetry of the structure. According to Perkins and Mote [110], for a symmetric structure the wavenumbers associated with symmetric

modes will tend to veer from one another, and so will those of antisymmetric modes. In contrast, for an asymmetric structure, the wavenumbers of antisymmetric modes will cross those of symmetric modes. In the case where small asymmetries are introduced in the structure, instances of rapid veering will occur between the wavenumbers of symmetric and antisymmetric modes [109].

For a singly symmetric cross-section, as is the case for the 60E1 rail, no other degrees of freedom are affected by this eccentricity.

2.8 Coupling due to curvature

Introducing curvature in the horizontal plane, Fig. 2.15 shows an infinitesimal element of length $Rd\theta$, where R is the radius of curvature. For a horizontally curved beam,

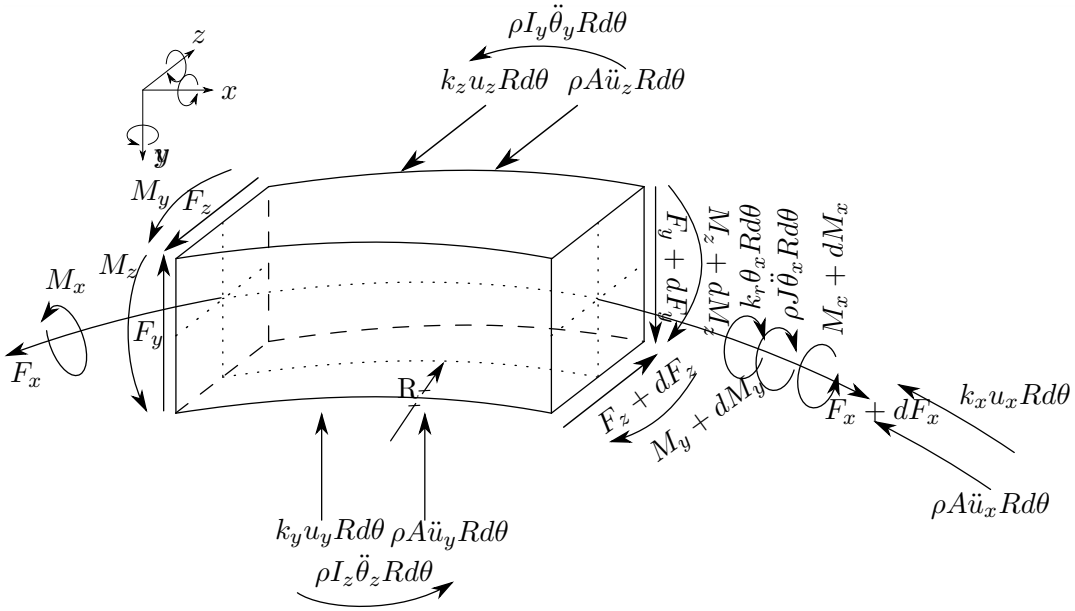

Figure 2.15: Infinitesimal element of curved beam

the response due to a vertical moment will couple with the torsional response, while the response due to a lateral force will couple with the extension. This can be seen by analysing the force and moment resultants in the infinitesimal element of length $Rd\theta$, reproduced in Fig. 2.16 for clarity, where $\sin(d\theta) \approx d\theta$ and $\cos(d\theta) \approx 1$ for infinitesimal $d\theta$.

For example, taking the sum of all moments about the x-axis at the right-hand end of the beam element, the following is obtained

$$\sum M_x = (M_x + dM_x) - M_x\cos(d\theta) + M_z\sin(d\theta) \tag{2.152}$$

$$\sum M_x = dM_x + M_z d\theta \tag{2.153}$$

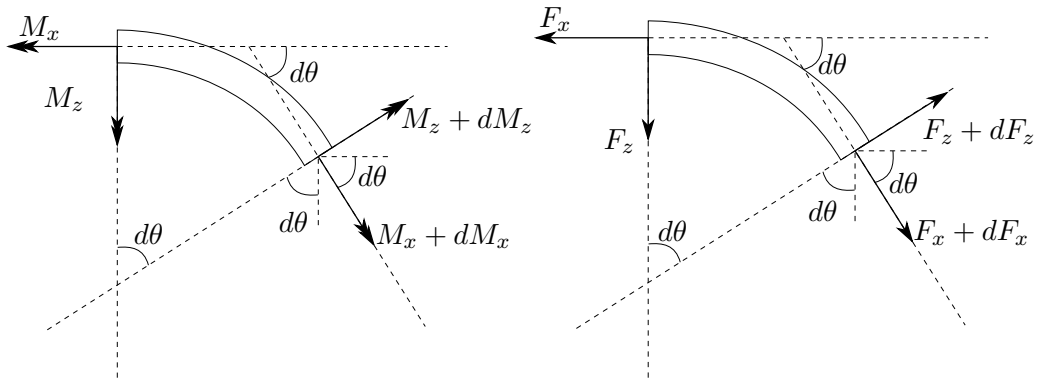

Figure 2.16: Force and moment resolution for a curved beam

Thus, the motion in the plane of the curvature is governed by the following equations:

$$-\frac{1}{R}\frac{\partial {F_z}'}{\partial \theta} + \frac{\partial F_x}{\partial R} + k_z u_z + m\ddot{u}_z = \tilde{F}_z \tag{2.154}$$

$$-\frac{1}{R}\frac{\partial {M_y}'}{\partial \theta} + F_z + \rho I_y \ddot{\theta}_y + k_{ry}\theta_y = \tilde{M}_y \tag{2.155}$$

$$-\frac{1}{R}\frac{\partial F_x}{\partial \theta} - \frac{\partial F_z}{\partial R} + k_x u_x + m\ddot{u}_x = \tilde{F}_x \tag{2.156}$$

where, from Eq. (2.75), the axial strain is given by

$$\epsilon_0 = u_x' + \frac{u_z}{R} (= \bar{\epsilon}_0) \tag{2.157}$$

the lateral bending strain by:

$$\hat{k}_y = \theta_y' (= \bar{k}_y) \tag{2.158}$$

and the lateral shear strain by:

$$\gamma_{xz} = u_z' + \theta_y - \frac{u_x}{R} (= \hat{\gamma}_{xy} - \frac{u_x}{R} = \bar{\gamma}_{xz}) \tag{2.159}$$

Similarly, for the out-of-plane response, the equations of motion are:

$$-\frac{1}{R}\frac{\partial F_y}{\partial \theta} + k_y u_y + m\ddot{u}_y = \tilde{F}_y \tag{2.160}$$

$$-\frac{1}{R}\frac{\partial {M_z}'}{\partial \theta} + \frac{M_x}{R} - F_y + \rho I_z \ddot{\theta}_z + k_{rz}\theta_z = \tilde{M}_z \tag{2.161}$$

$$-\frac{1}{R}\frac{\partial M_x}{\partial \theta} - \frac{M_z}{R} + \rho I_p \ddot{\theta}_x + k_{rx}\theta_x = \tilde{M}_x \tag{2.162}$$

and the corresponding strain-displacement equations are obtained again from Eq. (2.75), with the vertical bending strain given by:

$$\hat{k}_z = \theta_z' - \frac{\theta_x}{R} (= \bar{k}_z) \tag{2.163}$$

the vertical shear strain by:

$$\gamma_{xy} = u_y' - \theta_z \ (= \bar{\gamma}_{xy}) \tag{2.164}$$

and the torsional strain by:

$$\gamma_{sv} = \theta_x' + \frac{\theta_z}{R} (= \bar{\gamma}_{sv}) \tag{2.165}$$

where the over bar notation denotes the relevant strain including the effect of curvature.

In order to obtain the appropriate forces, the linear components of the strains should be considered, written in cylindrical co-ordinates. In the cylindrical co-ordinates, the x axis follows the centroid of the beam, curved over an angle θ with radius of curvature R, while the z axis is always perpendicular to the tangent of the curve pointing outwards and the y axis perpendicular to the $x-z$ plane, pointing downwards. Based on this convention, the strains in cylindrical co-ordinates are obtained by Love [82] as:

$$\epsilon_{xx} = \frac{1}{R^*}\frac{\partial u_x}{\partial \theta} + \frac{u_z}{R^*} \tag{2.166}$$

$$\gamma_{xy} = \frac{1}{R^*}\frac{\partial u_y}{\partial \theta} + \frac{\partial u_x}{\partial y} \tag{2.167}$$

$$\gamma_{xz} = \frac{1}{R^*}\frac{\partial u_z}{\partial \theta} - \frac{u_x}{R^*} + \frac{\partial u_x}{\partial z} \tag{2.168}$$

It is noted here that $\theta = x/R$ and $R^* = R + z$. Hence one can rewrite the strain-displacement equations as:

$$\epsilon_{xx} = \left(\frac{\partial u_x}{\partial x} + \frac{u_z}{R}\right)\frac{R}{R+z} \tag{2.169}$$

$$\gamma_{xy} = \frac{\partial u_y}{\partial x}\frac{R}{R+z} + \frac{\partial u_x}{\partial y} \tag{2.170}$$

$$\gamma_{xz} = \left(\frac{\partial u_z}{\partial x} - \frac{u_x}{R}\right)\frac{R}{R+z} + \frac{\partial u_x}{\partial z} \tag{2.171}$$

Assuming that $z/R < 1$, $R/(R+z)$ can be expanded as a geometric series:

$$\frac{R}{R+z} \approx \sum_{n_t=0}^{\infty} \left(-\frac{z}{R}\right)^n \tag{2.172}$$

For sufficiently large radius ($z/R \ll 1$) the above series can be truncated after terms of degree of $n = 1$ for axial strain, and $n = 0$ for shear strains, with the term z/R being dropped as it is considered a higher order effect (Gendy and Saleeb [86]). By combining

Eq. (2.1) with Eqs (2.169)- (2.171) and Eq. (2.172) the following relationships are derived (warping not considered):

$$\epsilon_{xx} = \left(\left(u'_{x,c} + \frac{u_{z,c}}{R}\right) + \left(\frac{\theta_{x,c}}{R} - \theta'_{z,c}\right) y + \theta'_{y,c} z\right)\left(1 - \frac{z}{R}\right) \tag{2.173}$$

$$= \left(\bar{\epsilon}_0 - \bar{k}_z y + \bar{k}_y z\right) \frac{R}{R+z} \tag{2.174}$$

$$\gamma_{xy} = \left(u'_{y,c} - \theta_{z,c}\right) - z\left(\theta'_{x,c} + \frac{\theta_{z,c}}{R}\right) \tag{2.175}$$

$$= \bar{\gamma}_{xy} - \bar{\gamma}_{sv} z \tag{2.176}$$

$$\gamma_{xz} = \left(u'_{z,c} + \theta_{y,c} - \frac{u_{x,c}}{R}\right) + y\left(\theta'_{x,c} + \frac{\theta_{z,c}}{R}\right) \tag{2.177}$$

$$= \bar{\gamma}_{xz} + \bar{\gamma}_{sv} y \tag{2.178}$$

Finally, the forces in the plane of curvature are obtained based on the above strain-displacement equations as [32]:

$$F_x = EA\epsilon_0 \qquad F_z = GA\kappa_z \gamma_{xz} \qquad M_y = EI_y \hat{k}_y \tag{2.179}$$

while those out of the plane of curvature are:

$$F_y = GA\kappa_y \gamma_{xy} \qquad M_x = GJ\gamma_{sv} \qquad M_z = EI_z \hat{k}_z \tag{2.180}$$

In order to show the coupling due to curvature alone, the terms with y and z in Eqs (2.173)–(2.178) have been ignored. The influence of these terms will be considered in the next chapter.

By substituting Eq. (2.179) into Eqs (2.154)–(2.156) and writing them in a complex form as in Eq. (2.84) for harmonic motion the following matrices are obtained for the in-plane response:

$$\mathbf{K}_0 = \begin{bmatrix} \frac{GA\kappa_z}{R^2} & 0 & -\frac{GA\kappa_z}{R} \\ 0 & \frac{EA}{R^2} & 0 \\ -\frac{GA\kappa_z}{R} & 0 & GA\kappa_z \end{bmatrix} \tag{2.181}$$

$$\mathbf{K}_1 = \begin{bmatrix} 0 & -\frac{A(E+G\kappa_z)}{R} & 0 \\ \frac{A(E+G\kappa_z)}{R} & 0 & -GA\kappa_z \\ 0 & GA\kappa_z & 0 \end{bmatrix} \tag{2.182}$$

$$\mathbf{K}_2 = \begin{bmatrix} -EA & 0 & 0 \\ 0 & -GA\kappa_z & 0 \\ 0 & 0 & -EI_y \end{bmatrix} \tag{2.183}$$

$$\mathbf{M} = \begin{bmatrix} m & 0 & 0 \\ 0 & m & 0 \\ 0 & 0 & I_y \end{bmatrix} \tag{2.184}$$

corresponding to a vector of complex amplitudes $\mathbf{U} = \{U_x, U_z, \Theta_y\}^T$. For an infinitely large radius, the above matrices reduce to those of a Timoshenko beam in lateral bending and an extensional rod as seen earlier, with no coupling between them.

Similarly, by substituting Eqs. (2.180) into Eqs. (2.160)–(2.162) the following are obtained for the out-of-plane response:

$$\mathbf{K}_0 = \begin{bmatrix} 0 & 0 & 0 \\ 0 & \dfrac{EI_z}{R^2} & 0 \\ 0 & 0 & GA\kappa_y + \dfrac{GJ}{R^2} \end{bmatrix} \tag{2.185}$$

$$\mathbf{K}_1 = \begin{bmatrix} 0 & 0 & GA\kappa_y \\ 0 & 0 & -\dfrac{EI_z + GJ}{R} \\ -GA\kappa_y & \dfrac{EI_z + GJ}{R} & 0 \end{bmatrix} \tag{2.186}$$

$$\mathbf{K}_2 = \begin{bmatrix} -GA\kappa_y & 0 & 0 \\ 0 & -GJ & 0 \\ 0 & 0 & -EI_z \end{bmatrix} \tag{2.187}$$

$$\mathbf{M} = \begin{bmatrix} m & 0 & 0 \\ 0 & I_p & 0 \\ 0 & 0 & I_z \end{bmatrix} \tag{2.188}$$

corresponding to a displacement vector of complex amplitudes $\mathbf{U} = \{U_y, \Theta_x, \Theta_z\}^T$. Again, for an infinitely large radius, the above matrices reduce to those of a Timoshenko beam in vertical bending and a torsional rod as seen earlier.

Figure 2.17 shows the dispersion graph for the in-plane behaviour of the beam for a radius of $R = 1.45$ m. Although this radius is not realistic for railway applications, it is used here to emphasize the effect of curvature. Figure 2.18 shows the dispersion

relationship for a more practical radius of $R = 100$ m. In both figures, the results for lateral bending of a straight Timoshenko beam and extension are shown for comparison.

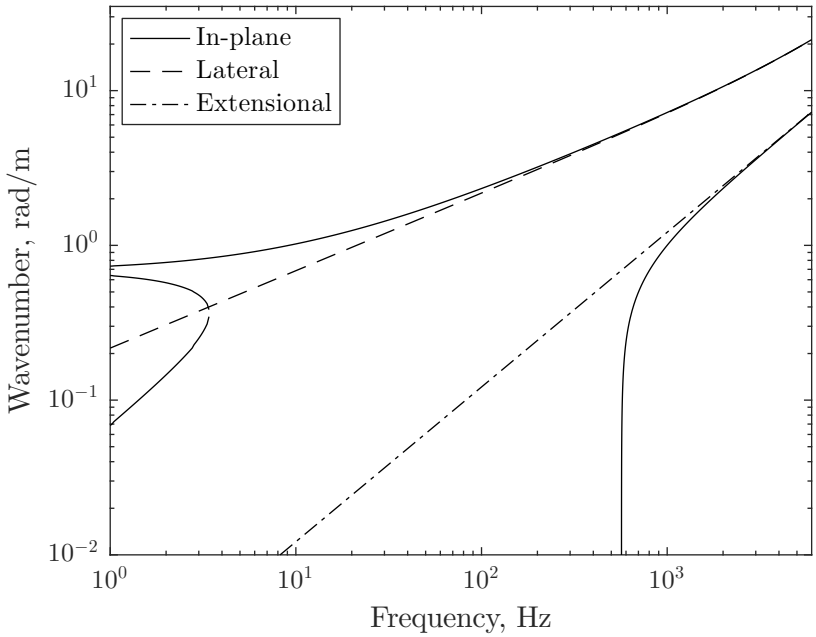

Figure 2.17: Dispersion relationship for the in-plane response of curved beam with radius of 1.45 m. Solid lines show the results including curvature, dashed and chain lines show the uncoupled results for a straight beam.

As seen, the in-plane response is composed of a predominantly bending wave similar to that of the Timoshenko beam and a predominantly extensional wave, similar to the axial rod.

By investigating the extensional wave, a non-zero cut-on frequency is seen. This frequency can be obtained from analysis of the in-plane response according to Eq. (2.84). Solving for ω with ξ set to zero, the cut-on frequencies for the in-plane response are obtained as:

$$f_{co,1} = \frac{1}{2\pi R}\sqrt{\frac{E}{\rho}} \tag{2.189}$$

$$f_{co,2} = \frac{1}{2\pi}\sqrt{\frac{G(A + I_y/R^2)\kappa_z}{\rho I_y}} \tag{2.190}$$

The first of these frequencies is identified as the ring frequency [32]. It is associated with the first order longitudinal wave, and is also referred to as the breathing or radial mode. In this mode, the ring expands and contracts in the radial direction uniformly. It can be seen as a lateral motion of the cross-section, but since this is uniform throughout the curved beam, the axis of the beam extends/contracts. This is depicted in Fig. 2.19(a). For $R = 1.45$ m it occurs at 545 Hz whereas for $R = 100$ m it occurs at 7.5 Hz.

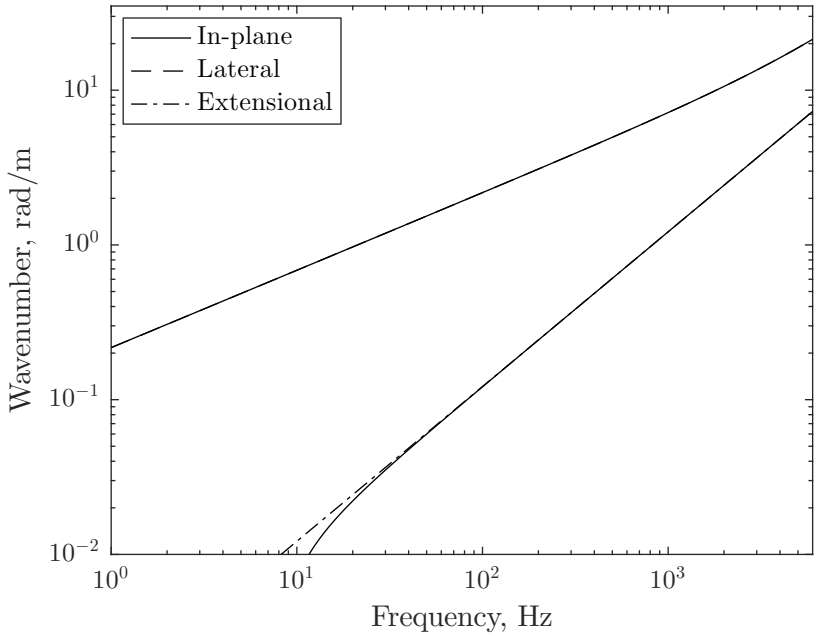

Figure 2.18: Dispersion relationship for the in-plane response of curved beam with radius of 100 m. Solid lines show the results including curvature, dashed and chain lines show the uncoupled results for a straight beam.

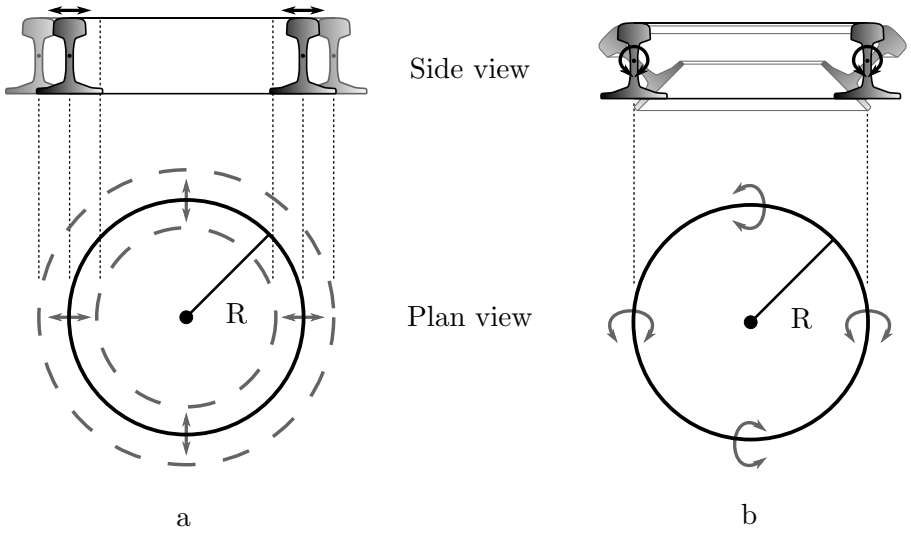

Figure 2.19: Rigid body modes for rings associated with a) $f_{co,1}$ (breathing mode) and b) $f_{co,3}$ (torsional mode)

The second cut-on frequency corresponds to the shear waves of a Timoshenko beam, modified to account for the curvature effect of the beam. This occurs at approximately 14 kHz as identified previously for the lateral motion of a straight Timoshenko beam.

The predominantly bending wave is the same as the bending wave for a straight beam at high frequencies, but at low frequencies the wavenumber tends to $1/R$, corresponding to a wavelength of $2\pi R$. Below this wavenumber, the dispersion curve has a wave with a negative slope (and thus a negative group velocity while maintaining a positive phase

velocity and vice versa) corresponding to an extensional wave [111]. Such cases have been previously identified in cylindrical shells, for example by Langley [112] and Walsh and White [113]. Another wave exists with a smaller wavenumber and a positive slope, corresponding to a lateral bending wave [111]. These two waves cut off at around 3 Hz for a radius R of 1.45 m.

The out-of-plane response is shown in Fig. 2.20 and 2.21 for a radius of $R = 1.45$ m and 100 m respectively. This motion is composed of a predominantly bending wave, similar to the vertical Timoshenko beam, and a predominantly torsional wave.

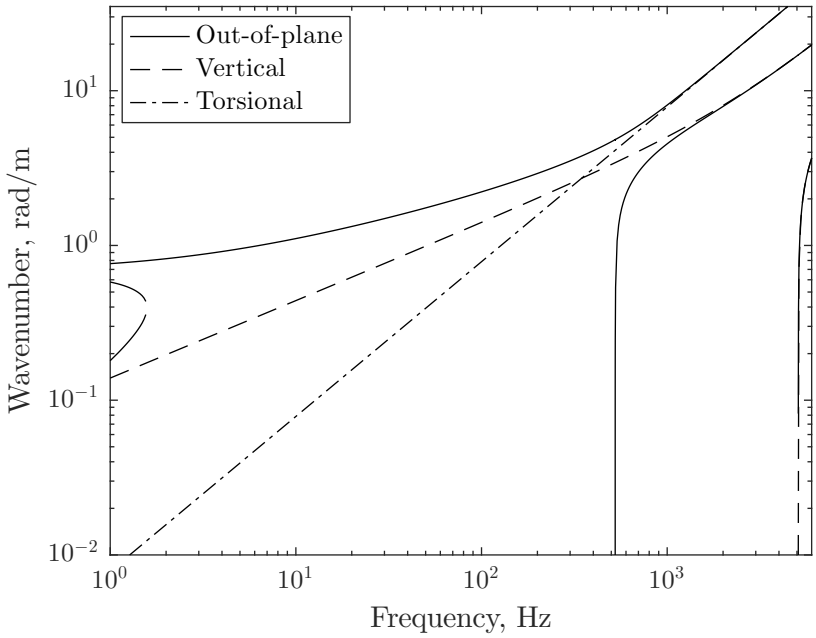

Figure 2.20: Dispersion relationship for the out-of-plane response of curved beam with radius of 1.45 m. Solid lines show the results including curvature, dashed and chain lines show the uncoupled results for a straight beam.

As for the in-plane response, a non-zero cut-on frequency occurs at about 500 Hz. Investigating the cut-on frequencies for the out-of-plane response, by setting ξ=0, the following frequencies are obtained:

$$f_{co,3} = \frac{1}{2\pi R}\sqrt{\frac{EI_z}{\rho I_p}} \tag{2.191}$$

$$f_{co,4} = \frac{1}{2\pi}\sqrt{\frac{GA\kappa_y + GJ/R^2}{\rho I_z}} \tag{2.192}$$

The first frequency can be identified as that of the uniform torsion of the beam [32]. This mode is similar to the rigid body torsional mode for a straight beam. This is related to the uniform rotation of the ring cross-section about the shear centre, the mode shape of which is depicted in Fig. 2.19(b). This corresponds to a rigid body mode of the beam in torsion for straight beams, but for curved beams it will include some bending of the

beam in the vertical direction, as the beam rotates (Basset [114], Love [82]). It is seen that this mode does not depend on the torsional rigidity as no relative torsion takes place, this being a rigid body rotation, but rather on the bending stiffness of the beam and the polar moment of inertia.

The second cut-on frequency corresponds to the higher order wave of the Timoshenko beam, modified again to account for the curvature effect of the beam. This occurs at approximately 5 kHz as identified previously for the vertical Timoshenko beam in vertical bending.

Curve veering, as for the case of coupled bending/torsional response, is observed, where the predominantly bending wave changes to a predominantly torsional wave and vice versa between 100 Hz and 1000 Hz. Although $f_{co,3}$ is a cut-on frequency for the torsional wave, at higher frequencies this wave follows the behaviour of the flexural wave. As before, the flexural wave tends to the wavenumber $1/R$ as frequency tends to zero, corresponding to a wavelength of $2\pi R$, but at higher frequencies, this wave follows the behaviour of the pure torsional wave. Below this wavenumber, the dispersion curve again has two waves, one with a negative slope corresponding to a torsional wave and one with a smaller wavenumber and a positive slope, corresponding to a vertical bending wave.

In order to separate the veering effect, results for a larger radius ($R = 100$ m) are shown in Fig. 2.21, this leading to a lower cut-on frequency for the torsional mode ($f_{co,3}$). In this case the cut-on frequency becomes 8 Hz. The curve veering is very localised in this case, occurring between 300 Hz and 400 Hz. In terms of the other coupling sources, only the bi-moment is affected, and Eq. (2.18) becomes:

$$M_x^s = \int_A G\left(\gamma_{xy}\phi_{,y} + \gamma_{xz}\left(\phi_{,z} - \frac{\phi}{R+z}\right)\right)\frac{R+z}{R}dA \tag{2.193}$$

2.9 Accounting for arbitrary excitation forces

So far, sources of mechanical coupling have been discussed but no consideration was given to the excitation forces. Excitation forces due to wheel/rail contact are often assumed to be applied at the centroid of the rail. Practically, however, the forces are applied with some eccentricity, both vertically and laterally from the centroid, as shown in Fig. 2.22. Thus, a vertical force will also excite the rail torsionally as will a lateral force.

Considering their components in the vertical and lateral direction with regard to the rail co-ordinate axes, the following expressions can be derived for the external excitation

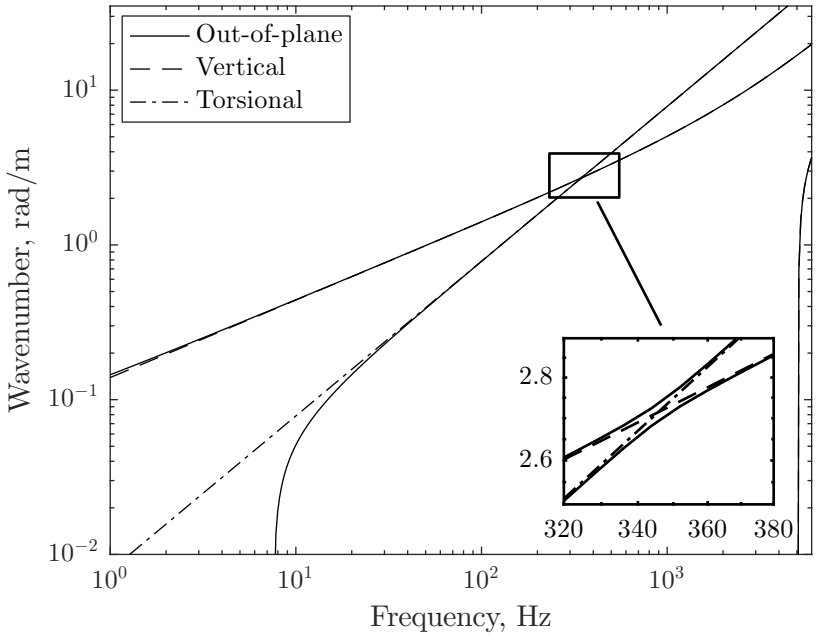

Figure 2.21: Dispersion relationship for the out-of-plane response of curved beam with radius of 100 m. Solid lines show the results including curvature, dashed and chain lines show the uncoupled results for a straight beam.

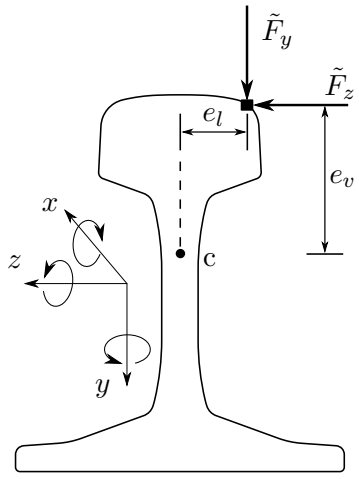

Figure 2.22: Vertical and lateral excitation forces applied with some eccentricity from the centroid

forces:

$$F^e_{x,c} = \tilde{F}_x \tag{2.194}$$

$$F^e_{y,c} = \tilde{F}_y \tag{2.195}$$

$$F^e_{z,c} = \tilde{F}_z \tag{2.196}$$

$$M^e_{x,c} = -e_l\tilde{F}_y + e_v\tilde{F}_z + \tilde{M}_x \tag{2.197}$$

$$M^e_{y,c} = e_l\tilde{F}_x + \tilde{M}_y \tag{2.198}$$

$$M^e_{z,c} = -e_v\tilde{F}_x + \tilde{M}_z \tag{2.199}$$

$$M^e_{w,c} = \phi_h\tilde{F}_x + \tilde{M}_w \tag{2.200}$$

where $\tilde{F}_x, \tilde{F}_y, \tilde{F}_z, \tilde{M}_x, \tilde{M}_y, \tilde{M}_z$ and $\tilde{M}_w$ are external applied loads and e_v and e_l are the vertical and lateral offsets of the external applied load from the centroid, taken as positive in the positive direction of the co-ordinate axis. For railway applications, moment loads are typically not considered. In addition, forces are applied as normal and tangential with some angle to the rail because of the geometry of the rail and the wheel (not applied in the model).

The influence of the location of excitation loads will be investigated in Chapter 5, where the forced response of the beam is considered.

2.10 Conclusions

In this chapter, individual theories accounting for the vibration of rails in various directions including several coupling mechanisms have been presented. It is found that the effect of restrained warping is significant for the torsional response of the beam, affecting frequencies above 500 Hz. Accounting for shear forces due to the restrained warping only has an influence at higher frequencies, above 3000 Hz. Accounting for the location of the shear centre introduces a coupling between the torsional response and the lateral bending of the beam, with curve veering occurring at about 800 Hz. The inclusion of curvature is significant only for small radii. The rigid body modes of the lateral and torsional waves occur with a non-zero cut-on frequency. These frequencies are at about 500 Hz for a radius of 1.45 m while for a radius of 100 m they are below 10 Hz. Finally, the excitation forces can excite the torsional response (since they are applied with an eccentricity from the rail centreline) which is coupled with the lateral and in some instances vertical responses.

In the next chapter, the various phenomena investigated here will be assembled into a fully coupled vertical/lateral beam model. The inclusion of an elastic foundation will also be investigated.

Chapter 3

Coupled vibration of rails

In this chapter, a complete model for the vertical/lateral vibration of rails is presented, assembled from the models introduced in Chapter 2. The dynamic track model adopted is based on a static beam model presented by Kim et al. [90] for the stability of beam columns. This combines all the submodels investigated in Chapter 2, utilising the Timoshenko beam theory for bending in the vertical and lateral directions, an axial rod in extension and a torsional rod. The model also accounts for shear-centre eccentricity and non-uniform torsion. Kim et al's [90] model has been extended here to include inertial effects and an elastic support at an arbitrary location relative to the centroid. After introducing the model, the dispersion relationship for a free rail is compared with a Finite Element (FE) model developed using COMSOL and a Waveguide Finite Element (WFE) model [69]. For the case of a straight rail this is done for both a singly symmetric rail (60E1) and an asymmetric rail (60R1). In the case of curvature, comparisons are made only with the FE model that can account for a curved structure. Finally, the influence of the support and the support location relative to the centroid is investigated.

3.1 Strain-displacement relations

By using the strains of Eq. (2.114) for warping of the beam, Eqs (2.163)–(2.165) for out-of-plane bending and Eqs (2.157)–(2.159) for in-plane bending and substituting those in Eqs (2.173)–(2.177), the latter take the following form:

$$\epsilon_{xx} = \left(\bar{\epsilon}_0 + \bar{k}_y z - \bar{k}_z y + \bar{k}_w \phi\right)\left(1 - \frac{z}{R}\right) \tag{3.1}$$

$$\gamma_{xy} = \bar{\gamma}_{xy} - (z + \phi_{,y})\,\bar{\gamma}_{sv} + \phi_{,y}\gamma_w \tag{3.2}$$

$$\gamma_{xz} = \bar{\gamma}_{xz} + \left(y - \phi_{,z} + \frac{\phi}{R}\right)\bar{\gamma}_{sv} + \left(\phi_{,z} - \frac{\phi}{R}\right)\gamma_w \tag{3.3}$$

for curved beams and

$$\epsilon_{xx} = \epsilon_0 + \hat{k}_y z - \hat{k}_z y + \hat{k}_w \phi \tag{3.4}$$

$$\gamma_{xy} = \hat{\gamma}_{xy} - (z + \phi_{,y})\,\gamma_{sv} + \phi_{,y}\gamma_w \tag{3.5}$$

$$\gamma_{xz} = \hat{\gamma}_{xz} + (y - \phi_{,z})\,\gamma_{sv} + \phi_{,z}\gamma_w \tag{3.6}$$

for straight beams, where the terms containing $1/R$ vanish in Eqs (3.4)–(3.6) as $R \to \infty$. The above expressions are the same as those obtained by Gendy and Saleeb [86].

It has been shown earlier from the strain-displacement equations for the motions in the plane and out of the plane of curvature of the beam (Eq. (2.114), Eqs (2.157)–(2.159) and Eqs (2.163)–(2.165)) how, when the radius tends to infinity (i.e. its reciprocal to zero), the axial strain decouples from the lateral displacement, the lateral shear strain from the axial displacement, and the torsional strain (uniform and non-uniform) from the vertical rotation. This would then lead to the decoupled equations for a straight beam, as described in Chapter 2.

3.2 Force-deformation equations

Having derived expressions for the normal stress in the elementary beam section, the stress resultants can now be obtained, according to Eqs (2.11)–(2.14). Taking Eq. (2.11) for example, the integration can be performed as:

$$F_x = E \int_A \left(\bar{\epsilon}_0 + \bar{k}_y z - \bar{k}_z y + \bar{k}_w \phi\right) \left(1 - \frac{z}{R}\right) dA \tag{3.7}$$

$$= E \int_A (1, z, -y, \phi) \left(1 - \frac{z}{R}\right) dA \begin{pmatrix} \bar{\epsilon}_0 \\ \bar{k}_y \\ \bar{k}_z \\ \bar{k}_w \end{pmatrix} \tag{3.8}$$

where

$$\int_A \frac{z}{R} dA = 0 \qquad \int_A \frac{y}{R} dA = 0 \qquad \int_A 1 dA = A \qquad \int_A \phi dA = 0$$

Similarly, by performing the remaining integrations, the following relationships are derived which can be given in a matrix form:

$$\begin{pmatrix} F_x \\ M_y \\ M_z \\ M_w \end{pmatrix} = E \begin{bmatrix} A & -I_y/R & I_{yz}/R & -I_{wy}/R \\ -I_y/R & \hat{I}_y & -\hat{I}_{yz} & \hat{I}_{wy} \\ I_{yz}/R & -\hat{I}_{yz} & \hat{I}_z & -\hat{I}_{wz} \\ -I_{wy}/R & \hat{I}_{wy} & -\hat{I}_{wz} & \hat{I}_w \end{bmatrix} \begin{pmatrix} \bar{\epsilon}_0 \\ \bar{k}_y \\ \bar{k}_z \\ \bar{k}_w \end{pmatrix} \tag{3.9}$$

where

$$\hat{I}_y = I_y - I_{yyy}/R \qquad \hat{I}_{yz} = I_{yz} - I_{yyz}/R \qquad \hat{I}_z = I_z - I_{yzz}/R$$
$$\hat{I}_{wz} = I_{wz} - I_{wyz}/R \qquad \hat{I}_{wy} = I_{wy} - I_{wyy}/R \qquad \hat{I}_w = I_w - I_{wwy}/R$$

and

$$\begin{aligned}
I_{wyy} &= \int_A \phi z^2 dA = \int (\phi_S - e_z y + e_y z) z^2 dA \\
&= I_{S,wyy} + e_y I_{yyy} - e_z I_{yyz} \\
I_{wyz} &= \int_A \phi yz dA = \int (\phi_S - e_z y + e_y z) yz dA \\
&= I_{S,wyz} + e_y I_{yyz} - e_z I_{yzz} \\
I_{wwy} &= \int_A \phi^2 z dA = \int (\phi_S - e_z y + e_y z)^2 z dA \\
&= I_{S,wwy} + e_y^2 I_{yyy} + e_z^2 I_{yzz} + 2e_y I_{S,wyy} - 2e_z I_{S,wyz} - 2e_y e_z I_{yyz} \\
I_{zzz} &= \int_A y^3 dA \qquad I_{yyz} = \int_A y z^2 dA \qquad I_{yzz} = \int_A y^2 z dA
\end{aligned}$$

The interaction of the forces created due to normal stresses can be observed in Eq. (3.9). It can be readily seen from the first row of Eq. (3.9) that, in the absence of curvature, the axial force F_x will decouple from the bending moments and warping, being equivalent to that of an axial rod. In order for the bending moments in the vertical and lateral directions to be decoupled, both the product moment of area I_{yz} and warping sectional properties I_{wy}, I_{wz} have to be zero, yielding independent flexure in both directions.

Similarly, the stress resultants for the shear stresses can be calculated by the use of Eqs (2.15)–(2.18) along with Eqs (3.2)–(3.3). Performing the above calculations for a non-symmetric cross-section, the following relationships are obtained in matrix form:

$$\begin{pmatrix} F_y \\ F_z \\ T_w \end{pmatrix} = G \begin{bmatrix} A_y & A_{yz} & Q_{yr} \\ A_{yz} & A_z & Q_{zr} \\ Q_{yr} & Q_{zr} & J_r \end{bmatrix} \begin{pmatrix} \bar{\gamma}_{xy} \\ \bar{\gamma}_{xz} \\ \bar{\gamma}_w \end{pmatrix} \tag{3.10}$$

with

$$A_y = A_{S,y} \qquad A_z = A_{S,z} \qquad A_{yz} = 0$$
$$Q_{yr} = -A_{S,y} e_z \qquad Q_{zr} = A_{S,z} e_y \qquad J_r = J_S + A_{S,z} e_y^2 + A_{S,y} e_z^2$$

where $A_S = \kappa A$ denotes the effective shear area accounting for the correction factor based on the Timoshenko beam theory. For the case of a mono-symmetric rail (e.g. 60E1) the term e_z becomes zero.

In terms of the shear forces, it can be seen that for the case of a doubly-symmetric cross-section, the shear forces will decouple completely, with only the diagonal elements

of the above matrix being non-zero. In the case of a mono-symmetric cross-section with the axis of symmetry being the y-axis (e.g. 60E1), the lateral shear force will remain coupled with the bi-moment while the vertical shear force will decouple from the other two.

3.3 Equations of motion

In Fig. 2.15 an infinitesimal element of length $Rd\theta$ was shown, along with the forces acting on it. By taking the sum of the forces and moments acting on the centroid in all three directions, as well as bi-moment in the axial direction and writing the equations of motion in a complex form as in Eq. (2.84), it follows that:

$$\left(\mathbf{K}_p + \mathbf{K}_0 - \omega^2\mathbf{M} - i\xi\mathbf{K}_1 - \xi^2\mathbf{K}_2\right)\tilde{\mathbf{U}} = \tilde{\mathbf{F}} \tag{3.11}$$

where

$$\mathbf{K}_p = \mathrm{diag}(k_x, k_y, k_z, k_{xr}, k_{yr}, k_{zr}, k_w) \tag{3.12}$$

$$\mathbf{K}_0 = \begin{bmatrix} t_1/R^2 & 0 & 0 & 0 & -t_1/R & -e_y t_1/R^2 & -e_y t_1/R \\ 0 & 0 & 0 & 0 & 0 & 0 & 0 \\ 0 & 0 & EA/R^2 & -E\hat{I}_{yz}/R^3 & 0 & 0 & 0 \\ 0 & 0 & -E\hat{I}_{yz}/R^3 & E\hat{I}_z/R^2 & 0 & 0 & 0 \\ -t_1/R & 0 & 0 & 0 & t_1 & e_y t_1/R & e_y t_1 \\ -e_y t_1/R^2 & 0 & 0 & 0 & e_y t_1/R & t_2 & t_3/R \\ -e_y t_1/R & 0 & 0 & 0 & e_y t_1 & t_3/R & t_3 \end{bmatrix} \tag{3.13}$$

$$\mathbf{K}_1 = \begin{bmatrix} 0 & 0 & -t_4 & t_5/R & 0 & 0 & 0 \\ 0 & 0 & 0 & 0 & 0 & t_6 + t_6 e_z/R & t_6 e_z \\ t_4 & 0 & 0 & 0 & -EI_y/R^2 - t_1 & t_5/R & -t_7 \\ -t_5/R & 0 & 0 & 0 & t_5 & -t_9 - t_6 e_z & -t_{10} \\ 0 & 0 & EI_y/R^2 + t_1 & -t_5 & 0 & 0 & 0 \\ 0 & -t_6 - t_6 e_z/R & -t_5/R & t_9 + t_6 e_z & 0 & 0 & 0 \\ 0 & -t_6 e_z & t_7 & t_{10} & 0 & 0 & 0 \end{bmatrix} \tag{3.14}$$

$$\mathbf{K}_2 = \begin{bmatrix} -EA & 0 & 0 & 0 & EI_y/R & -EI_{yz}/R & EI_{wy}/R \\ 0 & -t_6 & 0 & t_6 e_z & 0 & 0 & 0 \\ 0 & 0 & -t_1 & -e_y t_1 & 0 & 0 & 0 \\ 0 & t_6 e_z & -e_y t_1 & -t_8 & 0 & 0 & 0 \\ EI_y/R & 0 & 0 & 0 & -E\hat{I}_y & E\hat{I}_{yz} & -E\hat{I}_{wy} \\ -EI_{yz}/R & 0 & 0 & 0 & E\hat{I}_{yz} & -E\hat{I}_z & E\hat{I}_{wz} \\ EI_{wy}/R & 0 & 0 & 0 & -E\hat{I}_{wy} & E\hat{I}_{wz} & -E\hat{I}_w \end{bmatrix} \tag{3.15}$$

$$\mathbf{M} = \rho \begin{bmatrix} A & 0 & 0 & 0 & 0 & 0 & 0 \\ 0 & A & 0 & 0 & 0 & 0 & 0 \\ 0 & 0 & A & 0 & 0 & 0 & 0 \\ 0 & 0 & 0 & I_p & 0 & 0 & 0 \\ 0 & 0 & 0 & 0 & I_y - I_{wy} & -I_{yz} & I_{wy} \\ 0 & 0 & 0 & 0 & -I_{yz} & I_z + I_{wz} & -I_{wz} \\ 0 & 0 & 0 & 0 & I_{wy} & -I_{wz} & I_w \end{bmatrix} \tag{3.16}$$

with

$$\begin{aligned} t_1 &= GA\kappa_z & t_2 &= G(A\kappa_y R^2 + 2A\kappa_y e_z R + J_r + J)/R^2 \\ t_3 &= G(J_r + A\kappa_y e_z R)/R & t_4 &= (EA + t_1)/R \\ t_5 &= E\hat{I}_{yz}/R - e_y t_1 & t_6 &= GA\kappa_y \\ t_7 &= EI_{wy}/R^2 + e_y t_1 & t_8 &= G(J_r + J) \\ t_9 &= (E\hat{I}_z + t_8)/R & t_{10} &= GJ_r - E\hat{I}_{wz}/R \end{aligned}$$

The vector of the complex amplitudes is given by

$$\tilde{\mathbf{U}} = \{U_x, U_y, U_z, \Theta_x, \Theta_y, \Theta_z, F_w\}^T \tag{3.17}$$

and the vector of external forces acting at the centroid

$$\tilde{\mathbf{F}}_c^e = \{\tilde{F}_{x,c}^e, \tilde{F}_{y,c}^e, \tilde{F}_{z,c}^e, \tilde{M}_{x,c}^e, \tilde{M}_{y,c}^e, \tilde{M}_{z,c}^e, \tilde{M}_{w,c}^e\}^T \tag{3.18}$$

In the absence of restrained warping, the seventh row and column of the above matrices will vanish, as will the terms I_{wy} and I_{wz}. The torsional behaviour of the beam will then be described as a torsional rod and will not affect the axial response. Uniform torsion thus will take place, as described by the Saint-Venant pure torsion theory.

The effect of shear centre eccentricity is not readily seen in the equations of motion since it mainly affects the behaviour of the forces internally (i.e. the strains in Section 2.1), and the above forces are expressed relative to the centroid.

By neglecting the product of inertia I_{yz}, the bending of the beam in the y direction (about z-axis) will further decouple from the rotation about the y-axis and vice versa.

Neglecting the curvature of the beam, terms in $d/Rd\theta$ become d/dx while terms pre-multiplied by $1/R$ vanish. In conjunction with the above decoupled behaviour, the equations of motion can be separated into two uncoupled equations (axial, Eq. (2.21), and torsional, Eq. (2.41)) and two pairs of coupled equations (Timoshenko beams for vertical, Eqs (2.68)–(2.69), and lateral, Eqs (2.78)–(2.79), bending).

The effect of restrained warping and shear centre eccentricity can be considered separately for each direction of beam bending, thus coupling individually the torsional behaviour to each bending direction.

3.4 Dispersion relationship for a free rail

In order to validate the fully coupled beam model, two additional methods for obtaining the dispersion relationship are used. The first is to employ a commercial Finite Element (FE) package, while the other is based on a Waveguide Finite Element (WFE) model.

3.4.1 Based on the analytical model

So far the force-deformation equations, Eqs (3.9)–(3.10), as well as the equations of motion of the system, Eq. (3.11), have been developed. By assuming the response to be harmonic in both space and time, a relationship can be derived between the frequency and the wavenumber based on Eq. (2.84) and Eq. (3.11) as $|\mathbf{A}| = 0$.

In this case the resulting problem will be a 7-by-7 dual (non-linear) quadratic eigenvalue problem in ξ and ω which is rewritten as an equivalent 14-by-14 linear problem [101], similar to Eq. (2.85), yielding 14 solutions for ξ. Due to the forms of the various matrices, these solutions can be divided into two sets (ξ_1, ξ_2) with $\mathrm{Im}(\xi_1) \leq 0$ propagating in the positive direction and $\mathrm{Im}(\xi_2) \geq 0$ propagating in the negative direction, with the second set given by $\xi_2 = -\xi_1$. When damping is included there are no solutions with $\mathrm{Im}(\xi) = 0$.

3.4.2 Based on the Finite Element Analysis

In order to validate the developed model for both a straight and a curved beam, the COMSOL Multiphysics [98] Finite Element package has been used. The comparisons are made in terms of the dispersion relationship of a free rail only. Firstly the geometry of the rail (60E1) was introduced in COMSOL and the geometric properties were derived to be used in the theoretical model for the comparison (Table 2.1). Then a 3D model with a length of 1.2 m consisting of 199,335 elements for the straight and 215,945 elements for the curved rail was created (see Fig. 3.1 in this case for a curved rail) and a modal analysis was performed in order to find the eigen-frequencies and

the mode shapes of the system. This was done for three different boundary conditions at the ends of the rail section, namely symmetric-symmetric, antisymmetric-symmetric and antisymmetric-antisymmetric. These boundary conditions are chosen because the corresponding modeshapes are sinusoidal.

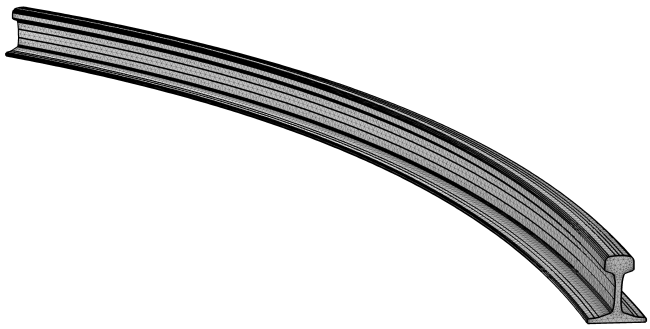

Figure 3.1: Mesh for Finite Element model of a curved rail

After obtaining the eigen-frequencies of the system, and by observing the mode shapes, the wavenumber can be obtained using the following formulas according to the boundary conditions (see Ryue et al. [65]). For symmetric-symmetric (or antisymmetric-antisymmetric) conditions, the wavenumber is obtained as $n\pi/L$ where L is the length of the rail section (centreline) modelled in COMSOL and n is an integer indicating the number of half-waves within the length. For antisymmetric-symmetric conditions, the wavenumber is obtained as $(2n+1)\pi/2L$ where n is an integer with $2n+1$ indicating the number of quarter-waves. The dispersion analysis using COMSOL was performed for both a straight and a curved rail. This model was used to validate the developed model for both the straight and curved rail.

One of the limitations of the Finite Element approach to obtain the dispersion relationship, is that a fine resolution, especially at low frequencies in terms of a logarithmic scale, can only be achieved by using a very long section of rail. This is due to the fact that the wavenumber is inversely proportional to the length of the model. Thus, the Waveguide Finite Element method is also employed.

3.4.3 Based on the Waveguide Finite Element model

In addition to the FE model, a waveguide finite element (WFE) model based on that presented by Nilsson et al. [69] has also been utilised[1] to obtain the dispersion relations for a free and supported straight rail (where $\mathbf{K}_p = \mathbf{0}$ for a free rail). This model uses the same form of equations of motion in matrix form as in Eq. (3.11), although with much larger matrices to account for all the nodal degrees of freedom. The rail is represented by

[1]The Waveguide Finite Element model has been kindly provided by F. Dai from Southwest Jiaotong University, Chengdu, People's Republic of China.

32 eight-noded quadrilateral elements, as shown in Fig. 3.2, and the support by spring elements under each node at the base of the rail foot (not shown). The model has 423 degrees of freedom. The solution method is similar to that used for the analytical model.

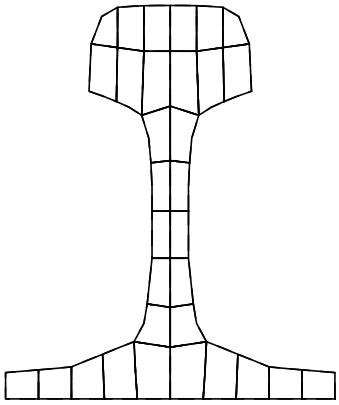

Figure 3.2: Mesh of 60E1 rail in the WFE model

3.4.4 Dispersion relationship for 60E1 rail

Figure 3.3 shows the dispersion relationship for a free 60E1 rail obtained from both the present beam model (solid lines) and the FE model (markers). Each wave is identified by a Roman numeral, with lower case letters for vertical/longitudinal waves and upper case for lateral waves [4, 115]. Due to symmetry of the rail section, it is found that the sets of lateral and vertical/longitudinal waves are uncoupled from each other as their dispersion curves cross without veering (e.g. wave i and wave II).

In order to provide a finer wavenumber-frequency resolution, the dispersion relationship based on the WFE model is depicted in Fig. 3.4 and compared with the present beam model. Both the FE and WFE methods produce virtually identical results. The corresponding modeshapes (here obtained from the FE model, with a length of 1.2 m) are shown in Fig 3.5 for lateral motion and Fig. 3.6 for vertical.

The vertical motion includes two main wave-types. The first is the vertical bending (type i) which is well predicted by the beam model while the second is a higher-order wave associated with the foot flapping (type ii) which cuts on at about 5 kHz and is not represented by the present beam model. Longitudinal waves include the first order axial wave (type iii) and a higher order axial wave (type iv) both of which are well predicted by the present beam model. The first two lateral wave types correspond to lateral bending (type I) and torsion (type II) which are well represented at least up to 1 kHz. Two higher-order waves appear at higher frequencies, corresponding to the bending (type III) and double bending (type IV) of the web [20]. For the 60E1 rail, these cut on at about 1.3 and 3.8 kHz in the WFE model but are not predicted by the

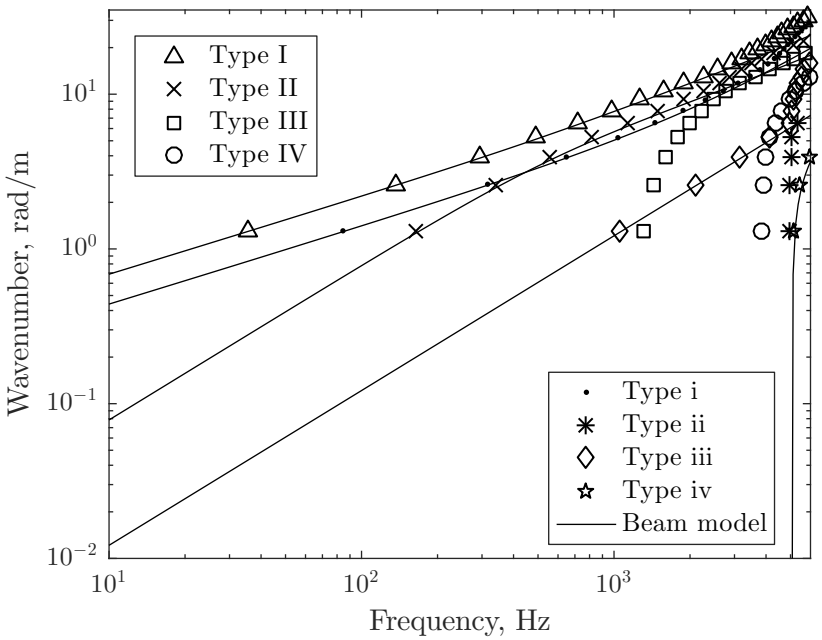

Figure 3.3: Comparison of dispersion curves for a free 60E1 rail with those from the FE model

beam model. Table 3.1 summarises the different waves existent in the beam, including three waves (namely the vertical and lateral evanescent waves and the warping wave) which will be further discussed in the following sections.

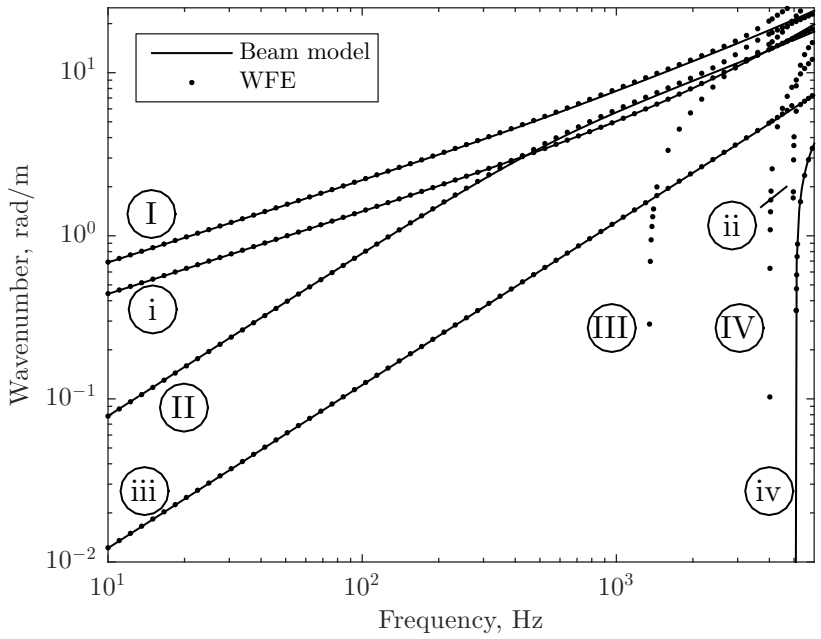

Figure 3.4: Comparison of dispersion curves for a free 60E1 rail with those from the WFE model

Because the cross-section deformation is not included in the present beam model (i.e. no separation of head, web and flange) the higher order wave-types are not accounted for.

Table 3.1: Summary of main wave-types.

	Wave-type	Description	Model
Vertical	i	Vertical bending	All
	ii	Foot-flapping	FE/WFE
	iii	Axial	All
	iv	Higher order axial	All
	Ve	Vertical evanescent	Analytical
Lateral	I	Lateral bending	All
	II	Torsional	All
	III	Web-bending	FE/WFE
	IV	Double web-bending	FE/WFE
	Le	Lateral evanescent	Analytical
	w	Warping	Analytical/FE

This also means that, for example, the lateral bending wave above 3 kHz does not match so well that of the FE/WFE models since in the latter case it is influenced by the cross-section deformation. The added flexibility of the web in the FE/WFE models causes waves to travel at higher wavenumbers for a given frequency. Similarly, the torsional wave (type II) is seen to be influenced by the web bending in the FE/WFE models at higher frequencies.

Figure 3.5: Normalised lateral wave mode shapes from Fig. 3.3 obtained using FE model

Figure 3.6: Normalised vertical wave mode shapes from Fig. 3.3 obtained using FE model

3.4.5 Effect of rail curvature on the dispersion relationship

The dispersion relationship for a curved beam of radius 1.45 m is plotted in Fig. 3.7 from the analytical model and the FE model. The agreement between the results for the current beam model and the FE model remains very good, as in the case of a straight rail. It can be seen that the main differences from the case of a straight rail (Fig. 3.3) occur below about 1.5 kHz. The most obvious difference is that two of the waves, namely the first longitudinal (type iii) and second lateral wave (type II), cut on at around 500 Hz (550 and 510 Hz respectively), whereas for a straight rail they cut on at 0 Hz (as discussed in Section 2.8). No other significant differences are seen. For more realistic curve radii for railway tracks, these cut-on frequencies fall much lower, to less than 10 Hz, thus the dispersion relationship is very similar to that for a straight track.

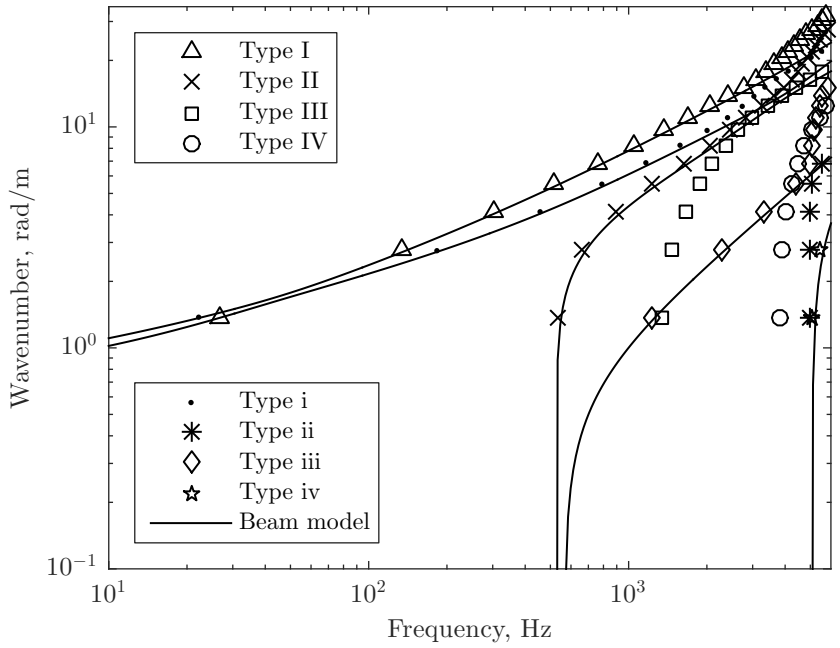

Figure 3.7: Comparison of dispersion curves for a free curved 60E1 rail with those obrained using FE model ($R = 1.45$m)

3.4.6 Dispersion relationship for 60R1 rail

For groove rails, such as the 60R1, the shear centre and centroid are offset laterally as well as vertically. This in turn causes coupling between torsion and the vertical bending as well as the lateral bending. In Fig. 3.8, the dispersion relationship obtained using the current beam model for a free 60R1 rail is presented and is compared with the results obtained using the WFE model. The parameters for the 60R1 rail are given in Table 2.1.

There are two major differences that can be noted between the results in Fig. 3.4 and Fig. 3.8. The first is that there is an overall tendency for the wavenumbers of the 60R1

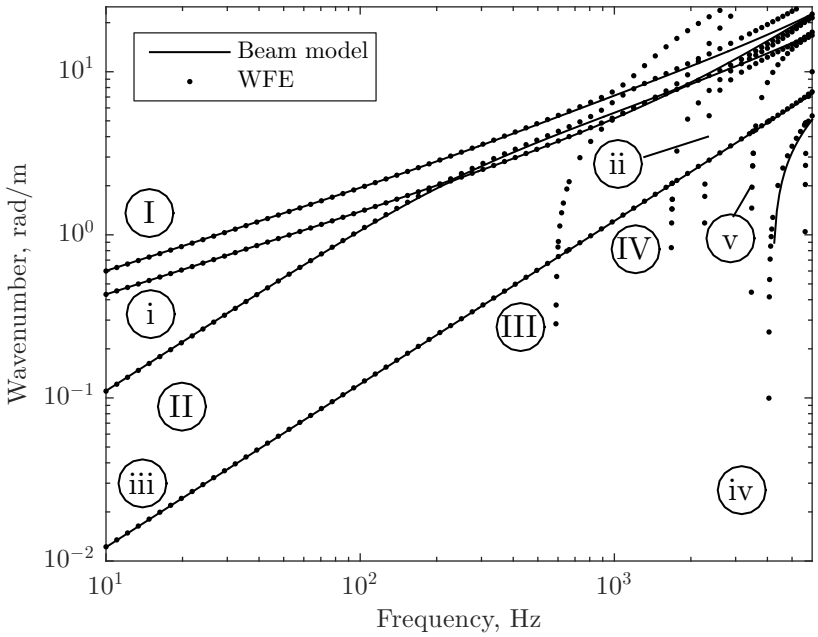

Figure 3.8: Comparison of dispersion curves for a free 60R1 rail with those from the WFE model

rail to be higher than that for 60E1 for a given frequency. This occurs because its cross-section is less stiff than those of the 60E1 rail, leading to cross-sectional deformations, such as the web bending, having an influence at lower frequencies. Wave types III and IV cut on at lower frequencies, 590 and 1670 Hz respectively compared with 1.3 and 3.8 kHz for 60E1.

Secondly, a new mode (type v) is observed in Fig. 3.8 which occurs due to the geometry of the rail head and cuts on at 3.1 kHz. The groove that is present in the rail head, allows the two sides of the head to move relative to the web. This mode is depicted in Figure 3.9 and is not found for the analytical model.

Figure 3.9: Head flapping of 60R1 rail (3109 Hz - $\xi = 0$ rad/m)

Good agreement is seen between the analytical model and the WFE model in Fig. 3.8 for frequencies up to 1 kHz, with only the type II lateral wave starting to diverge above

800 Hz. Because the 60R1 rail cross-section has a lower stiffness than the 60E1 rail, deviations due to higher order effects and cross-sectional deformations are evident at frequencies as low as 800 Hz for lateral motion and 1.5 kHz for vertical motion.

3.5 Dispersion relationship for a rail supported at the centroid

In the previous section, the dispersion relationship was investigated for a free rail, i.e. for a support stiffness of zero. The foundation support stiffness has been included in the derivation of the equations of motion in Chapter 2, but was neglected for all results presented so far. Here, the influence of the foundation is shown through dispersion plots.

The dispersion relationship for a rail supported at the centroid will be presented in this section. The effect of support eccentricity will be considered later in Section 3.6. The properties used for the railpads are shown in Table 3.2, representing a relatively soft track.

Table 3.2: Railpad properties.

Property	Value
Railpad axial stiffness, k_x^{pp}	40 MN/m
Railpad vertical stiffness, k_y^{pp}	120 MN/m
Railpad lateral stiffness, k_z^{pp}	40 MN/m
Sleeper spacing, l_{ss}	0.6 m

Here k_x^{pp}, k_y^{pp} and k_z^{pp} are the spring stiffnesses in the x, y and z directions for a single pad, indicated by the superscript pp (per pad). For a continuously supported track, the equivalent stiffness per unit length is derived from the stiffness per pad by dividing by the sleeper spacing (e.g. $k_y = k_y^{pp}/l_{ss}$).

For simplicity the rotational stiffnesses are estimated from the translational stiffnesses per pad, assuming a homogeneous material for the pad [116], as:

$$k_{xr}^{pp} = k_{zr}^{pp} = \frac{l_p^2}{12} k_y^{pp} \tag{3.19}$$

in which it is assumed that the pad is square with length l_p. Excellent agreement was found by Thompson et al. [116] between values calculated using the above equation and those measured directly, with an average difference of 1%. Similarly k_{yr}^{pp} is given by:

$$k_{yr}^{pp} = \frac{l_p^2}{12} k_x^{pp} + \frac{l_p^2}{12} k_z^{pp} \tag{3.20}$$

In the same way as for the translational stiffnesses, these are also converted into stiffness per unit length (e.g. $k_{yr} = k_{yr}^{pp}/l_{ss}$). The foundation resistance to warping k_w is similarly

defined as (see Appendix A):

$$k_w^{pp} = (\kappa_w e_s)^2 \frac{l_p^2}{12} k_x^{pp} \tag{3.21}$$

where κ_w is a factor relating the axial deformation of the rail foot due to warping to its value at the centroid (assuming a linear profile) and e_s is the vertical distance between the rail foot and the rail shear centre $(y_f - e_y)$. Again this needs to be converted to a stiffness per unit length in the same manner.

The dispersion relationship for a continuously supported 60E1 rail is shown Fig. 3.10. Compared with Fig. 3.4, the influence of the support is mainly seen at frequencies below 400 Hz, where the wavenumbers of the first vertical bending wave (type i), the first-order longitudinal wave (type iii) and the lateral bending waves (types I & II) now have non-zero cut-on frequencies. These frequencies are identified for the supported rail as 292.5, 168.1, 168.1 and 188.7 Hz respectively. The shear wave cut-on frequencies for the vertical and lateral waves are virtually unchanged.

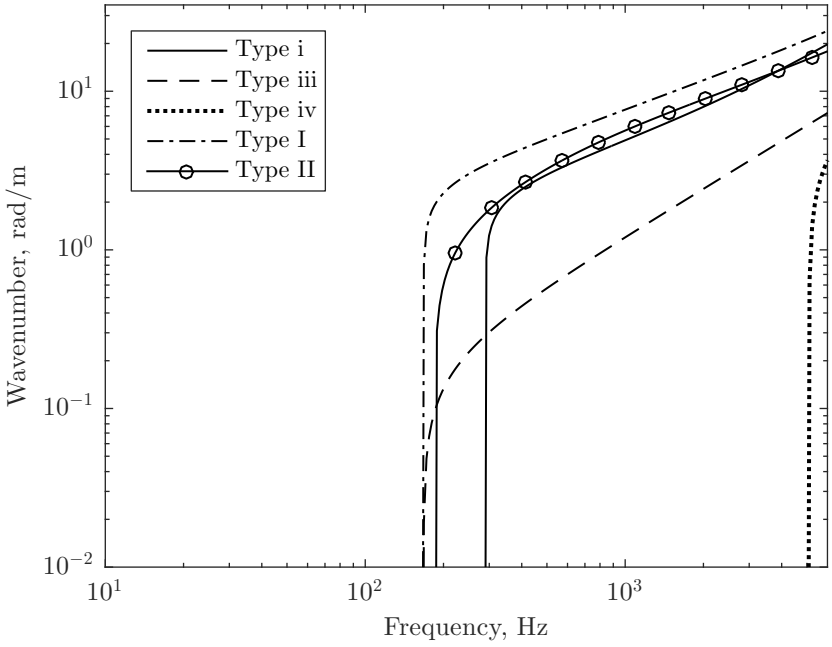

Figure 3.10: Dispersion relationship for a supported 60E1 rail

The cut-on frequencies can be identified analytically by solving Eq. (2.88), where $\mathbf{K}_0$ and $\mathbf{M}$ are as identified earlier and:

$$\mathbf{K}_p = \mathrm{diag}(k_x, k_y, k_z, k_{xr}, k_{yr}, k_{zr}, k_w) \tag{3.22}$$

Solving Eq. (2.88) gives the following cut-on frequencies, for the main propagating waves:

$$f_{co,a} = \frac{1}{2\pi}\sqrt{\frac{k_x}{\rho A}} \tag{3.23}$$

$$f_{co,v} = \frac{1}{2\pi}\sqrt{\frac{k_y}{\rho A}} \tag{3.24}$$

$$f_{co,l} = \frac{1}{2\pi}\sqrt{\frac{k_z}{\rho A}} \tag{3.25}$$

$$f_{co,t} = \frac{1}{2\pi}\sqrt{\frac{k_{xr}}{\rho I_p}} \tag{3.26}$$

The same expressions for the cut-on frequencies have also been identified in Chapter 2.

3.6 Coupling due to foundation forces

Practically, the rail is not supported at the rail centroid, as in the above formulation, but rather at the rail foot. When considering the vertical dynamics of a singly-symmetric rail, such as the 60E1, this has no consequence for the behaviour of the rail, but when lateral dynamics are also of interest, the location of the support has to be taken into account.

3.6.1 Formulation

The generalised displacement field at the rail foot can be written as:

$$\begin{bmatrix} u_{x,f} \\ u_{y,f} \\ u_{z,f} \end{bmatrix} = \begin{bmatrix} u_{x,c} \\ u_{y,c} \\ u_{z,c} \end{bmatrix} + \begin{bmatrix} 0 & -\theta_{z,c} & \theta_{y,c} \\ \theta_{z,c} & 0 & -\theta_{x,c} \\ -\theta_{y,c} & \theta_{x,c} & 0 \end{bmatrix} \begin{bmatrix} 0 \\ y_f \\ z_f \end{bmatrix} + \phi_f f_{w,c} \begin{bmatrix} 1 \\ 0 \\ 0 \end{bmatrix} \tag{3.27}$$

or in expanded form:

$$\underbrace{\begin{bmatrix} u_{x,f} \\ u_{y,f} \\ u_{z,f} \\ \theta_{x,f} \\ \theta_{y,f} \\ \theta_{z,f} \\ f_{w,f} \end{bmatrix}}_{\mathbf{U}_{r,f}} = \underbrace{\begin{bmatrix} 1 & 0 & 0 & 0 & z_f & -y_f & \phi_f \\ 0 & 1 & 0 & -z_f & 0 & 0 & 0 \\ 0 & 0 & 1 & y_f & 0 & 0 & 0 \\ 0 & 0 & 0 & 1 & 0 & 0 & 0 \\ 0 & 0 & 0 & 0 & 1 & 0 & 0 \\ 0 & 0 & 0 & 0 & 0 & 1 & 0 \\ 0 & 0 & 0 & 0 & 0 & 0 & 1 \end{bmatrix}}_{\mathbf{T}_f} \underbrace{\begin{bmatrix} u_{x,c} \\ u_{y,c} \\ u_{z,c} \\ \theta_{x,c} \\ \theta_{y,c} \\ \theta_{z,c} \\ f_{w,c} \end{bmatrix}}_{\mathbf{U}_{r,c}} \tag{3.28}$$

where the subscript f stands for rail foot and the subscript c stands for rail centroid with y_f and z_f being the offset distances of the centre of the rail foot from the rail centroid in the y and z axes respectively (see Fig. 2.1). Similarly the forces acting at the foot ($\mathbf{F}^R_{r,f}$), as for example shown in Fig. 3.11(a) for the vertical and lateral forces, can be related to those acting at the centroid ($\mathbf{F}^R_{r,c}$) by:

$$\mathbf{F}^R_{r,f} = \mathbf{T}_f^{T^{-1}} \mathbf{F}^R_{r,c} \rightarrow \mathbf{F}^R_{r,c} = \mathbf{T}_f^T \mathbf{F}^R_{r,f} \tag{3.29}$$

leading to the following expanded form:

$$\begin{bmatrix} F^R_{x,c} \\ F^R_{y,c} \\ F^R_{z,c} \\ M^R_{x,c} \\ M^R_{y,c} \\ M^R_{z,c} \\ M^R_{w,c} \end{bmatrix} = \begin{bmatrix} 1 & 0 & 0 & 0 & 0 & 0 & 0 \\ 0 & 1 & 0 & 0 & 0 & 0 & 0 \\ 0 & 0 & 1 & 0 & 0 & 0 & 0 \\ 0 & -z_f & y_f & 1 & 0 & 0 & 0 \\ z_f & 0 & 0 & 0 & 1 & 0 & 0 \\ -y_f & 0 & 0 & 0 & 0 & 1 & 0 \\ \phi_f & 0 & 0 & 0 & 0 & 0 & 1 \end{bmatrix} \begin{bmatrix} F_{x,f} \\ F_{y,f} \\ F_{z,f} \\ M_{x,f} \\ M_{y,f} \\ M_{z,f} \\ M_{w,f} \end{bmatrix} \tag{3.30}$$

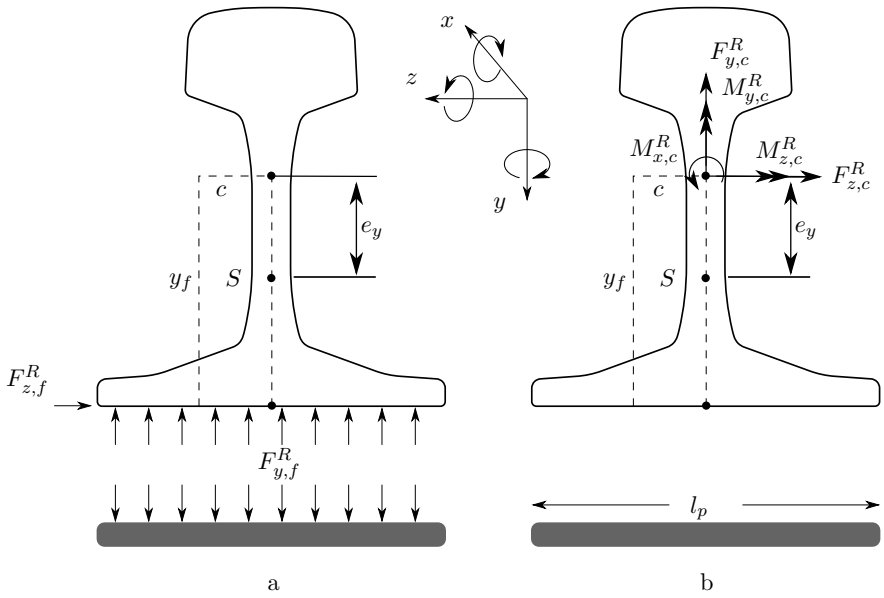

Figure 3.11: Railpad reaction forces (a) at rail foot and (b) at centroid

The following reaction forces are applied by the foundation at the rail foot:

$$\begin{bmatrix} F^R_{x,c} \\ F^R_{y,c} \\ F^R_{z,c} \\ M^R_{x,c} \\ M^R_{y,c} \\ M^R_{z,c} \\ M^R_{w,c} \end{bmatrix} = - \underbrace{\begin{bmatrix} k_x & 0 & 0 & 0 & 0 & 0 & 0 \\ 0 & k_y & 0 & 0 & 0 & 0 & 0 \\ 0 & 0 & k_z & 0 & 0 & 0 & 0 \\ 0 & -z_f k_y & y_f k_z & k_{xr} & 0 & 0 & 0 \\ z_f k_x & 0 & 0 & 0 & k_{yr} & 0 & 0 \\ -y_f k_x & 0 & 0 & 0 & 0 & k_z r & 0 \\ \phi_f k_x & 0 & 0 & 0 & 0 & 0 & k_w \end{bmatrix}}_{\mathbf{K}_p} \begin{bmatrix} u_{x,f} \\ u_{y,f} \\ u_{z,f} \\ \theta_{x,f} \\ \theta_{y,f} \\ \theta_{z,f} \\ f_{w,f} \end{bmatrix} \tag{3.31}$$

The above system of equations can also be written to give the effective reaction forces due to the rail pads at the rail centroid as:

$$\mathbf{F}^{ps}_{r,c} = -\mathbf{T}^T_f \mathbf{K}_p \mathbf{T}_f \mathbf{U}_r \tag{3.32}$$

In most cases, z_f can be considered to be zero as the reaction force from the rail pad is assumed to be applied symmetrically over the rail foot. Thus, the main contribution to coupling will be the lateral reaction force due to the torsional response in addition to the coupling between the lateral and torsional responses through the beam theory described in Section 2.7.

3.6.2 Dispersion relationship

In order to identify the influence of the foundation location on the wave propagation in the rail, the dispersion relationship for a rail supported at the railfoot is shown in Fig. 3.12 using the same parameters as previously. Here it is evident that the location of foundation has a significant influence on the dispersion relationship of the rail. Specifically, the wave type I (lateral) cuts on at a lower frequency compared to that in Section 3.5, while the wave type II (torsional) cuts on at a higher frequency. The vertical and longitudinal waves remain virtually unaffected, as are the higher order waves.

Figure 3.13 shows the effect of the distance between the rail foot and the centroid on the cut-on frequencies of the rail. This relationship is obtained by solving the eigenvalue problem $|\mathbf{K}_0 - \omega^2 \mathbf{M}| = 0$ (from Eq. (2.88)) for ω. The vertical (type i) wave cut-on frequency (solid line) remains unchanged, since the foundation is acting at a location directly under the centroid ($z_f = 0$). This frequency is described by Eq. (3.24), which is independent of y_f. Although the axial (type iii) wave cut-on frequency (dash line) is dependent on y_f similarly to the lateral motion, it is coupled with vertical bending through the vertical shear wave, hence leading to minimal variation in cut-on frequency (with a maximum difference of less than 0.2 Hz i.e. 0.12%), with a value approximately equal to that given by Eq. (3.23). The vertical shear wave (type Ve - not shown) increases

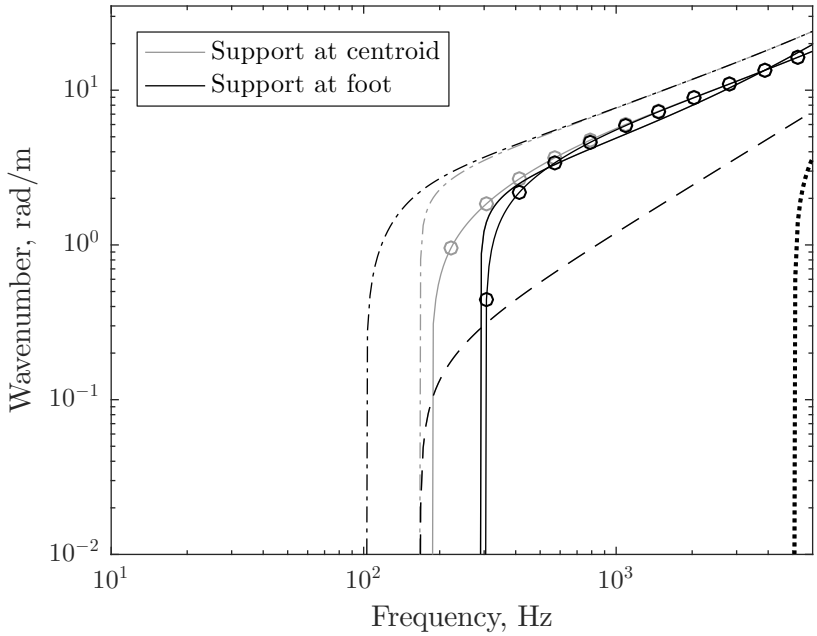

Figure 3.12: Dispersion relationship for rail with foundation located at centroid (grey) and rail foot (black). Wave types as in Fig. 3.10.

by approximately 6 Hz at $y_f = 0.1$ m, that is approximately 0.14%. The values for the vertical and axial cut-on frequencies are 292.1 Hz and 168.5 Hz respectively.

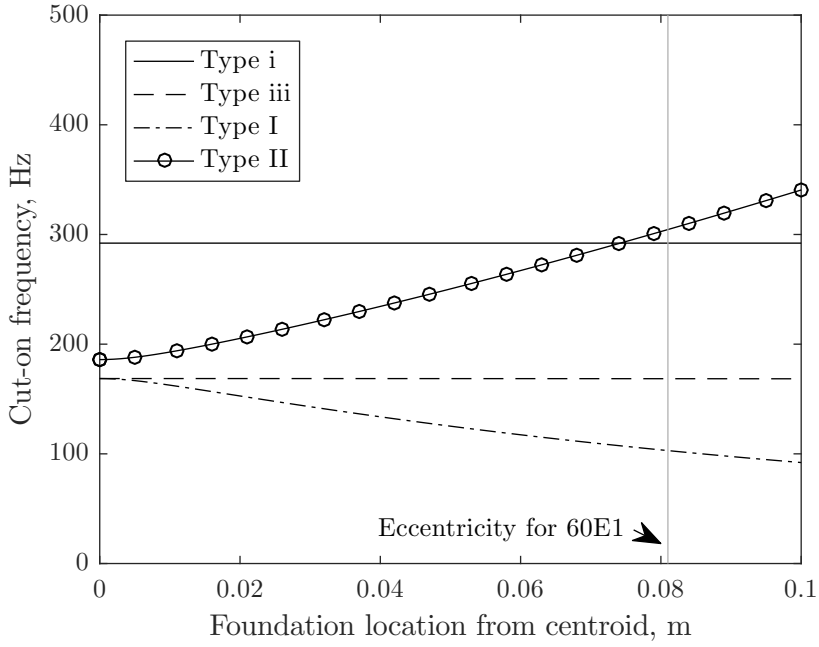

Figure 3.13: Influence of distance from rail foot to centroid on the cut-on frequencies of the rail on the elastic foundation

In contrast, the lateral and torsional cut-on frequencies are strongly dependent on the distance between the rail foot and the centroid. If the two locations coincide, then the frequencies are given by Eqs (3.25) and (3.26) respectively. As the distance increases,

the two motions become highly coupled, with the cut-on frequency of one decreasing (chain line - wave type I), while the other increases (solid-circle line - wave type II), leading to deviations in cut-on frequency of up to about -45% and +83% respectively for $y_f = 0.1$ m (-39% and +63% for the actual distance to the centroid respectively). Due to the high level of coupling, the motion can no longer be separated into purely lateral and purely torsional motion and their wave types, will be referred to as types I and II respectively, hereafter.

For a 60E1 rail, and the railpad stiffnesses given in Table 3.2, the cut-on frequencies for the two lateral waves are 103.0 Hz (type I) and 304.5 Hz (type II) respectively, whereas the original values for $y_f = 0$ are 168.6 Hz for the lateral (uncoupled type I) and 185.9 Hz for the torsional (uncoupled type II) waves. These values can also be identified in Fig. 3.12. This is an important finding as typically, when fitting models to measured data to determine rail pad stiffness values (e.g. Thompson [4], Venghaus et al. [117]), the cut-on frequency is used for the lateral motion of the rail. Thus, if the eccentricity of the foundation is not properly accounted for, it can lead to a significantly different estimation of the lateral pad (or assembly) stiffness. This will be explored further in Chapter 5

The cut-on frequencies for rotation about the y and z axes, as well as for warping, are not shown in Fig. 3.13 as they are mainly influenced by the beam properties in bending (higher order wave cut-on frequencies for Timoshenko beam) and warping. Their respective frequencies are 14.7 kHz for bending around the y axis, 5.1 kHz for bending around the z axis and 23.4 kHz for warping.

3.6.3 Equivalent two-degree-of-freedom system

As it has been shown in Section 3.6.2, the primary influence of considering the correct foundation location for a singly symmetric rail, is to introduce coupling between wave types I and II. In order to gain insight into the coupling between wave type I and II modes, an equivalent two-degree-of-freedom system of a mass with rotational inertia on a lateral-torsional foundation is introduced. The mass is allowed to translate laterally and to rotate, with the foundation applied at some distance from its centre. This system is used in order to verify the mode shapes as well as the cut-on frequencies. The properties of the mass are chosen to be the same as those of the rail, and for visualisation purposes the rail cross-section is used. The equation of motion for the free vibration of such a system is:

$$\rho A \ddot{u}_{z,c} + F^R_{z,c} = 0 \tag{3.33}$$

$$\rho I_p \ddot{\theta}_{x,c} + M^R_{x,c} = 0 \tag{3.34}$$

where ρA is the mass, ρI_p is the rotational inertia and the reaction forces due to the lateral (k_z) and torsional ($k_{x,r}$) stiffnesses are given as:

$$F^R_{z,c} = k_z \left(u_{z,c} + y_f \theta_{x,c}\right) \tag{3.35}$$

$$M^R_{x,c} = k_{x,r}\theta_{x,c} + k_z \left(u_{z,c} + y_f \theta_{x,c}\right) y_f \tag{3.36}$$

For harmonic motion, substituting the complex form of the lateral translation and rotation of the mass system, the following is obtained:

$$-\omega^2 \rho A U_{z,c} + k_z U_{z,c} + k_z y_f \Theta_{x,c} = 0 \tag{3.37}$$

$$-\omega^2 \rho I_p \Theta_{x,c} + k_{x,r}\Theta_{x,c} + k_z y_f U_{z,c} + k_z y_f^2 \Theta_{x,c} = 0 \tag{3.38}$$

or in matrix form:

$$\left(\underbrace{\begin{bmatrix} k_z & k_z y_f \\ k_z y_f & k_{x,r} + k_z y_f^2 \end{bmatrix}}_{\mathbf{K}} - \omega^2 \underbrace{\begin{bmatrix} \rho A & 0 \\ 0 & \rho I_p \end{bmatrix}}_{\mathbf{M}} \right) \begin{Bmatrix} U_{z,c} \\ \Theta_{x,c} \end{Bmatrix} = \begin{Bmatrix} 0 \\ 0 \end{Bmatrix} \tag{3.39}$$

The resonance frequencies (which are cut-on frequencies for the full system) are obtained by solving the eigenvalue problem $|\mathbf{K} - \omega^2 \mathbf{M}| = 0$ for ω. Here, the coupling between the torsional and lateral behaviour of the system due to the foundation location can be clearly seen in the terms involving y_f in the stiffness matrix $\mathbf{K}$. For a value of y_f =0 this system is completely decoupled.

It can be seen from Eq. (3.39) that the resonance frequencies are a function of the two stiffnesses ($k_{x,r}$ and k_z), the polar moment of area (I_p), the density of the beam (ρ), the cross-sectional area (A) and the distance between the centroid and the foundation (y_f). For this system, the corresponding ratio between the translation and rotation in each mode shape is plotted in Figs 3.14(a) and (b) for the frame of reference at the bottom and centroid of the mass respectively. The vertical grey line represents the location of the foundation from the centroid for a 60E1 rail. In Fig. 3.14(a), also the mode shape is depicted in arbitrary units for the case when the foundation is located at the rail foot ($y_f = 0$ m).

From Fig. 3.14(a), it can be seen that for wave type I, the top and bottom of the mass (visualised here as the rail head and foot) move in phase while for type II they move out of phase. Both modes include a significant amount of rotation, but with a different centre of rotation. The centre of rotation for the type I wave is located below the rail cross-section, giving the mode a greater lateral component. For a foundation eccentricity value of zero, it is located at infinity, making this a purely translational mode. The centre of rotation for the wave type II is located at the centroid for a foundation eccentricity of zero (foundation at centroid), and with increasing eccentricity it moves above the centroid.

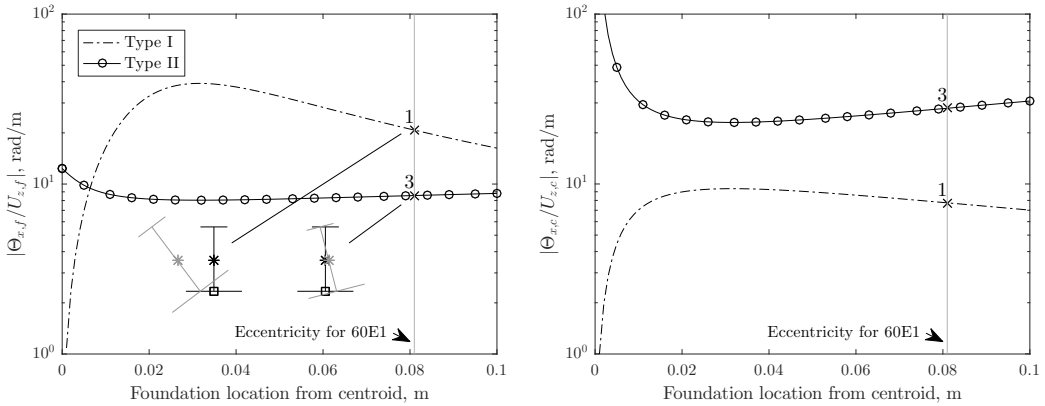

a) Location at bottom of mass b) Location at mass centroid

Figure 3.14: Mode shape ratio for mass system on lateral/torsional springs in terms of displacement at: a) bottom of mass and b) mass centroid

When expressed in terms of the displacement at the centroid, although the lateral component of wave type I is higher than for type II, the former is affected more by the torsional stiffness and thus the vertical stiffness, see e.g. Eq. (3.19). This in turn means that the vertical pad stiffness will significantly influence the lateral behaviour of the track. In the next section, the wave modes for the full system are presented.

3.6.4 Wave modes for a supported rail

In order to identify the predominant behaviour of the individual waves for the full system, the evolution of the mode shapes between 50 Hz and 300 Hz for a rail supported on an elastic foundation is shown in Fig. 3.15. The axial and warping waves are not shown, as they cannot be represented in a two-dimensional graph. As well as the various propagating waves, evanescent waves exist associated with bending denoted Ve and Le. These cut on as shear waves at high frequency in a Timoshenko beam. From this graph, it can be seen that at 300 Hz the type I mode is dominated by lateral movement, while that of wave type II is dominated by the rotation of the cross-section. This is the opposite of what is seen at 50 Hz, where both modes have a high lateral component at the centroid. In this case, type I is primarily a rotation around the rail foot while type II is a lateral movement of the whole rail. At about 100 Hz, the mode shapes of the type I and II waves are very similar. Near this frequency, a change of mode shapes is observed, whereas it can be seen from Fig. 3.16 that the real parts of their wavenumbers cross with the corresponding imaginary parts of their wavenumbers being significantly different (type I lateral wave is in a propagating region while type II lateral wave is in the evanescent region).

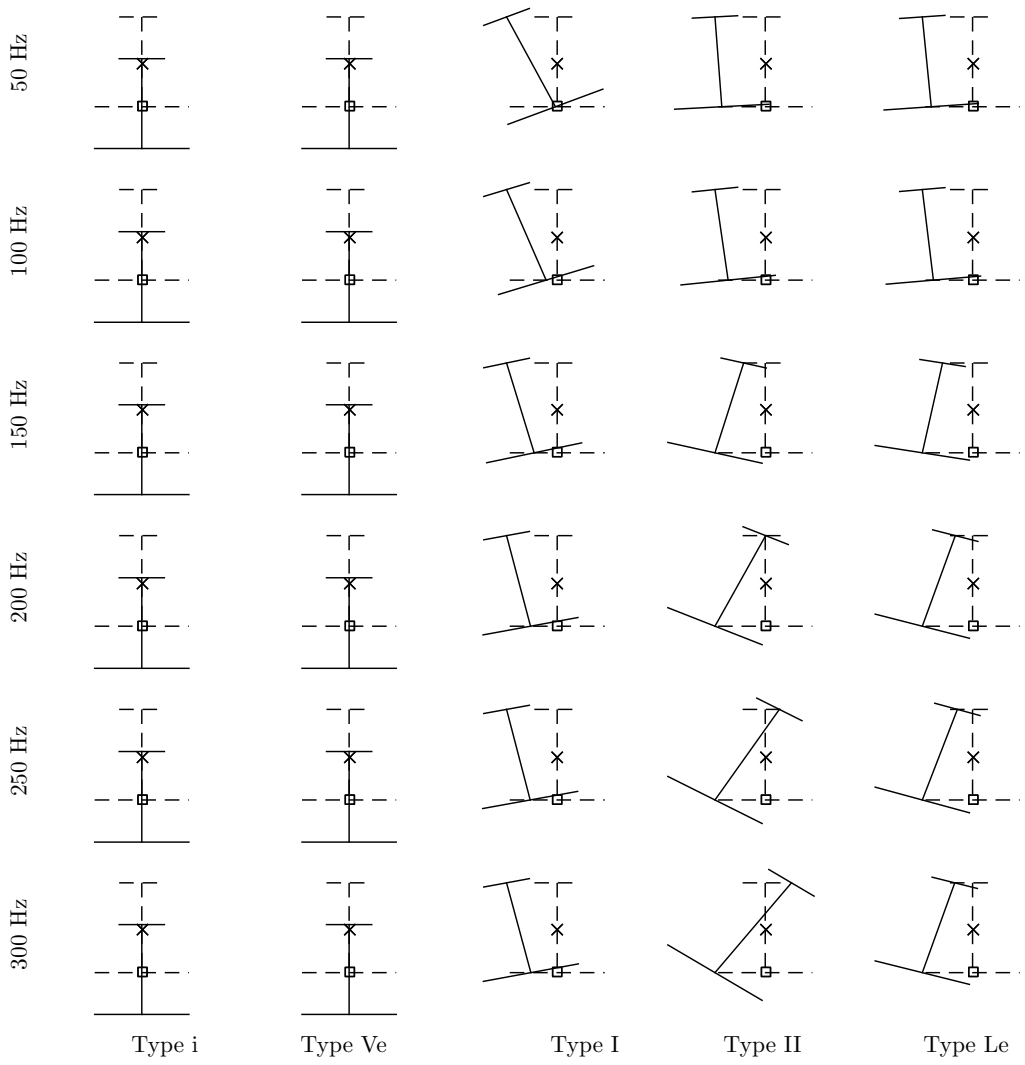

Figure 3.15: Evolution of mode shapes with frequency

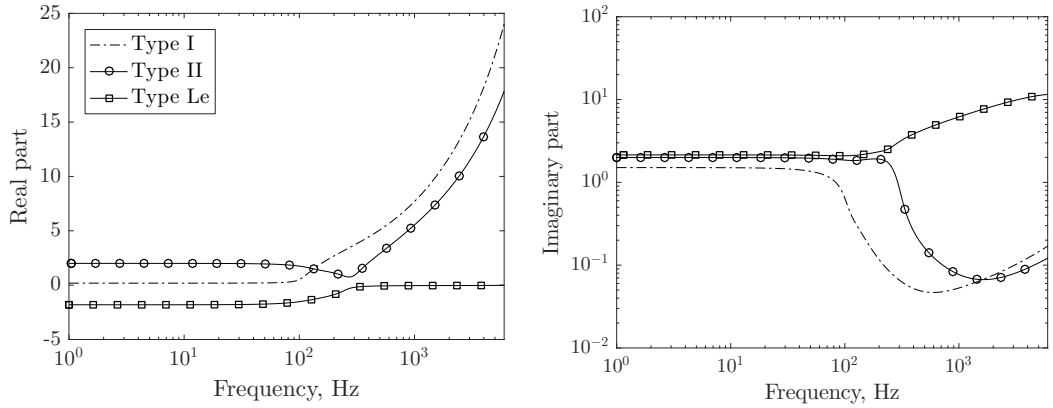

a) Real part b) Imaginary part

Figure 3.16: Wavenumbers for supported rail on an elastic foundation

3.6.5 Parametric study for pad stiffness

If the support is located at the centroid, the variation of the cut-on frequency with changes to the vertical stiffness is depicted in Fig. 3.17. The vertical stiffness only affects the vertical and lateral type II (torsional) cut-on frequencies. The lateral type I and axial cut-on frequencies are virtually identical and remain unaffected. Similarly (not shown), varying the lateral stiffness would only influence the axial and lateral type I cut-on frequencies (assuming that the lateral and axial stiffnesses are equal). In each case the frequencies are proportional to the square root of the pad stiffness.

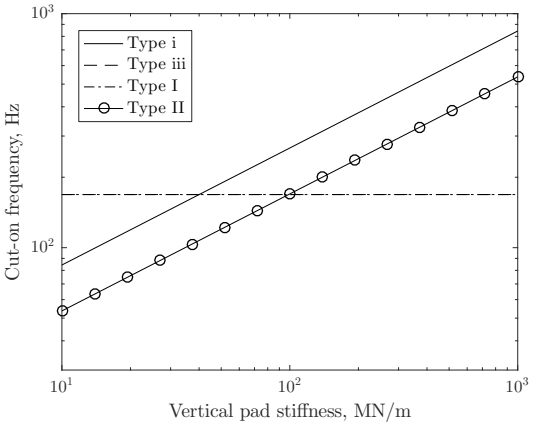

Figure 3.17: Cut-on frequencies of rail supported at the centroid for varying vertical pad stiffness

Accounting for the correct location of the foundation, i.e. at the rail foot, the effect of varying the pad vertical and lateral stiffness on the cut-on frequencies is shown in Fig. 3.18.

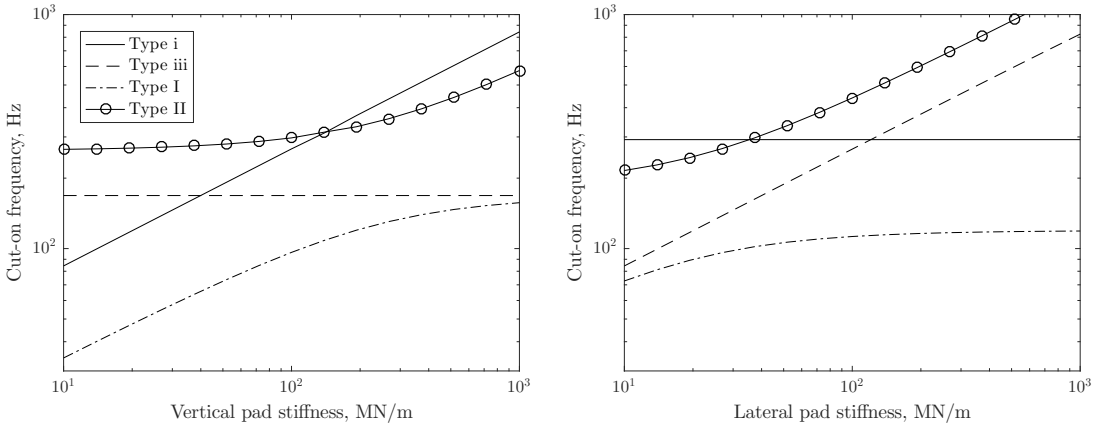

a) Varying vertical stiffness b) Varying lateral stiffness

Figure 3.18: Cut-on frequencies of rail supported at the rail foot for varying pad stiffness

Figure 3.18(a) shows the effect of the vertical pad stiffness; the lateral stiffness is maintained at 40 MN/m. As expected, the cut-on frequencies of wave types i and II are

highly influenced by the vertical pad stiffness. Due to the coupling of the type I and II waves, as seen in Fig. 3.13, also the type I wave cut-on frequency is significantly affected. For large values of vertical pad stiffness, the type I wave cut-on frequency tends to that shown in Fig. 3.17; here this has the same value as wave type iii. The axial type iii cut-on frequency is virtually unchanged over the whole stiffness range.

The result of varying the lateral and axial pad stiffness is presented in Fig. 3.18(b). The vertical stiffness is kept as 120 MN/m. In this case, the cut-on frequencies of lateral wave type II and axial wave iii experience the highest variation. The lateral type I wave cut-on frequency increases slightly with lateral pad stiffness while the vertical wave cut-on frequency remains unchanged. The lateral pad stiffness has a more significant influence on wave type II than I, except for when it has very small values. This is the result of the coupling due to the location of the support.

3.7 Conclusions

In this chapter, a detailed model for rail vibration based on the Timoshenko beam formulation has been presented, obtained by combining the various models presented in Chapter 2. This rail model takes into account the effect of vertical/lateral coupling due to the cross-sectional geometry as well as the effect of curvature and warping. Validation of the model has been performed against both a Finite Element and Waveguide Finite Element model for a straight rail and against a Finite Element model for a curved rail.

It has been seen that the agreement between the analytical and numerical models is very good for both straight and curved beams of singly-symmetric or asymmetric cross-sections. The main discrepancies arise due to the neglect of cross-sectional deformation, where modes such as foot-flapping or web bending are not represented with this analytical model.

In addition to the free rail, the inclusion of an elastic support beneath the rail and its effect on the dispersion relationship has been considered. The effect of coupling through the supports has been investigated in detail, with the largest effect seen due to the coupling of the lateral and torsional responses. For the values of stiffness used, when changing the location of the foundation from the centroid to the rail foot, the cut-on frequency of the type II lateral wave for a single layer support is seen to increase by 64%. Similarly, the cut-on frequency of the type I lateral wave is seen to decrease by 39%. A brief parametric study has also been conducted for the various support stiffnesses. Based on the change in the cut-on frequencies for the varying support conditions, it is concluded that it is important to account for the location of the foundation and the coupling of the lateral and torsional responses through the supports. Additionally, assuming that the rotational pad stiffness is related to the vertical stiffness, the latter has a significant influence on the lateral behaviour of the rail.

In the next chapter, the inclusion of additional layers of support is investigated, accounting for ballast and sleepers, including both rigid and flexible sleeper models.

Chapter 4

Effect of a two-layer support including sleepers and ballast

The rails are usually supported on sleepers via elastic pads. The sleepers are further supported in ballast which can be considered as another elastic layer. For a continuous support model, the sleeper mass can be assumed to be uniformly distributed beneath the rail but to have no bending or torsional stiffness along the rail axis [4].

In this chapter, the sleeper is modelled either as a rigid block (half a bibloc sleeper) in which case the bending of the sleeper itself in the transverse direction is ignored, or as a flexible (monobloc) sleeper accounting for its dynamic behaviour. The cross-section of a bibloc sleeper attached to the rail is depicted in Fig. 4.1. This will be used as a general schematic view for the coupling of the second support layer (representing the sleeper and ballast).

4.1 General formulation

In this section, the equation of motion of a rail supported on a two-layer foundation will be presented. For convenience, the rail is represented only as a mass and the model is considered to be two-dimensional, i.e. there is no wave propagation along the rail. This allows the equations of motion to be derived irrespective of the wavenumber, and thus gain better insight into the coupling mechanism.

The reaction forces between the rail foot and the top surface of the sleeper due to the rail pads can be written, similarly to Section 3.6, as:

$$\mathbf{F}_{r,f}^{ps} = \mathbf{K}_p \left(\mathbf{U}_{r,f} - \mathbf{U}_{s,t} \right) \tag{4.1}$$

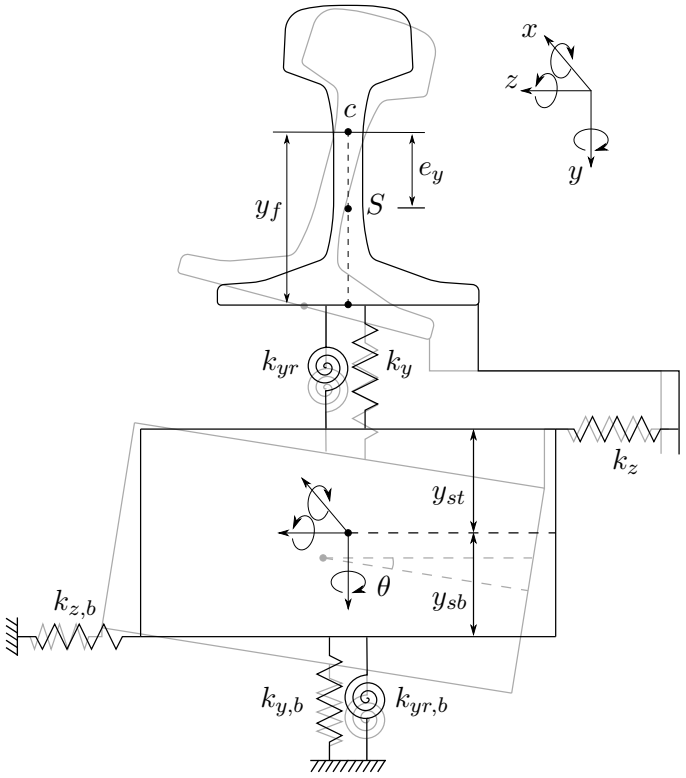

Figure 4.1: Rigid bibloc sleeper attached to the rail

where $\mathbf{K}_p$ is the diagonal matrix of stiffness between the rail and the sleeper and $\mathbf{U}_{r,f}$ and $\mathbf{U}_{s,t}$ are responses at the rail foot and sleeper top surface respectively. This can be expressed in terms of the responses at the rail centroid $\mathbf{U}_r$ and sleeper centroid $\mathbf{U}_s$ as:

$$\mathbf{F}^{ps}_{r,f} = \mathbf{K}_p \left(\mathbf{T}_f \mathbf{U}_r - \mathbf{T}_{s,t} \mathbf{U}_s\right) \tag{4.2}$$

where $\mathbf{T}_f$ is the same as in as in Eq. (3.28) and $\mathbf{T}_{s,t}$ is a 7×6 matrix for the transformation of the co-ordinates from the six degrees of freedom at the sleeper centroid to the seven degrees of freedom at the sleeper top surface. $\mathbf{F}^{ps}_{r,f}$ contains the reaction forces acting at the bottom of the rail. The equivalent reaction forces from the railpads expressed at the rail centroid can be written from Eq. (3.29) as:

$$\mathbf{F}^{ps}_{r,c} = \mathbf{T}^T_f \mathbf{F}^{ps}_{r,f} \tag{4.3}$$

$$= \mathbf{T}^T_f \mathbf{K}_p \left(\mathbf{T}_f \mathbf{U}_r - \mathbf{T}_{s,t} \mathbf{U}_s\right) \tag{4.4}$$

and the reaction forces from the railpads expressed at the sleeper centroid as:

$$\mathbf{F}^{ps}_{s,c} = \mathbf{T}^T_{s,t} \mathbf{F}^{ps}_{s,t} \tag{4.5}$$

$$= \mathbf{T}^T_{s,t} \mathbf{K}_p \left(\mathbf{T}_f \mathbf{U}_r - \mathbf{T}_{s,t} \mathbf{U}_s\right) \tag{4.6}$$

where the superscript (ps) denotes the pad/sleeper interface, the subscripts (r, f), (r, c)

denote the rail foot and rail centroid and the subscripts (s,t), (s,c) and (s,b) the sleeper top surface, sleeper centroid and sleeper bottom surface respectively.

At this stage, the displacement vector at the sleeper centroid $\mathbf{U}_s$ needs to be determined in order to solve for the response of the system. In order to allow for both sleeper models in a unified way, the forces acting at the centroid of the sleeper are written in a generic form as:

$$\mathbf{F}_{s,c}^{sb} = \mathbf{K}_s \mathbf{U}_s \tag{4.7}$$

where the sleeper dynamic stiffness matrix $\mathbf{K}_s$ will depend on the sleeper model used. The forces acting at the rail centroid in the positive direction are thus:

$$\mathbf{F}_r = -\mathbf{F}_{r,c}^{ps} \tag{4.8}$$

while those at the sleeper centroid are:

$$\mathbf{F}_s = \mathbf{F}_{s,c}^{ps} - \mathbf{F}_{s,c}^{sb} \tag{4.9}$$

or written in a matrix form, from Eqs (4.4), (4.6) and (4.7), as:

$$\begin{Bmatrix} \mathbf{F}_r \\ \mathbf{F}_s \end{Bmatrix} = \begin{bmatrix} -\mathbf{T}_f^T \mathbf{K}_p \mathbf{T}_f & \mathbf{T}_f^T \mathbf{K}_p \mathbf{T}_{s,t} \\ \mathbf{T}_{s,t}^T \mathbf{K}_p \mathbf{T}_f & -\mathbf{T}_{s,t}^T \mathbf{K}_p \mathbf{T}_{s,t} - \mathbf{K}_s \mathbf{U}_s \end{bmatrix} \begin{Bmatrix} \mathbf{U}_r \\ \mathbf{U}_s \end{Bmatrix} \tag{4.10}$$

Newton's second law of motion can then be applied at the rail and sleeper centroid, for harmonic motion with respect to time (i.e. $\mathbf{u}_{r/s} = \mathbf{U}_{r/s} e^{i\omega t}$), as:

$$\left(\begin{bmatrix} \mathbf{T}_f^T \mathbf{K}_p \mathbf{T}_f & -\mathbf{T}_f^T \mathbf{K}_p \mathbf{T}_{s,t} \\ -\mathbf{T}_{s,t}^T \mathbf{K}_p \mathbf{T}_f & \mathbf{T}_{s,t}^T \mathbf{K}_p \mathbf{T}_{s,t} + \mathbf{K}_s \end{bmatrix} - \omega^2 \begin{bmatrix} \mathbf{M}_r & \mathbf{0}_{7\times 6} \\ \mathbf{0}_{6\times 7} & \mathbf{M}_s \end{bmatrix} \right) \begin{Bmatrix} \mathbf{U}_r \\ \mathbf{U}_s \end{Bmatrix} = \begin{Bmatrix} \mathbf{F}_r \\ \mathbf{F}_s \end{Bmatrix} \tag{4.11}$$

or equivalently this can be written in compact form as:

$$\left(\mathbf{K}_{r/s} - \omega^2 \mathbf{M}_{r/s} \right) \mathbf{U} = \begin{Bmatrix} \mathbf{F}_r \\ \mathbf{F}_s \end{Bmatrix} \tag{4.12}$$

The stiffness $\mathbf{K}_s$ and mass $\mathbf{M}_s$ matrices for the bibloc and monobloc sleeper models will now be derived.

4.2 Rigid sleepers (bibloc)

In the case of a bibloc sleeper, half the sleeper is considered as a rigid mass that can translate in three directions and rotate about three axes, and the coupling between the two blocks is ignored.

4.2.1 Formulation

The reaction forces between the sleeper bottom and the ballast can be given as:

$$\mathbf{F}_{s,b}^{sb} = \mathbf{K}_b \mathbf{U}_{s,b} \tag{4.13}$$

$$= \mathbf{K}_b \mathbf{T}_{s,b} \mathbf{U}_s \tag{4.14}$$

where $\mathbf{T}_{s,b}$ is a 6×6 matrix for the transformation of the coordinates from the bottom surface of the sleeper to the sleeper centroid, the superscript (sb) denotes the sleeper/ballast interface and

$$\mathbf{K}_b = \text{diag}(k_{b,x}, k_{b,y}, k_{b,z}, k_{b,rx}, k_{b,ry}, k_{b,rz}) \tag{4.15}$$

is the ballast stiffness matrix.

The reaction forces from the ballast can then be written in terms of the degrees of freedom at the sleeper centroid as:

$$\mathbf{F}_{s,c}^{sb} = \mathbf{T}_{s,b}^T \mathbf{F}_{s,b}^{sb} \tag{4.16}$$

$$= \mathbf{T}_{s,b}^T \mathbf{K}_b \mathbf{T}_{s,b} \mathbf{U}_s \tag{4.17}$$

Thus, the ballast stiffness matrix for a bibloc sleeper is:

$$\mathbf{K}_s = \mathbf{T}_{s,b}^T \mathbf{K}_b \mathbf{T}_{s,b} \tag{4.18}$$

while the mass matrix is that of a mass in translation and rotation:

$$\mathbf{M}_s = \text{diag}(m, m, m, \rho I_x, \rho I_y, \rho I_z) \tag{4.19}$$

These can be substituted into Eq. (4.11), leading to:

$$\left(\begin{bmatrix} \mathbf{T}_f^T \mathbf{K}_p \mathbf{T}_f & -\mathbf{T}_f^T \mathbf{K}_p \mathbf{T}_{s,t} \\ -\mathbf{T}_{s,t}^T \mathbf{K}_p \mathbf{T}_f & \mathbf{T}_{s,t}^T \mathbf{K}_p \mathbf{T}_{s,t} + \mathbf{T}_{s,b}^T \mathbf{K}_b \mathbf{T}_{s,b} \end{bmatrix} - \omega^2 \begin{bmatrix} \mathbf{M}_r & \mathbf{0}_{7\times6} \\ \mathbf{0}_{6\times7} & \mathbf{M}_s \end{bmatrix} \right) \begin{Bmatrix} \mathbf{U}_r \\ \mathbf{U}_s \end{Bmatrix} = \begin{Bmatrix} \mathbf{F}_r \\ \mathbf{F}_s \end{Bmatrix} \tag{4.20}$$

Table 4.1 contains the properties used for the bibloc sleeper, where b, L and h are the breadth, length and height of the sleeper block respectively. These properties are for a single sleeper block and are converted to those applying for a distributed layer by dividing by the distance between the sleepers, l_{ss}.

Table 4.2 contains the properties used for the ballast layer.

The rotational stiffnesses of the ballast are derived in a similar fashion to those for the railpads, considering the dimensions of the sleeper. Assuming that the ballast restrains

Table 4.1: Properties of bibloc sleeper

Property	Value	Units
Mass, m	125	kg
Density, ρ	2500	kg/m^3
Height, h	0.25	m
Length, L	0.8	m
Breadth, b	0.25	m
Second moment of area, I_x	0.0029	m^5
Second moment of area, I_y	0.0005	m^5
Second moment of area, I_z	0.0029	m^5

Table 4.2: Properties of ballast layer per sleeper block.

Property	Value	Units
Ballast axial stiffness, $k_{b,x}$	120	MN/m
Ballast vertical stiffness, $k_{b,y}$	200	MN/m
Ballast lateral stiffness, $k_{b,z}$	120	MN/m
Axial damping loss factor, $\eta_{b,x}$	2	-
Vertical damping loss factor, $\eta_{b,y}$	1	-
Lateral damping loss factor, $\eta_{b,z}$	2	-

the sleeper only on its bottom surface, it follows that:

$$k_{b,rx} = \frac{L^2}{12} k_{b,y} \tag{4.21}$$

$$k_{b,rz} = \frac{b^2}{12} k_{b,y} \tag{4.22}$$

$$k_{b,ry} = \frac{L^2}{12} k_{b,x} + \frac{b^2}{12} k_{b,z} \tag{4.23}$$

4.2.2 Results

The point mobility of the bibloc sleeper when excited at its centroid is shown in Fig. 4.2. Results are shown for when the sleeper is supported either at its centroid or at the sleeper bottom surface. In Fig. 4.2(a), the vertical mobility shows no difference between the two support locations, as expected due to symmetry, with the peak corresponding to the resonance of the sleeper mass on the vertical ballast stiffness. For the lateral point mobility in Fig. 4.2(b), a reduction in frequency of the main peak is seen when the correct support location is taken into account. This is similar to the behaviour seen in Section 3.6.3 for the single layer support, although the cut-on frequency of the wave type II is not distinct. The first peak corresponds to the resonance of the sleeper mass on the ballast lateral stiffness, while the second to the rotation of the sleeper block on the ballast rotational stiffness. Similar results are also seen for the axial mobility in Fig. 4.2(c), although here the effects are more pronounced. This is due to the smaller sleeper cross-section in the axial direction, which results in a lower rotational ballast stiffness around the z axis, see Eqs (4.21) and (4.22).

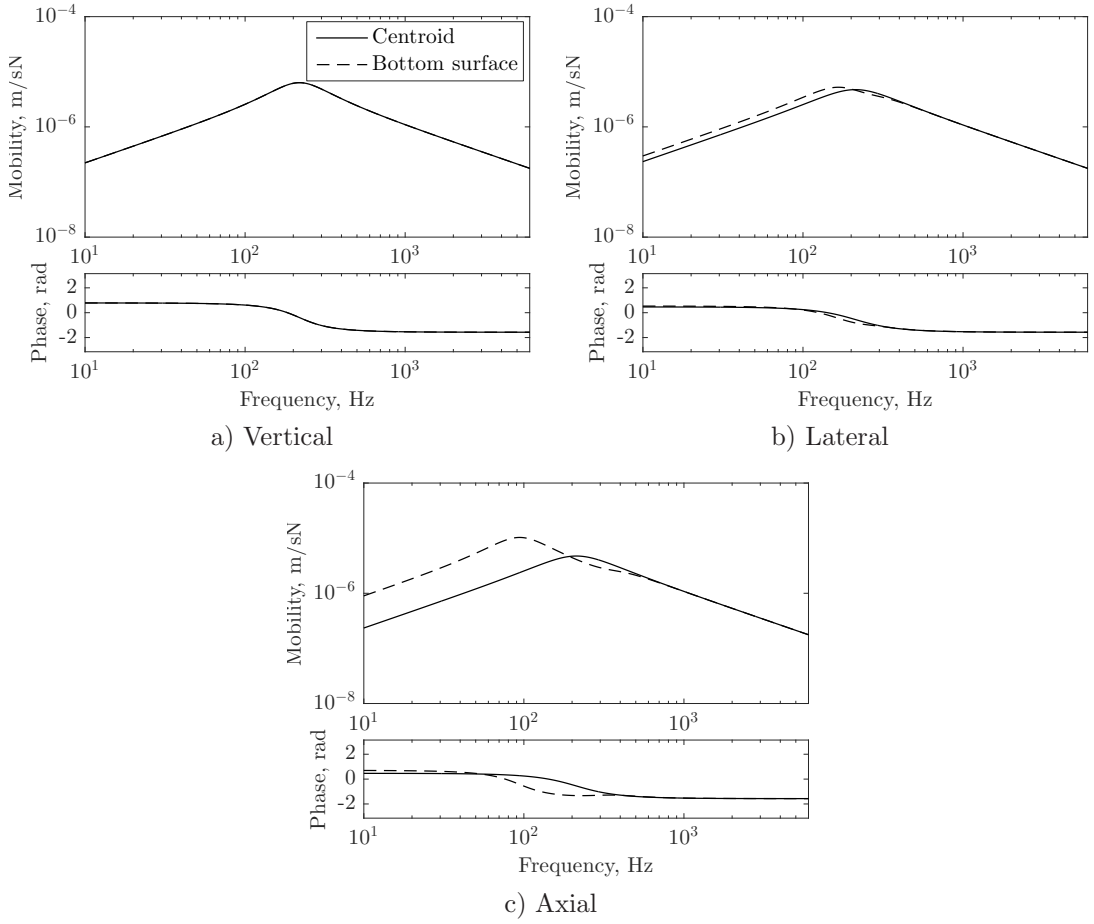

Figure 4.2: Point mobility of bibloc sleeper accounting for support at the sleeper centroid (solid lines) and sleeper bottom surface (dash lines) for a) vertical, b) lateral and c) axial excitation at the sleeper centroid

The effect of the second support layer on the track dispersion relation (rail modelled as a beam), accounting for the bibloc sleeper, is shown in Fig. 4.3 (properties for the rail and pads as tabulated in Tables 2.1 and 3.2) only for the vertical wave type i. This wave is seen to cut-on at around 160 Hz, reaching a peak at 230 Hz and then suddenly cutting off at that frequency. Within this frequency range, free wave propagation occurs, with the sleeper having a larger amplitude of vibration than that of the rail [4]. From 230 Hz to about 340 Hz, there is a 'blocked' region where no free wave propagation occurs [4]. Above 340 Hz, free wave propagation cuts on again, with the wavenumber tending to that of the unsupported rail. At this frequency, the relative vibration of the rail is much higher than that of the sleeper.

Similarly, Fig. 4.4 shows the dispersion relationship of all the waves for a continuously supported 60E1 rail on a double layer support. Between 60 Hz and 350 Hz, a series of cut-on frequencies are seen. In particular, each of the waves is seen to cut on, then off, and then on again as described for the vertical wave type i in Fig. 4.3. The frequencies where the waves initially cut on correspond to the resonance of the combined mass of the

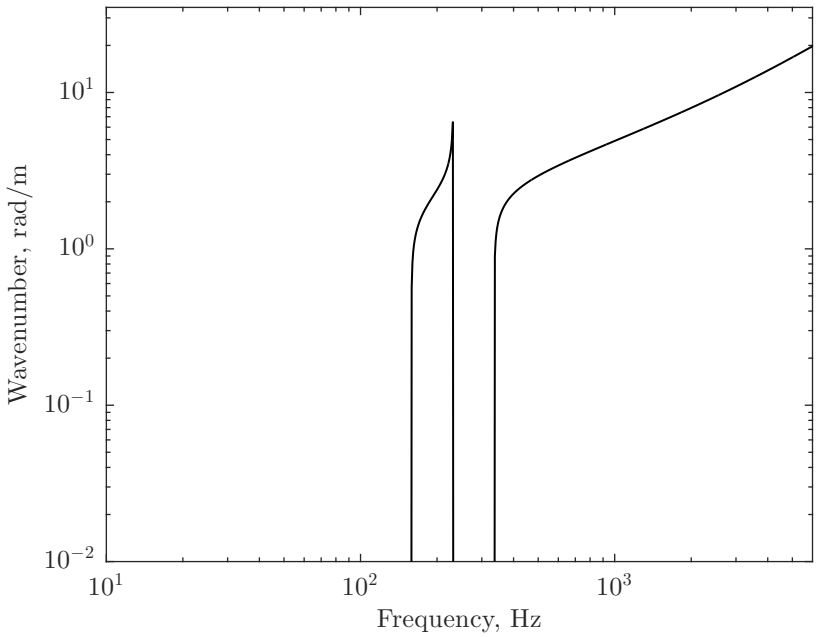

Figure 4.3: Dispersion relationship of vertical type i wave for a supported 60E1 rail on a double layer support

rail and sleeper on the ballast stiffness in translation and rotation. At higher frequencies, the rail decouples from the sleepers, with the various waves in the rail cutting on again. These cut-on frequencies can be identified as the resonance of the rail on the respective pad stiffness.

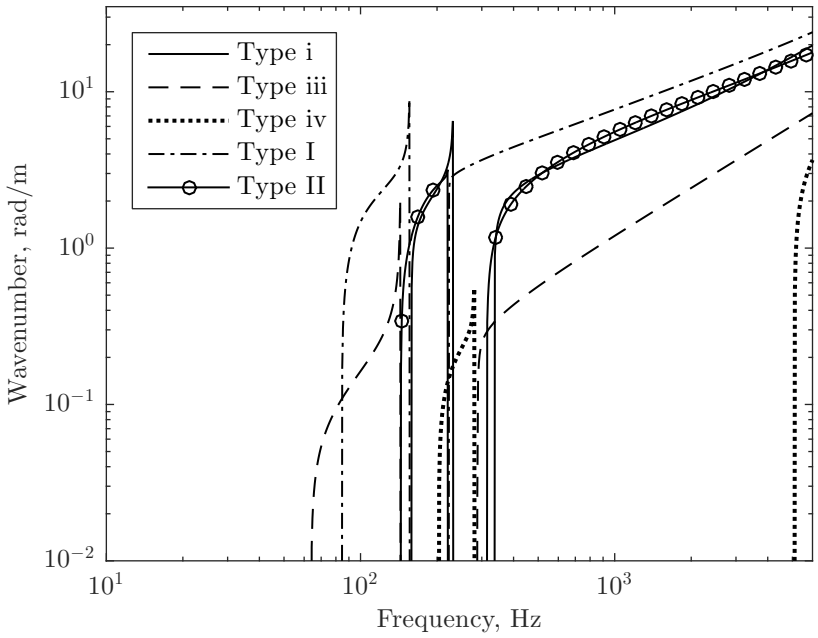

Figure 4.4: Dispersion relationship for a supported 60E1 rail on a double layer support

Figure 4.5 shows the effect of the distance between rail foot and centroid on the cut-on

frequencies of the rail on the double layer foundation. This relationship is obtained by solving the eigenvalue problem of $|\mathbf{K}_{r/s} - \omega^2\mathbf{M}_{r/s}| = 0$ (similar to Eq. (2.88)) for ω. For clarity, here they are separated into the cut-on frequencies of the combined rail and sleeper mass on the ballast, termed first cut-on frequencies, Fig. 4.5(a), and those of the rail on the pad, termed second cut-on frequencies, Fig. 4.5(b).

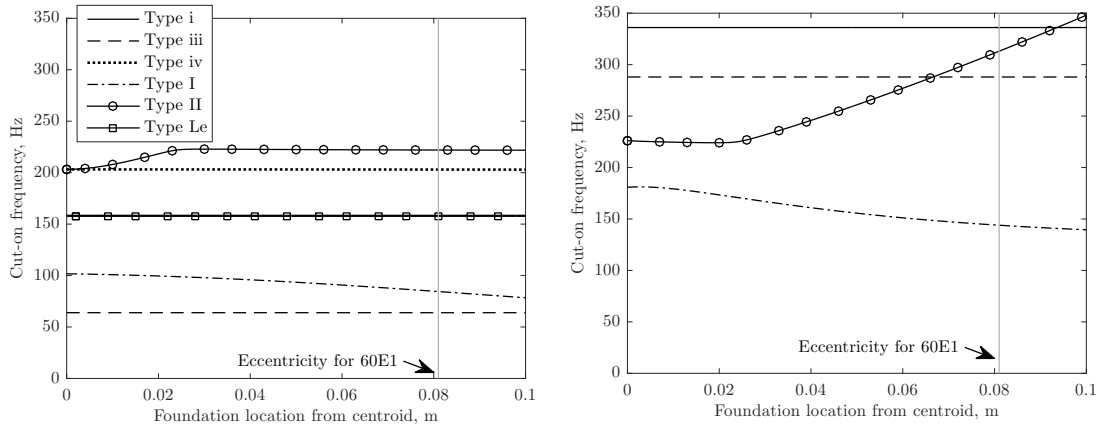

a) First cut-on frequencies

b) Second cut-on frequencies

Figure 4.5: Influence of rail foot to centroid distance on the cut-on frequencies of the rail on the double layer foundation

The changes seen in Fig. 4.5 are not as straightforward as for the case of a single layer support (see Fig 3.13). Because the ballast is considered to act at the sleeper bottom surface and the railpads at the sleeper top surface, a vertical offset exists creating further coupling through the transfer matrices $\mathbf{T}_{s,t}$ and $\mathbf{T}_{s,b}$. In order to understand the nature of the cut-on frequencies, the parameters have been varied progressively, with results shown in Fig. 4.6. Here, initially y_{sb} is increased from 0, corresponding to the sleeper centroid, to $h/2 = 0.125$ m corresponding to the sleeper bottom surface. Subsequently, y_{st} is changed from 0, being the sleeper centroid, to $h/2 = -0.125$ m, being the sleeper top surface (with the minus sign as it is in the opposite direction). Finally y_f (the distance from the the rail centroid to the location of application of the reaction forces) is varied from 0, where the centroid and location of application of the reaction forces coincide, to 0.1 m.

Due to the low inertial properties of the sleeper block in rotation, it is difficult for the various wave types to be identified uniquely, with wave types changing with both frequency and offset distance. The corresponding cut-on frequencies (for the actual geometry of the rail and sleeper) are tabulated in Table 4.3. It can be seen from Fig. 4.6 that, similar to the single layer support (see Fig. 3.13), the first cut-on frequencies of the type I and II waves corresponding to the combined mass of the rail and the sleeper (chain and solid-circle lines respectively as identified in Fig. 4.5(a)) change as the distance of the location of the pads and ballast increases. The cut-on frequency of the type II wave decreases with increasing y_{sb} and increases with decreasing y_{st}. Due to the coupling of

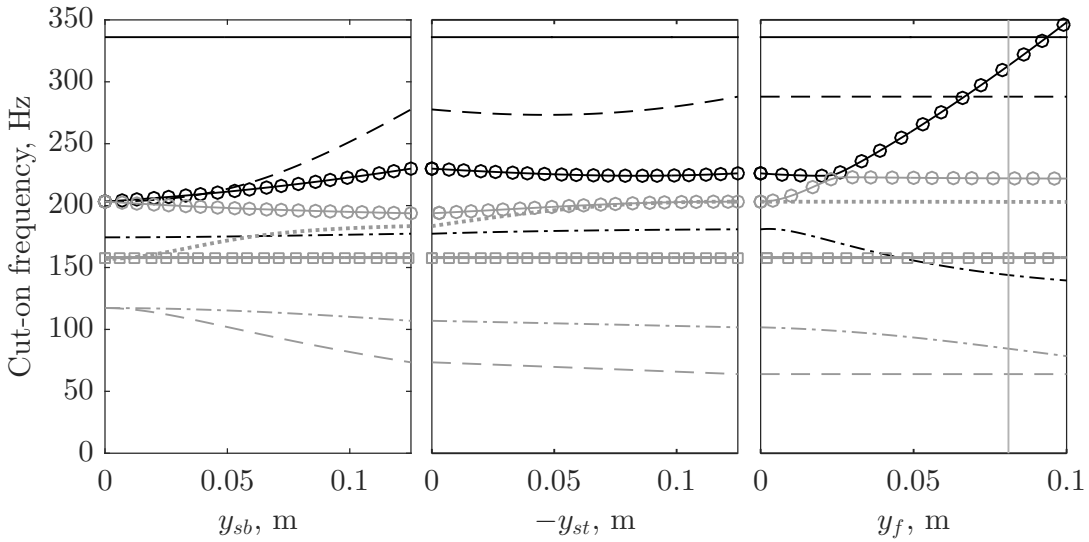

Figure 4.6: Influence sleeper/rail eccentricities on the cut-on frequencies of the rail on the double layer foundation; black for rail on pads and grey for rail and sleeper on ballast. Key = same as Fig. 4.5

Table 4.3: Cut-on frequencies for double layer support corresponding to Fig. 4.6

Line type	Type	f_{co} for 60E1 rail
Dash (grey)	Rail and sleeper on $k_{b,x}$	64 Hz
Chain (grey)	Rail and sleeper on $k_{b,z}$	84 Hz
Dot (grey)	Rail and sleeper on $k_{b,rz}$	203 Hz
Solid-circle (grey)	Rail and sleeper on $k_{b,rx}$	222 Hz
Solid (grey)	Rail and sleeper on $k_{b,y}$	159 Hz
Solid-square (grey)	Rail and sleeper on $k_{b,ry}$	158 Hz
Chain (black)	Rail on k_z	144 Hz
Dash (black)	Rail on k_x	288 Hz
Solid-circle (black)	Rail on k_{rx}	313 Hz
Solid (black)	Rail on k_y	336 Hz
Not visible	Rail on k_{rz} (shear wave)	5 kHz
Not visible	Rail on k_{ry} (shear wave)	14 kHz
Not visible	Rail on k_w	23 kHz

the type II wave on the rail and sleeper, for increasing y_f veering is seen to occur between their respective cut-on frequencies. The cut-on frequency of type I wave decreases with increasing y_{sb}, decreasing y_{st} and increasing y_f.

The axial behaviour (type iii wave) of the combined mass is coupled with the rotation of the combined mass around the z axis. This occurs for the double-layer foundation as the sleeper has no bending stiffness along the x axis, contrary to the rail in the single layer foundation. Similarly to the lateral waves (types I and II), a change of mode shapes can be expected.

It can be confirmed from Fig. 4.6 that some of the cut-on frequencies remain virtually

unchanged throughout the variation of the contact locations for the ballast and railpads, specifically the cut-on frequencies corresponding to the vertical mode of the rail on the pads, the rotation mode of the sleeper around the y axis) and the warping mode (not shown). More substantial deviations are seen in four of the cut-on frequencies, corresponding to the lateral type I and II waves of both the rail on the pads and the combined rail/sleeper mass on the ballast.

The changes in cut-on frequency seen with the eccentric double support layer are very similar to those found for the eccentric single support studied in Section 3.6. As seen, the consideration of the vertical eccentricity mainly affects the lateral and torsional responses, increasing the level of coupling between them.

4.2.3 Effect of varying pad and ballast stiffness

The effects of varying the pad vertical and lateral stiffness on the cut-on frequencies for a double-layer support are shown in Figs 4.7 and 4.8 respectively. Again, these are separated into the first and second cut-on frequencies for each wave type.

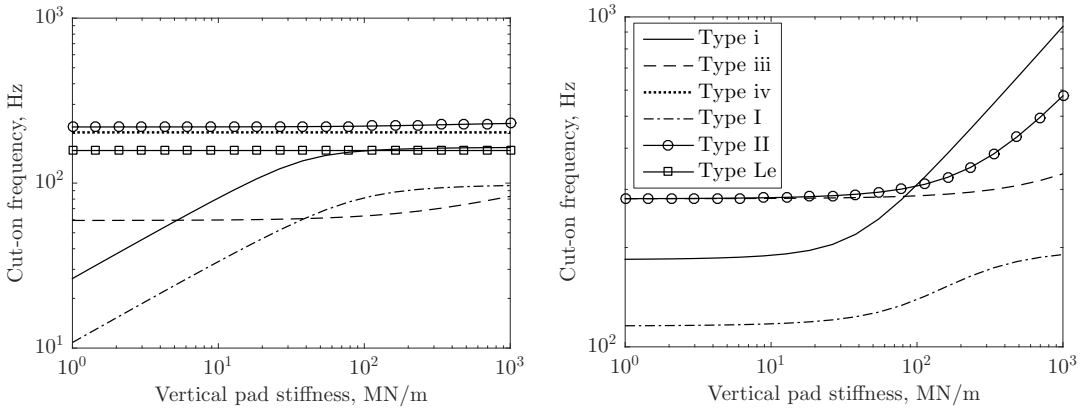

a) First cut-on frequencies b) Second cut-on frequencies

Figure 4.7: Cut-on frequencies of supported rail for varying vertical pad stiffness - double-layer support

In Fig. 4.7 the effect of vertical pad stiffness variation is shown. The greatest variation in frequency occurs for the vertical (solid line) and lateral type II (solid-circle line) cut-on frequencies of the rail on the pad in Fig. 4.7(b). Smaller differences are also seen in Fig. 4.7(a) for the vertical (solid line), lateral type I (chain line) and II (solid-circle line) cut-on frequencies of the combined mass on the ballast stiffness.

The effect of the variation of the lateral pad stiffness is shown in Fig. 4.8. The most significant changes are seen in Fig. 4.8(b) with an increase in the lateral type II cut-on frequency of the rail on the pads as well as the axial (axial pad stiffness changes along with the lateral). Small changes are seen for the lateral type I cut-on frequency, which is in this case primarily controlled by the rotational stiffness.

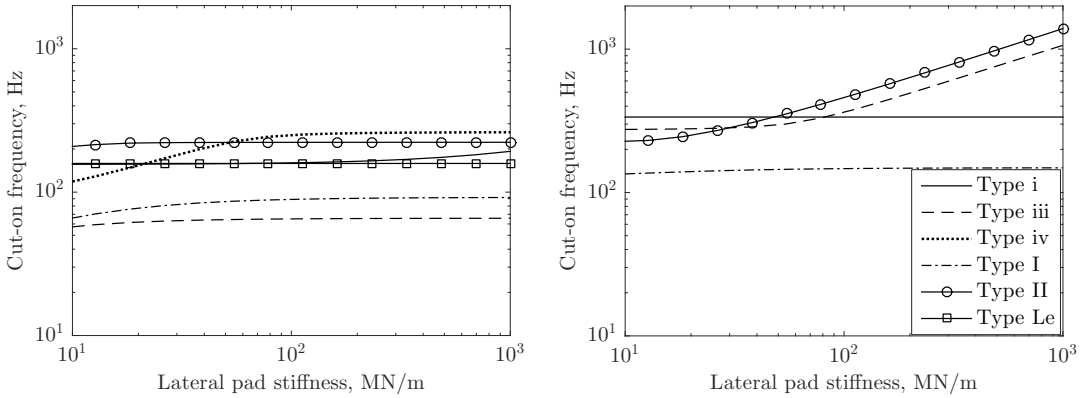

a) First cut-on frequencies b) Second cut-on frequencies

Figure 4.8: Cut-on frequencies of supported rail for varying lateral pad stiffness - double-layer support

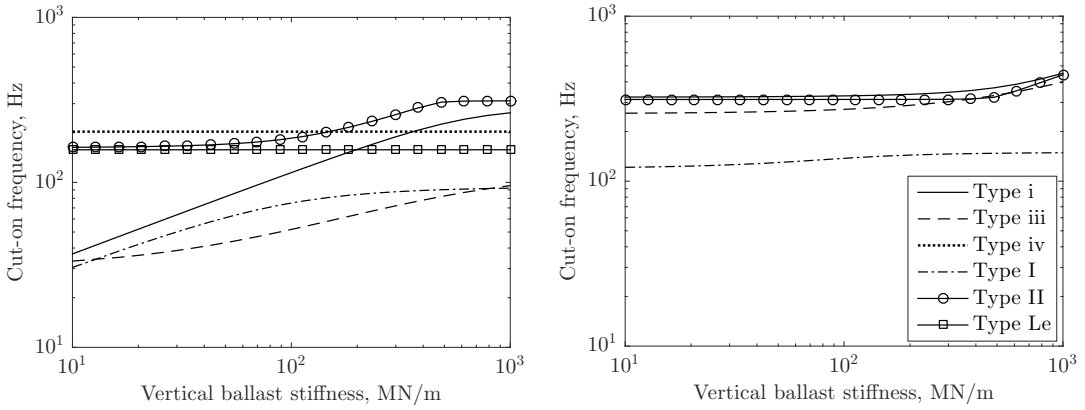

a) First cut-on frequencies b) Second cut-on frequencies

Figure 4.9: Cut-on frequencies of supported rail for varying vertical ballast stiffness - double-layer support

Figure 4.9 shows the effect of variation of the vertical ballast stiffness. Here, the influence is mainly on the first cut-on frequencies. Specifically, the greatest variations are seen in the vertical type i and lateral type II cut-on frequencies, as well as the axial wave. Due to the coupling of the type I and II waves, also the type I cut-on frequency is affected.

Finally, the effect of the lateral ballast stiffness is depicted in Fig. 4.10. It can be seen that this mainly affects the cut-on frequencies for the combined mass (lateral type I and II) in Fig. 4.10(a) and to a lesser extent the type I and II cut-on frequencies of the rail on the pads in Fig. 4.10(b).

4.3 Flexible sleepers (monobloc)

The modelling approach developed for the monobloc sleeper is similar to that described by Thompson [4], where the dynamic stiffness of the sleeper is obtained based on its

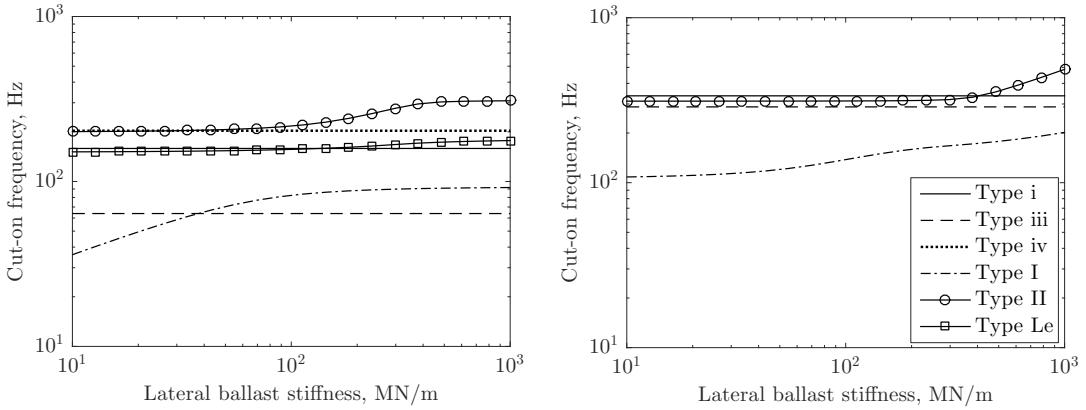

a) First cut-on frequencies b) Second cut-on frequencies

Figure 4.10: Cut-on frequencies of supported rail for varying lateral ballast stiffness - double-layer support

forced response. This model assumes a uniform cross-section of the sleeper along its length, and is extended here to account for the sleeper flexibility not only in vertical bending, but also in the axial, lateral and torsional directions. This has been achieved in a similar manner to that for the uncoupled rail modelling, i.e. considering models for the extension, torsion and bending in vertical and lateral directions but in this case with no coupling through the beam. The justification behind this assumption stems from the fact that the sleeper cross-section is almost symmetric. Thus the sleeper model can be seen as two separate models, one involving the axial sleeper response (lateral to the rail) and vertical sleeper bending, and the other involving the torsional response and lateral sleeper bending (axial to the rail). Nevertheless coupling in the sleeper model originates from the foundation eccentricity, where the ballast is assumed to act at the bottom of the sleeper. Finally, appropriate consideration of the boundary conditions is taken into account to accommodate the finite length of the sleeper. For the following formulation, the local coordinate axes of the sleeper are considered, where x is the axis along the sleeper length. A transfer matrix will be used to convert the local dynamic stiffness matrix to the global (rail) co-ordinate system.

When modelling a flexible sleeper, the damping properties of the sleeper are important for its dynamic behaviour, since the undamped modes of a finite length beam are pronounced [4]. In order to include this, the elastic properties of the sleeper (E and G) are made complex by introducing a material damping loss factor, η. Thus, the Young's modulus of the sleeper is replaced by $E(1 + i\eta)$. With the inclusion of damping, the wavenumbers become imaginary. The dynamic response of the sleeper model is calculated numerically and an eigenvalue problem in terms of ω is not easily determined due to the frequency-dependent ballast stiffness (discussed in Section 4.6.1). Thus, for the case of a flexible sleeper, only the forced response will be presented, and compared with that of the bibloc sleeper.

4.3.1 Lateral bending and torsion

Figure 4.11 shows a flexible sleeper resting on an elastic foundation, accounting for lateral bending and torsion.

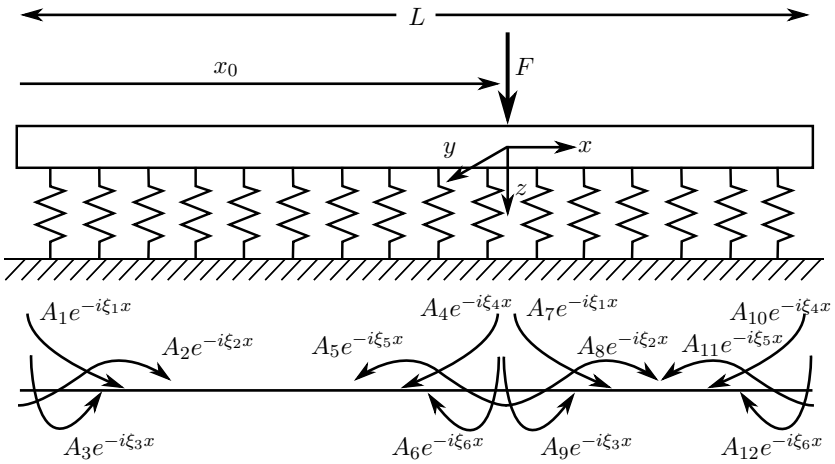

Figure 4.11: Lateral/torsional waves on a sleeper resting on an elastic foundation, excited by a point force at x=0.

The equations of motion for a beam in lateral bending and torsion are given by Eq. (2.41) and Eqs (2.78)–(2.79), as:

$$-F_z' + \rho A \ddot{u}_z + \tilde{F}_z^R = 0 \tag{4.24}$$

$$-M_y' + F_z + \rho I_y \ddot{\theta}_y + \tilde{M}_y^R = 0 \tag{4.25}$$

$$-\frac{\partial M_x}{\partial x} + \rho I_p \ddot{\theta}_x + \tilde{M}_x^R = 0 \tag{4.26}$$

with the internal forces:

$$F_z = GA\kappa_z(u_z' + \theta_y) \tag{4.27}$$

$$M_y = EI_y\theta_y' \tag{4.28}$$

$$M_x = GJ\theta_x' \tag{4.29}$$

and the foundation forces, here representing the ballast, arising from:

$$\begin{Bmatrix} \tilde{F}_z^R \\ \tilde{M}_y^R \\ \tilde{M}_x^R \end{Bmatrix} = \begin{bmatrix} 1 & 0 & y_b \\ 0 & 1 & 0 \\ 0 & 0 & 1 \end{bmatrix}^T \begin{bmatrix} k_{b,z} & 0 & 0 \\ 0 & k_{b,ry} & 0 \\ 0 & 0 & k_{b,rx} \end{bmatrix} \begin{bmatrix} 1 & 0 & y_b \\ 0 & 1 & 0 \\ 0 & 0 & 1 \end{bmatrix} \begin{Bmatrix} u_z \\ \theta_y \\ \theta_x \end{Bmatrix} \tag{4.30}$$

When an excitation is applied at location x_0 from the left sleeper end, three waves are generated for each direction away from the point of excitation (wave types I, II and Le), along with three reflected waves at each end due to the finite length of the sleeper (e.g.

$\xi_{n+3} = -\xi_n$ for n=1,2,3). In total there are six waves. The wavenumbers ξ_n can then be obtained by solving the eigenvalue problem of Eq. (2.85).

The beam is divided into two parts at the force location $x = 0$ and the forced response is determined directly, with the displacement written as:

$$u_{z-} = \sum_{n=1}^{6} A_n e^{-i\xi_n x}, \qquad \text{for } -x_0 \leq x \leq 0. \tag{4.31}$$

$$u_{z+} = \sum_{n=1}^{6} A_{n+6} e^{-i\xi_n x}, \qquad \text{for } 0 < x < L - x_0. \tag{4.32}$$

Similarly the rotation around the y and x axis of the sleeper can be written as:

$$\theta_{y-} = \sum_{n=1}^{6} B_n e^{-i\xi_n x}, \qquad \text{for } -x_0 \leq x \leq 0. \tag{4.33}$$

$$\theta_{y+} = \sum_{n=1}^{6} B_{n+6} e^{-i\xi_n x}, \qquad \text{for } 0 \leq x \leq L - x_0. \tag{4.34}$$

$$\theta_{x-} = \sum_{n=1}^{6} C_n e^{-i\xi_n x}, \qquad \text{for } -x_0 \leq x \leq 0. \tag{4.35}$$

$$\theta_{x+} = \sum_{n=1}^{6} C_{n+6} e^{-i\xi_n x}, \qquad \text{for } 0 \leq x \leq L - x_0. \tag{4.36}$$

where A_n, B_n and C_n are the complex amplitudes of the respective degrees of freedom for a given wavenumber ξ_n.

Three boundary conditions are required at each end of the beam. The shear force is zero at each end:

$$GA\kappa_z \left(\frac{\partial u_z}{\partial x} + \theta_y \right) \bigg|_{x=-x_0} = 0 \tag{4.37}$$

$$GA\kappa_z \left(\frac{\partial u_z}{\partial x} + \theta_y \right) \bigg|_{x=L-x_0} = 0 \tag{4.38}$$

Similarly, the bending moment is zero at each end:

$$EI_y \frac{\partial \theta_y}{\partial x} \bigg|_{x=-x_0} = 0 \tag{4.39}$$

$$EI_y \frac{\partial \theta_y}{\partial x} \bigg|_{x=L-x_0} = 0 \tag{4.40}$$

and the torsional moment is also zero at each end:

$$GJ\frac{\partial\theta_x}{\partial x}\bigg|_{x=-x_0} = 0 \tag{4.41}$$

$$GJ\frac{\partial\theta_x}{\partial x}\bigg|_{x=L-x_0} = 0 \tag{4.42}$$

Six more conditions apply at $x = 0$; continuity of displacement, rotation and torsion:

$$u_{z-}(0) = u_{z+}(0) \tag{4.43}$$

$$\theta_{y-}(0) = \theta_{y+}(0) \tag{4.44}$$

$$\theta_{x-}(0) = \theta_{x+}(0) \tag{4.45}$$

as well as equilibrium of forces:

$$GA\kappa_z\left(\frac{\partial u_{z-}}{\partial x} + \theta_{y-}\right)\bigg|_{x=0} - GA\kappa_z\left(\frac{\partial u_{z+}}{\partial x} + \theta_{y+}\right)\bigg|_{x=0} = \tilde{F}_z \tag{4.46}$$

$$EI_y\frac{\partial\theta_{y-}}{\partial x}\bigg|_{x=0} - EI_y\frac{\partial\theta_{y+}}{\partial x}\bigg|_{x=0} = \tilde{M}_y \tag{4.47}$$

$$GJ\frac{\partial\theta_{x-}}{\partial x}\bigg|_{x=0} - GJ\frac{\partial\theta_{x+}}{\partial x}\bigg|_{x=0} = \tilde{M}_x \tag{4.48}$$

This gives 12 boundary conditions. Although there are 36 unknown amplitudes, they are interrelated. By writing the equation of motion for the free vibration of the sleeper in the frequency-wavenumber domain, it follows:

$$\mathbf{A}(\xi,\omega)\tilde{\mathbf{U}}(\xi,\omega) = \mathbf{0} \tag{4.49}$$

$\tilde{\mathbf{U}}$ contains the complex amplitudes of the sleeper centroid and $\mathbf{A}$ is the dynamic stiffness matrix of the sleeper, written as:

$$\mathbf{A} = \mathbf{K}_0 + \mathbf{K}_b - \omega^2\mathbf{M} - i\xi\mathbf{K}_1 - \xi^2\mathbf{K}_2 \tag{4.50}$$

where:

$$\mathbf{K}_b = \begin{bmatrix} k_{b,z} & 0 & k_{b,z}y_b \\ 0 & k_{b,ry} & 0 \\ k_{b,z}y_b & 0 & k_{b,z}y_b^2 + k_{b,rx} \end{bmatrix} \tag{4.51}$$

$$\mathbf{K}_0 = \begin{bmatrix} 0 & 0 & 0 \\ 0 & GA\kappa_z & 0 \\ 0 & 0 & 0 \end{bmatrix} \tag{4.52}$$

$$\mathbf{K}_1 = \begin{bmatrix} 0 & -GA\kappa_z & 0 \\ GA\kappa_z & 0 & 0 \\ 0 & 0 & 0 \end{bmatrix} \tag{4.53}$$

$$\mathbf{K}_2 = \begin{bmatrix} -GA\kappa_z & 0 & 0 \\ 0 & -EI_y & 0 \\ 0 & 0 & -GJ \end{bmatrix} \tag{4.54}$$

$$\mathbf{M} = \begin{bmatrix} \rho A & 0 & 0 \\ 0 & \rho I_y & 0 \\ 0 & 0 & \rho I_p \end{bmatrix} \tag{4.55}$$

The amplitudes B_n and C_n can be written as a function of the amplitude A_n for a given wave n. Since there are six waves at either side of the applied load, 24 more equations are obtained for the amplitudes B_n and C_n. If combined with the 12 boundary conditions, they can be written as a 36×36 matrix of equations and solved to find the wave amplitudes A_n, B_n and C_n. The equations will have to be solved separately for a unit force, unit bending moment and unit torsion moment to give the receptance matrix. The receptance matrix at a general position x is then given by Eqs (4.31)–(4.36). For each location considered, a dynamic stiffness matrix can be determined from the receptance matrix by inversion, thus creating a 3×3 dynamic stiffness matrix, $\mathbf{K}^D_{s,l}(\omega)$. The point of interest $x = 0$ is at the rail seat, where the rail is connected to the sleeper.

4.3.2 Vertical bending and extension

Similarly, Fig. 4.12 shows a flexible sleeper, accounting for vertical bending and extension, resting on an elastic foundation.

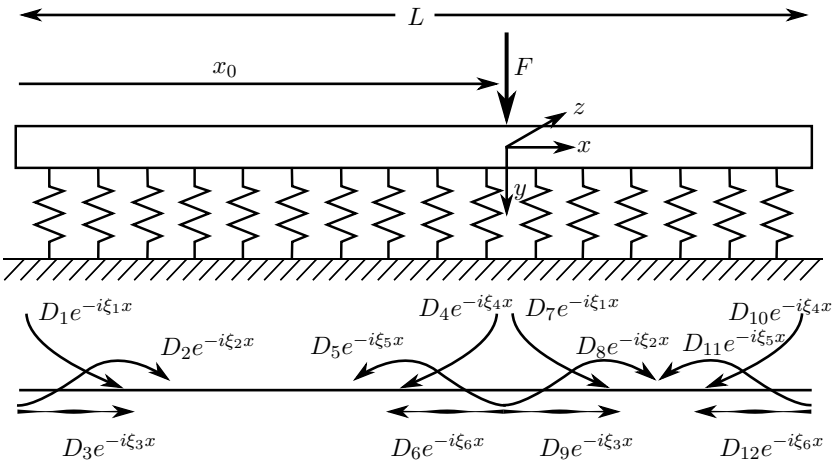

Figure 4.12: Vertical/axial waves on a sleeper resting on an elastic foundation, excited by a point force at x=0.

The equations of motion for a beam in vertical bending and extension are given by Eq. (2.21) and Eqs (2.68)–(2.69), as:

$$-F_y' + \rho A \ddot{u}_y + \tilde{F}_y^R = 0 \tag{4.56}$$

$$-M_z' - F_y + \rho I_z \ddot{\theta}_z + \tilde{M}_z^R = 0 \tag{4.57}$$

$$-\frac{\partial F_x}{\partial x} + m\ddot{u}_x + \tilde{F}_x^R = 0 \tag{4.58}$$

with the internal forces:

$$F_y = GA\kappa_y(u_y' - \theta_z) \tag{4.59}$$

$$M_z = EI_z\theta_z' \tag{4.60}$$

$$F_x = EAu_x' \tag{4.61}$$

and the foundation forces, here representing the ballast, arising from:

$$\begin{Bmatrix} \tilde{F}_y^R \\ \tilde{M}_z^R \\ \tilde{F}_x^R \end{Bmatrix} = \begin{bmatrix} 1 & 0 & 0 \\ 0 & 1 & 0 \\ 0 & -y_b & 1 \end{bmatrix}^T \begin{bmatrix} k_{b,y} & 0 & 0 \\ 0 & k_{b,rz} & 0 \\ 0 & 0 & k_{b,x} \end{bmatrix} \begin{bmatrix} 1 & 0 & 0 \\ 0 & 1 & 0 \\ 0 & -y_b & 1 \end{bmatrix} \begin{Bmatrix} u_y \\ \theta_z \\ u_x \end{Bmatrix} \tag{4.62}$$

Again, when an excitation is applied at location x_0 from the left sleeper end, three waves are generated for each direction away from the point of excitation (wave types i, iii and Ve), along with three reflected waves at each end due to the finite length of the sleeper (e.g. $\xi_{n+3} = -\xi_n$ for n=1,2,3). Similar to the lateral direction, there are six waves in total, the wavenumbers ξ_n of which are obtained by Eq. (2.85), with the wavenumbers for the vertical vibration of the sleeper being different than the lateral ones.

The beam is again divided into two parts at the force location $x = 0$ and the forced response is determined directly, with the displacement written as:

$$u_{y-} = \sum_{n=1}^{6} D_n e^{-i\xi_n x}, \qquad \text{for } -x_0 \le x \le 0. \tag{4.63}$$

$$u_{y+} = \sum_{n=1}^{6} D_{n+6} e^{-i\xi_n x}, \qquad \text{for } 0 \le x \le L - x_0. \tag{4.64}$$

Similarly the rotation around the z axis and displacement along the x axis of the sleeper can be written as:

$$\theta_{z-} = \sum_{n=1}^{6} E_n e^{-i\xi_n x}, \qquad \text{for } -x_0 \leq x \leq 0. \tag{4.65}$$

$$\theta_{z+} = \sum_{n=1}^{6} E_{n+6} e^{-i\xi_n x}, \qquad \text{for } 0 \leq x \leq L - x_0. \tag{4.66}$$

$$u_{x-} = \sum_{n=1}^{6} F_n e^{-i\xi_n x}, \qquad \text{for } -x_0 \leq x \leq 0. \tag{4.67}$$

$$u_{x+} = \sum_{n=1}^{6} F_{n+6} e^{-i\xi_n x}, \qquad \text{for } 0 \leq x \leq L - x_0. \tag{4.68}$$

where D_n, E_n and F_n are the complex amplitudes of the respective degree of freedom for a given wavenumber ξ_n.

Three boundary conditions are required at each end of the beam. The shear force is zero at each end:

$$GA\kappa_y \left(\frac{\partial u_y}{\partial x} - \theta_z \right) \bigg|_{x=-x_0} = 0 \tag{4.69}$$

$$GA\kappa_y \left(\frac{\partial u_y}{\partial x} - \theta_z \right) \bigg|_{x=L-x_0} = 0 \tag{4.70}$$

Similarly, the bending moment is zero at each end:

$$EI_z \frac{\partial \theta_z}{\partial x} \bigg|_{x=-x_0} = 0 \tag{4.71}$$

$$EI_z \frac{\partial \theta_z}{\partial x} \bigg|_{x=L-x_0} = 0 \tag{4.72}$$

and so is the axial force:

$$EA \frac{\partial u_x}{\partial x} \bigg|_{x=-x_0} = 0 \tag{4.73}$$

$$EA \frac{\partial u_x}{\partial x} \bigg|_{x=L-x_0} = 0 \tag{4.74}$$

Six more conditions apply at $x = 0$; continuity of displacement, rotation and extension, as:

$$u_{y-}(0) = u_{y+}(0) \tag{4.75}$$

$$\theta_{z-}(0) = \theta_{z+}(0) \tag{4.76}$$

$$u_{x-}(0) = u_{x+}(0) \tag{4.77}$$

as well as equilibrium of forces:

$$GA\kappa_y \left(\frac{\partial u_{y-}}{\partial y} - \theta_{z-} \right) \Bigg|_{x=0} - GA\kappa_y \left(\frac{\partial u_{y+}}{\partial x} - \theta_{z+} \right) \Bigg|_{x=0} = \tilde{F}_y \tag{4.78}$$

$$EI_z \frac{\partial \theta_{z-}}{\partial x} \Bigg|_{x=0} - EI_z \frac{\partial \theta_{z+}}{\partial x} \Bigg|_{x=0} = \tilde{M}_z \tag{4.79}$$

$$EA \frac{\partial u_{x-}}{\partial x} \Bigg|_{x=0} - EA \frac{\partial u_{x+}}{\partial x} \Bigg|_{x=0} = \tilde{F}_x \tag{4.80}$$

This gives 12 boundary conditions. Similar to the lateral sleeper vibration, although there are 36 unknown amplitudes, they are interrelated according to Eq. (4.49), where:

$$\mathbf{K}_b = \begin{bmatrix} k_{b,y} & 0 & 0 \\ 0 & k_{b,x} y_b^2 + k_{b,rz} & -k_{b,x} y_b \\ 0 & -k_{b,x} y_b & k_{b,x} \end{bmatrix} \tag{4.81}$$

$$\mathbf{K}_0 = \begin{bmatrix} 0 & 0 & 0 \\ 0 & GA\kappa_y & 0 \\ 0 & 0 & 0 \end{bmatrix} \tag{4.82}$$

$$\mathbf{K}_1 = \begin{bmatrix} 0 & GA\kappa_y & 0 \\ -GA\kappa_y & 0 & 0 \\ 0 & 0 & 0 \end{bmatrix} \tag{4.83}$$

$$\mathbf{K}_2 = \begin{bmatrix} -GA\kappa_y & 0 & 0 \\ 0 & -EI_z & 0 \\ 0 & 0 & -EA \end{bmatrix} \tag{4.84}$$

$$\mathbf{M} = \begin{bmatrix} \rho A & 0 & 0 \\ 0 & \rho I_z & 0 \\ 0 & 0 & \rho A \end{bmatrix} \tag{4.85}$$

The amplitudes E_n and F_n can be then be written as a function of the amplitude D_n for a given wave n. Since there are six waves at either side of the applied load, 24 more equations are obtained for the amplitudes E_n and F_n. If combined with the 12 boundary conditions, they can be written as a 36×36 matrix of equations and solved to find the wave amplitudes D_n, E_n and F_n. Again, the equations will have to be solved separately for a unit vertical force, unit bending moment and unit axial force. The receptance matrix at a general position x is then given by Eqs (4.63)–(4.68). For each location considered, a dynamic stiffness matrix can be determined from the receptance matrix by inversion, thus creating a 3×3 dynamic stiffness matrix, $\mathbf{K}^D_{s,v}(\omega)$. Again, the point of interest $x = 0$ is at the rail seat, where the rail is connected to the sleeper.

4.3.3 Combining the vertical and lateral flexible sleeper models

By combining the vertical and lateral flexible sleeper models, by assembling the two dynamic stiffness matrices that have been derived, this model can be coupled directly to the rail. The resulting dynamic stiffness matrix $\mathbf{K}^D_{s,loc}(\omega)$ is assembled from the two derived dynamic stiffness matrices, $\mathbf{K}^D_{s,v}(\omega)$ and $\mathbf{K}^D_{s,l}(\omega)$ in the local co-ordinate system of the sleeper. Since the inertial properties of the sleeper are already incorporated in the dynamic stiffness matrix $\mathbf{K}^D_{s,loc}(\omega)$, the sleeper mass matrix for the flexible sleeper model is not required (i.e. $\mathbf{M}_s = \mathbf{0}$).

To account for the difference in orientation of the rail and sleeper beams, the dynamic stiffness matrix must be converted from the local (sleeper) co-ordinate system to the global (rail) co-ordinate system. This is performed by applying a transfer matrix:

$$\mathbf{K}^D_s = (\mathbf{T}_g^T \mathbf{K}^D_{s,loc} \mathbf{T}_g)/l_{ss} \tag{4.86}$$

where

$$\mathbf{T}_g^T = \begin{bmatrix} 0 & 0 & -1 & 0 & 0 & 0 \\ 0 & 1 & 0 & 0 & 0 & 0 \\ 1 & 0 & 0 & 0 & 0 & 0 \\ 0 & 0 & 0 & 0 & 0 & -1 \\ 0 & 0 & 0 & 0 & 1 & 0 \\ 0 & 0 & 0 & 1 & 0 & 0 \end{bmatrix} \tag{4.87}$$

The division with l_{ss} is also performed in Eq. (4.86) in order to obtain properties per unit length, for a continuous support layer.

Finally, the dynamic equation of motion for the track will take the following form:

$$\left(\begin{bmatrix} \mathbf{T}_f^T(\mathbf{K}_p \mathbf{T}_f) & -\mathbf{T}_f^T(\mathbf{K}_p \mathbf{T}_{s,t}) \\ -\mathbf{T}_{s,t}^T(\mathbf{K}_p \mathbf{T}_f) & \mathbf{T}_{s,t}^T(\mathbf{K}_p \mathbf{T}_{s,t}) + \mathbf{K}^D_s(\omega) \end{bmatrix} - \omega^2 \begin{bmatrix} \mathbf{M}_r & \mathbf{0}_{7\times 6} \\ \mathbf{0}_{6\times 7} & \mathbf{0}_{6\times 6} \end{bmatrix} \right) \begin{Bmatrix} \mathbf{U}_r \\ \mathbf{U}_s \end{Bmatrix} = \mathbf{F} \tag{4.88}$$

4.4 Validation measurements

In order to validate the monobloc sleeper model, a series of mobility measurements using an impact hammer were conducted on a pre-stressed type G44 concrete sleeper. The design of the G44 sleeper is depicted in Fig. 4.13.

The aim of these experiments is to measure the dynamic behaviour of the sleeper up to about the eighth bending mode (expected at approximately 3 kHz for vertical excitation [4]), corresponding to four and a half wavelengths. The sleeper was supported on a stack of nine elastic rail pads, at a location below the rail seat at each end. This was sufficiently soft to ensure that the resonance frequency of the rigid body mode (sleeper

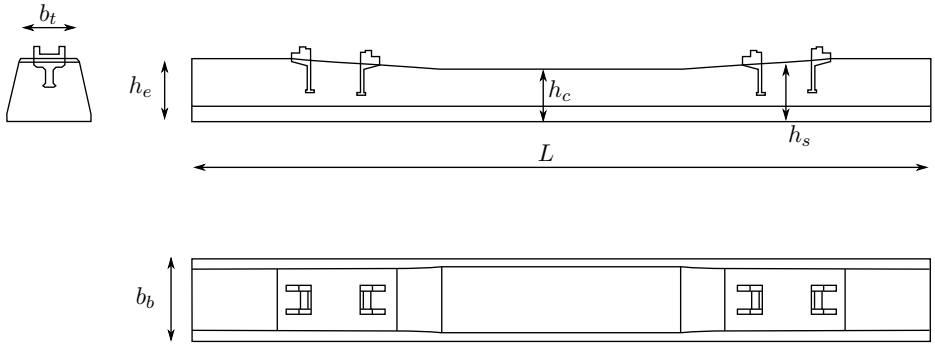

Figure 4.13: G44 sleeper design

mass on support stiffness) was well below those of the flexible modes. In this case the rigid body modes were found at 20 Hz in the vertical direction and at 3 Hz in the lateral direction.

In order to establish the displaced shape of the sleeper, a grid of six points per minimum wavelength was chosen, corresponding to a spacing of $4.5 \times 6/L \approx 11$ cm. Because of the fastening system present on the sleeper, this spacing was not possible near the locations of the rail clips, but was ensured in all other locations. A symmetric grid relative to the sleeper centre was thus selected, consisting of 25 force positions, as well as an additional force position at the sleeper end. The force positions on one half of the sleeper are listed in Table 4.4 and shown schematically on the full sleeper in Figure 4.14.

Table 4.4: Sleeper measurement locations (from sleeper end).

Point	1	2	3	4	5	6	7	8	9	10	11	12	13
Distance x (cm)	2	12	22	28	43	49	55	70	81	92	103	114	125
Separation (cm)		10	10	6	15	6	6	15	11	11	11	11	11

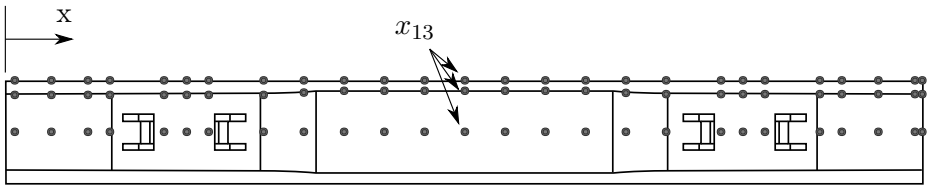

Figure 4.14: Excitation force positions along the sleeper

As shown in Fig. 4.15, four accelerometers were attached by wax at one end of the sleeper ($x = 0$)[1]. Two accelerometers were used for the vertical response (on the sleeper centre line (a) and sleeper edge (b)), one for the lateral response (at the side of the sleeper, mid-height (c)) and one for the axial response (at the centre of the sleeper cross-section (d)). The accelerometer at the sleeper edge (b) was used to obtain the vertical response including a torsional component, when the sleeper was excited at positions

[1]Note that the origin for x is set at the end of the sleeper for these measurements.

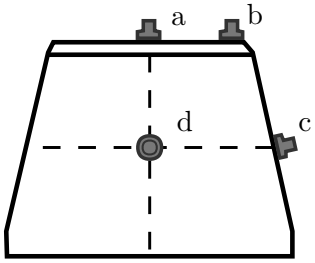

Figure 4.15: Accelerometer positions at the sleeper end

away from its centreline. The sleeper was then excited using an instrumented hammer[2] at the corresponding positions around the sleeper cross-section, at the locations along the sleeper as tabulated in Table 4.4 and shown in Fig. 4.14. The frequency response functions were obtained based on an average of 10 excitations in each case.

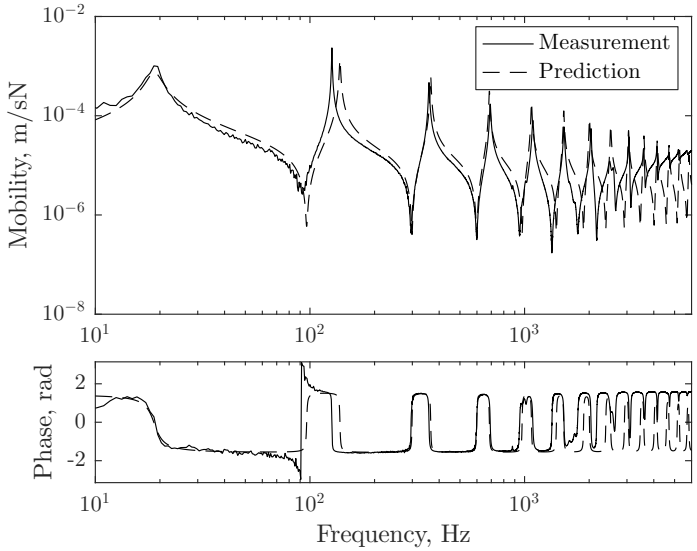

Figure 4.16: Point mobility of concrete monobloc sleeper for vertical excitation at $x = 0$, at the centreline of the sleeper upper surface.

An example of the mobility of the sleeper when excited vertically at point 1 is shown in Fig. 4.16, along with the prediction from the current sleeper model. The first peak at 20 Hz corresponds to the rigid body mode of the sleeper while the peaks at 100 Hz and above correspond to the vertical bending modes. At frequencies above 3 kHz, an overall increase in the mobility is seen in the measurements. This is attributed to the effect of local elasticity of the sleeper when the excitation point is in close proximity to the response point. This behaviour is only present for the first two excitation positions and is not seen for measurements at subsequent excitation locations.

[2]The hammer used for the experiments was a PCB Piezoelectronics instrumented hammer using a metal tip. The hammer and the accelerometers were attached through leads to a portable four-channel Data Physics analyser.

For the predicted mobility, all the geometric parameters are derived from the actual geometry of the sleeper. In the model, the elastic layer below the sleeper is continuous, here with a constant stiffness value. This mainly affects the rigid body mode of the sleeper. The only exception was the torsional constant which, due to the varying cross-section of the sleeper, was selected to provide a good fit with the measured data for the torsional response. The sleeper support stiffness was adjusted accordingly to provide a good fit to the first peak from the measured data. The mass of the sleeper was fixed at 303 kg, as well as the Poisson's ratio at 0.2. The Young's modulus was then chosen by fitting the second and third bending modes of the predicted responses to the measured ones. The fitting was performed accounting for the lateral, axial, torsional as well as vertical responses. The first mode was not considered as it is not so well predicted by the uniform beam model for this non-uniform sleeper [71]. The geometric and material parameters can be found in Table 4.5. These parameters will be used for the monobloc sleeper in subsequent chapters.

Table 4.5: Properties of G44 monobloc sleeper used in laboratory

Property	Value	Units
Young's modulus, E	57.0	GPa
Shear modulus, G	23.8	GPa
Mass (full sleeper), m	303	kg
Density, ρ	2688	kg/m^3
Length, L	2.5	m
Poisson's ratio, ν	0.2	-
Damping loss factor, η	0.0083	-
Height at centre, h_c	0.172	m
Height at rail seat, h_s	0.197	m
Breadth at centre (top), $b_{c,t}$	0.210	m
Breadth at centre (bottom), $b_{c,b}$	0.282	m
Breadth at rail seat (top), $b_{s,t}$	0.203	m
Breadth at rail seat (bottom), $b_{s,b}$	0.283	m
Second moment of area for ver. bending, $I_{p,x}$	1.27×10^{-4}	m^4
Second moment of area for lat. bending, $I_{p,y}$	2.24×10^{-4}	m^4
Polar moment of area, $I^s_{p,z}$	3.51×10^{-4}	m^4
Torsional constant, J	2.70×10^{-4}	m^4
Vertical shear coefficient, κ_y	0.83	-
Lateral shear coefficient, κ_z	0.83	-
Vertical shear centre eccentricity, e_y	0	m

The displaced shape of the sleeper at the first nine peaks is shown in Fig. 4.17 for both measured and predicted responses. This is normalised by the amplitude of the mobility at the excitation position. The frequencies listed above each plot correspond to those obtained experimentally. The predicted results are obtained at the corresponding resonance frequency. Overall, an excellent agreement is seen between the measured and predicted displaced shape for all modes presented.

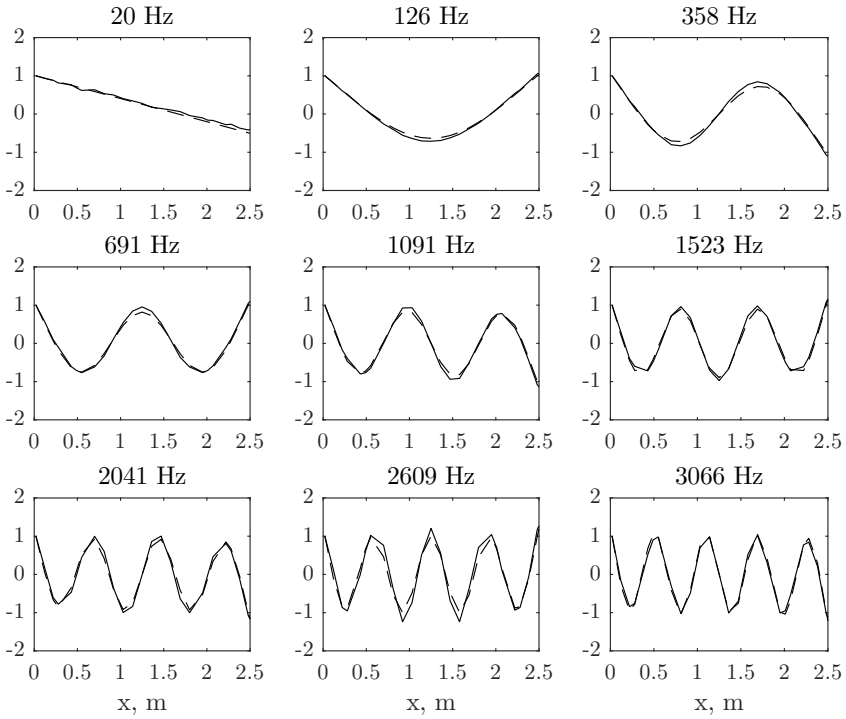

Figure 4.17: Measured (solid) and predicted (dash) vertical displaced shape at centreline versus distance along the sleeper at peaks of mobility, normalised at excitation position for a vertical force

Similar results for the lateral mobility are shown in Fig 4.18 and the lateral displaced shapes are given in Fig 4.19. Because of the sloped geometry of the sleeper sides, the actual force and response were measured at an angle to the horizontal plane. This was compensated by decomposing the measured mobility (u) into vertical (u_y) and lateral (u_z) components and removing the influence of the vertical component by using the vertical response measured with an eccentric excitation force. Thus, the lateral component was obtained as:

$$u_z = \frac{u - u_y \cos^2 \theta}{\sin^2 \theta} \tag{4.89}$$

where θ is the angle between the sleeper bottom surface and sleeper side (77.7° at point 2 from Table 4.4). A better approach would be to use a wedge to create a plane normal to the horizontal for both excitation force and accelerometer. Despite the post-processing of the response, the influence of the vertical bending modes is still seen at frequencies above 1.5 kHz. Again, local elasticity effects are seen at frequencies above 2.5 kHz where the overall mobility increases.

The vertical response of the sleeper at the edge, when it is excited vertically at the edge of its top surface, is depicted in Fig. 4.20 along with the results predicted using the model. The mobility in Fig. 4.20 strongly resembles that for vertical excitation at the centre of the sleeper cross-section (see Fig. 4.16) although additional modes are present,

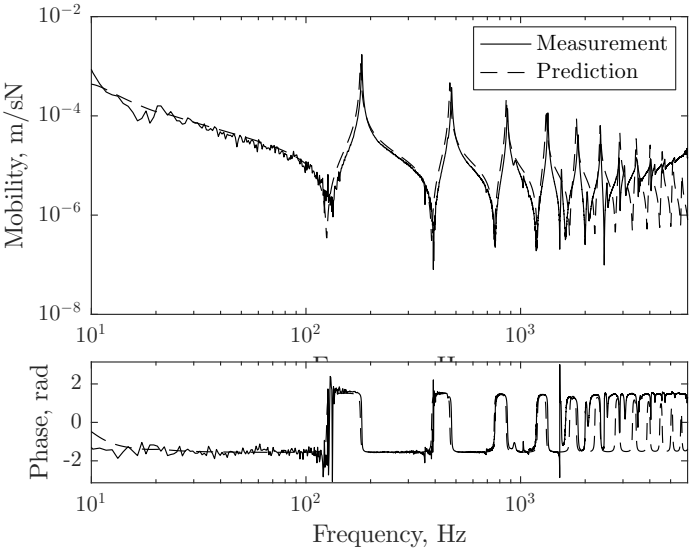

Figure 4.18: Point mobility of concrete monobloc sleeper for lateral excitation at $x = 0$, at the mid-height of the sleeper cross-section.

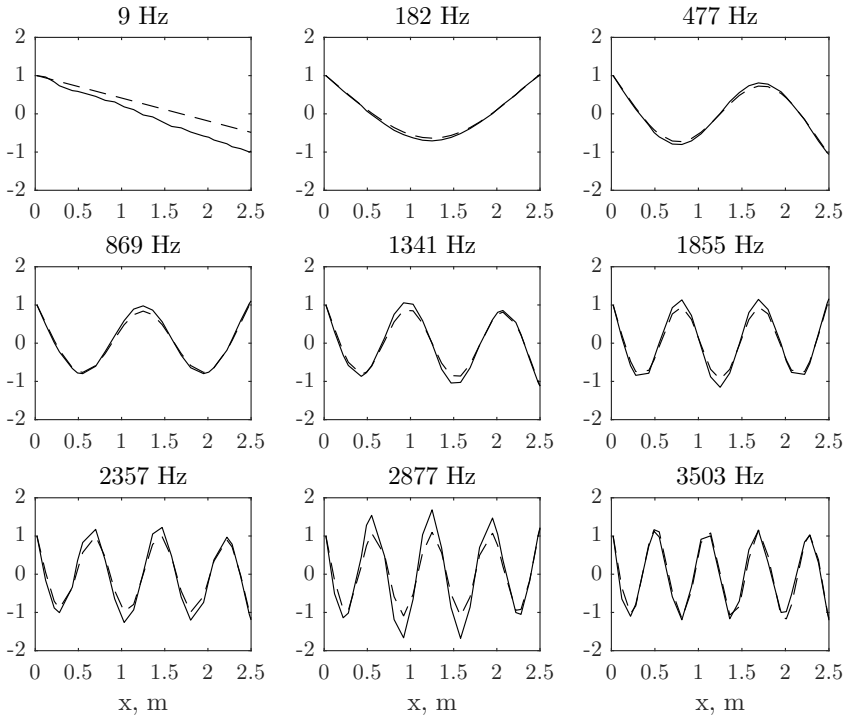

Figure 4.19: Measured (solid) and predicted (dash) lateral displaced shape for a lateral force obtained at centreline versus distance along the sleeper at peaks of mobility, normalised at excitation position

e.g. at 460 Hz. These modes correspond to the torsional modes of the sleeper, and can be seen from the displaced shape of the sleeper in Fig. 4.21. Here, the sleeper torsional constant J has been adjusted to provide a good fit for the second and third torsional modes (sixth and ninth modes in Fig. 4.21).

Finally, the axial response of the sleeper was measured by attaching an accelerometer

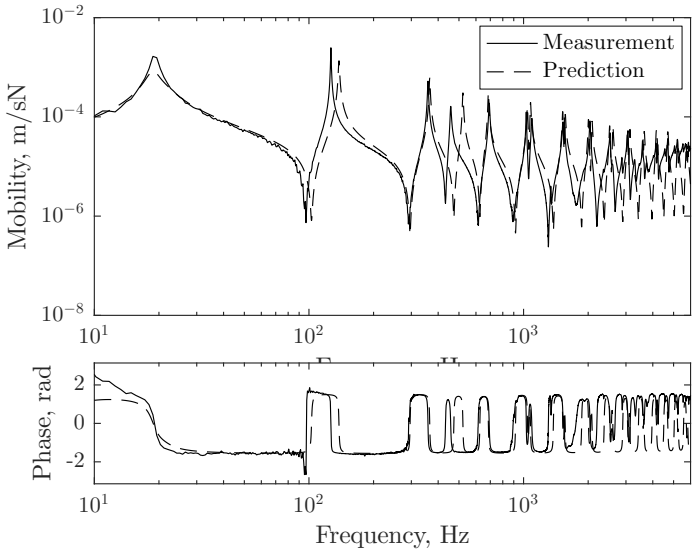

Figure 4.20: Point mobility of concrete monobloc sleeper for vertical excitation at $x = 0$, at the edge of the sleeper.

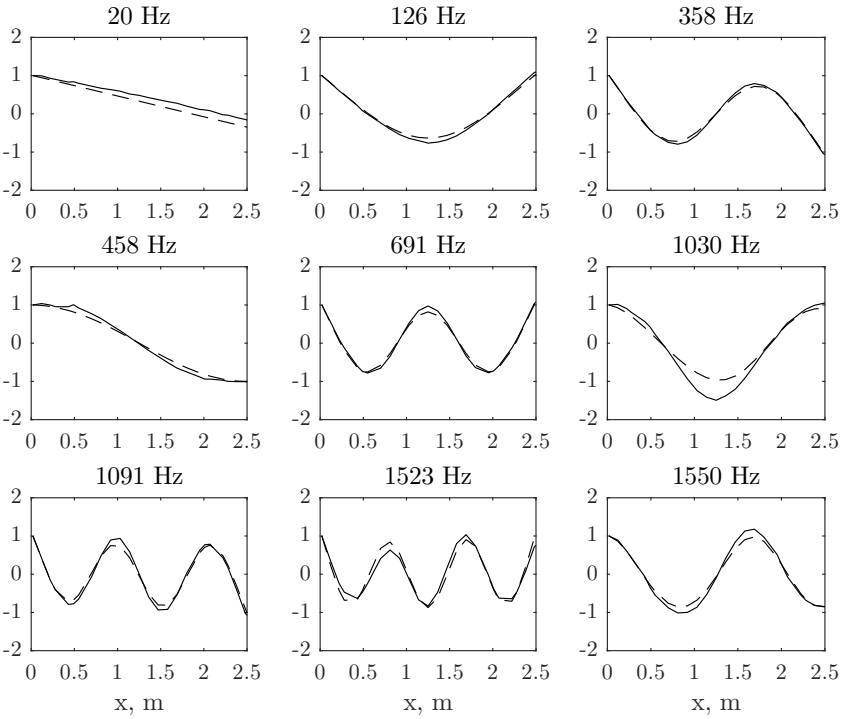

Figure 4.21: Measured (solid) and predicted (dash) vertical displaced shape for a vertical eccentric force obtained at sleeper edge versus distance along the sleeper at peaks of mobility, normalised at excitation position

at one end, at the centre of the sleeper cross-section, position (d) in Figure 4.15, and exciting the other end, again at the centre of the sleeper cross-section. These results are compared with the model in Fig. 4.22. Excellent agreement is shown over the entire frequency range, with only the frequency of the first bending mode being slightly over-predicted by the uniform beam model.

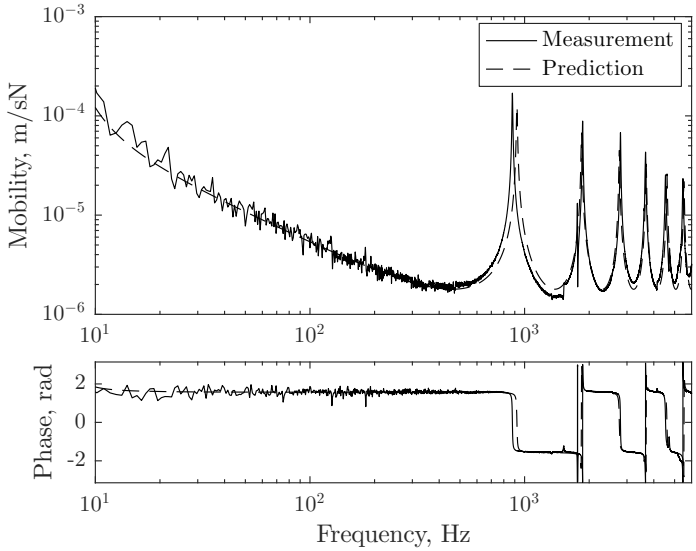

Figure 4.22: Transfer mobility of concrete monobloc sleeper for axial excitation, at the centre of the sleeper cross-section.

Overall, the model is seen to predict the modes of the sleeper well up to about 3 kHz for the vertical and lateral response, and up to about 2 kHz for the torsional response. The average error in the predicted modal frequencies is about 2% for the vertical modes, 1% for the lateral modes and 5% for the torsional modes. The difference falls to about 1% for all directions when the first vibration mode is not considered. Tables 4.6 and 4.7 list the natural frequencies of the rigid body and flexible vibration modes, up to the seventh mode, obtained from the vertical/axial and lateral/torsional responses respectively. Also the modal damping loss factor (η_{exp}) is shown based on the experiments. This has been derived by the circle fitting method, as described by Ewins [118].

Table 4.6: Measured and predicted natural frequencies for vertical and axial modes

Mode	Vertical				Axial			
#	Expt	Pred	% Diff	η_{exp}	Expt	Pred	% Diff	η_{exp}
0	18.75	18.83	-0.43	0.0990	7.81	7.70	1.45	0.0471
1	126.6	137.9	-8.99	0.0050	877.3	919.3	-4.79	0.0068
2	358.6	365.7	-1.97	0.0085	1864	1843	1.11	0.0057
3	691.4	686.2	0.75	0.0106	2798	2765	1.16	0.0057
4	1093	1078	1.40	0.0129	3662	3679	-0.48	0.0076
5	1526	1522	0.22	0.0102	4537	4611	-1.65	0.0091
6	2038	2007	1.53	0.0082	5469	5519	-0.92	0.0083
7	2489	2519	-1.20	-	6280	6455	-2.79	0.0064

Table 4.7: Measured and predicted natural frequencies for lateral and torsional modes

Mode	Lateral				Torsional			
#	Expt	Pred	% Diff	η_{exp}	Expt	Pred	% Diff	η_{exp}
0	9.38	9.32	0.57	0.0630	-	-	-	-
1	182.0	179.4	1.47	0.0051	457.8	522.1	-14.05	0.0114
2	477.3	468.2	1.91	0.0077	1030	1042	-1.20	0.0061
3	868.8	858.7	1.16	0.0087	-	-	-	-
4	1341	1318	1.70	0.0061	-	-	-	-
5	1852	1819	1.75	0.0105	-	-	-	-
6	2359	2351	0.36	0.0062	-	-	-	-
7	2874	2901	-0.94	0.0076	-	-	-	-

4.5 Effect of fatigue on sleeper properties

Apart from the sleeper tested for the validation of the monobloc sleeper model, an additional G44 sleeper was tested, which had been extensively used in the laboratory for long term cyclic ballast loading experiments. In these the sleeper was located in ballast and a cyclic load from 5 kN to 100 kN was applied over the two rails. Approximatelly 30 to 50 million cycles had been applied altogether. Despite some minor geometric differences, the sleeper was visually identical to the newer sleeper (used for the measurements in the previous section). For the old sleeper, only the vertical mobility was measured, using the same excitation positions as listed in Table 4.4. Figure 4.23 shows the mobility

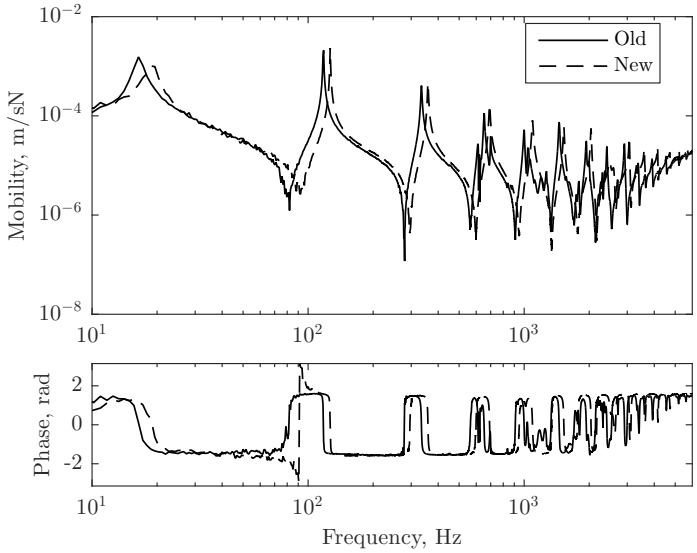

Figure 4.23: Comparison of point mobility of new and old concrete monobloc sleepers for vertical excitation at $x = 0$

for excitation at the first location for both sleepers. As can be seen, there is an overall reduction of the bending mode frequencies, which is on average about 5.7% (ignoring the rigid body mode). Since the modal frequencies depend on the square root of the Young's modulus, this reduction corresponds to a reduction of approximately 11% in Young's

modulus. The same conclusion is drawn by fitting the model to the measured data for the old sleeper, where a Young's modulus of 51 GPa provides the best fit, instead of 57 GPa for the newer sleeper. This reduction is likely to be either due to small cracks appearing in the sleeper, or due to de-bonding of the reinforcement from the concrete. The damping is not significantly affected. In order to determine the effect of fatigue on the bending behaviour of the sleeper, further investigation would be required in order to assess the effects of prolonged service of a sleeper on its dynamic behaviour.

4.6 Equivalent bibloc model

To provide a means of comparing the bibloc and monobloc sleeper models, the equivalence between the properties of the two is sought. Thompson [4], by comparing point mobilities, found that a single block with the mass of half a monobloc sleeper, had a similar mobility at low frequencies to a flexible monobloc sleeper of length $L = 2.5$ m when excited at $x_0 = 0.5$ m from the sleeper end. Here, a more rigorous approach is investigated.

A uniform monobloc sleeper of length L, mass m and rotational inertia I is considered, as in Fig. 4.24, resting on an elastic support (representing the ballast) of stiffness per unit length k. The flexibility of the sleeper is ignored for this derivation. The sleeper is excited by a point force F at a distance $x_c = L/2 - x_0$ from the centre of mass. This system can represent the monobloc sleeper in either the vertical or lateral directions.

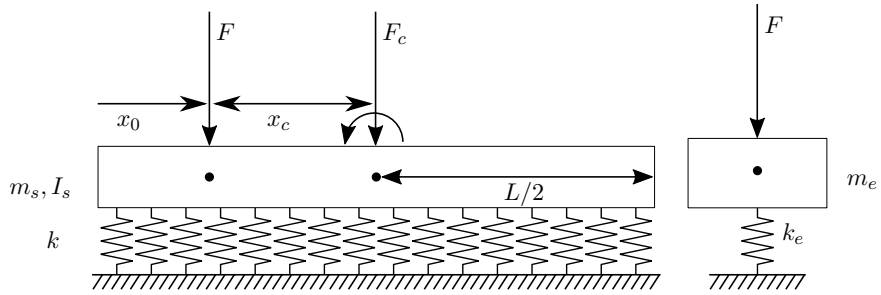

Figure 4.24: Monobloc and equivalent bibloc sleepers

The point force F at x_c can be equated to a force and a moment acting at the centroid as:

$$F_c = F \tag{4.90}$$

$$M_c = -x_c F \tag{4.91}$$

Now, the equations of motion for this system expressed at the centroid are:

$$ku_c + m\ddot{u}_c = F_c \tag{4.92}$$

$$k_r\theta_c + I\ddot{\theta}_c = M_c \tag{4.93}$$

where

$$k_r = \frac{kL^2}{12} \tag{4.94}$$

$$I = \frac{mL^2}{12} \tag{4.95}$$

Assuming a harmonic response in time, the equations of motion take the form:

$$\left(k - m\omega^2\right) U_c = F_c \tag{4.96}$$

$$\left(k_r - I\omega^2\right) \Theta_c = M_c \tag{4.97}$$

where U_c and Θ_c are the complex amplitudes for translation and rotation respectively. By utilising Eqs (4.94) and (4.95) this leads to:

$$\left(k - m\omega^2\right) U_c = F \tag{4.98}$$

$$\frac{\left(k - m\omega^2\right) L^2}{12}\Theta_c = -x_c F \tag{4.99}$$

Similarly, the equation of motion can be written in terms of the forces and responses at location x_c. For this, an equivalent system of a single mass (m_e) on an elastic foundation (k_e) is considered at that location, and the equation of motion is written as:

$$\left(k_e - m_e\omega^2\right) U_y = F \tag{4.100}$$

The displacement at x_c is a function of the displacement as well as the rotation at the centroid (i.e. $x_c = 0$), in the form:

$$U_y = U_c - x_c\Theta_c \tag{4.101}$$

Thus Eq. (4.100) becomes:

$$\left(k_e - m_e\omega^2\right)\left(U_c - x_c\Theta_c\right) = F \tag{4.102}$$

Now the displacement and rotation of the centroid can be substituted from Eqs (4.98) and (4.99) to give:

$$\left(k_e - m_e\omega^2\right)\left(\frac{F}{k - m\omega^2} - x_c\frac{-12x_cF}{\left(k - m\omega^2\right)L^2}\right) = F \tag{4.103}$$

From the last equation the force F can be cancelled, and by rearranging, this gives:

$$k_e - m_e\omega^2 = \frac{1}{f_a}\left(k - m\omega^2\right) \tag{4.104}$$

where

$$f_a = 1 + \frac{12x_c^2}{L^2} \tag{4.105}$$

Thus, the dynamic stiffness of the equivalent system depends on the dynamic stiffness at the centroid of the monobloc sleeper, divided by a factor dependent on the length of the sleeper and the point of application of the load. This indicates that the dynamic stiffness depends on the offset of the excitation point from the sleeper midpoint. For $x_c = L/2$, it is 4 times smaller, while for the railseat, where $L = 2.5$ m and $x_c = 1$ m ($=2L/5$), the dynamic stiffness is $f_a = 2.08$ times smaller. These results justify the use of a rigid sleeper with mass equal to that of half the monobloc sleeper when an equivalent model of the flexible sleeper excited approximately at the position of the rails is used [4].

The equivalent mass and stiffness should be used for the bibloc sleeper mainly for the case of vertical and lateral sleeper excitation (where half the mass is used i.e. a factor of $f_a \approx 2$). In the case of axial sleeper excitation, the offset of the load is very small in comparison with the sleeper length, and the whole mass is required (i.e. $f_a \approx 1$). One limitation of the use of this approach is the neglect of the flexibility of the monobloc sleeper.

Figure 4.25 shows the mobility obtained from the monobloc and bibloc sleeper models for the lateral, vertical and axial directions, for when the monobloc sleeper is supported at the centroid ($y_{sb} = 0$) and when it is supported at the bottom. No foundation eccentricity is considered for the bibloc sleeper in this comparison. The same properties as for the G44 sleeper are used here, as tabulated in Table 4.5. For both sleeper models, the ballast stiffness is kept constant (i.e. no dynamic ballast stiffness is considered).

In the mobility for the bibloc sleeper model, a single peak exists corresponding to the resonance of the mass on the foundation stiffness. In contrast, for the monobloc sleeper model a series of peaks are seen. The lowest of the peaks is that of the bounce mode of the sleeper mass on the foundation stiffness, while subsequent peaks correspond to vibration modes of the sleeper.

Of the three directions, only the lateral response of the monobloc sleeper model is influenced by the foundation eccentricity, where the peak in the mobility is reduced in frequency by 40%, from about 200 Hz in Fig. 4.25(a) to 120 Hz in Fig. 4.25(b). This is due to the coupling between the lateral and torsion responses, as shown earlier for the eccentrically supported rail in Section 3.6. Figs 4.25(c)–(f) show no noticeable differences.

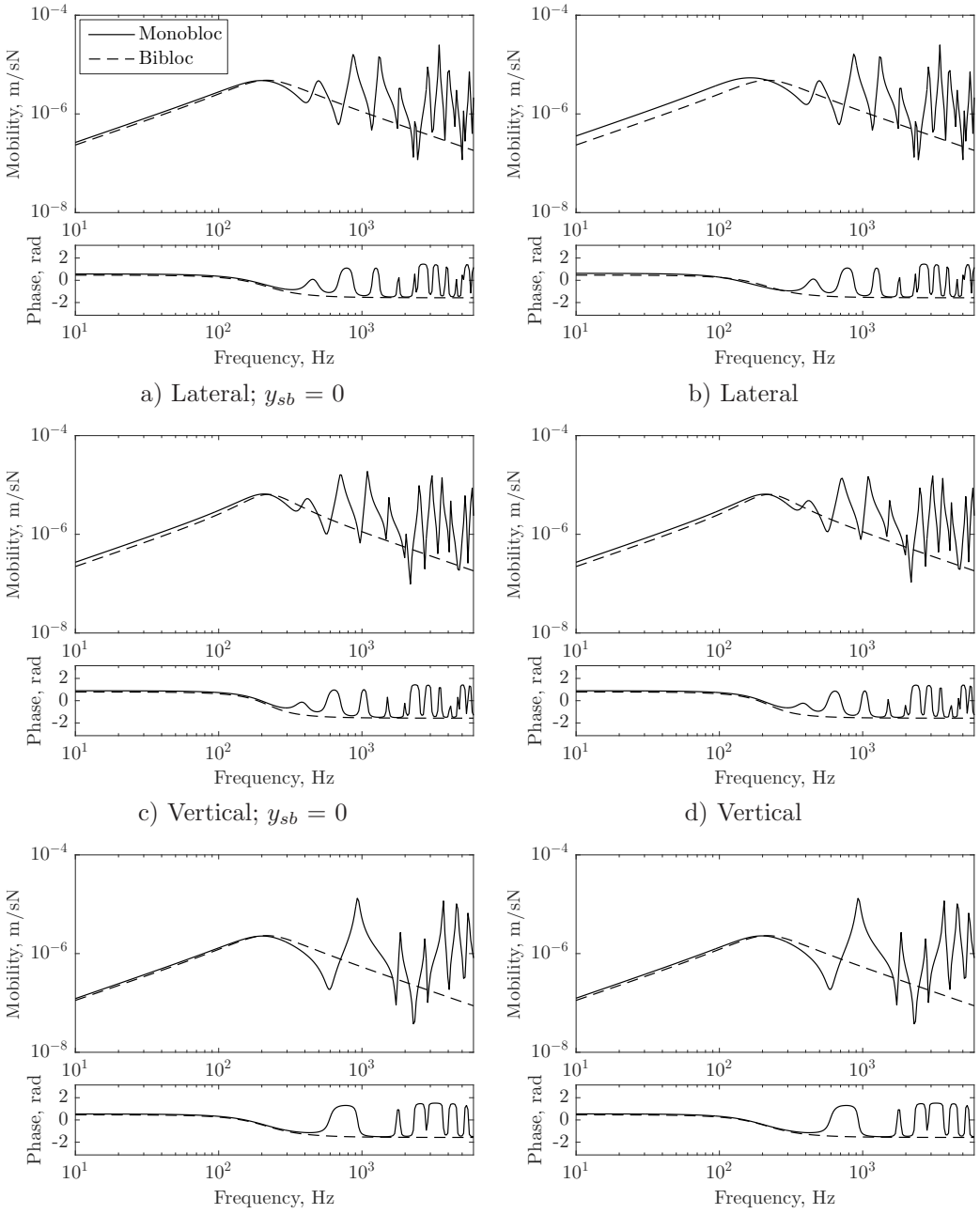

a) Lateral; $y_{sb} = 0$ b) Lateral

c) Vertical; $y_{sb} = 0$ d) Vertical

e) Axial; $y_{sb} = 0$ f) Axial

Figure 4.25: Point mobility of concrete sleeper using monobloc and bibloc sleeper models; supported at the centroid and sleeper bottom surface

4.6.1 Frequency dependent ballast stiffness

Measurements performed by Frémion et al. [74] have shown that the ballast stiffness can be frequency dependent. This has been approximated by Thompson [4] as shown in Fig. 4.26. A nominal value for the ballast stiffness is used up to 100 Hz. Above 100 Hz, the ballast stiffness increases with frequency. Figure 4.26 shows the frequency-dependent

ballast stiffness used for the comparison. For the ballast damping, a constant loss factor is assumed.

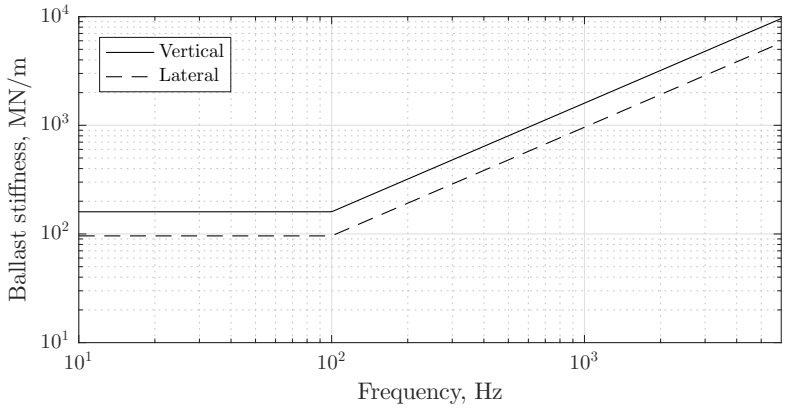

Figure 4.26: Frequency-dependent ballast stiffness assumed per sleeper end [4]

Results for the vertical point mobility at the rail seat for a G44 monobloc sleeper are shown in Fig. 4.27. At frequencies up to 100 Hz, where the two ballast models provide the same support stiffness, the point mobility is the same. Above 100 Hz, two main differences are seen. Firstly, since the support stiffness increases for the frequency dependent ballast model, the resonance frequencies of the sleeper embedded in the frequency dependent ballast stiffness increase. This is mainly seen to influence the rigid body mode, where the resonance frequency increases from 200 Hz to 245 Hz, and the first few bending modes. Additionally, the peaks and troughs are attenuated when using the frequency dependent ballast stiffness.

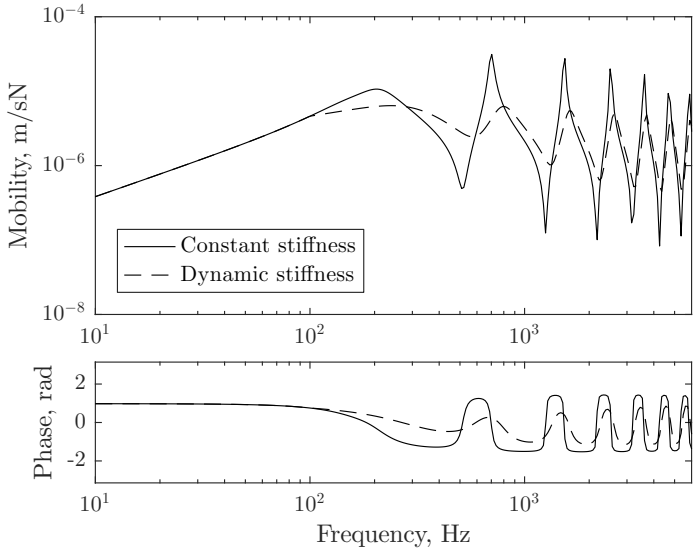

Figure 4.27: Point mobility at the rail seat for a G44 monobloc sleeper embedded in constant and frequency dependent ballast

In the next chapter, the flexible sleeper will be used with the frequency dependent ballast stiffness described above.

4.7 Conclusions

In this chapter, the inclusion of a second layer of elastic support beneath the rail has been investigated. Models have been presented for rigid and flexible sleepers. For the rigid sleepers, investigations have been performed on the cut-on frequencies identified in the dispersion relationship, as well as the effect of varying the ballast stiffness. For modelling flexible monobloc sleepers, a new model has been introduced that accounts not only for the vertical bending of the sleeper, but also for lateral, axial and torsional flexibility. Validation of this sleeper model has been performed against results obtained from laboratory measurements on a type G44 monobloc sleeper. By choosing suitable material properties the natural frequencies of the sleeper modes are well predicted, with an average error of only 1% for all cases considered, excluding the first mode. This mode is most influenced by the sleeper cross-section variation which is not directly accounted for in the model.

The effect of fatigue on the sleeper response has been investigated, by testing a heavily used sleeper. From a comparison of measured vertical mobilities, a reduction of 11% in Young's modulus is observed for the old sleeper, indicating that the service usage of a sleeper can significantly alter its dynamic behaviour.

Finally, an equivalent bibloc sleeper model was compared with the asymmetrically loaded monobloc sleeper and a stiffness conversion factor has been derived depending on the length of the sleeper and the location of application of the force.

In the next chapter, results for the rail mobility and track decay rate will be presented, in order to investigate further the influence of the vertical-lateral coupling on the overall track response. The validation of the forced response of a rail supported on a single layer foundation will be performed against the WFE model and comparisons for the double-layer support will be made with measurements from three different track sites.

Chapter 5

Mobility and decay rates

In Chapter 3 the frequency/wavenumber (dispersion) relation for the rail was found by solving the eigenvalue problem of Eq. (2.84). Additionally the effect of an elastic support on the dispersion relationship of a rail was investigated, while a two-layer support was considered in Chapter 4. In this chapter, the roots of the eigenvalue problem are utilised in determining a closed form solution for the forced response of the track. The forced response based on the present beam model is validated against the WFE model and also compared against the classical Timoshenko beam model. Finally, the model is compared with measurements from three different track sites, in order to test its applicability and extract the track parameters to be used for rolling noise predictions in Chapter 6.

5.1 Closed-form solution for the forced response

For a given frequency and wavenumber, Eq. (2.83) can be solved for the complex amplitudes, to give:

$$\tilde{\mathbf{U}} = \mathbf{A}^{-1}\tilde{\mathbf{F}} \tag{5.1}$$

where $\tilde{\mathbf{U}}$ is a vector of the complex amplitudes, $\tilde{\mathbf{F}}$ is a vector of the externally applied forces and $\mathbf{A}$ is the dynamic stiffness matrix. To find the response in the spatial domain $\mathbf{U}(x)$, the inverse Fourier transform is utilised:

$$\mathbf{U}(x) = \frac{1}{2\pi}\int_{-\infty}^{\infty} \mathbf{A}^{-1}\tilde{\mathbf{F}}e^{-i\xi x}d\xi \tag{5.2}$$

The above integration can be performed either numerically or analytically. Here, the latter is preferred, using the contour integration method from the theory of complex variables [119]. The integration of a function (here $f(\xi)e^{-i\xi x}$) along the real axis from $\xi_a \to -\infty$ to $\xi_b \to \infty$, is equivalent to the closed path integration along the real axis

from ξ_a to ξ_b plus the integration along the lower semicircle from ξ_b to ξ_a, provided that the integration along the semicircle tends zero. This is satisfied for $x \geq 0$, while for $x \leq 0$ the upper semicircle needs to be used instead.

Then the residue theorem is utilised. This states that the integral along any closed path on the complex plane is equal to the sum of the residues evaluated at the poles of the function contained within the path multiplied by a factor of $\pm 2\pi i$ ($+/-$ depending on whether the path encircles the poles in the anti-clockwise or clockwise direction). The poles of the function (ξ_n) are the same as the solutions for the eigenvalues obtained in Chapter 3. Thus the solution in the spatial domain is given for $x \geq 0$ as (see also [69]):

$$\mathbf{U}(x) = i \sum_{n=1}^{N} \frac{\boldsymbol{\Psi}_n^L \tilde{\mathbf{F}}}{\boldsymbol{\Psi}_n^L \mathbf{A}'(\xi_n) \boldsymbol{\Psi}_n^R} \boldsymbol{\Psi}_n^R e^{-i\xi_n x} \tag{5.3}$$

where $\boldsymbol{\Psi}_n^L$ and $\boldsymbol{\Psi}_n^R$ are the left and right eigenvectors of the eigenvalue problem in Eq. (2.85), the dash ($'$) indicates the derivative with respect to ξ and ξ_n are the N eigenvalues on the lower half-plane with Im(ξ_n)<0. From Eq. (2.84) the derivative can be written as:

$$\mathbf{A}'(\xi_n) = -i\mathbf{K_1} - 2\xi_n \mathbf{K_2} \tag{5.4}$$

Finally, if the force vector is set to unity in one direction and zero in the others, the mobility can be calculated as:

$$\mathbf{V} = i\omega \mathbf{U} \tag{5.5}$$

In the model described so far, damping has not been considered apart from the monobloc sleeper material damping. In practice, damping is present in both the support and the rail. In order to include this, the rail pad support stiffnesses and the rail moduli properties (E and G) are made complex by introducing damping loss factors, in the same way as for the monobloc sleeper. As discussed in Section 1.1, the material loss factor of the rail is also adjusted to take account of the foundation damping effect due to larger amplitude vibration of the foot at higher frequencies, in addition to the material damping. Thus, the elastic modulus of the rail E is replaced by $E(1 + i\eta_r)$. Similarly the support stiffness of the various layers, separately in each direction are made complex in the form $k(1+i\eta)$. Table 5.1 shows the values for the damping loss factors considered here for the rail, rail pads and ballast. Unless stated otherwise, a single layer support is considered in this section, with stiffness and damping loss factor values as tabulated in Tables 3.2 and 5.1 respectively.

Table 5.1: Damping loss factors for rail, rail pad and ballast.

Loss factor	Value
Rail, η_r	0.02
Rail pad (axial), $\eta_{p,a}$	0.2
Rail pad (vertical), $\eta_{p,v}$	0.25
Rail pad (lateral), $\eta_{p,l}$	0.2
Ballast (axial), $\eta_{b,a}$	1
Ballast (vertical), $\eta_{b,v}$	2
Ballast (lateral), $\eta_{b,l}$	1

5.2 Mobility and decay rate for Vignole rail - 60E1

In this section, the forced response for a 60E1 rail is presented. Results are firstly shown for the point mobility per wave in the vertical and lateral directions. The point mobility in all three principal axes is then investigated, followed by the cross mobility in the y-z plane as well as the track decay rates (obtained from the transfer mobility in the longitudinal direction). The locations considered for the forced response of the 60E1 rail are shown in Fig. 5.1.

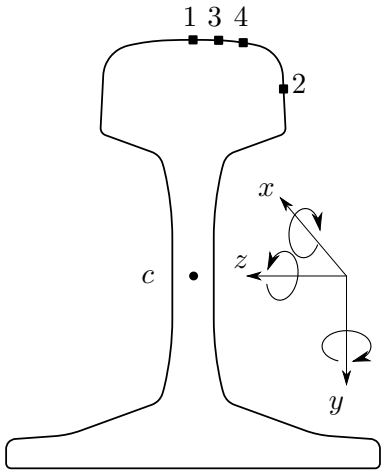

Figure 5.1: Excitation and response positions for 60E1 rail

5.2.1 Point mobility per wave

In Fig. 5.2, the point mobility using the developed beam model is presented for the vertical and lateral direction, for a rail supported on a single layer foundation. The excitation locations correspond to positions 1 and 2 of Fig. 5.1. Along with the overall point mobility, the point mobilities per wave are also shown. For the vertical direction, Fig. 5.2(a), two waves control the response, namely vertical wave types i and Ve, with the axial wave type iii having a marginal response (not shown in figure but seen through the phase). At the cut-on of the rail mass on the vertical pad stiffness (wave type i)

around 290 Hz (see Section 3.6.2), the relative contribution of wave type Ve starts to reduce significantly, and the response is dominated by the now propagating wave type i.

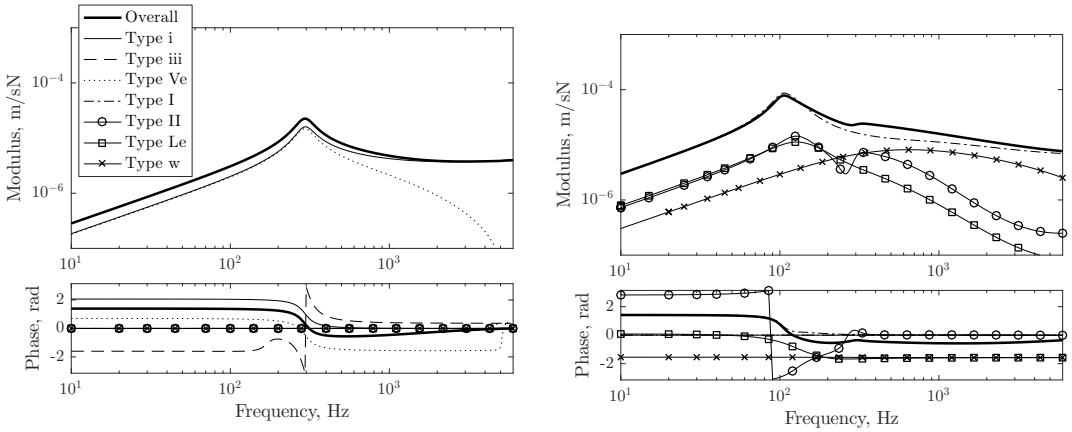

a) Vertical at Pos. 1

b) Lateral at Pos. 2

Figure 5.2: Point mobility per wave for 60E1 rail

In Fig. 5.2(b), where the lateral point mobility is presented, all four lateral waves are present. At all frequencies, the response is dominated by the lateral wave type I. A main peak is seen at around 105 Hz, corresponding to the cut on of vertical wave type I. A secondary peak is seen at around 300 Hz corresponding to the cut-on of wave type II (see Section 3.6.2). It is interesting to note here, that the warping wave type w has a higher contribution above 200 Hz than that of wave types II and Le. Wave types II and Le have similar response up to about 300 Hz, that is the cut-on of wave type II, after which the relative contribution of wave type Le is reduced.

5.2.2 Point and cross mobility

Figure 5.3 shows the point mobility of the 60E1 rail on a single layer elastic foundation, excited at various positions. Three different results are shown here in each case: from the current beam model presented above, the WFE model used for the dispersion relationship in Section 3.4.3 and the classical Timoshenko beam model. Figures 5.3(a) and 5.3(b) show the vertical and lateral mobility, excited at positions 1 and 2 respectively from Fig. 5.1. Two additional locations have also been selected, which are 20 mm from the web centreline for the vertical excitation (position 4) and at the top of the rail head for the lateral excitation (position 1 but force applied laterally). These results are shown in Figs 5.3(c) and 5.3(d) respectively.

For the vertical direction, Fig. 5.3(a), the current beam model shows excellent agreement with the WFE model for frequencies up to about 4 kHz. Above this frequency, cross-sectional deformation starts to become important and to influence the response of the rail. Two peaks occur in Fig. 5.3(a). The first occurs at the cut-on frequency of the vertical bending wave, $f_{co,v}$ at about 290 Hz (cf. Eq. (3.23)). The second is seen for

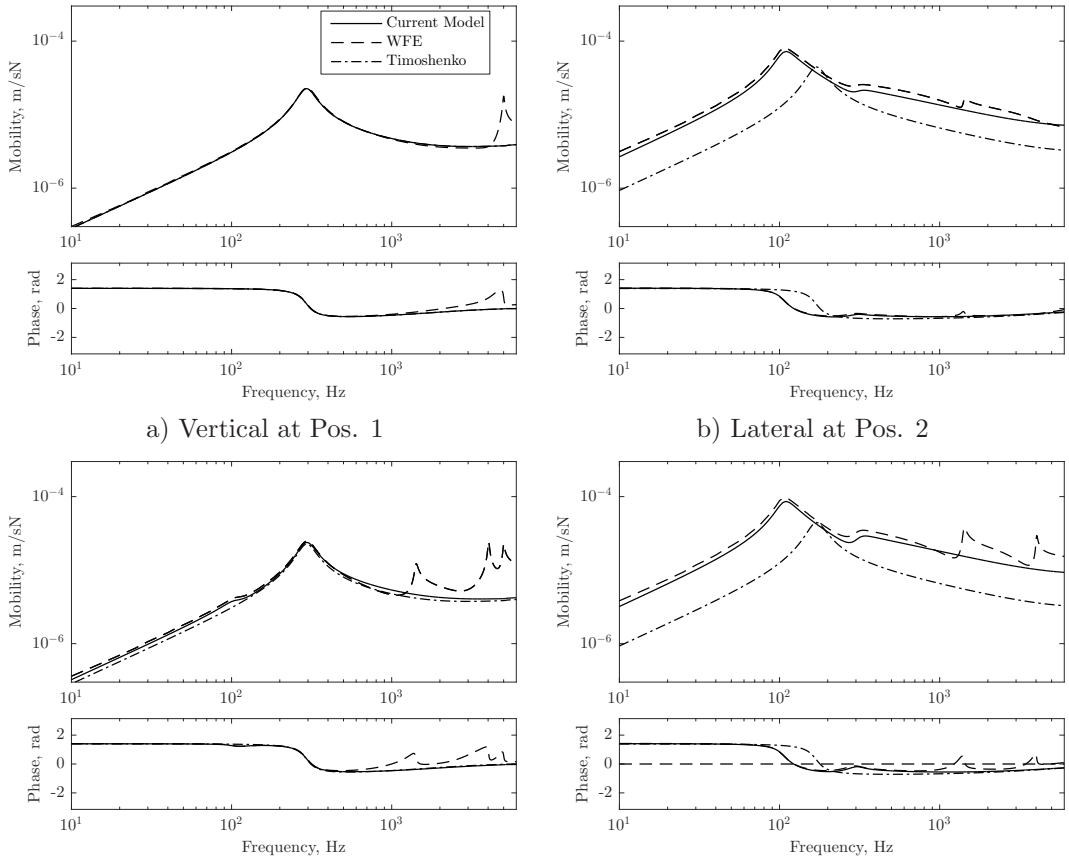

a) Vertical at Pos. 1

b) Lateral at Pos. 2

c) Vertical at Pos. 4

d) Lateral at Pos. 1

Figure 5.3: Point mobility for 60E1 rail

the WFE model only, at about 5 kHz. This corresponds to the cut-on frequency of the higher order vertical wave (type ii - foot flapping) see Fig. 3.4, which is not present for the current beam models. Comparing the developed beam model with the simpler Timoshenko one, no differences are seen in the vertical mobility at the centre of the railhead.

For the lateral direction, Fig. 5.3(b), the agreement between the present beam model and the WFE model is again good at all frequencies. Two peaks can be identified at low frequency, one at about 100 Hz, corresponding to the cut-on of wave type I and the other at about 300 Hz corresponding to wave type II (see Section 5.2.1). A third peak is seen in the results from the WFE model at about 1.4 kHz, corresponding to the cut-on frequency of the higher order lateral wave (type III - web bending). The average difference between the beam and WFE models is 14%. Significant differences are seen between the mobility of the present model and that of the classical Timoshenko beam model, which is on average a factor of 2 smaller. The cut-on frequency for the first lateral wave is seen in the Timoshenko beam model at $f_{co,l} = 167$ Hz, while that of the second lateral wave is not present, as torsion is neglected. The differences between the two analytical models are caused by two main effects. The first is related to the

foundation eccentricity. This causes the cut-on frequency of the lateral wave type I to reduce, thus shifting the peak in the mobility from 169 Hz to 103 Hz. The second is related to the inclusion of torsion in the beam model, since the rail is excited with an offset from the shear centre. Without torsion, the mobility is significantly lower over the whole frequency range. Even if the cut-on frequency for the Timoshenko beam in lateral bending is adjusted to 103 Hz (by setting $k_z^p = 15.2$ MN/m), the average difference in mobility between the models remains the same.

Figure 5.3(c) shows the results when an eccentric load is considered in the vertical direction. Apart from the peaks at the two vertical wave cut-on frequencies, three additional peaks are seen in the results from the WFE model, corresponding to the cut-on of lateral waves at 100 Hz, 1.4 kHz and 4 kHz (see Fig. 3.4). Of these, only the first is present in the results from the analytical model. At all frequencies, the mobility of the current beam model is slightly higher than that of the Timoshenko beam, with an average difference of 10%.

Figure 5.3(d) shows the lateral mobility at the top of the rail head. Compared with Fig. 5.3(b) it can be seen that the lateral mobility is higher than at the centre of the rail head. At high frequencies the higher order lateral waves lead to an increase in the WFE modelmobility by 60% on average above 1.4 kHz, compared with the centre of the rail head (see also [20]). At lower frequencies the difference between the mobility of the current beam model and that of the WFE model remains at about 10%.

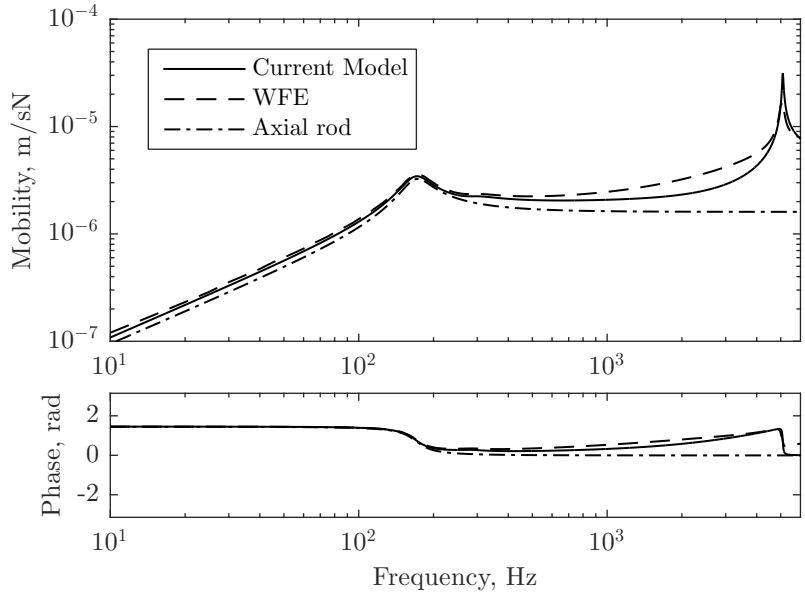

Figure 5.4: Axial mobility for 60E1 rail

Figure 5.4 shows the axial mobility of the rail when excited at position 1 from Fig. 5.1(a). For comparison, an axial rod model is shown as well as the current beam model and WFE model. For all three models, a peak is seen at about 170 Hz, corresponding to the cut-on of the first-order longitudinal wave (type iii), as seen from Fig. 3.4. A further

distinct peak is seen in the WFE results and those from the current model at about 5 kHz, corresponding to the cut-on of wave type iv. The agreement is good over the whole frequency range presented (from 10 Hz to 5 kHz).

5.2.3 Cross mobility

Figure 5.5 depicts the cross mobility: the lateral response at position 2 due to a vertical force for an offset of 10 mm and 20 mm (positions 3 and 4 respectively of Fig. 5.1). The cross receptance for the Timoshenko beam model is based on the geometrical average of the vertical (U_y) and lateral (U_z) receptances [62]:

$$U_{yz} = 10^{XdB/20}\sqrt{U_y U_z} \tag{5.6}$$

where $XdB = 20\log_{10}X$ is an empirical factor used in TWINS that is typically set around -10 dB. In order to obtain a suitable factor, calculations have been performed with the Timoshenko beam model for a range of values and the one providing the best fit with the beam model was selected. This is -14 dB for an offset of 10 mm (Fig. 5.5(a)) and -8 dB for an offset of 20 mm (Fig. 5.5(b)). Additionally, in the Timoshenko beam model, the lateral pad stiffness has been reduced to 15.2 MN/m to match the cut-on frequency of wave type I.

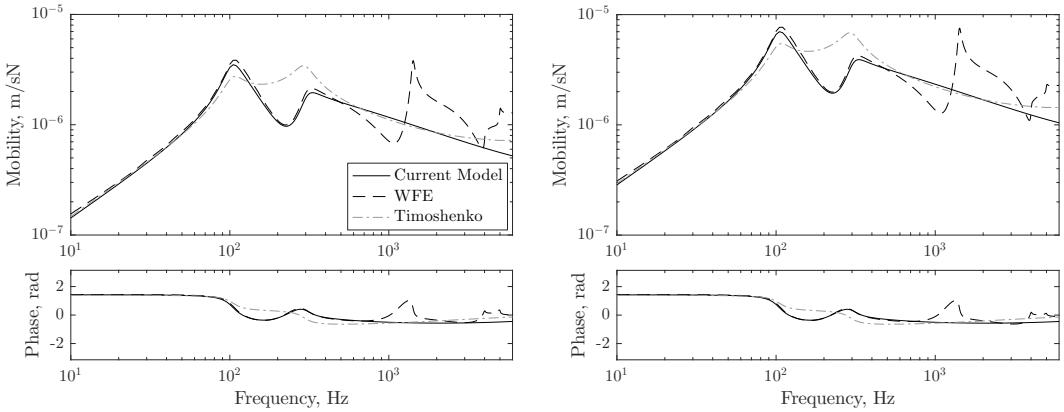

a) Position 3 (XdB = -14 dB) b) Position 4 (XdB = -8 dB)

Figure 5.5: Cross mobility for 60E1 rail

In both cases, the current beam model shows good agreement with the WFE model for frequencies up to about 1 kHz. Above this frequency, cross-sectional deformation, especially for an offset of 20 mm, starts to become important and to influence the response of the rail. The empirical relationship does not capture the drop in the mobility between 100 and 300 Hz but otherwise gives similar results to the present model. However it relies on the selection of a suitable value for the factor XdB whereas the offset in the present model is a more intuitive physical quantity.

5.2.4 Decay rate and transfer mobilities

Here, results are presented for the track decay rate and transfer mobility along the rail, calculated from the forced response. Results for both vertical and lateral excitations are presented for a rail on a single layer elastic foundation accounting for the rail pads, properties of which are listed in Table 3.2 and Table 5.1.

The track decay rate can be obtained by two different methods. The first is by considering the imaginary part of the damped wavenumbers from the dispersion relationship [20]. This results in a decay rate for each wave. The second is to calculate the total response at different positions along the rail (transfer mobility) and to obtain the decay rate following the experimental method [120, 121], thus obtaining the decay rate accounting for the combined response due to all wave types.

The decay rates (in dB/m) for each wave are obtained using the relationship [20]:

$$\Delta_{pw} = -8.686 \ \mathrm{Im}(\xi) \tag{5.7}$$

These are shown in Figure 5.6 for the vertical, axial and lateral waves. It is seen that the axial wave, type iii, has the lowest decay rate. For each of the propagating waves, types I, II, i and iii, the decay rate drops from an initially high value at around the cut-on frequency of the respective wave [4]. This also occurs for the higher order shear wave type Ve which becomes type iv at around 5 kHz. Finally, the wave type w consists of a predominantly warping motion of the cross-section. This wave has a high decay rate for all frequencies considered and is thus not expected to influence the response significantly away from the excitation point, although, it has a high contribution in the point mobility at high frequencies as seen in Section 5.2.1.

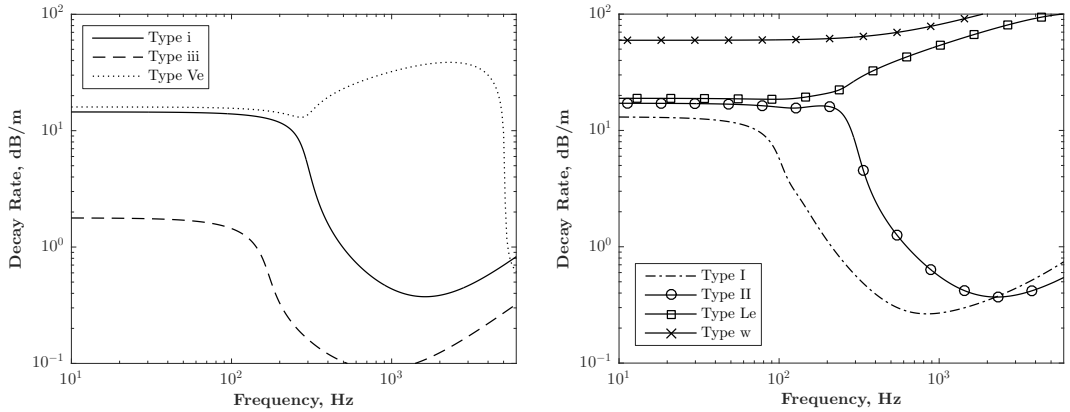

a) Vertical and axial waves

b) Lateral waves

Figure 5.6: Decay rates for each wave (a) vertical and axial waves; (b) lateral waves

The overall decay rate in each one-third octave band is evaluated from predicted transfer mobilities according to the experimental method found in the standards [120]:

$$\Delta = \frac{4.343}{\sum_{x_n=0}^{x_{max}} \frac{|A(x_n)|^2}{|A(x_0)|^2}\delta x_n} \tag{5.8}$$

where $A(x_n)$ is the calculated mobility at a distance x_n away from the excitation point, $A(x_0)$ is the mobility at the excitation point and δx_n is the length of rail segment associated with the point x_n. The calculation is carried out in one-third octave frequency bands, while the locations x_n are those defined by the standard [120]. The minimum decay rate that can be measured for a specific value of x_{max} is:

$$\Delta_{min} = \frac{4.343}{x_{max}} \tag{5.9}$$

which is approximately 0.1 dB/m for 66 sleepers with a spacing of 0.65 m. It is suggested in [120] that if the decay rate in any of the one-third octave bands of the spectrum is less than twice the minimum decay rate, the estimation should be regarded as unstable and a longer length of track should be considered.

According to the standard [120], the vertical response of the rail should be obtained using excitation at the middle of the rail head. Since this excitation would not result in any differences due to coupling sources in the rail (see Fig. 5.3(a)), a different location is used here for illustrative purposes. Thus, to calculate the vertical response in the present beam model, the rail is excited at position 4, 20 mm from the centre of the railhead, and the response is obtained at the same position at various distances x_n along the rail. The decay rate for vertical excitation is plotted in Fig. 5.7(a), while the corresponding point mobility can be seen in Fig. 5.3(c). Equivalent, results for the lateral track decay rate are shown in Fig. 5.7(b), where the force and response points are located at position 2, 20 mm below the top of the railhead, with the corresponding mobility seen in Fig. 5.3(b).

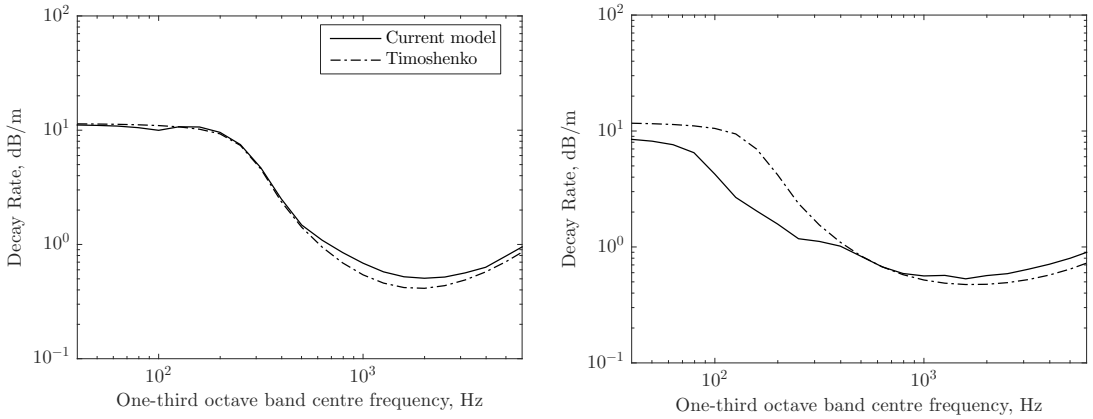

a) Vertical excitation b) Lateral excitation

Figure 5.7: Track decay rate for (a) vertical and (b) lateral excitation

At low frequencies, the vertical decay rates are high due to the blocking effect of the support stiffness, similar to the result for the vertical wave alone, Fig. 5.6(a). They drop at around the cut-on frequency of the rail vertical bending wave ($f_{co,i}$). At high frequencies, the predicted decay rate increases due to damping in the rail [121]. Similar behaviour is observed for the lateral direction, with the decay rate dropping at a lower cut-on frequency ($f_{co,I}$) due to the smaller foundation stiffness associated with this direction.

Results are also shown in Fig. 5.7 for the Timoshenko beam model. For the vertical direction, differences between the models occur mainly due to the eccentric applied load in the current model which excites the type I and II lateral waves as well as the vertical waves. Above 400 Hz, the decay rate of the current model becomes higher than the conventional Timoshenko model, due to the influence of the higher decay rate of the lateral wave type II. If the rail is excited through its centreline both curves would be identical.

The most significant difference is seen in the lateral track decay rate, where the result is considerably lower than that of the Timoshenko model for frequencies below 300 Hz. This is caused by the lowering of the cut-on frequency for the lateral wave type I discussed in Section 3.6. Consequently, if the track decay rate is used for parameter fitting from measurements, using the Timoshenko beam model will lead to a significantly different estimate of the lateral pad stiffness than using the current model. Conversely, above 300 Hz, the decay rate is higher than that obtained using the Timoshenko model.

The contribution of the individual waves to the overall mobility at different distances is shown in Fig. 5.8 for various example frequencies. For the vertical force and response point, at 50 Hz all waves have a relatively high decay rate, with the lateral wave I having the lowest (apart from the axial wave). Oscillations occur in the total response due to interference between the waves. At a distance away from the excitation, the response is seen to be influenced most by this lateral wave. As this first lateral wave cuts on at 100 Hz, by 150 Hz the response is strongly influenced by it. Above the cut-on frequency of the vertical bending wave (290 Hz), the vertical wave dominates the response.

When the rail is excited laterally, the vertical and axial waves are not excited. The lateral mobility is mainly influenced by the lateral wave I for the frequencies considered, as this has the lowest decay rate. As the second lateral wave cuts on at about 300 Hz, its mobility starts to increase in Fig. 5.8(f), but it still has a smaller amplitude than the first lateral wave at this frequency.

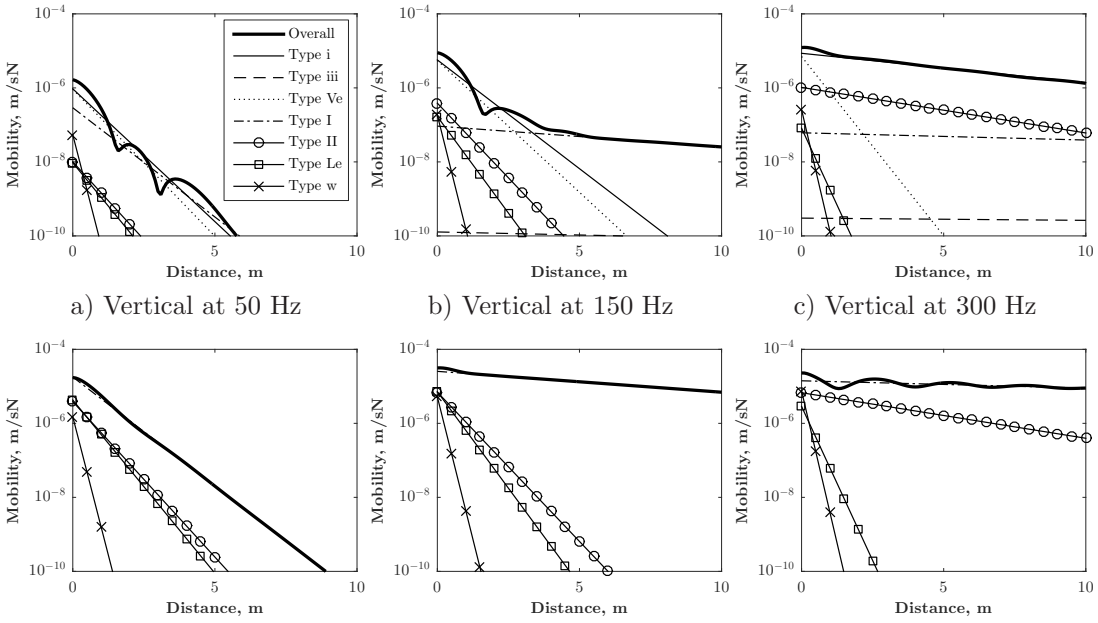

a) Vertical at 50 Hz b) Vertical at 150 Hz c) Vertical at 300 Hz

d) Lateral at 50 Hz e) Lateral at 150 Hz f) Lateral at 300 Hz

Figure 5.8: Vertical and lateral transfer mobility per wave

5.3 Mobility and decay rate for groove rail - 60R1

So far, the rail cross-section considered, 60E1, is symmetric about the y axis. In this section, the forced response for an asymmetric rail, the 60R1 rail profile, is investigated in terms of the point and cross mobilities. Figure 5.9 shows the excitation and response positions considered for the 60R1 rail profile.

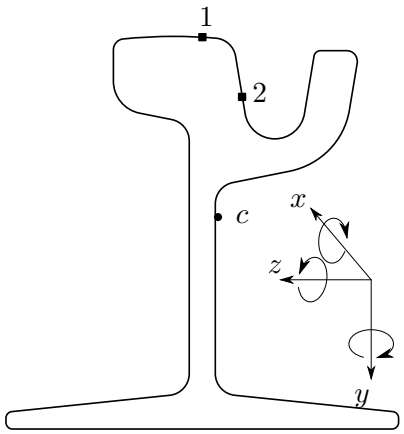

Figure 5.9: Excitation and response positions for 60R1 rail

5.3.1 Point mobility

As shown through the dispersion curves in Section 3.4.6, the 60R1 rail cross-section is more flexible, with the higher order waves (due to cross-sectional deformation) cutting on at lower frequencies. This in turn means that cross-sectional deformations will become apparent at lower frequencies in the mobility, limiting the range of validity of the current analytical model.

The points of excitation and response for the 60R1 rail differ slightly from those for the 60E1 rail. For the vertical response the first point is located above the centreline of the web, at position 1 as shown in Fig. 5.9. Equivalently, the first point for the lateral excitation is located inside the groove, 20 mm below the top of the railhead (position 2). The results for these two positions are shown in Fig. 5.10(a,b). Again, results are shown for the current model, the WFE model and the Timoshenko beam. The second point for vertical excitation is located 16.6 mm to the right of the centroid (position 2 - towards the groove) and results are shown in Fig. 5.10(c), while the second point for lateral excitation is located at the top of the railhead (position 1), with results shown in Fig. 5.10(d).

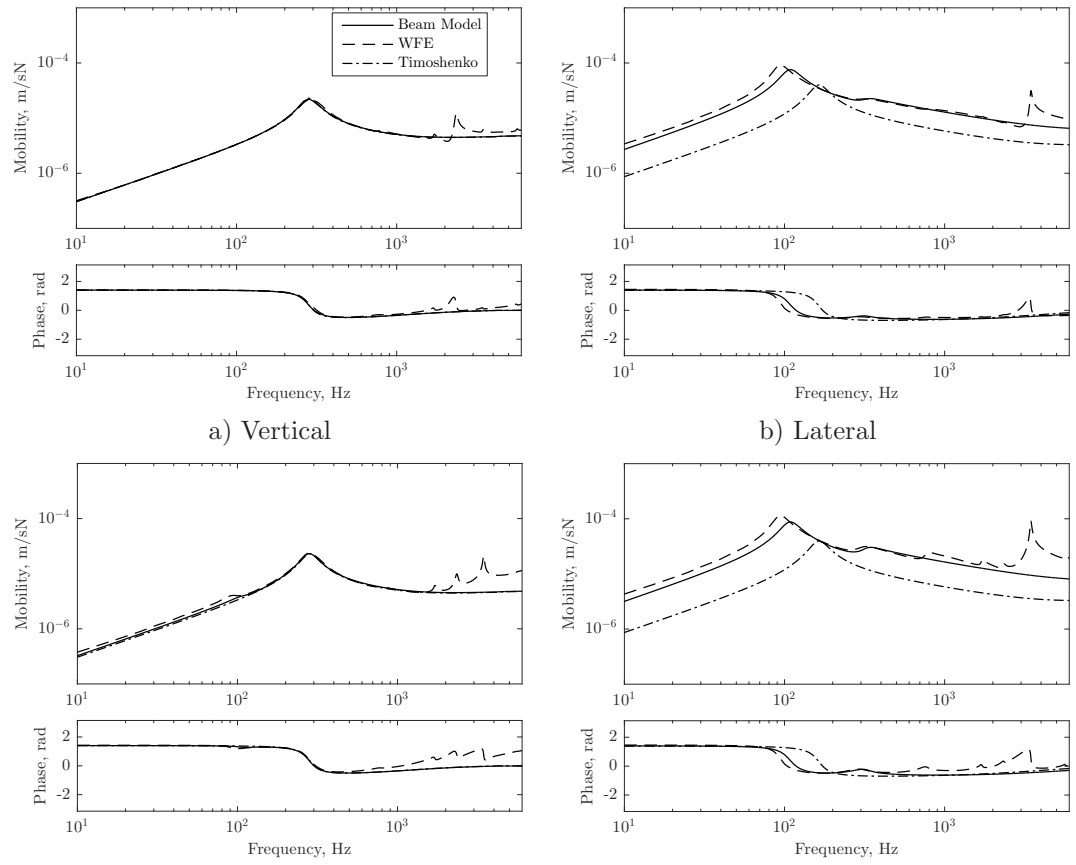

a) Vertical

b) Lateral

c) Vertical with 16.6 mm offset

d) Lateral at top of rail head

Figure 5.10: Comparison of mobility for 60R1 rail with the WFE model

When the rail is excited vertically in line with the centre of the web, Fig. 5.10(a), there is no coupling evident between the vertical and lateral directions, with the main peak occurring at 290 Hz. In contrast, when an offset is applied, an additional peak is observed at 100 Hz, corresponding to the cut-on frequency of the lateral waves. When the rail is excited laterally, Fig. 5.10(b), this is the dominant peak.

When lateral excitation is considered, Fig. 5.10(b), the agreement between the present beam model and the WFE model is not as good as for the 60E1 rail in Fig. 5.3. A peak is seen in the mobility at about 95 Hz for the WFE model, while in the current beam model it is predicted at 105 Hz. This difference is likely to be due to the fact that the cross-section of the 60R1 rail is less stiff than the 60E1 rail, and if combined with a higher torsional stiffness of the pad (pad width being 180 mm instead of 150 mm), will lead to greater cross-sectional deformation. Overall an acceptable agreement between the analytical and the WFE models can be seen for frequencies up to about 1.3 kHz.

Figure 5.10(c) shows the results when an eccentric load is considered in the vertical direction. Apart from the peaks at the two vertical wave cut-on frequencies, three additional peaks are seen in the results from the WFE model, corresponding to the cut-on of lateral waves at 100 Hz, 1.4 kHz and 4 kHz. Of these, only the first is present in the results from the analytical model. At all frequencies, the mobility of the beam model is higher than that of the Timoshenko beam, with an average difference of 3%.

Figure 5.10(d) shows the lateral mobility at the top of the rail head. Compared with Fig. 5.10(b) it can be seen that the lateral mobility is higher than at the centre of the rail head. At high frequencies the web bending and double web bending modes lead to an increase in the mobility predicted by the WFE model by 60% on average above 3 kHz, compared with the centre of the rail head (see also [20]). At lower frequencies the difference between the mobility of the current beam model and that of the WFE model remains at about 10%.

Comparing the results between the two beam models, similar conclusions can be drawn as for the 60E1 rail, although the deviations between the two models are slightly smaller. Since the torsional support stiffness is higher, the contribution of torsion for this rail is less than for 60E1.

5.3.2 Cross mobility

Figure 5.11 shows the cross mobility. This shows the lateral response to a vertical force at position 1 and 2 of Fig. 5.9. For the Timoshenko beam model, the factor XdB was selected as -14 dB at position 1 and -12 dB at position 2, while again the lateral pad stiffness has been reduced to 15.2 MN/m to match the cut-on frequency of the wave type I.

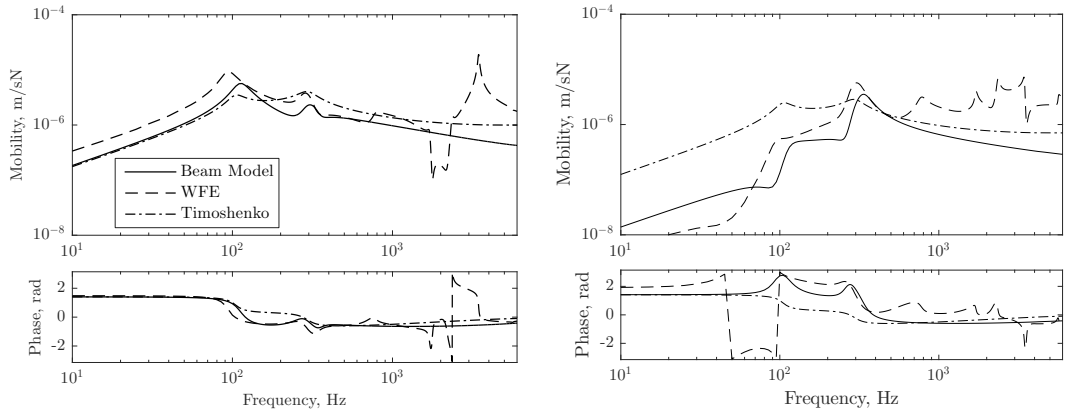

a) Position 1 (XdB = -14 dB) b) Position 2 (XdB = -12 dB)

Figure 5.11: Cross-mobility for 60R1 rail

The response for the WFE model and current beam model follow a similar trend in both cases, while for the Timoshenko beam model the only difference is the increased level of the response. The agreement between the present beam model and the WFE model is satisfactory only in the region of 100 Hz to 1 kHz. As discussed previously, the poor agreement is probably caused by the additional flexibility of the 60R1 cross-section as well as the higher torsional support stiffness.

5.4 Effect of track curvature

To investigate the effect of track curvature on the mobility and track decay rate, results are shown from the developed model for the case of a straight rail and curved rails with radii R of 100, 20 and 4 m. The vertical mobility and track decay rate are shown in Fig. 5.12 and the lateral mobility and track decay rate are shown in Fig. 5.13.

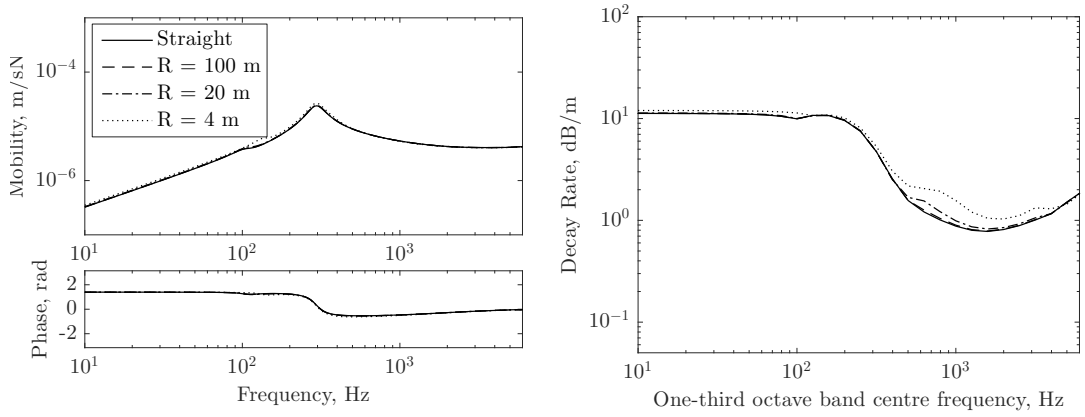

a) Mobility b) Decay rate

Figure 5.12: Vertical excitation for a straight and curved rail

It can be seen from Fig. 5.12(a) that the effect of curvature becomes noticeable only at a radius of 4 m. The differences in the point mobility occur at frequencies below 400 Hz for a radius of 4 m. From Fig. 5.12(b) it is seen that the curvature affects the decay rate above 200 Hz, for radii of 20 m and below. For a radius of 100 m, the influence of curvature is negligible.

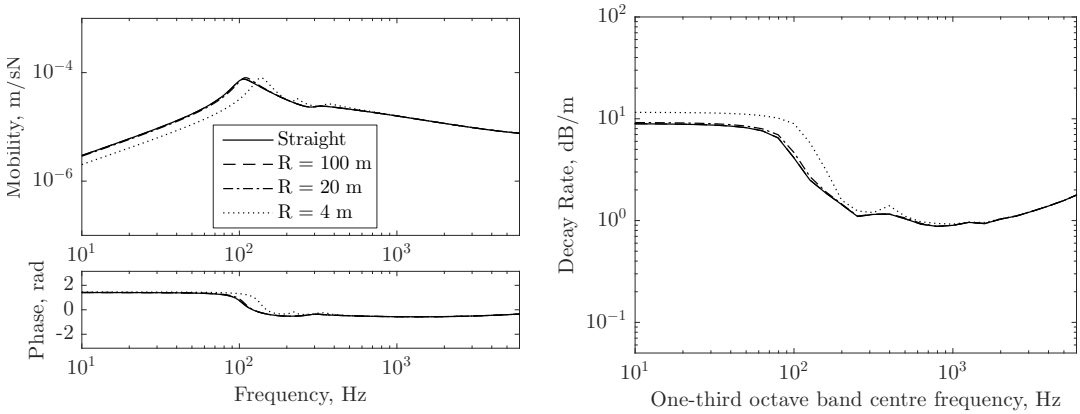

a) Mobility b) Decay rate

Figure 5.13: Lateral excitation for a straight and curved rail

The lateral mobility is more sensitive to the effects of curvature, with noticeable differences starting to occur below a radius of 20 m. Again, the differences in the point mobility occur at frequencies below 400 Hz for a radius of 4 m. The lateral track decay rates show the influence of curvature at frequencies below 1 kHz for a radius of 4 m and to a much lesser extent for a radius of 20 m.

For both the vertical and lateral directions, the effect of curvature is seen to be insignificant for a radius of 20 m and above. Since typical mainline and tram tracks will mostly have curvatures greater than this, it can be concluded that track curvature is not an important aspect in modelling the response of rails. Instead, a straight rail model is sufficient and should be preferred to avoid added complexity.

5.5 Effect of torsion, shear centre eccentricity and warping

In order to understand the influence of coupling through the beam model (i.e. excluding support location), the effect of torsion, shear centre eccentricity and warping is investigated here individually. Results are shown from the developed model for the case of a straight rail with these coupling sources considered individually. In order to investigate the influence of torsion, Eq. (2.45) is considered along with Eqs (2.68) and (2.69) for vertical bending, and Eqs (2.78) and (2.79) for lateral bending. Shear centre eccentricity is included by considering Eqs (2.140)-(2.142) along with the influence of torsion. Finally, to investigate the effect of warping, Eqs (2.45), (2.68), (2.69), (2.78) and (2.79) are considered along with Eq. (2.107).

In Figs 5.14 and 5.15, the mobility and decay rate due to vertical and lateral excitation are presented respectively. The solid line represents the current beam model accounting for all sources of coupling, the dash line represents the case without accounting for shear-centre eccentricity or warping, while the dash-dot and dot lines show the individual effect of shear centre eccentricity and warping respectively. The excitation force is applied at position 1 of Fig. 5.1 for the vertical response, while for the lateral responses it is applied at position 2.

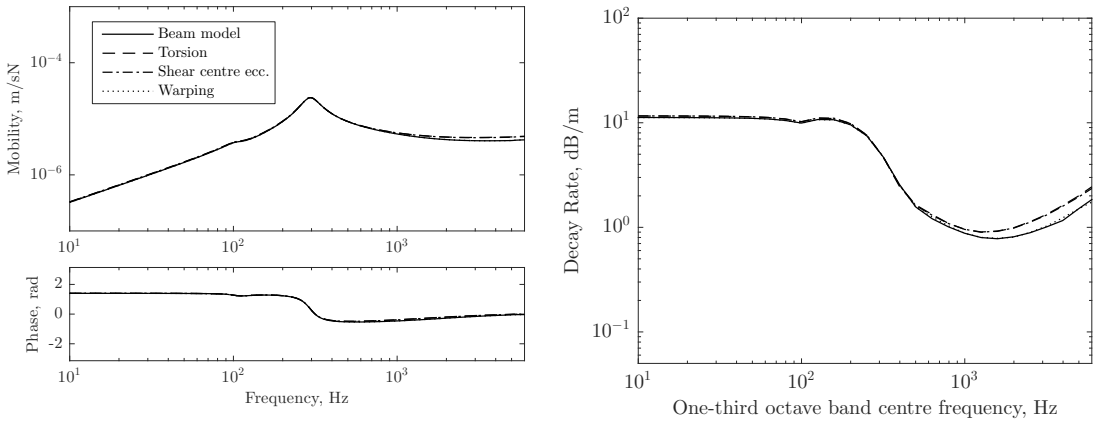

a) Mobility b) Decay rate

Figure 5.14: Vertical excitation for a straight rail with torsion, shear centre eccentricity and warping considered individually

At low frequencies, the behaviour of the rail is mainly controlled by the track support, and the point mobility and track decay rates are similar for all models. For the vertical direction, differences start to occur above 400 Hz, while for the lateral direction, the lateral mobility is seen to increase above 200 Hz.

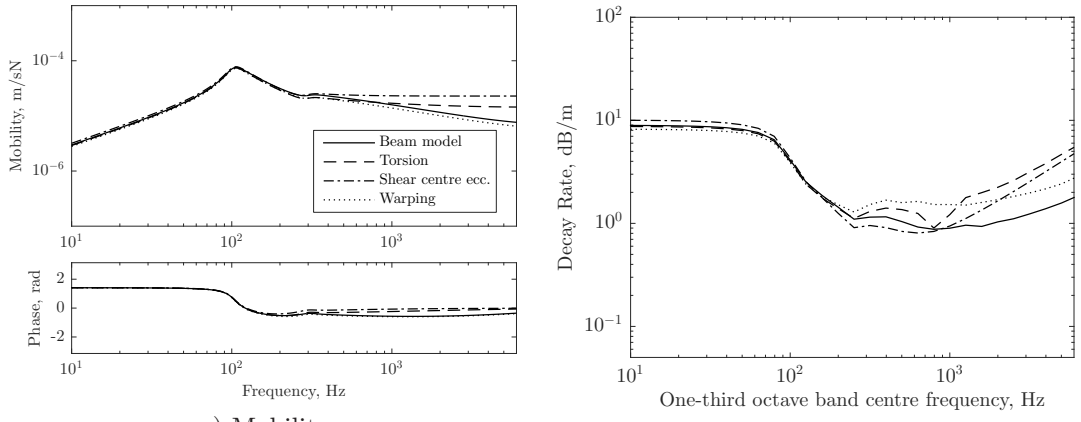

a) Mobility b) Decay rate

Figure 5.15: Lateral excitation for a straight rail with torsion, shear centre eccentricity and warping considered individually

From Fig.5.15, it is observed that the main contributing factors to the increased lateral mobility compared to the fully coupled model is the inclusion of torsion and the correct

account of the support location. The inclusion of torsion affects the response over the whole frequency spectrum whereas the shear centre eccentricity and warping influence the higher end of the frequency spectrum.

5.6 Effect of double-layer support

In Chapter 4, a double-layer support was introduced, accounting not only for the translational degrees of freedom of a bibloc sleeper, but also the rotational ones. In addition, the lateral bending, torsion and extension of a monobloc sleeper were considered, as well as the vertical bending. Here, results for the forced response of the rail in the vertical, lateral and axial directions are presented and compared for the two sleeper models. These results are shown in Figs 5.16–5.18. The sleeper and ballast parameters are tabulated in Tables 4.1, 4.2 and 5.1, where the frequency dependent ballast stiffness as in Section 4.6.1 has been used.

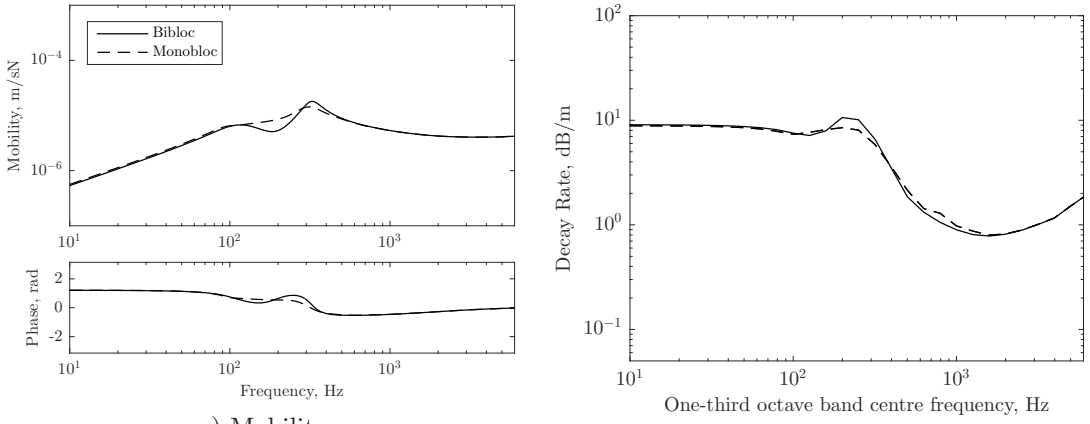

a) Mobility

b) Decay rate

Figure 5.16: Vertical response of 60E1 rail on double-layer elastic foundation

As seen in the previous chapter, the response of the rail on a double-layer foundation has additional resonance frequencies compared to the single layer support, as seen for example in Fig. 5.8. This can also be seen in Fig. 5.16, where a peak in the mobility is seen at about 100 Hz for the rail on the bibloc sleeper. This corresponds to the cut-on of the combined mass of the rail and sleeper block on the ballast stiffness. The second peak at 300 Hz corresponds to the cut-on frequency of the rail mass on the vertical pad stiffness. For the lateral and axial responses, the contribution of the sleeper and ballast is less evident, as seen in Figs 5.17 and 5.18, and the response resembles that of the single support layer (see Fig. 5.8(b)).

The overall trends of the rail response obtained using the two sleeper models are similar. The main differences are seen in the vertical and axial directions, where the frequency dependent ballast stiffness is used (see Section 4.6.1), leading to less prominent peaks in

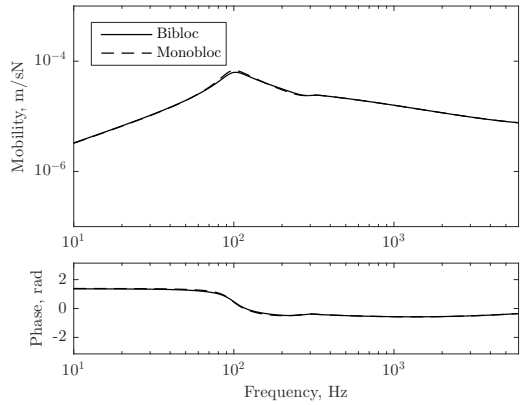

a) Mobility

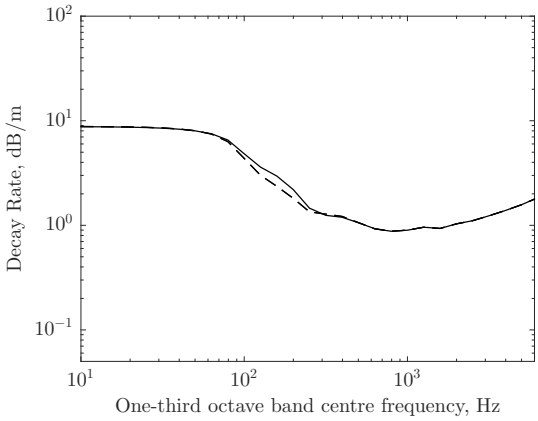

b) Decay rate

Figure 5.17: Lateral response of 60E1 rail on double-layer elastic foundation

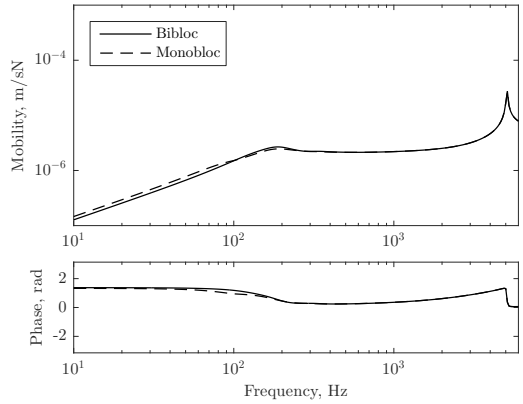

a) Mobility

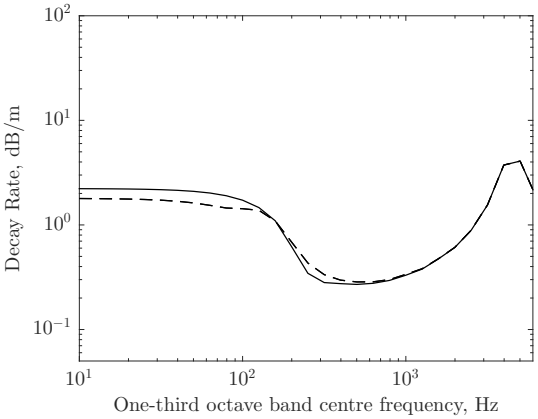

b) Decay rate

Figure 5.18: Axial response of 60E1 rail on double-layer elastic foundation

the rail response and some variations in the decay rate. The lateral responses using the two sleeper models are almost identical, as the longitudinal sleeper dynamic behaviour does not influence the response significantly. More noticeable differences are seen in the axial decay rate, in Fig. 5.18(b), but these are at low frequencies and are thus unlikely to be of any consequence to rolling noise.

5.7 Comparison with measurements

In order to calibrate the stiffness and damping parameters used in the numerical models, a comparison with measurements is first necessary. Here, track decay rates are preferred over point mobilities as they are most relevant to rolling noise. Since the track properties are not fully known, a basic curve fitting procedure is performed based on matching the predicted and measured track decay rate in order to aid the determination of the pad and

ballast stiffness and damping, while maintaining the same rail and sleeper properties. Here, measurements on three different tracks have been chosen.

The first is a 33 m long test track at the University of Southampton. This track has been chosen due to the ease of access in performing the various experiments, as well as the fact that previous measurements exist for this track. Here, results for the vertical and lateral mobilities and track decay rates are obtained from Betgen et al. [97], while new measurements were carried out on the same track for the axial direction[1]. In order to understand the effect of vertical/lateral coupling, the measured data are used to compare against the predictions. This is based on the point and cross mobilities for the rail when excited across the rail head at various positions, both vertically and laterally.

The second and third tracks are at an operational site at Fishbourne, Sussex. This set of measurements[2] has been conducted by previous researchers from the University of Southampton (e.g. Squicciarini et al. [28]). This site has been chosen for two reasons. Firstly, an operational site was desired for which train pass-by noise measurements are also available. Secondly, two tracks exist at this site, one of which underwent a major renewal. The unrenewed track has relatively stiff pads whereas the renewed track has soft pads. Having two tracks with different pad stiffnesses is of particular importance, especially when vertical/lateral coupling is considered, as has been pointed out by Vincent et al. [26].

5.7.1 University of Southampton test track

This site consists of two rails laid on approximately 50 sleepers, embedded in ballast. The rails are attached to the sleepers using Pandrol's fast-clip fastening system. A comparison is made between the model developed here and the measurements. Results are also shown for the Timoshenko beam model. The aim of these comparisons is two-fold; a) to compare the performance of the two models in extracting track parameters by visually fitting the responses based on the track decay rates and point mobilities and b) to validate the performance of the model in terms of vertical/lateral coupling through the prediction of the cross-mobilities.

In order to represent the track in the presented and Timoshenko beam models more accurately, the two-layer support has been introduced using the monobloc sleeper model, accounting for the dynamic stiffness ballast. Table 5.2 shows the derived parameters.

The measurement locations across the rail cross-section are shown in Fig. 5.19. For the measurement of the vertical and lateral mobilities, in order to calculate the respective decay rates, the points selected are those defined by [120]. These correspond to positions 1 and 2 in Fig. 5.19. For the cross mobility, the locations are at 10 and 20 mm away from

[1]These measurements were performed with the assistance of Dr Michał K.K. Kalkowski.

[2]Measurements for the two track sites at Fishbourne have been provided by Dr Martin G.R. Toward.

Table 5.2: Derived properties for test track.

	Current model	Timoshenko
Sleeper model	Monobloc	Monobloc
Sleeper mass (per rail), m_s^b	150 kg	150 kg
Sleeper spacing, l_{ss}	0.63 m	0.63 m
Rail loss factor, η_r	0.01	0.01
Pad axial stiffness, k_x^p	100 MN/m	25 MN/m
Pad vertical stiffness, k_y^p	120 MN/m	120 MN/m
Pad lateral stiffness, k_z^p	100 MN/m	25 MN/m
Pad vertical loss factor, $\eta_{p,v}$	0.25	0.25
Pad lateral loss factor, $\eta_{p,l}$	0.2	0.2
Ballast axial stiffness, $k_{x,b}$	100 MN/m	100 MN/m
Ballast vertical stiffness, $k_{y,b}$	100 MN/m	100 MN/m
Ballast lateral stiffness, $k_{z,b}$	100 MN/m	100 MN/m
Ballast axial loss factor, $\eta_{b,a}$	1.0	1.0
Ballast vertical loss factor, $\eta_{b,v}$	0.5	0.5
Ballast lateral loss factor, $\eta_{b,l}$	1.0	1.0

the rail centreline, corresponding to position 3 and 4 respectively. Finally, to measure the axial mobility, excitation position 1 was used on the end of the rail.

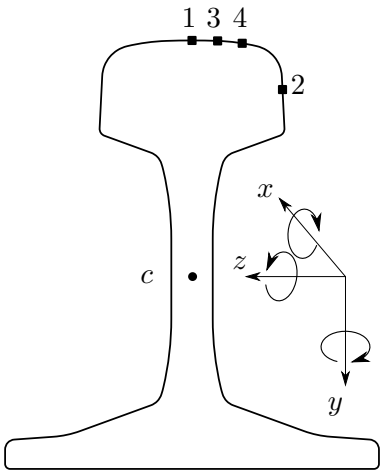

Figure 5.19: Measurement locations across the rail cross-section on University of Southampton test track

The point mobilities for vertical and lateral excitation are plotted in Fig. 5.20. The measured point mobility, when plotted in narrow frequency resolution, exhibits oscillations at frequencies above 600 Hz, attributed to reflections from the ends of the finite length of track. To avoid this, the results are presented here in one-third octave frequency bands, averaging the squared modulus and neglecting the phase.

The model shows a very good agreement with the measurements in terms of both the mobility and decay rates up to 2 kHz. The agreement for the vertical direction is slightly better than for the lateral direction for the decay rate, while the opposite applies for the point mobility. It is seen from Table 5.2 that the estimated lateral pad stiffness

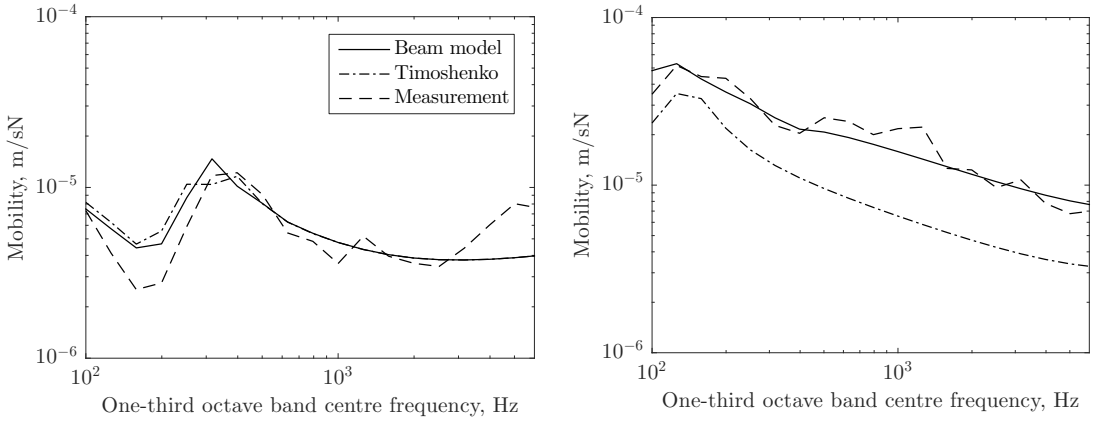

Figure 5.20: Mobility comparison against measurements for test track

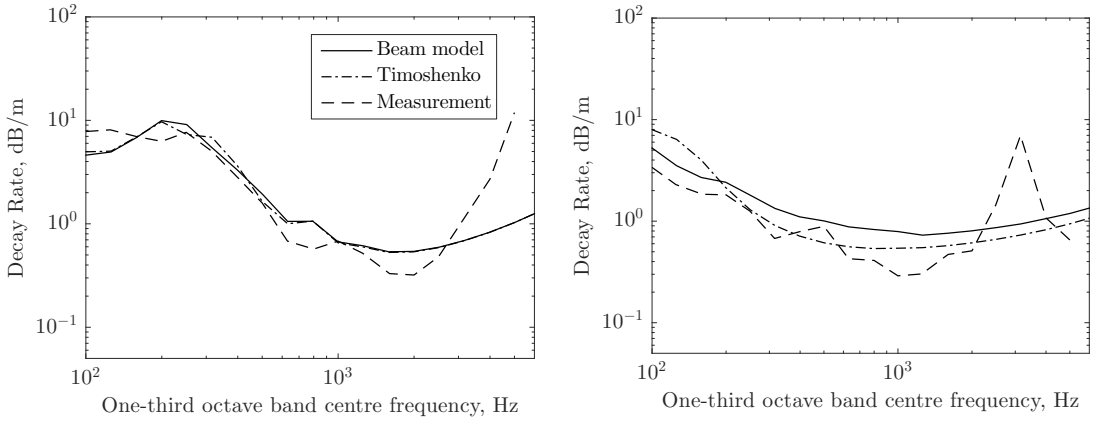

Figure 5.21: Track decay rate comparison against measurements for test track

required to fit the measured data is significantly higher than when fitting with a simple Timoshenko beam model.

As seen from Fig. 5.20(b), a significant improvement is obtained in the lateral mobility using the proposed model, compared with the Timoshenko beam model. The main reason for this, as discussed in previous sections, is the inclusion of torsion and support eccentricity in the model. What is important to note from Fig. 5.20(b) is the fact that, even though the current model does not include cross-sectional deformation, the main trend in the lateral mobility is adequately represented over the whole frequency range.

The track decay rates are plotted in Fig. 5.21. The overall comparison with the measured track decay rates is satisfactory for frequencies up to about 2 kHz. Above that frequency, the measured track decay rate increases significantly, for both the vertical and lateral directions, due to cross-sectional deformations. For the vertical direction, the current and Timoshenko beam models match closely. For the lateral direction, at low frequencies, the present beam model provides a better agreement with the measured

results. However, between 300 Hz and 2 kHz the Timoshenko beam model gives a better agreement.

The axial point mobility was measured at the top of the rail on its centreline (position 1 in Fig. 5.19) at one end of the finite length rail. The accelerometer was placed near the top of the rail while the excitation position was just below the accelerometer position, with the load applied along the rail. Since the model is based on an infinite rail, the predicted mobility was multiplied by 2 to compensate for the free end. In order to reduce the influence of peaks due to reflections in the measured data, the response time history has been post-processed manually. The signal is truncated after $t = 2L/c_L \approx 12.4$ ms, where L is the length of the finite rail and c_L is the speed of longitudinal waves (see Section 2.4.1). The factor of 2 is to account for waves travelling to one end of the rail and back. In addition, since the response at the end of this time history does not decay to zero (it is a lightly damped structure), an exponential window has been applied as [122]:

$$W_e(t) = e^{-t/\tau} \tag{5.10}$$

where τ is a time constant in seconds. Fladung [122] suggested that one quarter of the time record should be used for the time constant for lightly damped structures. In this case, this was found to be too low, overdamping the signal. Instead the actual length of the time record was used. Figure 5.22 shows the original and windowed time signals for a single impact excitation.

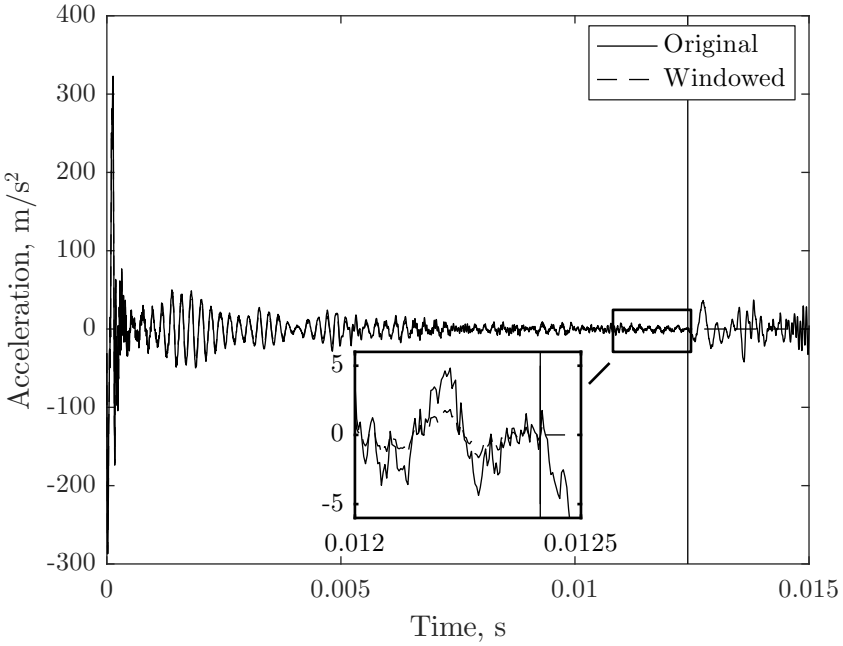

Figure 5.22: Axial acceleration due to a single impact excitation

The axial mobility is shown in Fig. 5.23. Three different curves are plotted, corresponding to the predicted response using the present beam model, the predicted response

using an axial rod and the measured response. Since the reflections have been treated here, the results are shown as narrow-band spectra.

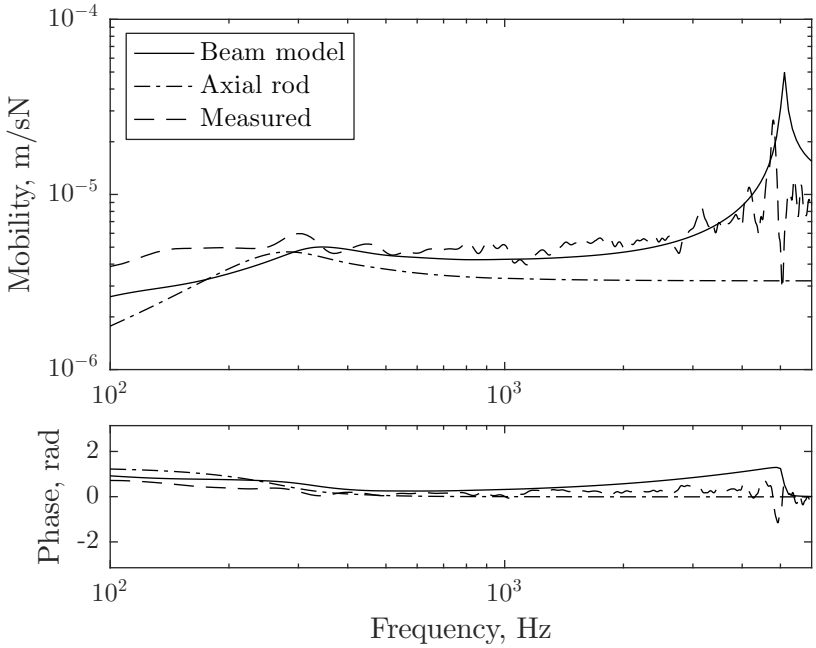

Figure 5.23: Axial mobility comparison with measurement for test track

Overall, the mobility obtained using the present beam model is seen to be higher than that of the axial rod, due to the coupling with vertical bending. Also, similar to Fig. 5.4, the axial rod model does not predict the peak at 5 kHz corresponding to the wave type iv, whereas the current model does.

Compared with the measured data in Fig. 5.23, the predicted mobility is slightly lower at low frequencies. The trend of the mobility is well captured over the whole frequency spectrum. Overall the model shows a very good agreement with the measurements for the point mobility and decay rates, up to about 2 kHz.

The cross mobility of the track is shown in Fig. 5.24, when the rail is excited vertically with an offset of 10 and 20 mm, i.e. at positions 3 and 4 respectively in Fig. 5.19. The lateral response in both graphs was measured at position 2. The cross mobility for the Timoshenko beam model is based on the geometrical average of the vertical and lateral receptances as in Eq. (5.6). By visually fitting the cross mobility to the model, the factor XdB was set to -14 dB for an offset of 10 mm (Fig. 5.24(a)) and -8 dB for an offset of 20 mm (Fig. 5.24(b)).

Here, agreement between the two models and the measurements is not so good although the main trends are captured. Although neither model accounts for cross-sectional deformation, the predictions based on the empirical relationship of Eq. (5.6) also lack information about the torsional behaviour of the rail, which has been shown to be

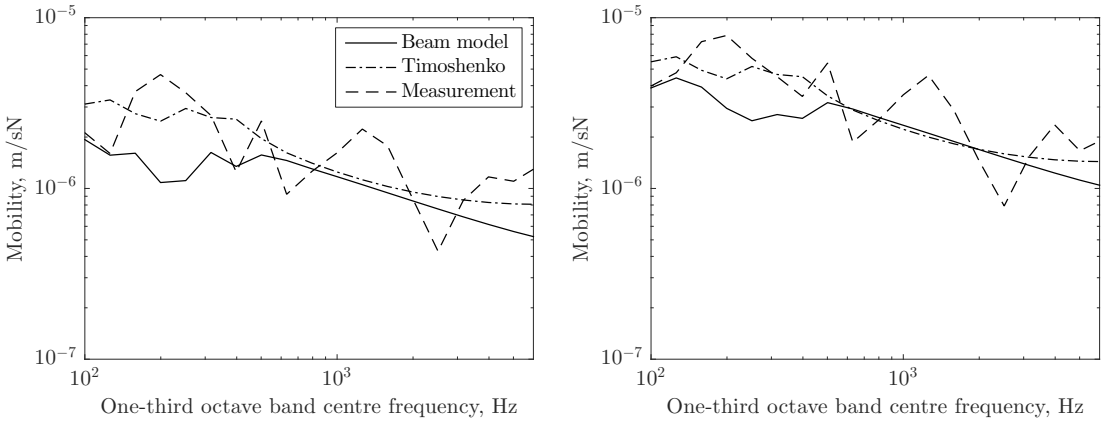

a) +10 mm offset (XdB = -14 dB) b) +20 mm offset (XdB = -8 dB)

Figure 5.24: Cross mobility comparisons against measurements for test track

essential to describe the lateral mobility. Therefore, it is suggested that the developed model is preferred for calculating the cross mobility.

5.7.2 Fishbourne

As discussed previously, one of the two tracks at Fishbourne, Sussex underwent a major renewal with complete replacement of ballast, sleepers, pads and rails. The track form of both the renewed and unrenewed track remained essentially the same. The main structural difference was that for the unrenewed track, the fastening mechanism consisted of Pandrol e-clip fastening system, while in the renewed track Pandrol fast-clip fastening system was used. The aim of this comparison is to extract the track parameters for the two tracks. They will also be used in Chapter 6 in predictions of the sound radiated during a train pass-by.

For both tracks at Fishbourne, the rail section used was 56E1. The material and geometric properties of this section are tabulated in Table 5.3. The sleepers were concrete monobloc.

Unrenewed track

Firstly, the unrenewed track is considered. Table 5.4 shows the parameters derived for this track using both models, where the dynamic ballast stiffness is used above 100 Hz. The parameters have been derived by visually fitting the predicted track decay rate to the measured one, in a similar fashion to the previous section, although here, better agreement was sought for higher frequencies that are more important for noise predictions. Although the lateral assembly stiffness extracted based on the developed beam model is expected to be higher than that using the Timoshneko beam model, this is not the case in Table 5.4. Due to the high vertical pad stiffness, the torsional stiffness

Table 5.3: Rail section properties (inertial properties relative to centroid)

	Value	Units
Section	56E1	-
Young's modulus, E	210	GPa
Shear modulus, G	80.769	GPa
Density, ρ	7860	kg/m^3
Poisson's ratio, ν	0.3	-
Cross-section area, A	7.12×10^{-3}	m^2
Second moment of area about y-axis, I_y	419.8×10^{-8}	m^4
Second moment of area about z-axis, I_z	2278×10^{-8}	m^4
Product moment of area, I_{yz}	0	m^4
Polar moment of area, I_p	2.6978×10^{-5}	m^4
Torsional constant, J	1.919×10^{-6}	m^4
Vertical shear coefficient, κ_y	0.425	-
Lateral shear coefficient, κ_z	0.542	-
Vertical shear centre eccentricity, e_y	0.0284	m
Lateral shear centre eccentricity, e_z	0	m
Warping constant, I_w	2.161×10^{-8}	m^6
Warping product moment of area, I_{wy}	1.6971×10^{-7}	m^5
Warping product moment of area, I_{wz}	0	m^5
Warping product moment of area, I_{wyy}	0	m^6
Warping product moment of area, I_{wyz}	-2.41×10^{-8}	m^6
Warping product moment of area, I_{wwy}	0	m^7
Rail foot/pad width, l_p	140	mm
Rail foot warping coefficient, k_f	-0.6	-

controls the lateral response of the model, hence making it less sensitive to variations of the lateral pad stiffness. Here, the lateral pad stiffness using the two models is found to be identical.

Figure 5.25 shows the track decay rates for the vertical and lateral excitation. In Fig. 5.25(a), three peaks are seen in the measured data, at about 60 Hz, 250 Hz and 800 Hz, corresponding to the cut-on of the combined mass on the ballast, the cut-on of the rail on the pads and the 'pinned-pinned' resonance. Although the 'pinned-pinned' resonance is not seen in the model since a continuous support is assumed, the fit is performed between 250 Hz and 800 Hz, to provide higher accuracy of the predicted decay rate at higher frequencies, as compared to the the fitting in Section 5.7.1 which was performed only for the main peaks at frequencies between 100 Hz and 400 Hz. The same procedure is followed for both the Timoshenko beam model and the present model. For the lateral track decay rate in Fig. 5.25(b), the Timoshenko model fails to predict the second peak at 400 Hz, corresponding to the wave type II cut-on frequency. The rail loss factor (η_r =0.015) has been adjusted to provide satisfactory agreement for both the vertical and lateral directions.

The point mobilities for vertical and lateral excitation are plotted in Fig. 5.26. For the

Table 5.4: Derived properties for the unrenewed track at Fishbourne site.

	Current model	Timoshenko
Rail cross-section	56E1	56E1
Sleeper model	Monobloc	Monobloc
Sleeper spacing, l_{ss}	0.775 m	0.775 m
Rail loss factor, η_r	0.015	0.015
Pad axial stiffness, k_x^p	30 MN/m	30 MN/m
Pad vertical stiffness, k_y^p	800 MN/m	800 MN/m
Pad lateral stiffness, k_z^p	30 MN/m	30 MN/m
Pad axial loss factor, $\eta_{p,a}$	0.1	0.1
Pad vertical loss factor, $\eta_{p,v}$	0.25	0.25
Pad lateral loss factor, $\eta_{p,l}$	0.1	0.1
Ballast axial stiffness, $k_{x,b}$	70 MN/m	70 MN/m
Ballast vertical stiffness, $k_{y,b}$	100 MN/m	100 MN/m
Ballast lateral stiffness, $k_{z,b}$	70 MN/m	70 MN/m
Ballast axial loss factor, $\eta_{b,a}$	2.0	2.0
Ballast vertical loss factor, $\eta_{b,v}$	0.25	0.25
Ballast lateral loss factor, $\eta_{b,l}$	2.0	2.0

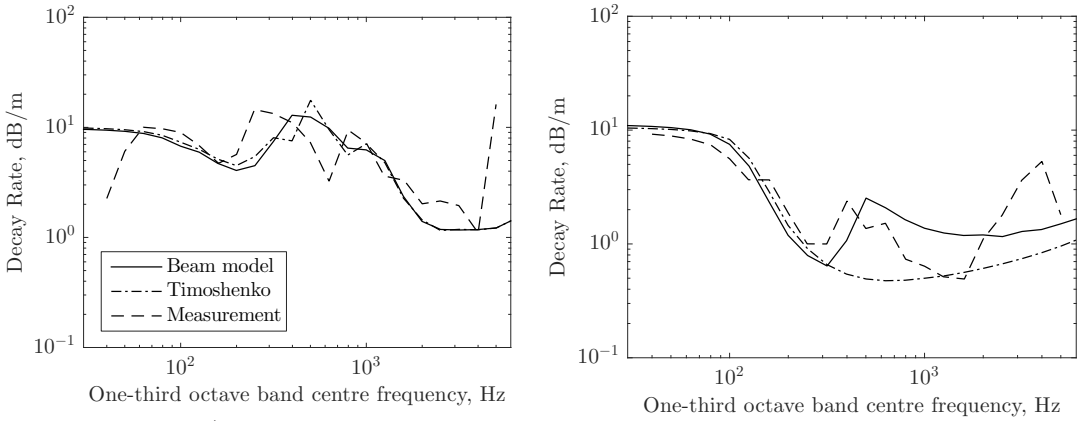

a) Vertical b) Lateral

Figure 5.25: Track decay rate comparison with measurements at Fishbourne - unrenewed track

vertical mobility, two distinct peaks can be seen in the measured mobility. The first occurs at about 120 Hz and corresponds to the cut-on of the combined mass of the rail and sleeper on the vertical ballast stiffness, i.e. the first cut-on of vertical wave type i. The second peak corresponds to the vertical 'pinned-pinned' resonance frequency occurring at about 700 Hz. The predicted results using the two models do not capture the 'pinned-pinned' resonance. Instead, multiple peaks of smaller magnitude are seen between 300 Hz and 1 kHz, corresponding to the flexible sleeper modes.

Similarly for the lateral mobility, three distinct peaks can be seen in the measured mobility. The first occurs at about 100 Hz and corresponds to the cut-on of the combined mass of the rail and sleeper on the ballast stiffness, i.e. the first cut-on of vertical wave type I. The second peak corresponds to the lateral 'pinned-pinned' resonance frequency

occurring at about 300 Hz. The third peak, at about 600 Hz corresponds to the cut-on of lateral wave type II. At low frequencies, in the lateral direction both models have a lower mobility than the measurement. At higher frequencies, the present beam model gives a better agreement with the measurement than the Timoshenko beam model, due to the inclusion of torsion as seen previously.

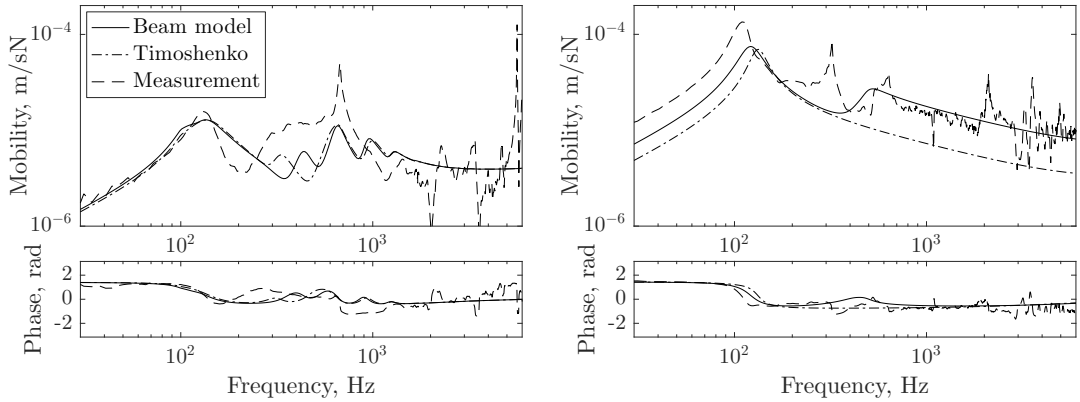

Figure 5.26: Mobility comparison with measurements at Fishbourne - unrenewed track

Renewed track

Table 5.5 presents the derived track parameters for the renewed track. Again, the dynamic ballast stiffness is used. The track decay rates for the vertical and lateral excitation are presented in Fig. 5.27 while the respective mobilities are presented in Fig. 5.28.

The estimated track parameters for the lateral direction are found to be significantly higher with the current model than when a fitting is performed with a simple Timoshenko beam model. This is due to the reduction in the lateral cut-on frequency when coupling is introduced through the foundation (see Section 3.6). Although the actual lateral pad stiffness is not expected to be as high as 100 MN/m [116], the rail fastening system is likely to provide a significant increase in the overall assembly stiffness in the lateral direction. In this case, the stiffness provided by the assembly (fastclip) is higher that that in the unrenewed track (where e-clips were used), and it is the same as that for the test track at the University of Southampton, where again Pandrol's fastclips are in place.

For both the track decay rates and point mobilities, the two models provide a satisfactory agreement with the measurements for the extracted parameters, given the limitations discussed so far.

Table 5.5: Derived properties for the renewed track at Fishbourne site.

	Current model	Timoshenko
Rail cross-section	56E1	56E1
Sleeper model	Monobloc	Monobloc
Sleeper spacing, l_{ss}	0.65 m	0.65 m
Rail loss factor, η_r	0.015	0.015
Pad axial stiffness, k_x^p	100 MN/m	15 MN/m
Pad vertical stiffness, k_y^p	100 MN/m	100 MN/m
Pad lateral stiffness, k_z^p	100 MN/m	15 MN/m
Pad axial loss factor, $\eta_{p,a}$	0.15	0.15
Pad vertical loss factor, $\eta_{p,v}$	0.2	0.2
Pad lateral loss factor, $\eta_{p,l}$	0.15	0.15
Ballast axial stiffness, $k_{x,b}$	70 MN/m	70 MN/m
Ballast vertical stiffness, $k_{y,b}$	60 MN/m	60 MN/m
Ballast lateral stiffness, $k_{z,b}$	70 MN/m	70 MN/m
Ballast axial loss factor, $\eta_{b,a}$	2.0	2.0
Ballast vertical loss factor, $\eta_{b,v}$	0.5	0.5
Ballast lateral loss factor, $\eta_{b,l}$	2.0	2.0

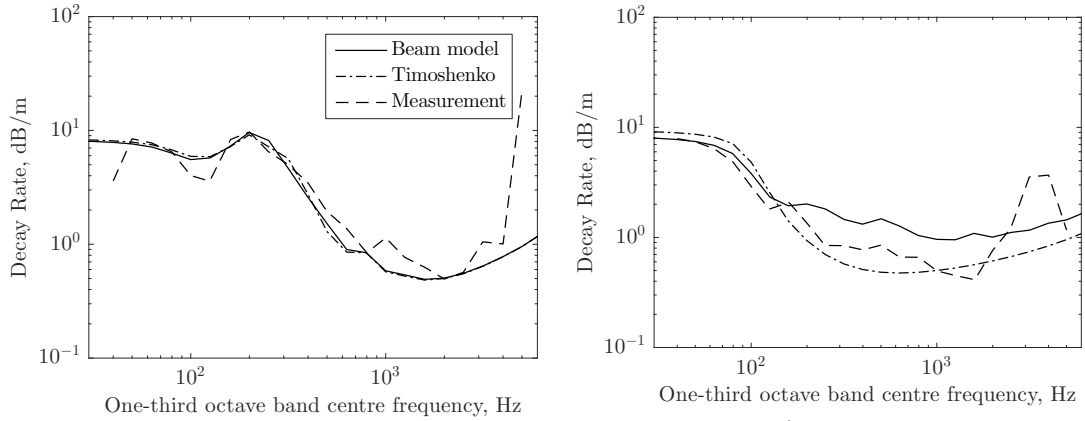

a) Vertical

b) Lateral

Figure 5.27: Track decay rate comparison with measurements at Fishbourne - renewed track

5.8 Fitting of the cross mobility

So far, the cross mobility of the developed model has been compared against the WFE model and measurements made at the University of Southampton test track. Measurements of cross mobility for the two tracks at Fishbourne are not available. Here, the XdB parameter is obtained when fitting the cross mobility of the existing Timoshenko beam model in TWINS to the present model. For the two tracks at Fishbourne, the fitting is performed at the asymptotic behaviour of the cross mobility of the current beam model at either end of the frequency spectrum (i.e. below 200 Hz and above 2 kHz). Table 5.6 shows the values of XdB for the parameters of the University of Southampton test track and the two tracks at Fishbourne.

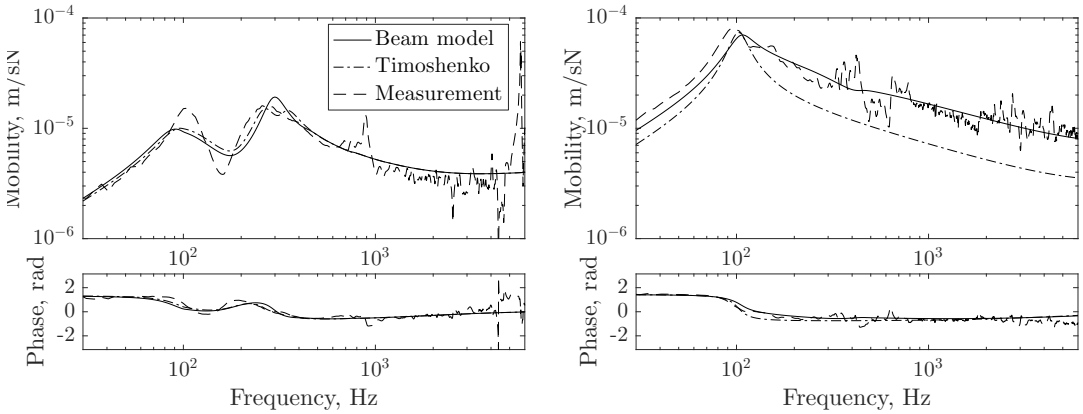

Figure 5.28: Mobility comparison with measurements at Fishbourne - renewed track

Table 5.6: XdB parameter for cross mobility fitted to current model.

Offset (mm)	Test track	Renewed	Unrenewed
5	-19	-17	-18
10	-14	-12	-15
15	-11	-10	-13
20	-8	-8	-12

As the point of contact approaches the rail centre, the required value of XdB decreases significantly. This is mainly due to the reduction of coupling in the present model, where if the rail was excited at the rail head centre, almost no coupling would occur. It is also seen that the XdB parameter for the test track is more similar to the renewed track than the unrenewed track at Fishbourne, as the properties of the test track and the renewed track at Fishbourne are more similar. To provide a look-up table for XdB values to be used, a more detailed study should be performed based on different track and contact conditions.

5.9 Conclusions

Using the model for the vibration of a railway track, developed in the previous chapters, results for the point mobility and track decay rate have been presented for a supported rail for both vertical and lateral excitation.

Of the various effects considered, the response in both the vertical and lateral directions is most influenced by the inclusion of torsion in the model. The effect of curvature is found to be negligible for the modelling of rails, and it can be concluded that a straight rail model is sufficient for all practical situations. To improve the model further at higher frequencies, consideration needs to be given to the cross-sectional deformation which is especially significant for the lateral response above 1.3 kHz.

The forced response obtained from the current model has also been compared with a WFE model that includes cross-sectional deformation as well as with measurements performed at three sites. Overall the model is shown to give excellent agreement with both the WFE predictions and measurements, within the frequency range of applicability of the developed model which is up to 3 kHz for the vertical direction and up to about 1 kHz for the lateral direction. The agreement is still good at higher frequencies with the exception of frequencies in the vicinity of the cut-on of waves relating to the cross-sectional modes. The cross mobility predicted using the developed model is shown to have a very good agreement with that predicted using the WFE model up to about 1.3 kHz, above which cross-sectional modes become important. In contrast, when the predicted cross mobility from the developed model is compared to measurements, the agreement is not very good, although the main trends are captured.

Chapter 6

Implications for rolling noise

In Chapter 5 it has been shown that the inclusion of torsion and support eccentricity can significantly affect the lateral vibration of the rail. In order to evaluate their effects on rolling noise, a Matlab implementation of TWINS ('Track-Wheel Interaction Noise Software') [17, 62, 123] is extended here to incorporate the coupled track model presented in the previous chapters, including the flexible sleeper model. The model is applied to the two tracks at the test site at Fishbourne at which measurements of noise, roughness and track decay rate have been made[1].

6.1 The TWINS model for rolling noise

The workflow of the TWINS model was introduced in Chapter 1. A description of the track representation is also given in Appendix B. In this section, the intermediate results used in the TWINS model to represent track dynamics and radiation are identified, and it is shown how these can be obtained using the model developed in the previous chapters.

6.1.1 Inclusion of the coupled track model in TWINS

It has been demonstrated in the literature that the noise radiated by the lateral track vibration can, in some cases, be higher than that due to the vertical vibration [26], especially when stiff rail pads are considered. The effective radiating length is inversely proportional to the wave decay rate, so a low decay rate corresponds to a large radiating length and vice versa. Thus, as seen from Chapter 5, lateral wave types I and II are likely to have a larger radiating length than vertical wave type i. If this lower decay rate is combined with an increased level of excitation for type I and II waves, their contribution

[1] All measurements at Fishbourne, Sussex used in this chapter are obtained from [28].

to the total radiated sound power can increase. As was shown in Chapter 5 the inclusion of torsion can significantly increase the lateral and cross mobilities and, thus, it is important to account for the coupling between the lateral and torsional behaviour of the rail provided by the developed beam model for rolling noise predictions. Although the axial waves have an even lower decay rate, they are not significantly excited and their radiated sound power is likely to be negligible. Similarly, the warping waves have a high decay rate, and combined with a small excitation, it is expected that their contribution will be negligible in comparison with the total radiated sound power. Despite the fact that the axial and warping waves are expected to have minimal contribution, they will still be included in the analysis for completeness.

In order to incorporate a track model in TWINS, the main quantities that need to be considered, as identified in Appendix B, are:

1. Rail receptance α_{jk} in the vertical and lateral directions, including the cross receptance, and partial receptance β_{kn} per wave n due to a force in direction k
2. Rail wave displaced shapes ψ_{jn} per wave n in direction j
3. Average sleeper receptance in the vertical direction (average sleeper response due to a force at the rail seat)
4. Average vertical sleeper receptance per wave n and wave displaced shapes $\psi_{s,jn}$ per wave n on the sleeper
5. Propagation constant s_n (or wavenumber $\xi_n = -\mathrm{i}s_n$)
6. Radiated sound power from the rail per unit length per wave n (W'_n) normalised by the peak velocity at the centroid.

In Chapter 2, the eigenvalue problem of Eq. (2.85) was used to derive the wavenumbers for the given model for each wave n and the corresponding left and right eigenvectors. This allowed the forced response of the rail to be determined from Eq. (5.2). These eigenvalues will be used here to calculate the propagation constants for each wave (see Eq. (B.2)).

The rail wave displaced shape (ψ_{jn}) corresponds to the right eigenvectors, based on Eq. (5.3) (compare with Eq. (B.3)), i.e.:

$$\boldsymbol{\psi}_n = \boldsymbol{\Psi}_n^R \tag{6.1}$$

where $\boldsymbol{\psi}_n$ is a vector containing the rail displaced shape in wave n for each degree of freedom j (ψ_{jn}), while the rail receptance per wave is given for a force in the vertical

and lateral direction at the contact point ($\tilde{\mathbf{F}}_k^1$) as:

$$\beta_{kn} = \frac{\boldsymbol{\Psi}_n^R \tilde{\mathbf{F}}_k^1}{\boldsymbol{\Psi}_n^L \mathbf{A}'(\xi_n) \boldsymbol{\Psi}_n^R} \tag{6.2}$$

The rail receptance is obtained as shown in Chapter 5.

To obtain the equivalent sleeper results, the sleeper displaced shapes are derived from the ratio of sleeper to rail vibration in each wave. Consider the second row from Eq. (4.88):

$$-\mathbf{T}_{s,t}^T \mathbf{K}_p \mathbf{T}_f \mathbf{U}_r + \mathbf{T}_{s,t}^T \mathbf{K}_p \mathbf{T}_{s,t} \mathbf{U}_s + \mathbf{K}_s^D(\omega) \mathbf{U}_s - \omega^2 \mathbf{M}_s \mathbf{U}_s = \mathbf{0} \tag{6.3}$$

Solving Eq. (6.3) for the sleeper displacement $\mathbf{U}_s$ leads to:

$$\mathbf{U}_s = (\mathbf{T}_{s,t}^T \mathbf{K}_p \mathbf{T}_{s,t} + \mathbf{K}_s^D(\omega) - \omega^2 \mathbf{M}_s)^{-1} \mathbf{T}_{s,t}^T \mathbf{K}_p \mathbf{T}_f \mathbf{U}_r \tag{6.4}$$

From Eq. (6.4), the ratio of rail to sleeper vibration is given by:

$$\mathbf{U}_{s/r} = \mathbf{U}_s \mathbf{U}_r^{-1} = (\mathbf{T}_{s,t}^T \mathbf{K}_p \mathbf{T}_{s,t} + \mathbf{K}_s^D(\omega) - \omega^2 \mathbf{M}_s)^{-1} \mathbf{T}_{s,t}^T \mathbf{K}_p \mathbf{T}_f \tag{6.5}$$

where $\mathbf{U}_{s/r}$ is a 6×7 matrix consisting of the ratios of sleeper to rail displacement, corresponding to six degrees of freedom and seven waves. From this, the sleeper displaced shapes can be found for each degree of freedom j by:

$$\psi_{s,jn} = \mathbf{U}_{s/r,jn} \psi_{jn} \tag{6.6}$$

Finally, the sound power per unit length, W_n' for the rail has to be calculated for each wave n. This is done using an in-house[2] Boundary Element software BEARS ('Boundary Element Acoustic Radiation Software') which solves the two-dimensional direct BEM Helmholtz integral equation with CHIEF points to account for the non-uniqueness problem using the method described in [124]. This is a two-dimensional model, so it assumes an infinite rail vibrating in phase over its length. The rail is assumed to be radiating in free space. The rail cross-section is defined by 73 elements as shown in Fig. 6.1. The displacements and rotations at the centroid are transferred to all the nodes and the normal velocity at each node is found and applied as the boundary conditions in the BE model for each frequency and each wavetype. Due to the track properties and frequency dependence of the wave shapes, the sound radiation for the new model must be calculated for each set of track parameters. For the sleeper radiation, the existing model from TWINS is used, only accounting for the vertical sleeper response, although for the present beam model this is obtained as a sum over all seven waves.

The rail sound power W_n' per wave is plotted in Fig. 6.2, where each wave shape is normalised to have a 1 m/s peak amplitude at the rail centroid. Results are shown for the two tracks at Fishbourne described in Section 5.7.2. Note that these are only

[2]Written by Dr C.J.C. Jones.

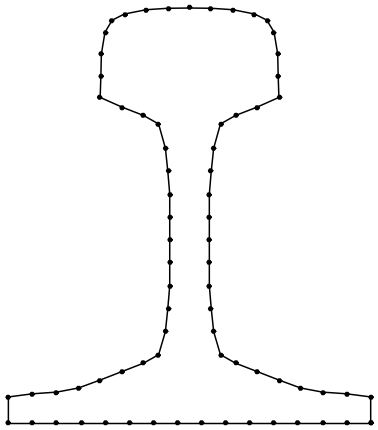

Figure 6.1: 60E1 rail cross-section discretisation for BE calculations

intermediate results as the final sound powers also depend on the wave amplitudes and decay rates. As expected the sound power radiated due to the warping and axial waves is significantly smaller than that of all other wave types. For the renewed track properties in Fig. 6.2(a), the wave type II has similar radiation to that of wave type I at low frequencies, mainly due to the coupling caused by the foundation eccentricity. Its sound radiation drops between 400 Hz and 1 kHz. In this frequency range, the rail is rotating about the centroid in this wave, behaving as an acoustic quadrupole, corresponding to two identical dipoles with opposite phase [125]. Above this frequency range, the acoustic wavelength becomes comparable to the height of the rail, and the head, foot and web are seen to radiate noise independently. For the Timoshenko beam model, the results for waves i and Ve will be identical, and so will I and Le. For the present beam model, the waves of type i, Ve, I and Le have small fluctuations due to coupling. For example, at high frequencies, the wave type Le follows the behaviour of the type i and Ve waves, but since it is an evanescent wave, it is not expected to influence the overall results significantly.

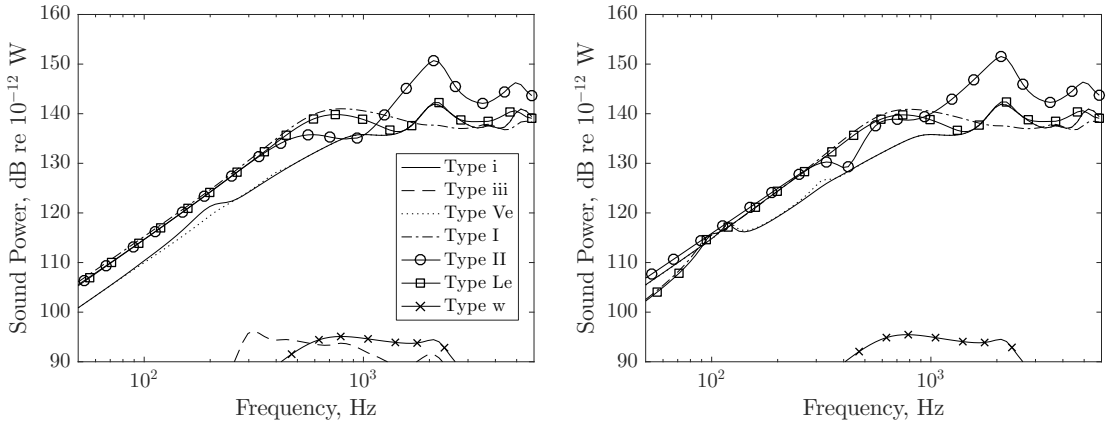

a) Renewed track b) Unrenewed track

Figure 6.2: Radiated sound power per metre of rail for 1 m/s peak velocity at the centroid in each wave

Similar conclusions can be drawn for the unrenewed track from Fig. 6.2(b). Two noticeable differences are the reduced axial radiation compared to the renewed track (it is no longer visible in Fig. 6.2(b)) and a coupling between the type i, II, Ve and Le waves at frequencies below 200 Hz. Analysis of wave shapes at low frequencies, similar to Fig. 3.15, has revealed that the vertical waves have a high lateral contribution and vice versa. Due to the higher pad stiffness of the unrenewed track, the sleeper vibration has a greater influence on the rail. In this case, the asymmetry of the applied loads on the flexible sleeper causes an additional coupling between the vertical and lateral waves at low frequencies. This influences the sound power in Fig. 6.2(b) at low frequencies, where below 200 Hz the radiation of vertical wave types i and Ve is more similar to that of lateral waves type I and Le from Fig. 6.2(a) and vice versa.

6.1.2 Wheel and rail roughness

Wheel and rail roughness data are obtained from measurements made at the test site at a similar time to the measurements of the track decay rates presented in Section 5.7.2 for both the renewed and unrenewed tracks. The wheel roughness used for both sites is that of a Class 377 Electric Multiple Unit. The wheel and rail roughness spectra are combined to provide the total roughness, and are used to calculate the wheel/rail interaction forces. The combined wheel and rail roughness is shown for both tracks in Fig. 6.3, along with the separate wheel roughness.

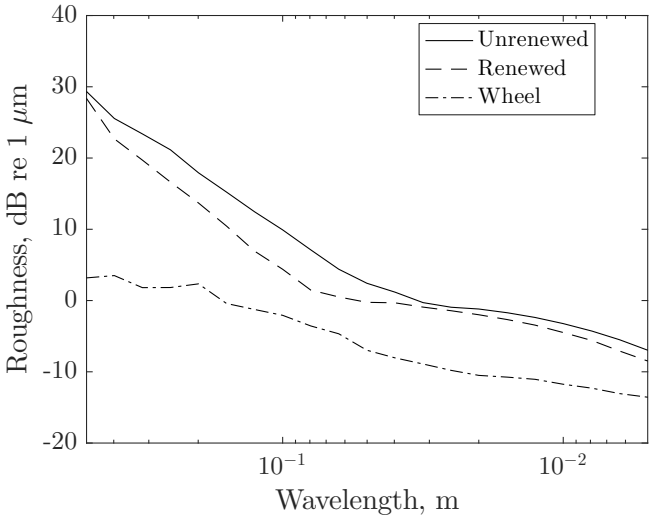

Figure 6.3: Combined wheel and rail roughness for Fishbourne site and measured wheel roughness for EMU Class 377

As expected, the rail roughness is higher overall before renewal took place. The roughness used for the wheel is the same for both tracks. For the contact filter, the analytical formula from [4] is used with a normal load of 50 kN, a rail head radius of curvature of 0.3 m and a wheel diameter of 0.841 m.

6.2 Rolling noise predictions

Rolling noise predictions are made for two example cases. These are based on the track parameters derived earlier for the Fishbourne site, at which also noise measurements have been performed previously [28]. The common parameters used in TWINS for the ground, microphone position, vehicle geometry and speed are presented in Table 6.1. It is noted here that for the wheel response, modal parameters (natural frequencies, damping ratios and modeshapes) from an existing FE wheel model have been used.

Table 6.1: Common parameters used in TWINS

Parameter	Value	Units
Ground height below railhead	1.5	m
Ground flow resistivity	3×10^3	Pa.s/m^2
Microphone height above railhead	1.2	m
Vehicle speed	118	km/h
Vehicle length	20	m

The sound pressure level (SPL) spectrum measured at 7.5 m from the track centreline during the passage of a Class 377 EMU is presented in Fig. 6.4 both for the renewed and unrenewed tracks. In each figure, as well as the measured results, two predicted results are shown, corresponding to the spectra predicted using the newly developed model and those predicted using TWINS with the existing Timoshenko beam model. For both tracks, the measured wheel and rail roughnesses presented in Section 6.1.2 have been used. For the current model, the offset of the contact point is set to 5 mm for both cases, while for the Timoshenko beam model the empirical factor, XdB, is set to -17 dB for the renewed track and to -18 dB for the unrenewed. These values are chosen according to the fitted cross mobility as tabulated in Table 5.6.

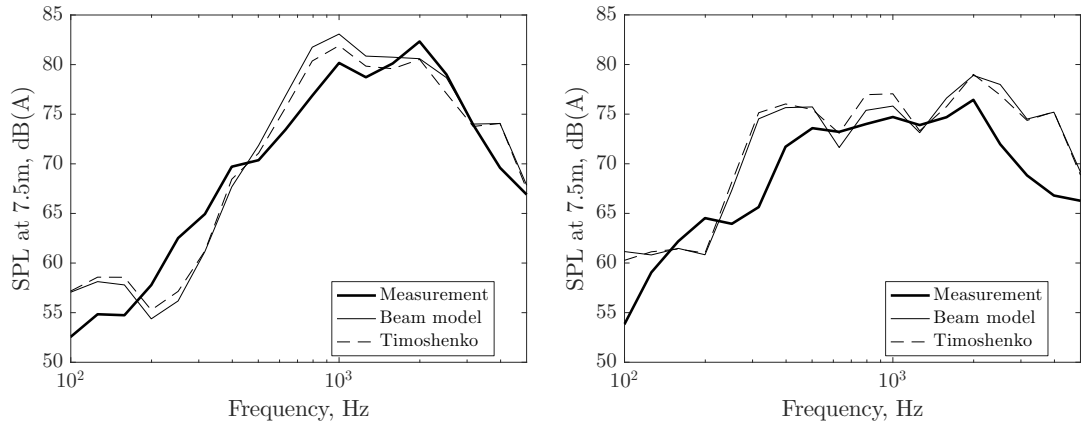

a) Renewed track b) Unrenewed track

Figure 6.4: Measured and predicted A-weighted sound pressure level at 7.5 m for Fishbourne site

Overall, for both tracks the main trend of the measured sound pressure level is reproduced in the predictions, although, the predictions for the renewed track provide a better agreement with the measured results especially at frequencies above 2 kHz. At lower frequencies, the predictions using the two models have slight differences. At higher frequencies, above 3 kHz, where the sound pressure level is mainly controlled by the wheel contribution, the two predictions are similar to each other. The main differences are therefore seen between 400 Hz and 3 kHz, where for the renewed track the present beam model gives overall a higher prediction than the Timoshenko beam model, while the opposite is true for the unrenewed track. For the unrenewed track, above 2 kHz, the two models show a high deviation from the measured data which is likely to be due to acoustic propagation effects (i.e. ground reflection) or the roughness data used.

The overall A-weighted levels are tabulated in Table 6.2, along with the separate contributions of the wheel, rail and sleeper. For the renewed track, the sound pressure level is more influenced by the rail contribution for both models, whereas for the unrenewed track, the levels of wheel, rail and sleeper contributions are more similar to each other.

Table 6.2: Overall A-weighted sound pressure level at 7.5 m for Fishbourne site in dB(A).

	Renewed			Unrenewed		
dB(A)	Current	Timoshenko	Measured	Current	Timoshenko	Measured
Wheel	80.4	80.2	-	81.5	81.3	-
Rail	88.9	87.7	-	83.2	82.3	-
Sleeper	73.4	75.3	-	81.1	82.9	-
Total	89.6	88.6	88.3	86.8	87.0	84.1

Figure 6.5 shows the predicted sound pressure level spectra for the present and Timoshenko beam models for the overall level as well as separate levels of the wheel, rail and sleeper noise predicted for the renewed track. In terms of the overall level in Fig. 6.5(a), the main difference between the two models is seen between 400 Hz and 3 kHz where the prediction using the Timoshenko beam model is about 3 dB lower. In the frequency range between 300 Hz and 1 kHz, the wheel contribution using the Timoshenko beam model is smaller than that for the present beam model. The reason for this difference is likely to be due to the cross mobility, where as seen in Section 5.2.3, the two models provide different results. In order to derive the parameter XdB, in Section 5.8, the asymptotic behaviour of the cross mobility was considered at either end of the spectrum (i.e. below 300 Hz and above 2 kHz). Thus, at frequencies below 300 Hz and above 2 kHz, the wheel contribution is expected to be similar since the cross mobilities are also similar. The rail contributions for the Timoshenko beam model are consistently lower than for the present beam model, while the opposite is observed for the sleeper contribution.

Equivalent results are presented in Fig. 6.6 for the unrenewed track. Overall, the same conclusions can be drawn, with two noticeable differences. Firstly, the differences in

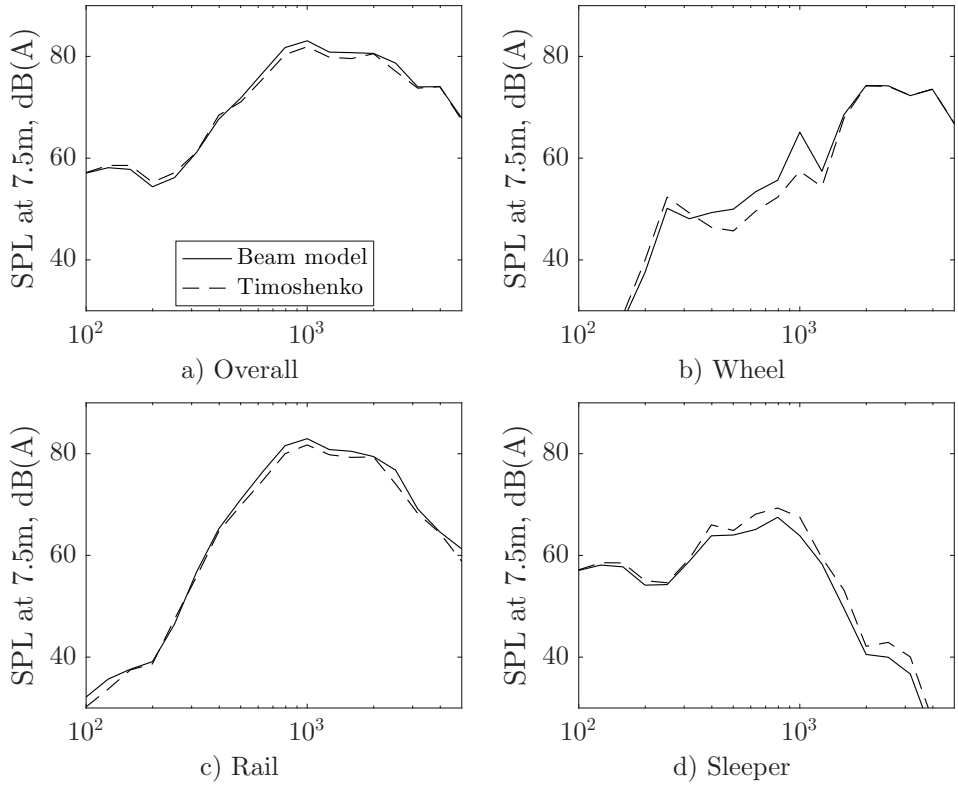

Figure 6.5: Comparison of present and Timoshenko beam models for total A-weighted sound pressure levels at 7.5 m and individual contributions of wheel, rail and sleeper - renewed track

wheel contribution to the sound pressure level at frequencies between 200 Hz and 1 kHz are more pronounced than for the renewed track. In addition, the sleeper sound pressure level from the predictions using both models has a more similar level to that of the rail at mid-frequencies. This is seen to influence the overall levels at frequencies up to about 1 kHz. These observations are also in line with the sound pressure levels presented in Table 6.2.

In order to identify the relative contribution of the wheel, rail and sleeper components to the total noise, their SPL spectra are compared in Fig. 6.7 along with the total spectrum for the current beam model, as an example. Here it is seen that at lower frequencies, the sleeper dominates the response, and thus the total sound pressure level up to 300 Hz. Above 300 Hz and up to about 2.5 kHz, the rail is the dominant noise source, and above 2.5 kHz the wheel component is seen to determine the total noise level.

The total sound power radiated by each wave for one wheel is shown in Fig. 6.8, where no A-weighting has been applied. Firstly, some general remarks can be made for the two tracks. As expected, the contribution of the axial wave is minimal. Similarly, a negligible contribution is expected for the warping wave, which is about 35 dB less than the total sound radiated over the whole frequency spectrum. The vertical evanescent wave has a similar contribution to the corresponding propagating wave at lower frequencies (where

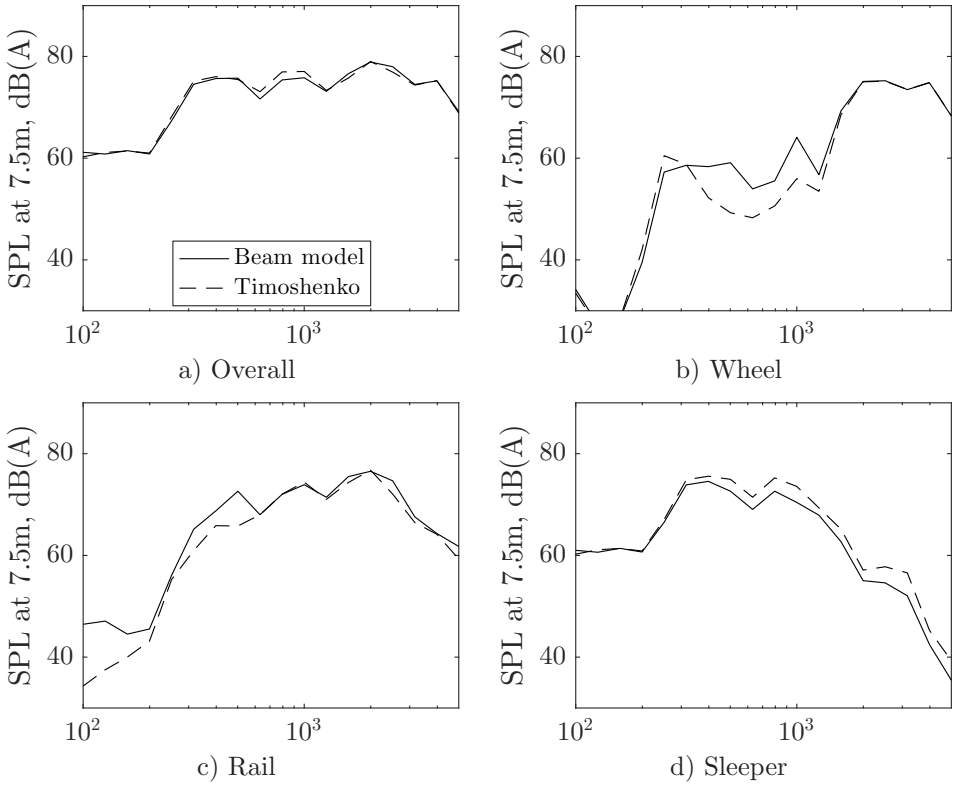

Figure 6.6: Comparison of present and Timoshenko beam models for total A-weighted sound pressure levels at 7.5 m and individual contributions of wheel, rail and sleeper - unrenewed track

the decay rates are equally high) and drops at higher frequency. The behaviour of wave type II is opposite to this, with a small contribution at low frequencies, increasing at higher frequency. At frequencies above 1 kHz, it has a similar contribution as that of the lateral wave type I.

Comparing Fig. 6.8(a) and (b), the vertical wave is seen to dominate the rail sound power level for the renewed track. In contrast, for the unrenewed track, the sound power level of lateral wave type I is higher than that of the vertical wave up to 125 Hz, and has similar level to the vertical wave type i between 300 Hz and 500 Hz.

Table 6.3 shows the overall sound power rail contributions for the individual waves. From this table, it is again seen that the contribution of wave type iii (the axial wave) is negligible for both the renewed and unrenewed tracks. Similarly, the contribution of wave types Le and w is also small. For the renewed track, a higher contribution than the unrenewed track is observed for wave type i, a smaller contribution for wave type I, while similar levels are seen for wave type II.

In the following section, measured track decay rates used in Chapter 5 are introduced in the model and used to adjust the predicted responses.

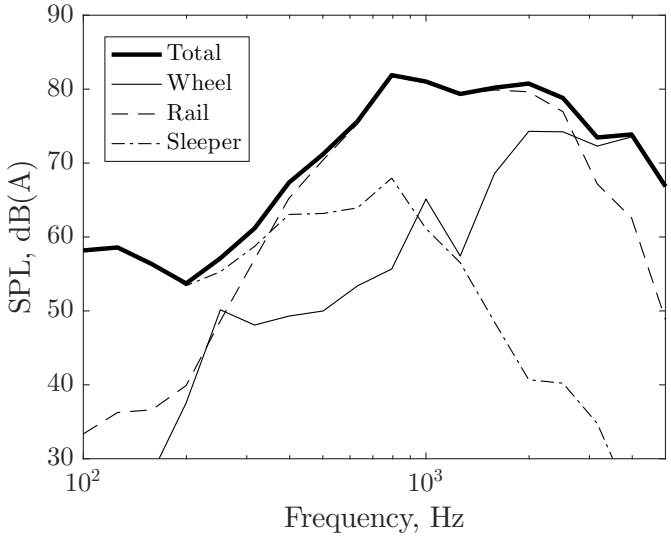

Figure 6.7: Relative contributions of wheel, rail and sleeper components to total A-weighted noise spectrum at 7.5 m using the current beam model for Fishbourne - renewed track

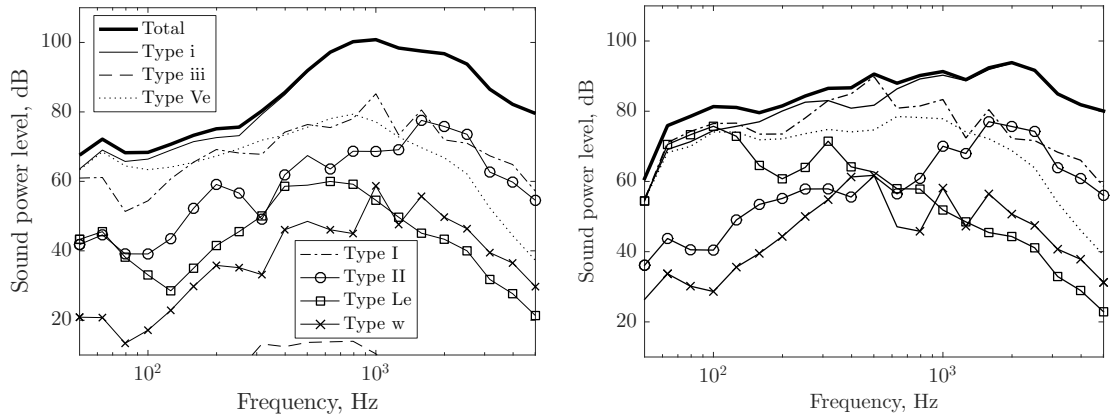

a) Renewed track b) Unrenewed track

Figure 6.8: Individual wave sound power contributions to the total rail sound power level

6.3 Predictions using measured track decay rates

So far the measured track decay rates have only been used to fit the predicted track decay rate from the two models to the measured one, in order estimate the track parameters required for the models. In TWINS, the measured track decay rates can also be used as an input, modifying the propagation constant. This process can lead to improved predictions, although this is not always the case as found by Jones and Thompson [24].

In this section, the process of substituting the decay rates into the propagation constant is first presented. Then the Timoshenko beam model is used with a modified approach, based on an iterative process to modify the propagation constant. For the present beam model, the same approach is used to modify the propagation constant for wave types i

Table 6.3: A-weighted sound power levels for individual waves in the rail in dB(A).

	Vertical waves			Lateral waves				Total
Wave type	i	iii	Ve	I	II	Le	w	
Renewed	106.9	18.6	83.7	88.2	82.7	63.9	62.0	107.0
Unrenewed	100.3	-0.3	84.2	91.0	82.4	68.9	64.5	100.9

and I, while for wave type II a simple adjustment is suggested. Finally, this relationship is used in conjunction with the modified process for the present beam model and the total sound pressure predictions are compared with those from the Timoshenko beam model.

6.3.1 The use of measured track decay rates in TWINS

When measured track decay rates are available (for either the vertical or lateral directions, or both), these can be used in TWINS to replace the real (decaying part) of the predicted propagation constant (s) for the corresponding propagating waves of the Timoshenko beam model, while maintaining the predicted imaginary part. This is done by assuming that the propagating waves control the overall decay rate, which is reasonable, as they have the lower decay rate (see Fig. 5.6) amd he evanescent waves have a higher decay rate. However, the overall track decay rate can then be found by using the experimental method [120] on the model and this will differ from the values used for the propagating waves, as shown by Jones et al. [121]. When a more sophisticated model is used accounting for more than one propagating waves in any direction, an iterative approach has to be used instead. This is due to the fact that the measured decay rate includes the combined effect of all the waves in that direction.

The overall predicted decay rate obtained using the original model, the adjusted decay rate found by using the experimental method on the model (with measured values substituted in the propagating wave) and measured track decay rate are shown in Fig. 6.9 for the renewed track, shown separately for the vertical and lateral directions.

Since the propagation constant of the wave with the lower decay rate for each direction is adjusted, the overall decay rate becomes more similar to the measured decay rate but there are slight differences due to the presence of the evanescent waves. For the vertical direction, slight differences are seen above 300 Hz. For the lateral direction, substantial differences can be seen above 160 Hz. Although the measured and predicted track decay rates are similar for frequencies between 160 Hz and 1 kHz, the adjusted track decay rate is higher. This indicates that the lateral evanescent wave has a high influence on the overall track decay rate in that frequency region. Above 1 kHz, the adjusted track decay rate is similar to the measured data.

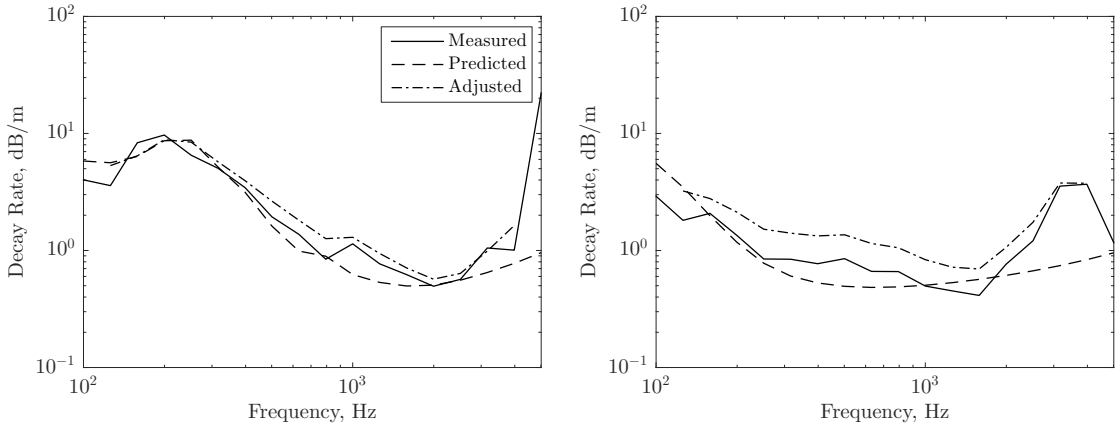

a) Vertical b) Lateral

Figure 6.9: Predicted, adjusted and measured track decay rates for Fishbourne site using the Timoshenko beam model - renewed track

As seen from Fig. 6.9, the adjusted decay rate obtained using the direct approach to modify the real part of the propagation constant is not the same as the measured one due to the presence of the evanescent wave. In order for the final decay rate to be the same as the measured decay rate, an iterative approach is proposed here. In the first step of the iterative approach, the above process is utilised where the individual wave decay rates are modified according to the direct approach and the adjusted overall track decay rate is calculated using the experimental method [120] on the model. In the next step, the decay rate used as an input to the model in the previous step is weighted at each frequency, depending on whether the adjusted decay rate is higher or lower than the measured one (weighting factor lower or higher than unity respectively). The process is then repeated until the adjusted decay rate matches the measured one within a certain error tolerance, here set at 1%. Due to the similar levels of decay for the type i and Ve waves for the vertical direction and type I and Le waves for the lateral direction, the first two frequency bands have been excluded from this process. For the renewed track, on average nine iterations are required per frequency for the vertical direction (iteration steps averaged over the number of bands), while four are required for the lateral direction.

The decay rates obtained following the iterative procedure described above are shown for the vertical wave type i in Fig. 6.10(a) and for the lateral wave type I in Fig. 6.10(b). Since the decay rate of the adjusted lateral wave type I is just above the 0.2 dB/m limit for the frequency band around 1500 Hz (cf. Section 5.2.4), according to [120], a longer length of track needs to be considered for the estimation of the decay rate (see also Eq. 5.9). Thus, in order to avoid limiting the minimum decay rate estimated when using the iterative approach, for both tracks a track length of 132 sleepers is considered (double the length suggested in [120]). Overall, the adjusted decay rate tends to be lower than the measured one. An exception to this is seen at 160 Hz and 200 Hz for the vertical

direction. In Section 5.7.2, the decay rates were fitted for frequencies between 250 Hz and 800 Hz, resulting in the resonance frequency of the rail mass on the pad stiffness being over-predicted. Using the iterative approach, a significantly higher wave decay is required to increase the overall decay rate (note that the evanescent wave maintains a high decay rate until the cut-on of wave type i), leading to the overshooting of the adjusted decay rate for wave type i at the frequency bands of 160 Hz and 200 Hz.

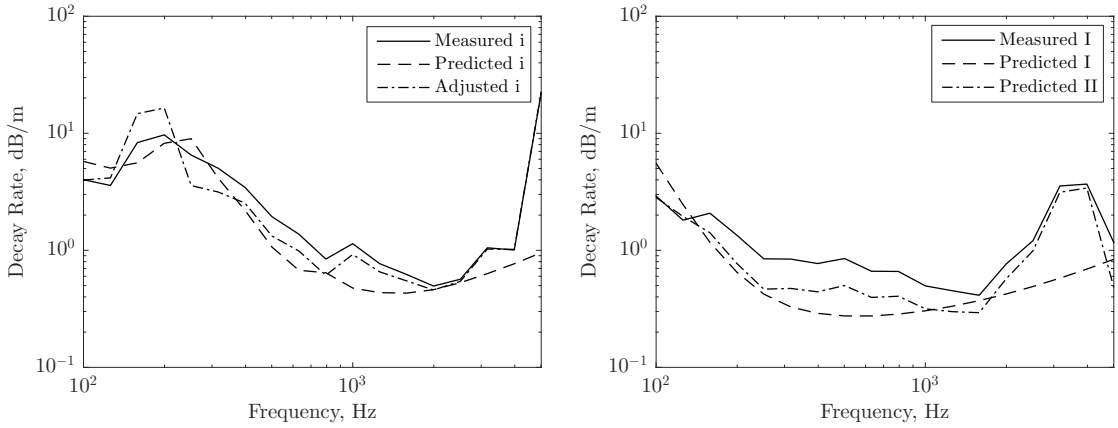

a) Vertical wave type i b) Lateral wave type I

Figure 6.10: Decay rates based on iterative approach using the Timoshenko beam model - renewed track

Results for the total sound pressure level are shown in Fig. 6.11(a) for the renewed track. Four lines are shown, one corresponding to the measured sound pressure level and three for the sound pressure level estimated using the predicted, measured (i.e. direct approach) and adjusted (iterative approach) track decay rates. Differences between the results obtained using the predicted track decay rates and those using the measured or adjusted track decay rates are seen over the entire frequency range, with all three estimates having similar deviations from the measured sound pressure level.

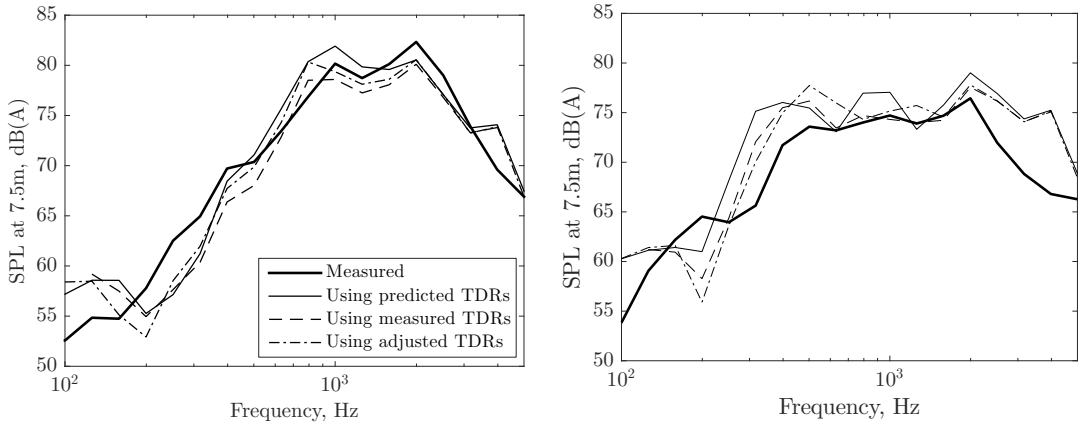

a) Renewed track b) Unrenewed track

Figure 6.11: Sound pressure level using the Timoshenko beam model in TWINS using measured track decay rates

Similarly, the sound pressure level for the unrenewed track is shown in Fig. 6.11(b). Although, at the frequency band around 200 Hz, the sound pressure level predicted using the measured track decay rates has a higher deviation from the measured level than that using the predicted decay rates, an improvement is seen between 250 Hz and 3 kHz.

6.3.2 The use of measured track decay rates when accounting for additional waves

The process of replacing the real part of the propagation constant with the measured track decay rates is straightforward to implement for the case of the Timoshenko beam model used in TWINS, as only one propagating wave exists in each direction for the frequency range of interest. For the current model, this is more complicated for the lateral waves as two coupled waves exist, namely types I and II, whereas the measured decay rate represents their combined effect. Here, this is accommodated within the iterative process described in Section 6.3.1 with a small modification. For the lateral direction, at each frequency, first the predicted decay rate of wave type I (Δ_I^P) is replaced by the total measured decay rate for the lateral direction (Δ_l^M), as for the Timoshenko beam model. Then, for wave type II (Δ_{II}^P), the same measured decay rate is used but weighted by the ratio between the predicted decay rates of the type I and II waves, i.e.:

$$\Delta_{II} = \frac{\Delta_{II}^P}{\Delta_I^P} \Delta_l^M \tag{6.7}$$

thus maintaining the relative level of the decay rates of wave types I and II. This is applied to the wave type II only for frequencies after free wave propagation starts to occur.

Once the individual wave decay rates have been substituted using the above process, the adjusted overall track decay rate after the first iteration can be calculated. The process is then repeated for both the vertical and lateral directions until the desired convergence criterion is reached, where for the type I and II waves, the ratio in Eq. (6.7) is maintained.

Examples of using the above iterative process accounting for the lateral wave type II are shown in Fig. 6.12 for the renewed track at Fishbourne, for the vertical and lateral directions, along with the predicted and measured track decay rates. No significant differences are seen between Figs 6.9(a) and 6.12(a), for the vertical decay rate. The main differences are seen in the lateral decay rate, where a higher decay rate is observed for the present beam model compared with the Timoshenko beam model for both the predicted and adjusted track decay rates.

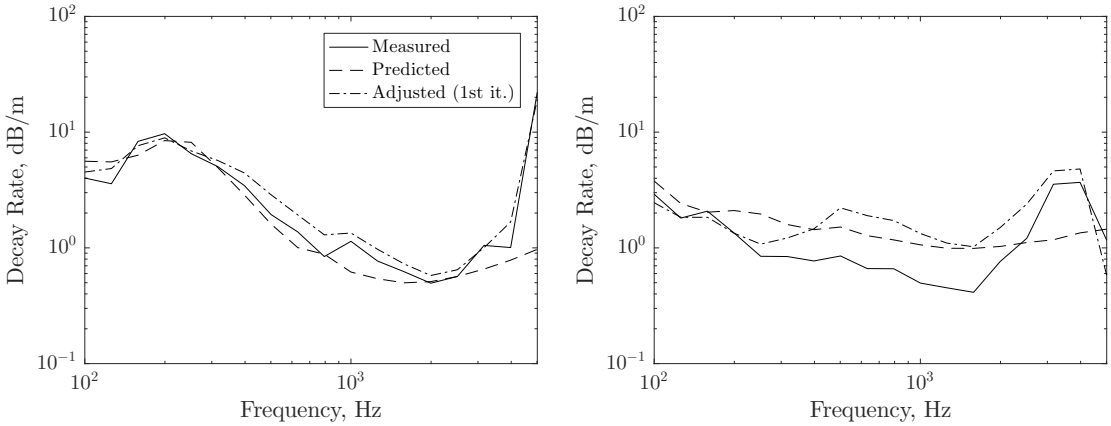

a) Vertical b) Lateral

Figure 6.12: Predicted, adjusted (after first iteration) and measured track decay rates for Fishbourne site using the current beam model - renewed track

Figure 6.13 shows the predicted and adjusted (final) decay rates of wave types i, I and II, along with the measured decay rates for the vertical and lateral directions. For the lateral direction, a significant reduction in the wave decay rate is seen for both lateral wave types I and II, between 200 Hz and 1.6 kHz. Although the individual waves have a low decay rate, the warping wave (which has a high decay rate) has a significant contribution in the point mobility (see Section 5.2.1), thus increasing the overall decay rate. For the vertical decay rate, on average, seven iteration steps are required at each frequency band to achieve 1% difference to the measured decay rate. Similarly, for the lateral decay rate, the number of iterations is eight for the same level of accuracy.

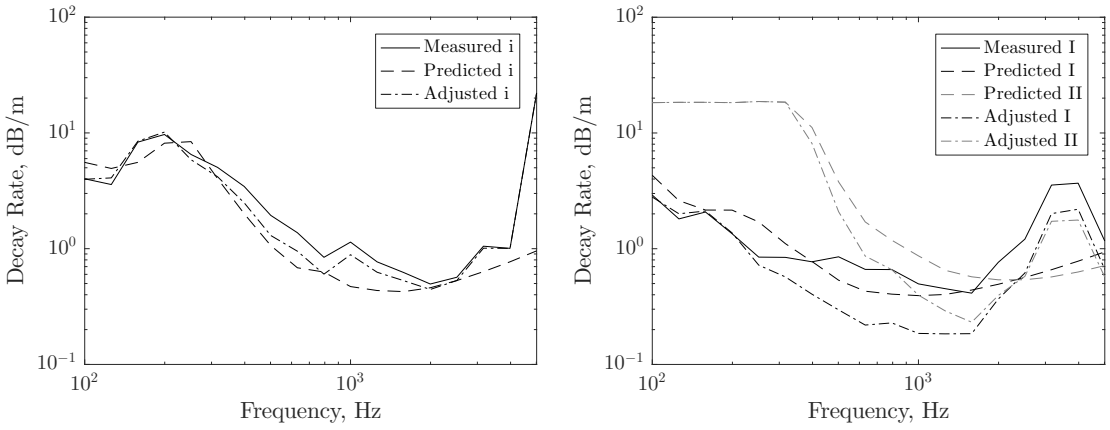

a) Wave type i b) Wave type I and II

Figure 6.13: Initial and adjusted predicted decay rates for individual waves for Fishbourne site - renewed track

From Fig. 6.13, it can be concluded that the predicted decay rate for propagating waves is lower than the measured decay rate due to the presence of other waves. In the following section, results for the pass by noise are presented for both the present and Timoshenko beam models using the above mentioned approach.

Given the level of uncertainty in the fitted track parameters, measured track and wheel roughness, as well as the measured decay rate fitting, it is not possible to conclude which beam model performs better. Nevertheless, the present beam model incorporates features that are not present in the existing model.

6.3.3 Rolling noise predictions using decay rates from the iterative approach

Although the iterative approach was not shown to necessarily give an improvement in the comparison of the Timoshenko beam model and the measured data, the measured track decay rates cannot be used for the present beam model without it. This is due to the fact that, as discussed in Section 6.3.2, the measured lateral decay rate accounts for the combined effect of wave types I and II. Therefore, estimates for the total sound pressure level using the two models with the iterative approach are compared with the measured levels in Fig. 6.14.

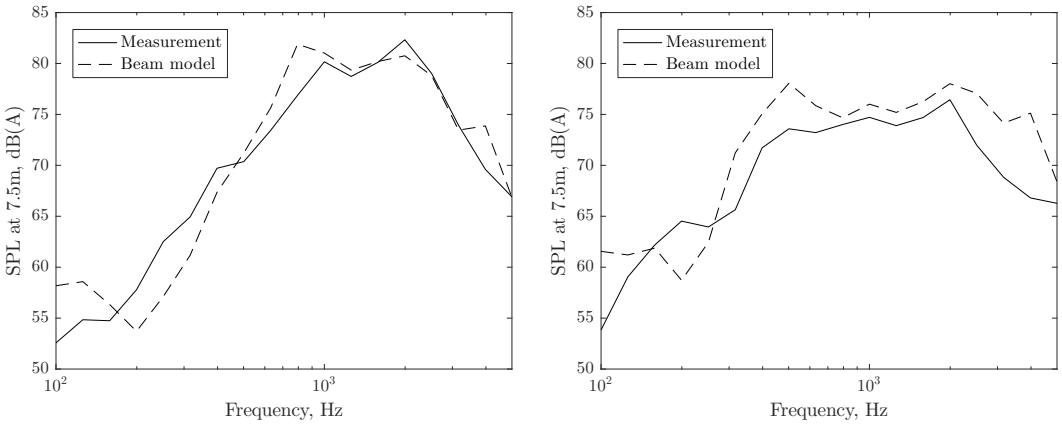

a) Renewed track b) Unrenewed track

Figure 6.14: Measured and predicted A-weighted sound pressure level at 7.5 m for Fishbourne site using the current and Timoshenko beam models with the iterative approach

Again, the predictions for the renewed track provide a better agreement with the measured data than those for the unrenewed track especially for frequencies above 2 kHz, although, for both tracks the main trend of the measured sound pressure level is well reproduced in the predictions.

The overall A-weighted SPL values are tabulated in Table 6.4, along with the separate contributions of the wheel, rail and sleeper. The iterative approach is seen to reduce the rail and sleeper contributions in comparison to the levels presented in Table 6.2. This reduction is seen to improve the total sound pressure level predicted for the current beam model for the renewed track when compared to the measured level.

Table 6.4: Overall A-weighted sound pressure level at 7.5 m for Fishbourne site in dB(A) using decay rates based on the iterative approach.

	Renewed		Unrenewed	
dB(A)	Current	Measured	Current	Measured
Wheel	80.4	-	81.5	-
Rail	88.1	-	83.0	-
Sleeper	73.1	-	81.5	-
Total	88.9	88.3	86.8	84.1

The total sound power radiated by each wave is shown in Fig. 6.15, where no A-weighting has been applied. Overall, the behaviour of the different waves is similar to that in Fig. 6.8. Slight differences are seen for the lateral wave type I, where it has a higher contribution when using the iterative approach to modify the propagation constant. Here, for the unrenewed track, the sound power level of lateral wave type I is higher than that of the vertical wave type i up to about 125 Hz and between 200 Hz and 500 Hz.

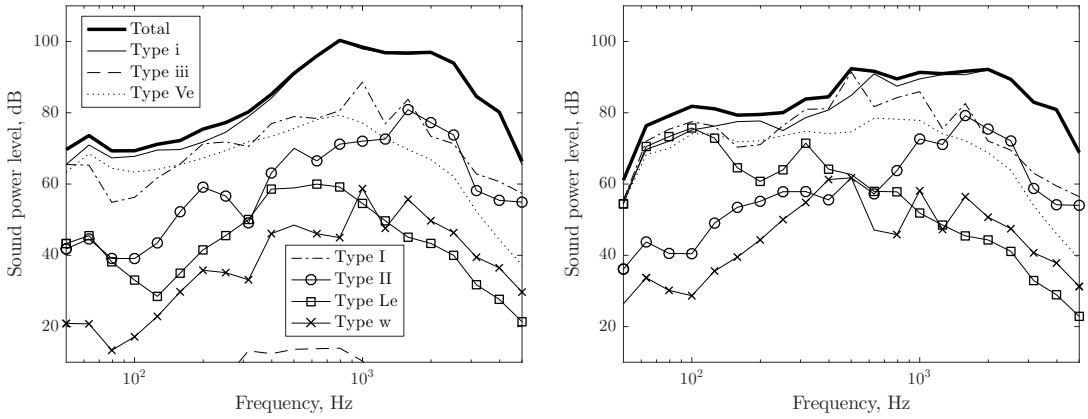

a) Renewed track b) Unrenewed track

Figure 6.15: Individual wave sound power contribution to the total rail sound power level

Table 6.5 shows the rail sound power contribution for individual waves. Again, no significant differences are seen compared with Table 6.3, apart from the fact that the relative contributions of vertical wave type i and lateral wave type I have become more similar for both tracks.

Table 6.5: A-weighted sound power levels for individual waves in the rail in dB(A), using the iterative approach.

	Vertical waves			Lateral waves				Total
Wave type	i	iii	Ve	I	II	Le	w	
Renewed	105.9	18.6	83.7	91.3	85.0	63.9	62.0	106.1
Unrenewed	99.5	-0.3	84.2	92.4	83.2	68.9	64.5	100.4

6.4 Effect of contact point location

As described in earlier chapters and also by Vincent et al. [26], one of the most important factors in considering vertical/lateral coupling is the location of the contact point on the rail head. The track model developed in this work readily allows the study of the effect of the contact position on rolling noise. Results for the sound pressure level at 7.5 m from the track are shown in Fig. 6.16, for both track conditions, for several positions of the contact in the rail model, from -20 mm to 20 mm from the railhead centre.

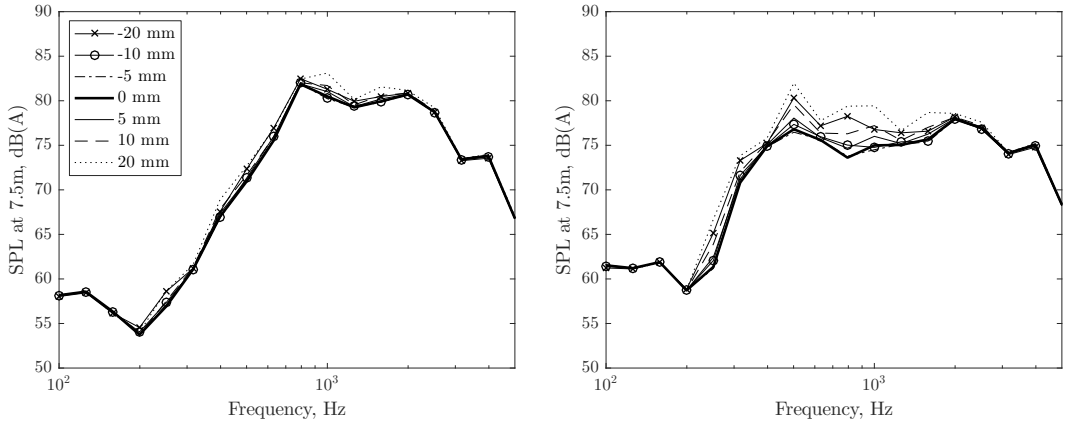

a) Renewed track b) Unrenewed track

Figure 6.16: Effect of contact point location on track sound pressure level

As can be seen from Fig. 6.16(a), the contact point position has a limited effect for the renewed track. In contrast, for the unrenewed track in Fig. 6.16(b), the changes in the contact point position significantly influence the sound pressure level between 200 Hz and 3 kHz, i.e. in the region where the rail is the most dominant source.

Table 6.6: Effect of contact point location on track A-weighted sound power level.

	Renewed		Unrenewed	
Position	Vertical	Lateral	Vertical	Lateral
-20 mm	105.7	97.3	99.5	98.1
-10 mm	105.9	91.6	99.6	91.9
-5 mm	106.0	88.0	99.6	87.6
0 mm	106.0	88.4	99.6	88.6
5 mm	106.0	92.2	99.6	93.0
10 mm	105.9	95.4	99.5	96.2
20 mm	105.7	99.5	99.4	100.4

Table 6.6 shows the total A-weighted sound power level for the contact positions considered in Fig. 6.16, split into vertical and lateral contributions. From this table, it is seen that the contribution of the vertical waves is not sensitive to the contact position. In contrast, the contribution of the lateral waves to the total sound power level is very sensitive to the contact position, with the farthest positions (here -20 mm and 20 mm)

giving increases of up to 10 dB. Overall, the contribution of the lateral waves to the total sound power level is smaller than that of vertical waves.

For the renewed track, the difference between the contribution of vertical and lateral waves is between 17 dB (for contact at 0 mm) and 6 dB (for contact at 20 mm). Thus, as also seen in Fig. 6.16(a), the influence of the contact position is limited. For the unrenewed track, the relative contributions of the vertical and lateral waves are more similar, and as the contact position is moved away from the rail head centre, the difference becomes smaller. For an offset of 20 mm, the contribution of lateral waves exceeds that of vertical waves by 1 dB. Although the contribution of the lateral waves to the sound power level for the unrenewed track is similar to that of the renewed track, their relative contribution level is higher (see also Table 6.3). Thus, for the unrenewed track, increasing the distance of the contact point from the rail centreline leads to an increased total sound power level (see also Fig. 6.16(b)). Vincent et al. [26] reached similar conclusions using the parameter XdB to account for the cross-coupling based on the contact point location.

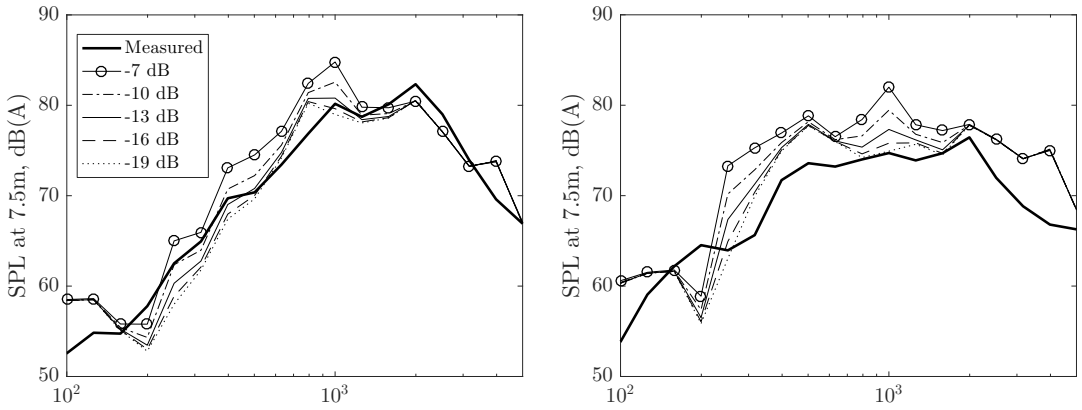

a) Renewed track b) Unrenewed track

Figure 6.17: Effect of parameter XdB on track sound pressure level

In Fig. 6.17, the effect of the parameter XdB on the track sound pressure level is investigated for the Timoshenko beam model, by varying XdB from -7 dB to -19 dB. In contrast with varying the contact position in the current beam model, XdB has an effect for both the renewed and unrenewed tracks. The effect of varying XdB, similar to the contact point location, is seen mainly for frequencies between 200 Hz and 2 kHz. For the case of the renewed track, Fig. 6.17(a), a value of around -10 dB seems to be the most suitable to give best agreement with the measured levels, while for the unrenewed track a value of -19 dB appears more appropriate. The problem remains, that these values cannot be linked with a contact point location, nor is it possible to determine the contribution of individual waves.

6.5 Conclusions

In this chapter, the model developed in the previous chapters has been implemented in TWINS, in order to predict rolling noise taking account of all sources of vertical/lateral coupling. The track parameters derived for the Fishbourne track site were used, and the results were compared with sound pressure measurements taken previously at the same site. Although it is not possible to assess directly whether the new model gives improved predictions, it allowed for the evaluation of the contribution of the individual waves, as well as the empirical process currently used within TWINS for estimating the cross mobility.

Overall, the noise radiated by the track is primarily controlled by the vertical rail response with a significant contribution from the lateral response. The axial and warping responses have a minimal effect on radiated noise from the track. Although allowing for torsion significantly affects the lateral response, the torsional wave by itself has a relatively small contribution to the noise at low frequencies. As frequency increases, its levels become similar to those of the lateral response. This is attributed to the fact that the rail head and foot radiate independently when the acoustic wavelength is smaller than the rail height.

An iterative approach has been introduced for modifying the propagation constant. Comparison with measured noise did not lead to firm conclusions. Nevertheless, this approach is essential when more than one propagating wave exists in any one direction, here the lateral.

By considering two different tracks, one with stiff pads and one with soft pads, it can be concluded that for tracks with soft pads, the contact location is not as critical as it is for those with stiff pads. For the latter, the vertical rail contribution becomes significantly smaller than for the track with soft pads, and comparable to the contribution of the lateral/torsional response. The value of the parameter XdB required in the classical TWINS model can be estimated by comparison of the cross mobility with the present model. However it is suggested that the current model is used, as this correctly accounts for the lateral/torsional coupling of the track.

Chapter 7

Conclusions

In order to fulfil the aims set out for this thesis, an analytical track model has been developed, based on a beam formulation. This model can more accurately account for the vertical, lateral and axial vibration of railway tracks, taking into account a variety of coupling mechanisms. The model has been validated against both a more detailed WFE model and measurements, showing very good agreement over the desired frequency range.

In addition, an improved flexible sleeper model has been introduced, taking into account not only the vertical, but also the axial, lateral and torsional vibration of the sleeper. The sleeper model has been validated with measurements performed in the laboratory showing very good agreement, apart from the first bending mode which is most influenced by the non-uniform geometry of the sleeper.

Finally, the track model has been used in TWINS to predict rolling noise and assess the effect of lateral and torsional wave contributions to the overall radiated noise. A process is also presented, by which measured track decay rates are not only combined with the predicted decay rates of the propagating waves (as previously used in TWINS), but are modified in an iterative manner until the predicted overall decay rate is the same as the measured one.

7.1 Summary of conclusions

The following conclusions can be drawn from the investigations presented in this thesis.

The inclusion of torsion in the dynamic models of railway tracks has a large effect on the dynamic behaviour of the track, especially through the changes in the lateral mobility. This affects the lateral response over the whole frequency range. Thus it is important for models that study the lateral vibration of rails and the coupling between the vertical and lateral directions to consider torsion.

In addition to the pure torsion theory, restrained warping during torsional behaviour has been taken into account, including both normal and shear stresses due to warping. This has been shown to affect the response at frequencies above 500 Hz. In contrast, the inclusion of shear deformations due to warping does not yield significant effects in the dispersion relationship of a free rail, only affecting the results at higher frequencies. The shear deformations due to warping have a minimal effect on the forced response of a supported rail.

The shear-centre eccentricity introduced by cross-sectional asymmetry for typical rail cross-sections has not been found to have a significant influence on the forced response for railway track applications. In the case where the shear centre and the mass centre of the beam coincide, the sources of coupling for a straight beam are mainly limited to those due to externally applied loads. When the two centres do not coincide, the lateral, and in the case of asymmetric rail also the vertical, motion of the beam will couple with the torsional motion. For the singly symmetric case, the shear-centre eccentricity is seen to affect the lateral response at higher frequencies. For the asymmetric case, the shear-centre eccentricity was not found to be more influential than for the singly symmetric case considered.

When the curvature of the beam is considered, the lateral bending motion of the rail is coupled with the axial motion. The major difference in this case is the presence of a non-zero cut-on frequency for the extensional wave. Similarly, for the vertical bending and torsion, a non-zero cut-on frequency exists for the torsional wave. In the case of the forced response of curved rails, the effect of curvature is found to be minimal for realistic curvatures of mainline and tram tracks, and instead it is found that a straight rail model is sufficient for radii greater than 20 m.

The second most important source of coupling, after the inclusion of torsion, is that of the foundation location. A two-layer foundation was introduced including a rigid body translation and rotation of a bibloc sleeper, as well as bending and rotation of a flexible sleeper in all three directions. The foundation reaction forces have a significant influence on the overall behaviour of the rail response, especially for the lateral and torsional response. The foundation eccentricity affects the lateral track stiffness, reducing significantly the lateral cut-on frequency and increasing the torsional one. The torsional pad stiffness, itself influenced by the vertical pad stiffness, will significantly affect the lateral vibration of the rail due to the coupling of the lateral and torsional responses. By fitting the predicted track decay rate to measured data, the proposed model yields significantly different estimates of the lateral pad stiffness of the track, compared with the classical Timoshenko beam model. It is seen from the measured data and the fitted parameters that the lateral stiffness is affected by the clips. Again, the effects of including rail pad eccentricity seem to be most influential for the lateral mobility.

In comparison with more advanced numerical models and measured data, the developed model gives improved predictions for the response of railway tracks relative to the Timoshenko beam, especially for the lateral direction. Although the predictions of the forced response show an improvement when compared with measured data, in order to extend the frequency range of application, cross-sectional deformations would need to be considered, such as for example, web bending, double web bending and foot flapping for a typical Vignole rail. The frequency range of validity of the developed model is up to 3 kHz for the vertical direction and up to about 1 kHz for the lateral direction. For grooved tram rails, the frequency range of validity is limited to 2 kHz, mainly due to the lower overall stiffness of the cross-section, making the contribution of the cross-sectional modes more influential at lower frequency.

By implementing the developed beam model in TWINS and making predictions of rolling noise, it is found that the noise radiated by the track is primarily controlled by the vertical rail response. The lateral response has a significant contribution to the overall response. The total noise contribution of lateral waves becomes more similar to that of vertical waves for a track with stiffer railpads, and can even exceed it. The axial and warping responses have a minimal effect on radiated noise from the track. Although allowing for torsion significantly affects the lateral response, the torsional wave by itself has a relatively small contribution to the noise at low frequencies. As frequency increases, its levels become similar to those of the lateral response. This is attributed to the fact that the rail head and foot radiate independently when the acoustic wavelength is smaller than the rail height.

An iterative approach has been suggested, based on which the propagation constant can be modified so that the total track decay rate predicted using the Timoshenko or present beam models matches the measured track decay rate. Although firm conclusions could not be made as to whether this approach leads to improved noise predictions, it is essential when more than one propagating wave exists in any given direction. Further investigation, as well as a way to measure the decay rate of wave type II, could lead to an increased reliability of using measured track decay rates in noise predictions.

Finally, the model allows for the contact location at the wheel/rail interface to be adjusted explicitly, and can provide a physical way to determine the empirical factor XdB used in the existing model in TWINS. In addition, the contribution of lateral and torsional waves can be separated and quantified. It is seen that at certain frequencies, the noise radiated due to lateral waves can exceed that of vertical waves when the track support stiffness is high. For tracks with lower stiffness, the influence of the contact location on the overall sound pressure level is found to be minimal.

7.2 Recommendations for future work

To understand more fully the effects of vertical/lateral coupling on noise generated from railway operations, the following aspects can be suggested for future investigation:

- Extend the model to account for the discrete nature of the support. The effect of discrete supports on vertical bending of the rail has been shown not to be significant for rolling noise predictions [39] but is important for corrugation. Although it is expected to be less significant for the lateral direction, as the support stiffness is lower, it should still also be investigated in terms of the lateral and torsional responses.
- Effect of curving behaviour on the loads applied to the track. Although rail curvature has been shown to have a minimal effect on the vibration of the rail, the steady state curving behaviour of a vehicle can change the magnitude and location of the applied loads. Utilising results from vehicle dynamic curving simulations of a vehicle negotiating a curve, the implications of track curvature on rolling noise can be investigated, since the contact position can be explicitly used in the developed model.
- One of the main limitations of most analytical track models, including the present one, is the neglect of cross-sectional deformations. The step required in order to improve the frequency limits of applicability of such models, is to incorporate the cross-sectional deformations, mainly those of web bending and double web bending. This could be achieved either by considering the cross-sectional flexibility in the fundamental theory, or potentially by introducing additional degrees of freedom at the centroid to correct for the cross-sectional behaviour (e.g. similar to warping).
- Investigation into the effects of temperature on rail vibration. The main influence of temperature on rolling noise is that due to the variation of the rail pad stiffness with temperature [28]. Temperature effects though, can also be considered in the rail, by the introduction of tensional/compressional forces. These loads affect both the bending and torsional dynamic behaviour of the rail, and if the loads reach significantly high values, they might influence the noise generated.
- Further development of the iterative approach for adjusting the propagation constant to match measured decay rates. When more than one propagating wave exists in any given direction, it is not possible to use a single set of measured track decay rates in that direction to separate the decay rates of individual waves. Measurement of the decay rate of wave type II can be achieved by selecting an additional location for the measurement of vertical or lateral track decay rates. Collection of such data, could be used to further develop the iterative approach and achieve a more robust process for modifying the propagation constant with measured track decay rates for use in the rolling noise prediction process.

- Perform a parametric study to identify which track parameters influence the relative level of vertical and lateral rail components of noise, as well as those of the sleeper and wheel. By varying the main track parameters, e.g. vertical railpad stiffness, ideal values can be found which minimise the total noise level generated. Although such studies have been performed in the past, the improved description of the lateral rail behaviour developed here could lead to further insight into the noise generation mechanism.

Appendix A

Derivation of warping factor and foundation resistance

A.1 Derivation of linear warping factor

The warping of the cross-section of the rail is defined based on the warping function, $\phi(y, z)$. It is assumed that the warping function at the rail foot is a linear function of y and z, i.e. $\phi_f = yz\kappa_{w,f} = e_s z\kappa_{w,f}$, where e_s is the vertical distance between the rail foot and the rail shear centre $(y_f - e_y)$.

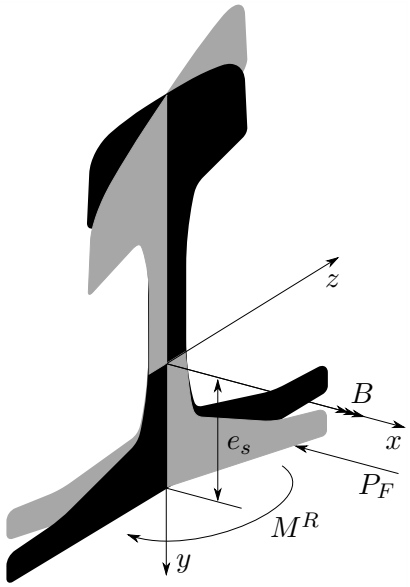

Figure A.1: Bi-moment due to warping foundation resistance

To define the warping factor for the rail foot, it is sufficient to fit a linear function in the actual warping function provided by COMSOL (see Fig. 2.5). Figure A.2 shows the warping function for the foot, and a linear fitted line.

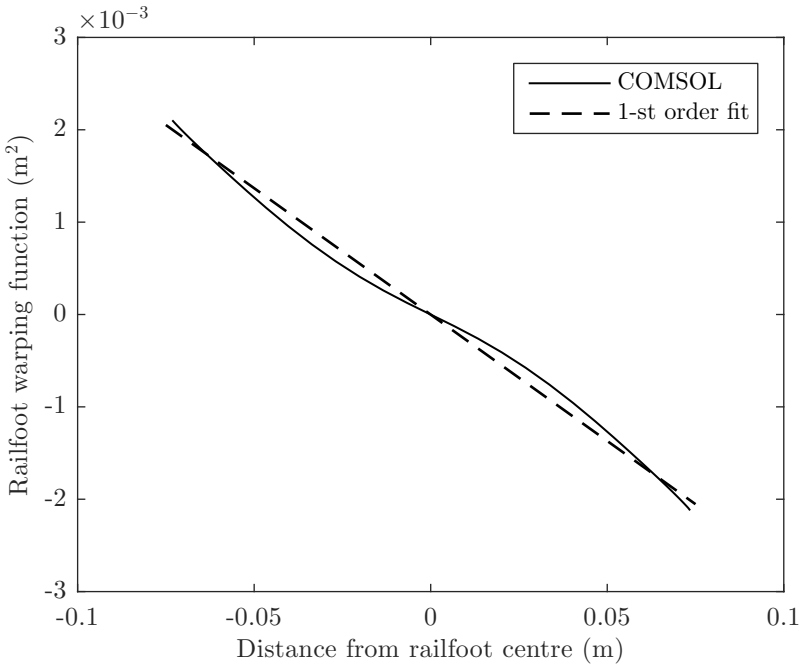

Figure A.2: Rail foot warping function and linear fitting

From this figure, it can be seen that the linear fit will tend to overestimate the amount of warping of the rail foot. This gives a linear factor $\kappa_{w,f}$ of -0.6.

A.2 Derivation of warping foundation resistance

The warping resistance due to the foundation can be defined similarly to the resistance to bending. Firstly, the resistance of an infinitesimal element is considered subjected to an axial force, and then this is integrated over the width of the railpad.

The bi-moment at the shear centre due to a single axial force (F) at a point is given by:

$$B_s = P_F \phi_F \tag{A.1}$$

When the cross-section undergoes warping, each point of the rail foot has an axial displacement due to warping, given by

$$u^w_{x,f} = \phi_f(y_f, z) f_w \tag{A.2}$$

The axial force at the rail foot due to the warping resistance of the foundation becomes:

$$P_F = \frac{k^{pp}_x}{l_p} u^w_{x,f} dz \tag{A.3}$$

Thus:

$$B_s = k_x^{pp}\phi_f^2(y_f, z)f_w \tag{A.4}$$

$$= (e_s z\kappa_{w,f})^2 \frac{k_x^{pp}}{l_p} f_w dz \tag{A.5}$$

Integrating the above expression over the railpad width it follows that:

$$B = \int_{-l_p/2}^{l_p/2} B_s dz \tag{A.6}$$

$$= \int_{-l_p/2}^{l_p/2} (e_s z\kappa_{w,f})^2 \frac{k_x^{pp}}{l_p} f_w dz \tag{A.7}$$

$$= (e_s\kappa_{w,f})^2 \frac{k_x^{pp}}{l_p} f_w \int_{-l_p/2}^{l_p/2} (z)^2 dz \tag{A.8}$$

$$= (e_s\kappa_{w,f})^2 \frac{l_p^2}{12} k_x^{pp} f_w \tag{A.9}$$

By dividing by the spacing between the supports, the foundation resistance due to warping per unit length is derived as:

$$k_w = (e_s\kappa_{w,f})^2 \frac{l_p^2}{12} k_x \tag{A.10}$$

where $k_x = k_x^{pp}/l_{ss}$ is the axial foundation resistance per unit length.

Appendix B

The track response in TWINS

In order to obtain the interaction forces in TWINS, the rail receptance is required for the vertical (α_{yy}) and lateral (α_{zz}) directions as well as the cross receptance at the contact point (α_{yz}). Once the contact forces due to the wheel/rail interaction are obtained by coupling the rail and wheel receptances, the spatially averaged response for a particular degree of freedom is given by:

$$\overline{v_j^2} = \frac{2}{L}\int_0^{L/2} |u_j(z)|^2 \, dx \approx \sum_n |\psi_{jn}|^2 \left| \sum_k F_k \beta_{kn} \right|^2 \left(\frac{1}{\delta_n L} \right) \tag{B.1}$$

where β_{kn} is the receptance per wave n for a force F_k in direction k, ψ_{jn} are the wave shapes (eigenvectors) for each direction j, L is the length of the rail contributing to the sound radiated, x is the longitudinal direction and δ_n is the real part of the propagation constant s (decaying part) for each wave, where s is related to the wavenumber by:

$$s = i\xi \tag{B.2}$$

The general response can be equivalently reconstructed based on the wave amplitudes (A_n) and the waveshape of each wave (ψ_{jn}) as, for example:

$$u_j(x) = \sum_n A_n \psi_{jn} e^{-s_n x} \tag{B.3}$$

where

$$A_n = \sum_k F_k \beta_{kn} \tag{B.4}$$

The sleeper response is obtained in the same manner, where the equivalent waveshapes are given by the ratio of sleeper to rail response. In addition, only the vertical sleeper response, taken as the square root of the spatial average of the squared response over the sleeper length, is considered to contribute to the total noise.

The equivalent sound powers are calculated by combining the predicted vibration spectra with radiation efficiencies in one-third octave bands. For the rail, an equivalent sources model is used which models the radiation from an infinitely long structure (i.e., assumed to be two-dimensional [126]). The radiation efficiency for vertical and lateral waves is based on predetermined calculations for unit amplitude motion of a rail in free space in either the vertical or lateral direction, depicted in Fig. B.1, and is then combined with the actual amplitude of the rail vibration. According to Zhang et al. [127], the proximity of the ground has a small effect at low frequencies for the lateral response, and to greater extent for the vertical response. For the sleeper, a model based on a baffled rectangular plate is used, which gives a radiation efficiency close to 1 for most frequencies within consideration.

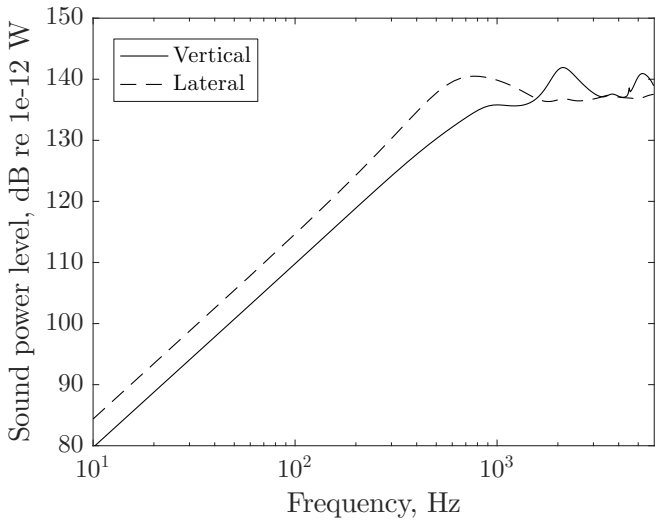

Figure B.1: TWINS radiated sound power per metre of 60E1 rail for 1 m/s peak velocity at the centroid due to vertical and lateral rigid motions

Once the sound radiation (power per unit length, W'_n) is determined for each wave with waveshape ψ_{jn}, it is combined with the average squared amplitude in each wave ($\overline{A_n^2}$) in one-third octave bands to give the total radiated power as:

$$W = \sum_n \overline{A_n^2} W'_n \tag{B.5}$$

in which

$$\overline{A_n^2} = \left| \sum_K F_k \beta_{kn} \right|^2 \left(\frac{1}{\delta_n L} \right) \tag{B.6}$$

where δ_n is the real part of the propagation constant s for wave n.

In Eq. (B.5), the assumption is made that the total power is the sum of the power for each wave. This is not accurate at low frequencies, since the phase of the individual waves

becomes important [4]. Once the waves propagate, they can be treated as incoherent as their wavelengths are different.

The above description is based on an arbitrary number of waves. TWINS is used either with a detailed FE model of the rail cross-section or by the simpler Timoshenko beam model for the vertical and lateral directions. For simplicity, the latter is considered, where only four waves exist.

In this model, the rail and sleeper responses are based a Timoshenko beam supported on a continuous double layer support, representing the pads, sleepers and ballast. The sleeper can be represented as a mass (bibloc) or as a flexible beam for the vertical direction only (monobloc). The same track model is used for both the vertical and lateral directions, with different parameter values.

The cross receptance is based on the geometrical average of the vertical (α_{yy}) and lateral (α_{zz}) receptances as in Eq. (5.6) [62]. The partial receptances (β_{kn}) satisfy the following:

$$\alpha_{yy} = \beta_{y1}\psi_1 + \beta_{y2}\psi_2 \tag{B.7}$$

$$\alpha_{zz} = \beta_{z3}\psi_3 + \beta_{z4}\psi_4 \tag{B.8}$$

$$\alpha_{yz} = \beta_{y3}\psi_3 + \beta_{y4}\psi_4 \tag{B.9}$$

$$= \beta_{z1}\psi_1 + \beta_{z2}\psi_2 \tag{B.10}$$

where y and z are the vertical or lateral directions and the partial cross receptances are also given based on Eq. (5.6).

References

[1] D. Kostovasilis, D.J. Thompson, and M.F.M. Hussein. The effect of vertical-lateral coupling of rails including initial curvature. In *Proceedings of the 22nd International Congress on Sound and Vibration (ICSV22)*, Florence, Italy, 2015.

[2] D. Kostovasilis, D.J. Thompson, and M.F.M. Hussein. A semi-analytical beam model for the vibration of railway tracks. *Journal of Sound and Vibration*, 393: 321–337, 2016.

[3] C.E. Hanson, J.C. Ross, and D.A. Towers. High-speed ground transportation noise and vibration impact assessment, FRA report number: DOT/FRA/ORD-12/15. Technical report, Department of Transportation, Federal Railroad Administration, 2012.

[4] D.J. Thompson. *Railway noise and vibration: mechanisms, modelling and means of control*. Elsevier Science, Oxford, UK, 2009.

[5] M.G. Dittrich and X. Zhang. The Harmonoise/IMAGINE model for traction noise of powered railway vehicles. *Journal of Sound and Vibration*, 293(3-5):986–994, 2006.

[6] P.J. Remington. Wheel/rail noise - Part I: Characterization of the wheel/rail dynamic system. *Journal of Sound and Vibration*, 46(3):359–379, 1976.

[7] J.D. Cutnell and K.W. Johnson. *Physics*. John Wiley and Sons, New York, 9^{th} edition, 2012.

[8] British Standards Institution. BS EN 61672-1:2013: Electroacoustics. Sound level meters. Specifications, 2013.

[9] K.L. Knothe and S.L. Grassie. Modelling of railway track and vehicle/track interaction at high frequencies. *Vehicle System Dynamics*, 22(3-4):209–262, 1993.

[10] S. Peters, B. Hemsworth, and B. Woodward. Noise radiation by a railway rail. *Journal of Sound and Vibration*, 35(1):146–150, 1974.

[11] E.K. Bender and P.J. Remington. The influence of rails on train noise. *Journal of Sound and Vibration*, 37(3):321–334, 1974.

[12] P.J. Remington. Wheel/rail noise-Part IV: Rolling noise. *Journal of Sound and Vibration*, 46(3):419–436, 1976.

[13] P.J. Remington and J.D. Stahr. The effects on noise of changes in wheel/rail system parameters. *Journal of Sound and Vibration*, 87(2):221–229, 1983.

[14] D.J. Thompson. Predictions of acoustic radiation from vibrating wheels and rails. *Journal of Sound and Vibration*, 120(2):275–280, 1988.

[15] P.J. Remington. Wheel/rail rolling noise, I: Theoretical analysis. *The Journal of the Acoustical Society of America*, 81(6):1805–1823, 1987.

[16] P.J. Remington. Wheel/rail rolling noise, II: Validation of the theory. *Journal of the Acoustical Society of America*, 81(6):1824–1832, 1987.

[17] D.J. Thompson, B. Hemsworth, and N. Vincent. Experimental validation of the TWINS prediction program for rolling noise Part 1: Description of the model and method. *Journal of Sound and Vibration*, 193(1):123–135, 1996.

[18] D.J. Thompson. Wheel-rail noise generation, part I: Introduction and interaction model. *Journal of Sound and Vibration*, 161(3):387–400, 1993.

[19] D.J. Thompson. Wheel-rail noise generation, part II: Wheel vibration. *Journal of Sound and Vibration*, 161(3):401–419, 1993.

[20] D.J. Thompson. Wheel-rail noise generation, part III: Rail vibration. *Journal of Sound and Vibration*, 161(3):421–446, 1993.

[21] D.J. Thompson. Wheel-rail noise generation, Part IV: Contact zone And results. *Journal of Sound and Vibration*, 161(3):447–466, 1993.

[22] D.J. Thompson. Wheel-rail noise generation, part V: Inclusion of wheel rotation. *Journal of Sound and Vibration*, 161(3):467–482, 1993.

[23] D.J. Thompson, P. Fodiman, and H. Mahé. Experimental validation of the TWINS prediction program for rolling noise Part 2: Results. *Journal of Sound and Vibration*, 193(1):137–147, 1996.

[24] C.J.C. Jones and D.J. Thompson. Extended validation of a theoretical model for railway rolling noise using novel wheel and track designs. *Journal of Sound and Vibration*, 267(3):509–522, 2003.

[25] T. Kitagawa and D.J. Thompson. Comparison of wheel/rail noise radiation on Japanese railways using the TWINS model and microphone array measurements. *Journal of Sound and Vibration*, 293(3-5):496–509, 2006.

[26] N. Vincent, P. Bouvet, D.J. Thompson, and P.E. Gautier. Theoretical optimization of track components to reduce rolling noise. *Journal of Sound and Vibration*, 193 (1):161–171, 1996.

[27] D.J. Thompson, C.J.C. Jones, T.P. Waters, and D. Farrington. A tuned damping device for reducing noise from railway track. *Applied Acoustics*, 68(1):43–57, 2007.

[28] G. Squicciarini, D.J. Thompson, M.G. Toward, and R. A. Cottrell. The effect of temperature on railway rolling noise. *Proceedings of the Institution of Mechanical Engineers, Part F: Journal of Rail and Rapid Transit*, 230(8):1777–1789, 2016.

[29] D.J. Thompson. Theoretical modelling of wheel-rail noise generation. *Proceedings of the Institution of Mechanical Engineers, Part F: Journal of Rail and Rapid Transit*, 205(2):137–149, 1991.

[30] D.J. Thompson. Railway noise and vibration: the use of appropriate models to solve practical problems. In *Proceedings of the 21st International Congress on Sound and Vibration (ICSV21)*, Beijing, China, 2014.

[31] M-Y. Kim, N.I. Kim, and H-T. Yun. Exact dynamic and static stiffness matrices of shear deformable thin-walled beam-columns. *Journal of Sound and Vibration*, 267:29–55, 2003.

[32] S.S. Rao. *Vibration of Continuous Systems*. John Wiley & Sons, Inc., New Jersey, 2007.

[33] M. Hetenyi. *Beams on elastic foundation: Theory with applications in the fields of civil and mechanical engineering*. University of Michigan Press, 1946.

[34] S.M. Han, H. Benaroya, and T. Wei. Dynamics of transversely vibrating beams using four engineering theories. *Journal of Sound and Vibration*, 225(5):935–988, 1999.

[35] Lord Rayleigh. *Theory of Sound*, volume 1. Dover Publications, New York, 1945.

[36] S.P. Timoshenko. On the correction for shear of the differential equation for transverse vibrations of prismatic bars. *Philosophical Magazine*, 41(245):744–746, 1921.

[37] S.P. Timoshenko. On the transverse vibrations of bars of uniform corss-section. *Philosophical Magazine*, 43(1):125–131, 1922.

[38] S.L. Grassie, R.W. Gregory, D. Harrison, and K.L. Johnson. The dynamic response of railway track to high frequency vertical excitation. *Journal of Mechanical Engineering Science*, 24(2):77–90, 1982.

[39] T.X. Wu and D.J. Thompson. The influence of random sleeper spacing and ballast stiffness on the vibration behaviour of railway track. *Acta Acustica*, 86(2):313–321, 2000.

[40] T.X. Wu and D.J. Thompson. On the parametric excitation of the wheel/track system. *Journal of Sound and Vibration*, 278(4-5):725–747, 2004.

[41] K. Popp, H. Kruse, and I. Kaiser. Vehicle-track dynamics in the mid-frequency range. *Vehicle System Dynamics*, 31:423–464, 1999.

[42] C.J.C. Jones, X. Sheng, and M. Petyt. Simulations of ground vibration from a moving harmonic load on a railway track. *Journal of Sound and Vibration*, 231 (3):739–751, 2000.

[43] J.C.O. Nielsen and T.J.S. Abrahamsson. Coupling of physical and modal components for analysis of moving non-linear dynamic systems on general beam structures. *International Journal for Numerical Methods in Engineering*, 33(9):1843–1859, 1992.

[44] L. Andersen, S.R.K. Nielsen, and P.H. Kirkegaard. Finite element modelling of infinite euler beams on Kelvin foundations exposed to moving loads in convected co-ordinates. *Journal of Sound and Vibration*, 241(4):587–604, 2001.

[45] K.K. Ang and J. Dai. Response analysis of high-speed train travelling on curved track. In Valery Telichenko, Andrey Volkov, and Irina Bilchuk, editors, *Proceedings of the 14th International Conference on Computing in Civil and Building Engineering (14th ICCCBE)*. Publishing House"ASV", 2012.

[46] T.X. Wu and D.J. Thompson. Wheel/rail non-linear interactions with coupling between vertical and lateral directions. *Vehicle System Dynamics*, 41(1):27–49, 2004.

[47] J. Yang and D.J. Thompson. A non-reflecting boundary for use in a finite element beam model of a railway track. *Journal of Sound and Vibration*, 337:199–217, 2015.

[48] D.G. Duffy. The response of an infinite railroad track to a moving, vibrating mass. *Journal of Applied Mechanics*, 57:66–73, 1990.

[49] M.F.M. Hussein and H.E.M. Hunt. Modelling of floating-slab tracks with continuous slabs under oscillating moving loads. *Journal of Sound and Vibration*, 297 (1-2):37–54, 2006.

[50] S.L. Grassie, R.W. Gregory, and K.L. Johnson. The dynamic response of railway track to high frequency lateral excitation. *Journal of Mechanical Engineering Science*, 24(2):91–95, 1982.

[51] G.A. Hunt. *Dynamic analysis of railway vehicle/track interaction forces*. PhD thesis, Loughborough University of Technology, 1986.

[52] W. Scholl. Schwingungsuntersuchungen an Eisenbahnschienen. *Acustica*, 52:10–15, 1982.

[53] W. Scholl. Two theoretical models for wave propagation in rails. In *Second International Conference in Recent Advances in Structural Dynamics*, pages 699–707, Southampton, 1984.

[54] T.X. Wu and D.J. Thompson. A double Timoshenko beam model for vertical vibration analysis of railway track at high frequencies. *Journal of Sound and Vibration*, 224(2):329–348, 1999.

[55] T.X. Wu and D.J. Thompson. Analysis of lateral vibration behavior of railway track at high frequencies using a continuously supported multiple beam model. *The Journal of the Acoustical Society of America*, 106(3):1369–1376, 1999.

[56] A. Bhaskar, K.L. Johnson, G.D. Wood, and J. Woodhouse. Wheel-rail dynamics with closely conformal contact. Part 1: dynamic modelling and stability analysis. *Proceedings of the Institution of Mechanical Engineers, Part F: Journal of Rail and Rapid Transit*, 211(1):11–26, 1997.

[57] B. Ripke and K. Knothe. Die unendlich lange Schiene auf diskreten Schwellen bei harmonischer Einzellasterregung. *Fortschritt-Berichte VDI*, Reihe 11(Nr. 155), 1991.

[58] J. Yang. *Dynamic models of railway track at high frequency.* MSc thesis, University of Southampton, 2009.

[59] J. Yang, D.J. Thompson, and A. Bhaskar. Dynamic models of railway track taking account of cross-section deformation at high frequency. In *10th International Workshop on Railway Noise, 18 - 22 Oct 2010*, Nagahama, Japan, 2010.

[60] M.A. Heckl. Coupled waves on a periodically supported Timoshenko beam. *Journal of Sound and Vibration*, 252(5):849–882, 2002.

[61] K. Popp and W. Schiehlen. System dynamics and long-term behaviour of railway vehicles, track and subgrade. In Friedrich Pfeiffer, editor, *Lecture Notes in Applied Mechanics*, volume 6. Springer-Verlag, 2005.

[62] D.J. Thompson and N. Vincent. Track dynamic behaviour at high frequencies. Part 1: Theoretical models and laboratory measurements. *Vehicle System Dynamics*, 24(sup1):86–99, 1995.

[63] J. Ryue, D.J. Thompson, P.R. White, and D.R. Thompson. Decay rates of propagating waves in railway tracks at high frequencies. *Journal of Sound and Vibration*, 320(4-5):955–976, 2009.

[64] K.L. Knothe, Z. Strzyzakowski, and K. Willner. Rail vibrations in the high frequency range. *Journal of Sound and Vibration*, 169(1):111–123, 1994.

[65] J. Ryue, D.J. Thompson, P.R. White, and D.R. Thompson. Investigations of propagating wave types in railway tracks at high frequencies. *Journal of Sound and Vibration*, 315(1-2):157–175, 2008.

[66] D.J. Mead. A general theory of harmonic wave propagation in linear periodic systems with multiple coupling. *Journal of Sound and Vibration*, 27:235–260, 1973.

[67] L. Gavrić. Computation of propagative waves in free rail using a finite element technique. *Journal of Sound and Vibration*, 185:531–543, 1995.

[68] L. Gry. Dynamic modelling of railway track based on wave propagation. *Journal of Sound and Vibration*, 195:477–505, 1996.

[69] C.M. Nilsson, C.J.C. Jones, D.J. Thompson, and J. Ryue. A waveguide finite element and boundary element approach to calculating the sound radiated by railway and tram rails. *Journal of Sound and Vibration*, 321(3-5):813–836, 2009.

[70] W. Li, R.A. Dwight, and T. Zhang. On the study of vibration of a supported railway rail using the semi-analytical finite element method. *Journal of Sound and Vibration*, 345:121–145, 2015.

[71] S.L. Grassie. Dynamic modeling of concrete railway sleepers. *Journal of Sound and Vibration*, 187(5):799–813, 1995.

[72] M.H.A. Janssens and D.J. Thompson. Improvements of ballast and sleeper description in TWINS. Step 2: development and implementation of theoretical models. Technical report, TNO report TPD-HAG-RPT- 960108, 1996.

[73] A. Nordborg. Vertical rail vibrations: parametric excitation. *Acustica*, 84:289–300, 1998.

[74] N. Frémion, J.P. Goudard, and N. Vincent. Improvement of ballast and sleeper description in TWINS. Technical report, VIBRATEC report ref. 072.028a for the account of the ERRI C163 committee, 1996.

[75] J.C.O. Nielsen. Acoustic optimization of railway sleepers. *Journal of Sound and Vibration*, 231(3):753–764, 2000.

[76] M. Oregui, Z. Li, and R. Dollevoet. An investigation into the vertical dynamics of tracks with monoblock sleepers with a 3D finite-element model. *Proceedings of the Institution of Mechanical Engineers, Part F: Journal of Rail and Rapid Transit*, 230(3):891–908, 2015.

[77] V.Z. Vlasov. *Thin-walled elastic beams*. Israel Program for Scientific Translations Ltd, 2^{nd} edition, 1961.

[78] E.J. Sapountzakis. Bars under torsional loading: A generalized beam theory approach. *ISRN Civil Engineering*, 2013:1–39, 2013.

[79] J.R. Banerjee. Explicit frequency equation and mode shapes of a cantilever beam coupled in bending and torsion. *Journal of Sound and Vibration*, 224:267–281, 1999.

[80] C. Adam. Forced vibrations of elastic bending-torsion coupled beams. *Journal of Sound and Vibration*, 221(2):273–287, 1999.

[81] J.F. Monsalve-Cano and J. Darío Aristizábal-Ochoa. Stability and free vibration analyses of an orthotropic singly symmetric Timoshenko beam-column with generalized end conditions. *Journal of Sound and Vibration*, 328(4-5):467–487, 2009.

[82] A.E.H. Love. *A treatise on the mathematical theory of elasticity*. Dover Publications, New York, 4^{th} edition, 1944.

[83] L.S.D. Morley. Elastic waves in a naturally curved rod. *The Quarterly Journal of Mechanics and Applied Mathematics*, XIV(2):155–172, 1961.

[84] T. Irie, G. Yamada, and I. Takahashi. The steady state in-plane response of a curved Timoshenko beam with internal damping. *Ingenieur-Archiv*, 49:41–49, 1980.

[85] T. Irie, G. Yamada, and I. Takahashi. The steady state out-of-plane response of a Timoshenko curved beam with internal damping. *Journal of Sound and Vibration*, 71:145–156, 1980.

[86] A.S. Gendy and A.F. Saleeb. Vibration analysis of coupled extensional/flexural/-torsional modes of curved beams with arbitrary thin-walled sections. *Journal of Sound and Vibration*, 174(2):261–274, 1994.

[87] S-P. Chang, S-B. Kim, and M-Y. Kim. Stability of Shear Deformable Thin-Walled Space Frames and Circular Arches. *Journal of Engineering Mechanics*, 122(9): 844–854, 1996.

[88] M-Y. Kim, B-C. Min, and M-W. Suh. Spatial stability of nonsymmetric thin-walled curved beams. I: Analytical approach. *Journal of Engineering Mechanics*, 126(5):497–505, 2000.

[89] N-I. Kim and M-Y. Kim. Spatial free vibration of shear deformable circular curved beams with non-symmetric thin-walled sections. *Journal of Sound and Vibration*, 276(1-2):245–271, 2004.

[90] M-Y. Kim, S-B. Kim, and N-I. Kim. Spatial stability of shear deformable curved beams with non-symmetric thin-walled sections. I: Stability formulation and closed-form solutions. *Computers and Structures*, 83:2525–2541, 2005.

[91] S. Nair, V.K. Garg, and Y.S. Lai. Dynamic stability of a curved rail under a moving load. *Applied Mathematical Modelling*, 9(1):220–224, 1985.

[92] K-F. Li, W-N. Liu, V. Markine, and Z-W. Han. Analytical study on the dynamic displacement response of a curved track subjected to moving loads. *Journal of Zhejiang University SCIENCE A*, 14(12):867–879, 2013.

[93] D. Kostovasilis, S.G. Koroma, M.F.M. Hussein, and J.S. Owen. The effect of curvature on the dynamic behaviour of a railway track. In *Proceedings of the Institute of Acoustics Vol. 35 Pt. 1. Acoustics 2013*, pages 170–175, Nottingham, United Kingdom, 2013.

[94] D. Kostovasilis, S.G. Koroma, M.F.M. Hussein, and J.S. Owen. A comparison between the use of straight and curved beam elements for modelling curved railway tracks. In *Proceedings of the 11th Biennial International Conference on Vibration Problems (ICOVP-2013)*, Lisbon, Portugal, 2013.

[95] J. Dai and K.K. Ang. Steady-state response of a curved beam on a viscously damped foundation subjected to a sequence of moving loads. *Proceedings of the Institution of Mechanical Engineers, Part F: Journal of Rail and Rapid Transit*, 229(4):375–394, 2015.

[96] VI-Rail 16.0. *Documentation*. VI-grade GmbH, Marburg, Germany, 2014.

[97] B. Betgen, G. Squicciarini, and D.J. Thompson. On the prediction of rail cross mobility and track decay rates using Finite Element Models. In *Proceedings of the 10th European Congress and Exposition on Noise Control Engineering (EURONOISE2015)*, pages 2019–2024, Maastricht, Netherlands, 2015. EAA-NAG-ABAV.

[98] COMSOL Multiphysics. *COMSOL 4.4*. COMSOL AB., Stockholm, Sweden, 2013.

[99] S.P. Timoshenko and J.N. Goodier. *Theory of elasticity*. McGraw-Hill Book Company, Inc., New York, 3^{rd} edition, 1951.

[100] J. Blaauwendraad. Axisymmetry in elasticity - "Old wine in new bottles". *Heron*, 31(1):33–48, 1986.

[101] F. Tisseur and K. Meerbergen. The quadratic eigenvalue problem. *SIAM Review*, 43(2):235–286, 2001.

[102] W.D. Pilkey. *Analysis and design of elastic beams: Computational methods*. Wiley, New York, 2002.

[103] W.A.M. Alwis and C.M. Wang. Wagner term in flexural-torsional buckling of thin-walled open-profile columns. *Engineering Structures*, 18(2):125–132, 1996.

[104] I. Senjanović, S. Tomašević, and N. Vladimir. An advanced theory of thin-walled girders with application to ship vibrations. *Marine Structures*, 22(3):387–437, 2009.

[105] R. Pavazza. Torsion of thin-walled beams of open cross-section with influence of shear. *International Journal of Mechanical Sciences*, 47(7):1099–1122, 2005.

[106] E.J. Sapountzakis and V.J. Tsipiras. Shear deformable bars of doubly symmetrical cross section under nonlinear nonuniform torsional vibrationsapplication to torsional postbuckling configurations and primary resonance excitations. *Nonlinear Dynamics*, 62(4):967–987, 2010.

[107] V.G. Mokos and E.J. Sapountzakis. Secondary torsional moment deformation effect by BEM. *International Journal of Mechanical Sciences*, 53(10):897–909, 2011.

[108] J.R. Kuttler and V.G. Sigillito. On curve veering. *Journal of Sound and Vibration*, 75(4):585–588, 1981.

[109] J.L. du Bois, S. Adhikari, and N.J. Lieven. Eigenvalue curve veering in stressed structures: An experimental study. *Journal of Sound and Vibration*, 322(4-5): 1117–1124, 2009.

[110] N.C. Perkins and C.D. Mote. Comments on curve veering in eigenvalue problems. *Journal of Sound and Vibration*, 106(3):451–463, 1986.

[111] B. Kang, C.H. Riedel, and C.A. Tan. Free vibration analysis of planar curved beams by wave propagation. *Journal of Sound and Vibration*, 260(1):19–44, 2003.

[112] R.S. Langley. Wave motion and energy flow in cylindrical shells. *Journal of Sound and Vibration*, 169(1):29–42, 1994.

[113] S.J. Walsh and R.G. White. Vibrational power transmission in curved beams. *Journal of sound and vibration*, 233(3):455–499, 2000.

[114] A.B. Basset. On the theory of elastic wires. *Proceedings of the London Mathematical Society*, 105(27):105–127, 1891.

[115] D.J. Thompson. Experimental analysis of wave propagation in railway tracks. *Journal of Sound and Vibration*, 203(5):867–888, 1997.

[116] D.J. Thompson, W.J. Van Vliet, and J.W. Werheij. Developments of the indirect method for measuring the high frequency dynamic stiffness of resilient elements. *Journal of Sound and Vibration*, 213(1):169–188, 1998.

[117] H. Venghaus, M.G. Toward, and E. Scossa-Romano. Characteristics of rail pads tested at laboratory and under track conditions. In *Proceedings of the 10th European Congress and Exposition on Noise Control Engineering (EURONOISE2015)*, pages 2059–2064, Maastricht, Netherlands, 2015.

[118] D.J. Ewins. *Modal Testing: Theory and Practice*. Research Studies Press Ltd., Letchworth, Hertfordshire, England, 1984.

[119] D.A. Wunsch. *Complex variables with applications*. Pearson Addison-Wesley, Boston, 3^{rd} edition, 2006.

[120] British Standards Institution. BS EN 15461:2008+A1:2010: Railway applications - Noise emission - Characterization of the dynamic properties of track selections for pass by noise measurements, 2010.

[121] C.J.C. Jones, D.J. Thompson, and R.J. Diehl. The use of decay rates to analyse the performance of railway track in rolling noise generation. *Journal of Sound and Vibration*, 293(3-5):485–495, 2006.

[122] W.A. Fladung. Windows used for impact testing. In *Proceedings of the 15th International Modal Analysis Conference (IMAC-XV)*, pages 1662–1666, Orlando, 1997.

[123] N. Vincent and D.J. Thompson. Track Dynamic Behaviour at High Frequencies. Part 2: Experimental Results and Comparisons with Theory. 24(sup1):100–114, 1995.

[124] T.W. Wu. *Boundary Element Acoustics*. WIT Press, Southampton, 2000.

[125] D.A. Russell, J.P. Titlow, and Y.-J. Bemmen. Acoustic monopoles, dipoles, and quadrupoles: An experiment revisited. *American Journal of Physics*, 67(8):660 – 664, 1999.

[126] D.J. Thompson, C.J.C. Jones, and N. Turner. Investigation into the validity of two-dimensional models for sound radiation from waves in rails. *The Journal of the Acoustical Society of America*, 113(1):1965–1974, 2003.

[127] X. Zhang, G. Squicciarini, and D.J. Thompson. Sound radiation of a railway rail in close proximity to the ground. *Journal of Sound and Vibration*, 362:111–124, 2016.